THE ANTINUCLEON–NUCLEON INTERACTION AT LOW ENERGY: SCATTERING AND PROTONIUM

Eberhard Klempt
Institut für Strahlen- und Kernphysik
der Rheinischen Friedrich-Wilhelms Universität
Nußallee 14-16, D–53115 Bonn, Germany

Franco Bradamante and Anna Martin
INFN and University of Trieste
Via A. Valerio 2, 34127 Trieste, Italy

Jean-Marc Richard
Institut des Sciences Nucléaires
Université Joseph Fourier–CNRS–IN2P3
53, avenue des Martyrs, F–38026 Grenoble Cedex
and
Institut de Physique Nucléaire
Université Claude Bernard–CNRS-IN2P3
4, rue Enrico Fermi, F–696222 Villeurbanne Cedex, France

June 12, 2002

Abstract

We present nucleon–antinucleon scattering experiments performed at the Low Energy Antiproton Ring (LEAR) of CERN. The data are reviewed and the underlying physics is discussed, in particular by comparison with the predictions of current models based on meson exchange and short-range absorption. A detailed description is given of protonium, which gives information on the interaction at zero energy and is the initial state when annihilation occurs at rest.

Acknowledgements

We would like to thank all the colleagues who shared our enthusiasm about this physics and with whom we had the pleasure to collaborate and interact over the past 20 years, in particular C.B. Dover, T.E.O. Ericson, L. Montanet, I.S. Shapiro, and J.J. de Swart. We also benefited from fruitful discussions with Mary Alberg, C. Amsler, Chr. Batty, T. Bressani, P. Dalpiaz, D. Gotta, D. Herzog, I. Iazzi, T. Johannson, K. Kilian, H. Koch, M. Kretschmar, F. Myhrer, K. Paschke, L. Simons, T. Shibata, J. Speth, R.G.E. Timmermans, R. Vinh Mau, Th. Walcher, and R.E. Welsh. Very special thanks are also due to all our collaborators in Grenoble, Mainz, and Trieste.

Several of our colleagues passed away during recent years. It is impossible to review this physics without remembering their important role and outstanding contributions. We would like to mention in particular G. Alberi, B. Deutsch, C.B. Dover, N. Hamann, R. Hess, K. Holinde, H. Poth and I.S. Shapiro.

One of the authors (J.-M. R.) gratefully acknowledges the generous support of the Alexander von Humboldt Stiftung and the enjoyable hospitality at the University of Bonn.

Contents

Chapter 1

Introduction

1.1 From the Dirac equation to the discovery of the antiproton

The history of antimatter is well-known and hardly needs to be presented in detail. Several interesting books have been written on the birth and the development of particle physics, with many entertaining anecdotes. One may quote here Pais [1], Segrè [2], Cahn and Goldhaber [3], Lederman [4], etc.

We wish to remind only a few points. First, the antiparticle associated with the electron was thought to be possibly the proton. The large mass of the proton, as compared to that of the electron, could have been due to its carrying the inertia of the Dirac sea. In modern particle physics, we are accustomed to symmetry breaking phenomena of such large magnitude. A serious problem with this hypothesis, however, was to understand how the hydrogen atom could survive internal annihilation. Of course, the discovery of the positron by Anderson in 1932 [5] clarified the situation.

A second problem arose after the measurement of the magnetic moment of the proton by O. Stern in 1933, with the result $\mu \simeq 2.8\mu_{\rm N}$, where $\mu_{\rm N} = e\hbar/(2m_{\rm p})$ is the value expected for a Dirac particle [3]. It was then not completely clear whether the proton possesses an associated antiparticle, since it does not obey the Dirac equation strictly. The answer was given by the famous experiment by Chamberlain et al. at Berkeley in 1955 [6]. We have eventually understood that the abnormal magnetic moment of the proton arises from its composite nature, and that particle–antiparticle symmetry is more general than a peculiar property of the Dirac equation.

Another surprise came with the first measurement of antiproton cross sections [7]. The annihilation part is much larger than the elastic one for low antiproton momenta. We shall often return to this observation along this review. Let us briefly say here that this large inelastic cross section is another consequence of the composite structure of the proton, i.e., its finite size.

1.2 Antiproton beams and facilities

In the early experiments performed at Berkeley, BNL, CERN or KEK, antiprotons were used just after being produced, in the form of secondary beams with low intensity, ill-defined energy, and a large contamination by negatively charged mesons. It was only in the last 20 years that new devices were elaborated to provide antiproton beams with high purity, intensity and momentum-resolution, at CERN and at Fermilab.

At CERN, in 1968, Simon van der Meer proposed the "stochastic cooling technique" to improve beam quality and intensity in storage rings, and in the following years, experiments (ICE, Initial Cooling Experiment) demonstrated its feasibility. In 1978, the decision to go ahead with the Antiproton Project was taken at CERN, and an Antiproton Accumulator (AA) was built to apply stochastic cooling to antiprotons. The AA started up in 1980, and in 1981 antiprotons were sent to

the ISR (Intersecting Storage Ring, dismounted in 1983) and soon afterwards to the Super Proton Synchrotron (SPS), converted into a proton-antiproton collider (the "S$\bar{\text{p}}$pS" collider). The $\bar{\text{p}}$ beam energy was first 270 GeV, and then increased up to 315 GeV. The collider experiments at CERN were stopped in 1990.

In 1982, LEAR (Low Energy Antiproton Ring) was launched for completion. This new machine, which will be described in some detail in Chap. 2, provided very high quality antiprotons beams with momenta between 100 MeV/c and 2 GeV/c in the period 1983-1996, when it was stopped.

An proton–antiproton collider with centre-of-mass energy $s^{1/2}$ in the range from about 2 to 8 GeV, SuperLEAR, was proposed at CERN, mainly to study CP violation with $\overline{\Lambda}\Lambda$ systems and heavy quark spectroscopy. The proposal was discussed by the CERN-SPSLC committee, but not recommended for approval. Presently at CERN the only $\bar{\text{p}}$ facility is AD (Antiproton Decelerator); it provides antiprotons with momentum from 300 to 100 MeV/c, without slow extraction.

Building on the CERN innovation and experiences, Fermilab constructed an antiproton source. The first $\bar{\text{p}}$p collider run began late in 1986; with its centre-of-mass energy of 1.8 TeV (900 GeV on 900 GeV) it is today the world's highest-energy accelerator. A crucial parameter is the luminosity, and an upgrade of the antiproton source and of the Main Injector has been done recently. Fermilab has today the world's highest-intensity source (the production rate is 10^{11} $\bar{\text{p}}$/hour) and work is going on for further improvement. Up to November 2000, precision experiments using $\bar{\text{p}}$ could be performed by putting a hydrogen gas target in the Accumulator, where the antiprotons have about 8 GeV kinetic energy: this medium-energy program is now terminated, and for the next five years the antiprotons will only be used for the Tevatron Run II.

In the future (very likely only after Run IIB), it is possible that a new, small, low-energy $\bar{\text{p}}$ facility will be built at Fermilab. The motivations for such a facility come both from nuclear and particle physics, and from long-term future technical projects, like $\bar{\text{p}}$p-annihilation-fuelled interstellar travel [8, 9]. Both a low-energy ring (from 2 GeV/c down to a few tens of MeV/c) and a larger storage ring (1 to 10 GeV/c) are being considered.

Two other projects are presently being pursued. The first in Japan, where the Japan Hadron Facility of KEK and the Neutron Science Project of JAERI (Japan Atomic Energy Research Institute) have been merged to one project: the JAERI-KEK Joint Project for high-intensity proton-accelerator facility. The Project was approved for construction in December 2000 by the Japanese Government. The accelerator for the joint project comprises a 15 μA, 50 GeV proton synchrotron, to explore a broad range range of topics in nuclear and particle physics [10, 11]. Secondary beams of antiprotons will have the highest intensity in the world in this energy domain, and ideas to store them in LEAR-like facilities will be pursued in the long term.

The second project has been proposed at GSI [12], as part of the hadron facility. It is based on a new accelerator ring, using the present SIS18 accelerator as injector, but with a rigidity more than an order of magnitude larger (protons will be accelerated to 50 GeV/c). The facility will comprise ring(s) to accumulate, store and cool intense, highest-quality primary and secondary beams, from short-lived exotic nuclei to antiprotons, for research in hadronic, nuclear, atomic and plasma physics.

1.3 Physics with antiprotons, an overview

The physics directly or indirectly associated with antiproton beams covers an enormous field. Already mentioned are particle–antiparticle symmetry, and the $\bar{\text{p}}$p cross sections, whose low-energy behaviour is discussed in Chapter 4.

Antiproton–proton colliders opened a new era in high-energy physics, reaching the TeV range. At these high energies, there is a considerable interest in studying the diffraction peak and the energy dependence of the cross sections. Colliders are more famous, however, for their contribution to the physics of intermediate bosons, jets or heavy flavours. The $\mathrm{W}^{\pm}$ and Z^{0} bosons were discovered at the CERN collider and the top quark at the Fermilab Tevatron, where the Higgs boson is presently searched for actively.

The quality of the new antiproton beams motivated experiments which were not conceivable earlier. In the CERN ISR, antiprotons interacted with a thin hydrogen jet target to form charmonium mesons. This experiment [13,14], later resumed at the Fermilab accumulator [15], gave very accurate information on heavy quark–antiquark bound states.

Many experiments have been performed at LEAR. They dealt with many facets of physics. Relevant to this review are experiments which measured $\bar{\mathrm{p}}\mathrm{p}$ and $\bar{\mathrm{n}}\mathrm{p}$ total, elastic, and annihilation cross-sections, and also $\bar{\mathrm{p}}\mathrm{p}$ charge-exchange and strangeness-exchange reactions. In many instances, precise differential cross-sections were first measured, as well as some spin parameters.

The first results at LEAR were obtained in experiments where antiprotons were scattered on nuclei. The results on elastic and inelastic cross sections stimulated many theoretical papers [16, 17]. Annihilation on nuclei was compared with $\overline{\mathrm{N}}\mathrm{N}$ annihilation [18], and heavy hypernuclei were produced by annihilation of antiprotons on heavy nuclei [19]. More recent experiments deal with fission and multifragmentation induced by antiprotons, and annihilation on peripheral neutrons [20].

Strong interactions at zero energy were studied with antiprotonic atoms. The topics involves some atomic physics to understand how antiprotons are captured and cascade down to low-lying orbits where they experience strong interactions. New metastable states of the (He, $\bar{\mathrm{p}}$, e^-) system have been found [21] and will be further studied [22]. Let us also mention that antiprotons can be used for some solid state experiments, where they are sometimes more appropriate than muons.

A large fraction of the LEAR experimental programme was devoted to spectroscopy, in particular to the search of exotic meson states ($\mathrm{qq}\bar{\mathrm{q}}\bar{\mathrm{q}}$ baryonium states, $\mathrm{q}\bar{\mathrm{q}}\mathrm{g}$ hybrids, gg glueballs) produced in the $\overline{\mathrm{N}}\mathrm{N}$ annihilation process, both at rest and in flight. The structure of the proton in the time-like region was probed by measuring the rare annihilation channel $\bar{\mathrm{p}}\mathrm{p}\rightarrow\mathrm{e}^+\mathrm{e}^-$.

Fundamental symmetries were tested, with the comparison of the inertial mass of the antiproton with that of the proton, as a test of CPT, and the investigation of CP asymmetries in the decay of neutral kaons by the so-called CPLEAR collaboration [23]. New measurements of inertial masses and gravitational tests are planned at the new AD facility of CERN [24]. The comparison of hydrogen and antihydrogen atomic spectroscopy will also probe symmetries with high accuracy.

The role of antimatter in astrophysics remains controversial. Some early cosmological models suggested that antimatter was as abundant as matter in the Universe. Modern cosmology tends to favour scenarios where antimatter has disappeared, thanks to baryon number violation, CP violation and absence of thermodynamical equilibrium in the early Universe. Antimatter had already disappeared when nucleosynthesis began: otherwise the present abundance of ^{3}He should be much larger, due to antiproton annihilation on ^{4}He, which yields ^{3}He with high probability, as shown by the experiment PS179 at LEAR [25]. For a recent discussion, see, e.g., [26]. Still, antiprotons and antinuclei are searched for in cosmic rays, perhaps as a result of dark matter interaction with galaxies. A new generation of balloon, satellite or space-station experiments has started [27, 28].

1.4 Nucleon–antinucleon interaction at low energy

In this review, we shall concentrate on the aspects dealing with strong interaction physics at low energy. This includes long-range and short-range $\overline{\mathrm{N}}\mathrm{N}$ forces, the possibility of $\overline{\mathrm{N}}\mathrm{N}$ bound states or resonances and the physics of protonium atoms. Both experimental and theoretical aspects will be discussed.

The challenge of antiproton scattering and annihilation at low energy consists of combining long-range physics, efficiently described by conventional meson-exchanges, and short-range physics, where direct interaction between quarks and antiquarks presumably takes place.

The situation is similar to the one encountered in NN physics, where long-range meson exchanges have to be supplemented by phenomenological hard cores, which still await a satisfactory description in terms of quark dynamics. Sophisticated potential models have been constructed (Paris, Bonn, Nijmegen,...), which summarise our theoretical knowledge of meson exchanges. The short

range parts of the potentials have been parametrised on the data, and the overall result is that predictions are in excellent agreement with the impressive NN data base.

Investigation of the $\overline{\mathrm{N}}\mathrm{N}$ sector allows to test on a new system the basic approach to NN physics (necessity of all exchanges, values of the coupling constants, symmetry requirements), in the presence of a short-range dynamics (annihilation) which plays a much more important role than in NN physics, and which is considerably more difficult to describe than the NN core repulsion.

The present approach to $\overline{\mathrm{N}}\mathrm{N}$ interaction is somewhat hybrid. The long-range part is described in terms of meson exchanges, the same as those used in the meson theory of nucleon–nucleon (NN) forces. The short-range part, and in particular the strong annihilation component is either mocked up by an *ad-hoc* imaginary potential or tentatively described in terms of quarks. Thus the phenomenological analyses aim at measuring the role of each part of the interaction. The theory should provide a unified picture of long- and short-range forces. In spite of the inherent difficulties of the problem (too many partial waves, complex phase-shifts), a phase-shift analysis of $\overline{\mathrm{N}}\mathrm{N}$ data has been carried out. It will be reviewed in Chaps. 3 and 6.

Optical-potential models incorporate our best knowledge of Yukawa forces, but describe annihilation empirically, and thus cannot provide much insight on the microscopic mechanisms operating at short distances. On the other hand, considerations based on flavour symmetry or on simple quark diagrams suggest relations between branching ratios for annihilation into various channels. To test these relations, one should take into account the probability of finding N and $\overline{\mathrm{N}}$ overlapping. This probability, which is likely to vary with spin and isospin, depends on the long-range dynamics.

$\overline{\mathrm{N}}\mathrm{N}$ physics is rich of many facets which are complementary and intimately connected. To extract the physics, one better applies some filters. For instance, some specific spin observables enhance the role of long-range forces, while in cross sections short-range dynamics plays a more important role.

When comparing the long-range NN and $\overline{\mathrm{N}}\mathrm{N}$ potentials, one notices a much stronger attraction in the latter case, at least in some channels (the $\overline{\mathrm{N}}\mathrm{N}$ potential turns out to depend on spin and isospin significantly). This led Shapiro and his collaborators [29] to speculate about the possibility of deuterium-like bound states and resonances of the $\overline{\mathrm{N}}\mathrm{N}$ system. A comprehensive review was given some years ago by Buck et al. [30].

The existence of such states, sometimes called quasi-nuclear bound states or resonances, or baryonia, heavily relies on annihilation not washing out the wave function built by the attractive elastic potential. The range of annihilation is thus a crucial quantity: simple baryon-exchange diagrams suggest a very short range, but huge form-factor corrections have to be applied; in the quark approach, the range is governed by the size of the quark distributions of the incoming nucleons and outgoing mesons, and turns out to be about 1 fm.

1.5 A guide to the related literature

The most direct and precise information on low-energy antiproton physics can be found in the Proceedings of the specialised Conferences and Workshops.

The series of European Antiproton Conferences was begun by L. Montanet at Chexbres [31] and continued regularly up to the Mainz conference [32–39].

The first LEAR Workshop was organised in 1979 at Karlsruhe [40] by Helmut Poth. Further Workshops were held [41–43] to discuss the machine developments, the planned experiments, and the interpretation of the results.

The European Symposia and the LEAR Workshops were merged in a new series of Low Energy Antiproton Physics (LEAP) conferences. The first one has been organised at Stockholm [44], the second in 1992 at Courmayeur, Italy [45], the third one in 1994, at Bled, Slovenia [21], the fourth at Dinkelsbühl, Germany in 1996 [46], the fifth at Villasimius, Italy, in 1998 [47], and the sixth one at Venice in 2000 [48]. Intermediate workshops were organized in Russia [49], [50] and [51].

More pedagogical introductions can be found in the Proceedings of the Low Energy Antiproton Schools organised at Erice irregularly [52–55]: the first one was devoted to fundamental symmetries,

the second to hadron spectroscopy, the third on $\overline{\mathrm{N}}\mathrm{N}$ and $\bar{\mathrm{p}}$-nucleus interaction, and the fourth was more oriented towards the physics issues of SuperLEAR.

The physics of SuperLEAR was discussed in particular at Tignes [42], and then presented in a document which was published in the Proceedings of a Workshop held at Les Houches [56]. A more updated and complete survey can be found in the Proceedings of the Zurich Workshop [57]. See also [58].

Finally, we shall also quote the reviews on $\bar{\mathrm{p}}$ physics by Walcher [59], Amsler and Myhrer [60], Dover et al. [61], Amsler [62], and Eades and Hartmann [63].

1.6 Outline

This review is organized as follows. In the next chapter (2), we present the antiproton beam available at CERN in the LEAR facility and discuss the set-up of the experiments mainly or partially devoted to study $\overline{\mathrm{N}}\mathrm{N}$ interaction. The formalism of elastic, charge-exchange and strangeness exchange $\overline{\mathrm{N}}\mathrm{N}$ scattering as well as protonium is presented in Chap. 3. The scattering data are presented and discussed in Chap. 4. Protonium formation and spectroscopy is the subject of Chap. 5. Chapter 6 contains a comparison between data and the most recent theoretical calculations. Conclusions are proposed in Chap. 7.

A second review article, presently in preparation, will be devoted to annihilation dynamics [64]. This overview of strong interaction physics at LEAR is split into two parts only for the sake of convenience, and for complying with the constraint of keeping a reasonable size. The physics of scattering and annihilation are, however, intimately correlated. Annihilation occurs from a protonium or $\overline{\mathrm{N}}\mathrm{N}$ scattering state which is strongly distorted by initial-state interaction. Also exotic mesons can be viewed either as composite of quarks, antiquarks and gluons or as hadron–hadron molecules. So a good knowledge of both quark–gluon dynamics and hadron–hadron interaction is required to analyse new meson states.

Chapter 2

Beams and major experiments

In this Chapter we sketch the technological achievements of LEAR with respect to conventional antiproton beams. The experiments at LEAR which investigated $\overline{\mathrm{N}}\mathrm{N}$ interactions are introduced and their design and performance are reviewed.

2.1 The LEAR facility at CERN

The possibility to store intense antiproton beams and to use them both in a high-energy proton-antiproton collider and at low energy, was put forward in 1976 by the Novosibirsk group [65, 66], soon after the feasibility of both stochastic and electron cooling had been demonstrated. As apparent from Fig. 2.1, which shows the $\bar{\mathrm{p}}$ yield (i.e., the number of $\bar{\mathrm{p}}$'s which can be captured into a beam channel of a given acceptance) as a function of the momentum of the $\bar{\mathrm{p}}$'s, the yield has a broad maximum at $3.5\,\mathrm{GeV}/c$ (the incident proton momentum is $23\,\mathrm{GeV}/c$, a typical CERN PS operation energy) and falls off by many orders of magnitude for lower momenta (dashed curve). On the other hand, if $3.5\,\mathrm{GeV}/c$ antiprotons were stored in a ring, cooled to reduce phase-space, and then decelerated to the desired energy, one could dispose of the same high flux at all energies. Cooling is an essential part in the process: if the stored beam is decelerated without any cooling, the density decreases due to the adiabatic increase of the emittance.

The LEAR project was approved at CERN in 1980, and in July '83 first beams were delivered to the users. Fig. 2.2 shows a schematic layout of the PS accelerator. The particles created by the extracted PS beam hitting the production target (typically a 3 cm diameter, 10 cm long metal rod through which a current of up to 200 kA is pulsed to focus the produced $\bar{\mathrm{p}}$'s) are stored in the Antiproton Accumulator (AA), at a rate of 6×10^6 per pulse. In the AA, the $\bar{\mathrm{p}}$'s are stochastically cooled and stacked into an intense stored beam, typically 3×10^{11} $\bar{\mathrm{p}}$'s, with vertical and horizontal emittance of about 2π, from which spills of 1 to 3×10^9 $\bar{\mathrm{p}}$'s are extracted and sent to the CERN PS, where they are decelerated at $609\,\mathrm{MeV}/c$ and transfered to LEAR.

Under the strong pressure to increase the $\bar{\mathrm{p}}$ flux to the SPS $\bar{\mathrm{p}}\mathrm{p}$ Collider program, the AA complex was stopped in 1987 to construct a new Antiproton Collector (ACOL) which allowed to separate the $\bar{\mathrm{p}}$ collection function from the $\bar{\mathrm{p}}$ stacking, still performed in AA. The use of two rings and important improvements of the antiproton production target system resulted in a net flux gain of a factor 10. The new AA-ACOL complex was operational at the end of 1987: about 6×10^{10} $\bar{\mathrm{p}}$'s could be accumulated per hour, in stacks of about 10^{12} $\bar{\mathrm{p}}$'s. All together, the $\bar{\mathrm{p}}$ CERN complex has performed remarkably well, as testified by the LEAR running statistics shown in Fig. 2.3. Up to 1991 LEAR was operated in parallel with the SPS $\bar{\mathrm{p}}\mathrm{p}$ Collider, but since 1992 LEAR was the only user. The program was terminated at the end of 1996.

A very important feature of LEAR was the ultra-slow extraction system, which allowed the users to dispose of essentially DC beams. The extraction system could provide continuous spills of

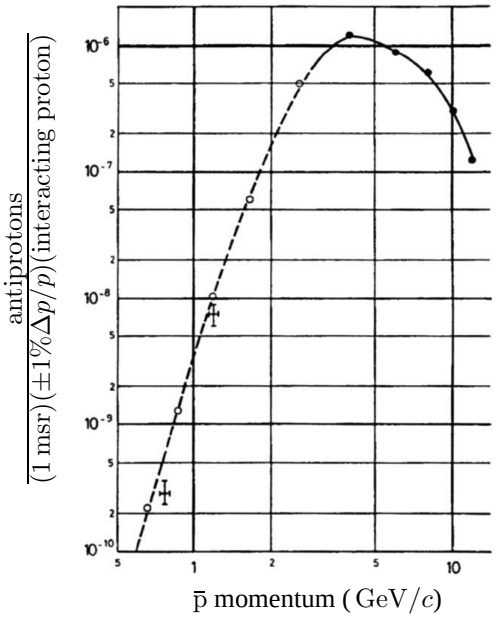

Figure 2.1: Momentum spectrum of antiprotons produced at 0° with 23 GeV/c protons on a lead target. The number of $\bar{\mathrm{p}}$ per interacting proton is normalised to 1 msr solid angle and $\pm 1\%$ momentum bite.

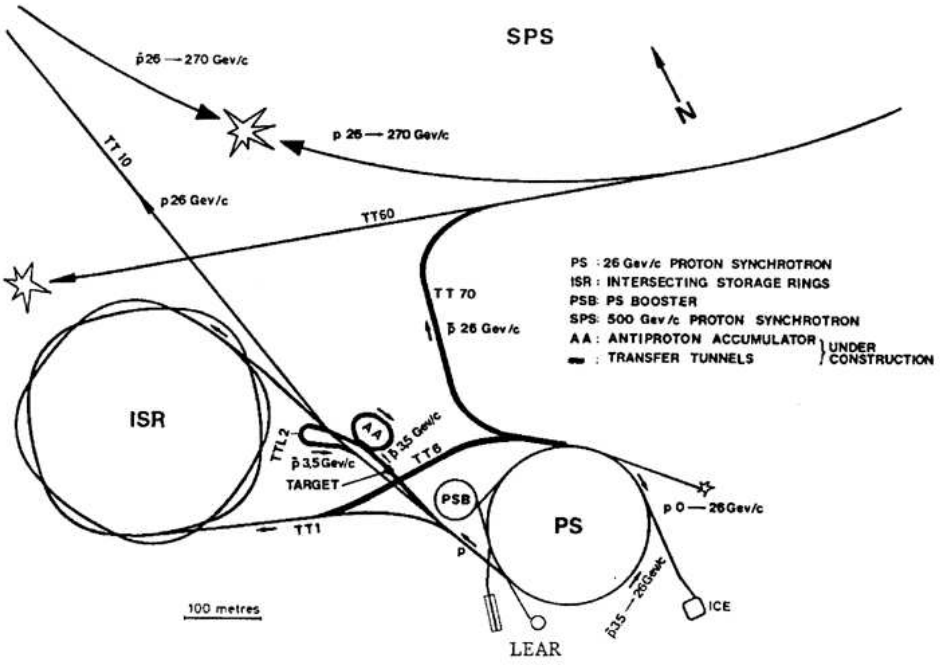

Figure 2.2: Layout of the PS accelerator complex.

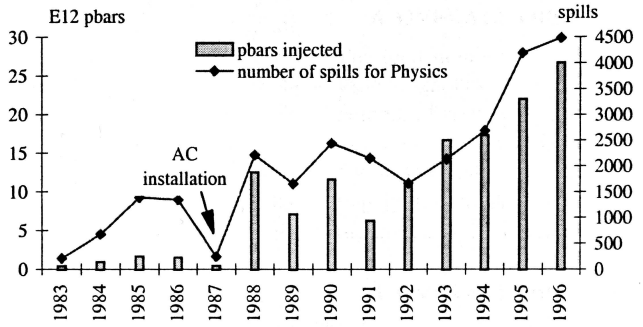

Figure 2.3: LEAR running statistics. The major gain occurring in 1988 is due to the Antiproton Collector entering into operation.

up to 15 hours, i.e., 10^3 times longer than the spills obtained in previous machines, corresponding to less than one particle per turn (on average) leaving the machine. This system was invented for LEAR [67], and is still regarded as the most innovative contribution of LEAR to accelerator physics and technology.

Other features worth mentioning are:
- beams were provided between 105 and 2000 MeV/c momentum;
- both stochastic and electron cooling were used;
- provisions were made for internal targets;
- three (later four) beam splitters on the extracted $\bar{\mathrm{p}}$ beam line allowed to deliver antiprotons simultaneously to four (five) experiments.

Fig. 2.4 shows the arrangement of the LEAR ring in the South Hall of the CERN PS, the extracted beam lines, and the locations of the experiments in the year 1983.

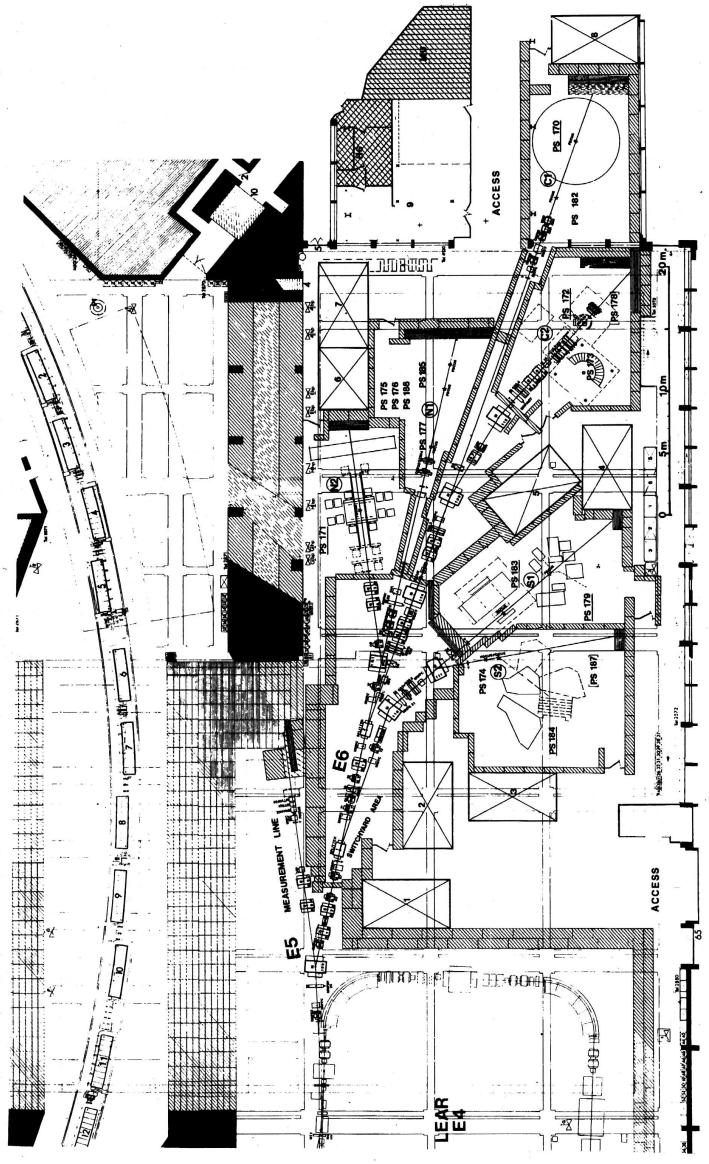

Figure 2.4: The LEAR extracted beam lines and the experimental areas in 1983, at the start-up of the physics programme.

2.2 Physics motivation of the LEAR scattering experiments

In the seventies, several ($qq\bar{q}\bar{q}$) baryonium candidates had been observed, with masses either below the $\overline{\mathrm{N}}\mathrm{N}$ threshold or above. At the time when LEAR was proposed and constructed the scientific community had a strong interest in studying $\bar{\mathrm{p}}\mathrm{p}$ scattering in the region of incident $\bar{\mathrm{p}}$ momenta around $500\,\mathrm{MeV}/c$, where many experiments had reported the presence of a narrow state, the S(1936). This state was observed as a bump over a smooth background in the $\bar{\mathrm{p}}\mathrm{p}$ total and annihilation cross-section. The observation came both from counter experiments and from bubble chamber measurements. For a review on the S(1936) and other baryonium candidates in the pre-LEAR era see, e.g., Ref. [68].

At LEAR several experiments were proposed to study baryonium states of mass smaller than two-nucleon mass, by spectroscopy studies of $\bar{\mathrm{p}}\mathrm{p}$ and $\bar{\mathrm{p}}\mathrm{d}$ annihilation at rest. In a complementary way, a number of experiments were proposed to study the formation of baryonium in $\bar{\mathrm{p}}\mathrm{p}$ scattering in the entire momentum range.

The first scattering experiments to be proposed and carried out (PS172 and PS173) did energy scans of the integrated cross-sections for momenta smaller than $600\,\mathrm{MeV}/c$ to confirm the existence of the S-meson, measure its width and formation cross-section, and possibly identify new states. As it is well known, far from confirming the original observations, these two experiments provided conclusive evidence against the existence of the S-meson. It should be remembered, however, that shortly before LEAR entered into operations the evidence for this state was questioned, in experiments at BNL and KEK[1]

Confirming the S-meson was only one point in the experimental program of the scattering experiments. Independently of the existence of narrow baryonium states, a rich spectrum of baryonium resonances, with typical strong-interaction width of about 100 MeV, was expected to exist and several possible candidates had been observed in the momentum region from 1 to $2\,\mathrm{GeV}/c$. These observations were done by studying the two-meson annihilation channels $\bar{\mathrm{p}}\mathrm{p}\to\pi^-\pi^+$ and $\bar{\mathrm{p}}\mathrm{p}\to\mathrm{K}^-\mathrm{K}^+$. The scattering matrix of these reactions depends on only two complex amplitudes, which can be reconstructed in a phase-shift analysis if the differential cross-section and the analysing power are measured at a sufficient number of energies. This programme was proposed by PS172 at LEAR in the momentum interval from about 500 to $1500\,\mathrm{MeV}/c$ (to overlap with the previous measurements). It was carried through successfully and subsequent amplitude analyses of the data have suggested a number of high-spin resonances.

In parallel to $\bar{\mathrm{p}}\mathrm{p}\to\pi^-\pi^+$ and $\bar{\mathrm{p}}\mathrm{p}\to\mathrm{K}^-\mathrm{K}^+$, PS172 has measured the elastic channel $\bar{\mathrm{p}}\mathrm{p}\to\bar{\mathrm{p}}\mathrm{p}$: a comparison of the coupling of the resonances to $\overline{\mathrm{N}}\mathrm{N}$ and to the mesons was regarded as necessary to access the nature of the state, since ($qq\bar{q}\bar{q}$) baryonium states were expected to couple more strongly to $\overline{\mathrm{N}}\mathrm{N}$ than to multi-meson channels. For a correct isospin-value assignment, a similar investigation of the $\bar{\mathrm{p}}\mathrm{p}\to\bar{\mathrm{n}}\mathrm{n}$ charge-exchange channel was proposed (experiment PS199, measurement of differential cross-section and analysing power in the momentum range 500 to $1300\,\mathrm{MeV}/c$), approved, and performed.

The search of baryonium states was undoubtedly the main motivation of the scattering experiments at LEAR. Later, annihilation channels as a function of the $\bar{\mathrm{p}}$ momentum were studied in a comprehensive way by the Crystal Barrel Collaboration. A large number of meson resonances were identified. For none of these resonances a particularly strong coupling to $\overline{\mathrm{N}}\mathrm{N}$ was reported.

A second strong motivation for the scattering experiments was the understanding of the $\overline{\mathrm{N}}\mathrm{N}$ reaction dynamics and its comparison with the known $\mathrm{N}\mathrm{N}$ interaction. As discussed in detail in this review, potential models, based on well-known meson exchanges and supplemented by phenomenological description of annihilation, resulted in a number of definite predictions for cross-sections, spin observables, and initial-state interaction in annihilation processes. Many experiments, PS172, PS173, PS198, PS199, either had the study of $\overline{\mathrm{N}}\mathrm{N}$ reaction dynamics as important part of their program, or were fully dedicated to it. A special mention has to be made of the PS185 experiment, devoted to the study of the dynamics of strangeness production. The threshold for $\bar{\mathrm{p}}\mathrm{p}\to\overline{\Lambda}\Lambda$ is at

[1] See, for instance, Ref. [69].

$1.435\,\mathrm{GeV}/c$. The Lorentz boost provided by the large $\bar{\mathrm{p}}$ incident momentum makes the study of these reactions near to threshold an interesting experimental problem.

The use of polarised targets and of the intense $\bar{\mathrm{p}}$ beam of LEAR allowed to detect large spin effects in PS172, PS198 and PS199, and new proposals were put forward. At the Cogne meeting in 1990 [70], these proposals were not approved by the CERN Committee, and the investigation of the $\overline{\mathrm{N}}\mathrm{N}$ reaction dynamics was stopped at LEAR.

With two exceptions. Experiment PS206 was approved to measure the πNN coupling constant from a precision measurement of the differential cross-section of $\bar{\mathrm{p}}\mathrm{p} \rightarrow \bar{\mathrm{n}}\mathrm{n}$. Experiment PS201 (OBELIX), whose main objectives were spectroscopy studies, could use the general-purpose apparatus to obtain a variety of cross-section data, in different channels, particularly at very low energy.

2.3 Description of the antiproton scattering experiments

Given the momentum range of interest, all the proposed experiments consisted of detectors typical of particle physics (scintillation counters, multi-wire proportional chambers, drift chambers, limited streamer tubes, etc.), and in spite of the capability of LEAR of delivering antiprotons with very low momentum, no dedicated experiment was proposed to explore $\overline{\mathrm{N}}\mathrm{N}$ scattering at momenta smaller than $200\,\mathrm{MeV}/c$. The FILTEX Collaboration considered [71] the possibility of exploring this low energy region, by using a polarised atomic hydrogen gas target in the LEAR ring, but the project was not encouraged [70]. In the ACOL era, only the PS201 experiment (a Bologna - Brescia - Cagliari - Dubna - Frascati - Legnaro - Padua - Pavia - Turin - Trieste - Udine collaboration, about 100 physicists) has measured cross-sections down to about 1 MeV $\bar{\mathrm{p}}$ energy, using special techniques, as will be described in Section 2.3.3.

Six experiments were specifically devoted to $\overline{\mathrm{N}}\mathrm{N}$ scattering:

- PS172 (SING), an Amsterdam - Geneva - Queen Mary College - Surrey - Trieste collaboration, (about 20 physicists);
- PS173, a Heidelberg - Laval - Mainz - Rutgers collaboration, (about 15 physicists);
- PS185, a Carnegie Mellon - CERN - Erlangen - Freiburg - Urbana - Jülich - Uppsala - Vienna collaboration, (about 25 physicists);
- PS198, a Karlsruhe - Lyon - Saclay - PSI Villigen collaboration, (about 25 physicists);
- PS199 (POLCEX), a Cagliari - CERN - Geneva - Saclay - Trieste - Turin collaboration, (about 35 physicists);
- PS206 (CEX), a Cagliari - CERN - Geneva - Saclay - Trieste - Turin collaboration, (about 30 physicists).

The PS172 and PS173 experiments were designed, constructed, and operated in the pre-ACOL era of LEAR, the other ones ran with ACOL. PS185 took data over the full LEAR life-time. Table 2.1 shows a survey of the data taken by the various experiments.

From Table 2.1 it should be apparent that the experiments at LEAR could perform only an exploratory work and no systematic study of the $\overline{\mathrm{N}}\mathrm{N}$ dynamics. In particular, proposals to polarise the LEAR $\bar{\mathrm{p}}$ beam, either by filtering one spin component by recirculation through a polarised jet target (FILTEX), or by a coherent Stern-Gerlach mechanism using a "spin-splitter" [72–74], a combination of two quadrupoles separated by a solenoidal magnet, were not accepted.

Scattering data have been obtained also by the experiment E760 (collaboration Irvine - Fermilab - Ferrara - Genoa - Northwestern University - Penn State University - Turin) at the Fermilab Antiproton Accumulator Ring.

Table 2.1: Survey of low-energy antiproton and antineutron cross-section and scattering measurements at LEAR.

Measurement	Incoming $\bar{\mathrm{p}}$ momenta (MeV/c)	Experiment
integrated cross-sections		
$\sigma_{\mathrm{tot}}(\bar{\mathrm{p}}\mathrm{p})$	222 to 599 (74 momenta)	PS172
	181, 219, 239, 261, 287, 505, 590	PS173
$\sigma_{\mathrm{ann}}(\bar{\mathrm{p}}\mathrm{p})$	177 to 588 (53 momenta)	PS173
	38 to 174 (14 momenta)	PS201
$\sigma_{\mathrm{tot}}(\bar{\mathrm{n}}\mathrm{p})$	80 to 293 (18 momenta)	PS201
$\sigma_{\mathrm{ann}}(\bar{\mathrm{n}}\mathrm{p})$	50 to 400 (18 momenta)	PS201
$\bar{\mathrm{p}}\mathrm{p}$ elastic scattering		
ρ	233, 272, 550, 757, 1077	PS172
	181, 219, 239, 261, 287, 505, 590	PS173
$\mathrm{d}\sigma/\mathrm{d}\Omega$	679 to 1550 (13 momenta)	PS172
	181, 287, 505, 590	PS173
	439, 544, 697	PS198
A_{0n}	497 to 1550 (15 momenta)	PS172
	439, 544, 697	PS198
D_{0n0n}	679 to 1501 (10 momenta, 23 points)	PS172
$\bar{\mathrm{p}}\mathrm{p}$ charge-exchange		
$\mathrm{d}\sigma/\mathrm{d}\Omega$	181 to 595 (several momenta)	PS173
	546, 656, 693, 767, 875, 1083, 1186, 1287	PS199
	601.5, 1202	PS206
A_{0n}	546, 656, 767, 875, 979, 1083, 1186, 1287	PS199
D_{0n0n}	546, 875	PS199
$\bar{\mathrm{p}}\mathrm{p} \to \overline{\mathrm{Y}}\mathrm{Y}$		
several observables	1424 to 1922 (several momenta)	PS185

2.3.1 Experiment PS172

Experiment PS172 was designed to perform several different measurements, both with a liquid hydrogen target and a polarised proton target. For most of the measurements an energy scan was foreseen, which was done by setting LEAR to the desired energies. This procedure was inconvenient for the total cross-section measurement, because of the number of steps required for a fine scan. For these reasons, only a few energies were selected within the range of the scan and the beam was slowed down with a suitably designed Carbon degrader.

The beam line and the measurement of $A_{\bar{\mathrm{p}}\mathrm{C}}$

The C2 beam line was designed according to the needs of the measurements of the total cross-section and of the analysing power in $\bar{\mathrm{p}}$C elastic scattering ($A_{\bar{\mathrm{p}}\mathrm{C}}$).

The layout of the beam line is shown in Fig. 2.5. There, F_1 and F_2 give the positions of the

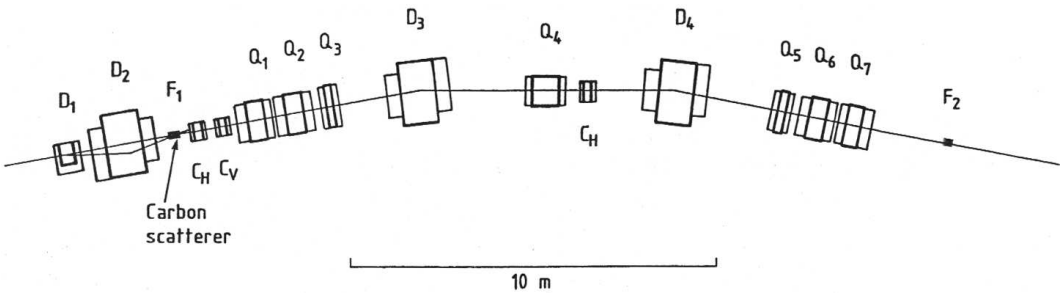

Figure 2.5: Layout of the C2 beam line: Q denotes quadrupoles, D bending magnets and C_H and C_V collimators in the horizontal and vertical planes. The first and second carbon scatterers are located at the two focal points F_1 and F_2.

first and second focal points. The layout was symmetric between F_1 and F_2 (where the experimental apparatus was located), so the magnification was 1. Momentum analysis was performed by the horizontal collimator C_H put at the intermediate focus. The main characteristics of the beam are:

- large angular acceptance, ± 18 mrad horizontally and ± 36 mrad vertically, giving a good intensity of the degraded beams;
- good momentum resolution, ($\Delta p/p \simeq \pm 1\%$), necessary to reject antiprotons inelastically scattered off carbon;
- achromatism, to minimise the beam spot, obtained with the use of the quadrupole Q_4 in between the two momentum-analysing bending magnets D_3 and D_4.

In order to perform the measurement of $A_{\bar{\mathrm{p}}\mathrm{C}}$, the first two bending magnets D_1 and D_2 gave the possibility of sweeping the extracted LEAR beam in the horizontal plane. This option was used to measure $A_{\bar{\mathrm{p}}\mathrm{C}}$, by hitting the carbon scatterer in F_1 at an angle varying from -9° to +9°. The large angular acceptance of the beam line guaranteed a reasonable intensity for the scattered beams. The beam at F_1 was monitored continuously using a MWPC with 1 mm wire spacing and a scintillation counter B0.

The analysing power $A_{\bar{\mathrm{p}}\mathrm{C}}$ was measured in order to assess the possibility of polarising antiprotons by scattering off light nuclei. A large $A_{\bar{\mathrm{p}}\mathrm{C}}$ would have allowed to set up a polarised $\bar{\mathrm{p}}$ beam in analogy with what is routinely done with protons. Unfortunately, the value of $A_{\bar{\mathrm{p}}\mathrm{C}}$ [75, 76] turned out to be too small.

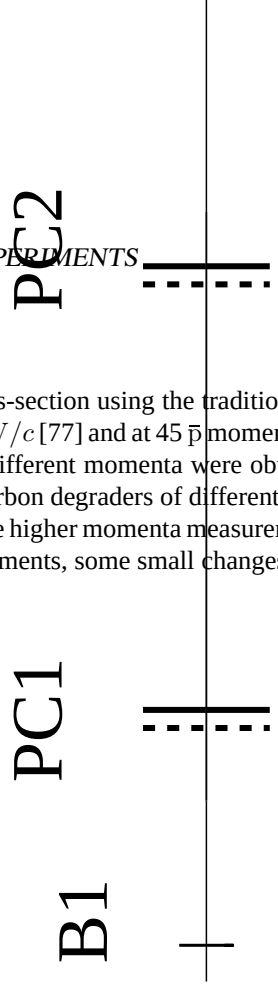

Figure 2.6: PS172: Schematic side view of the set-up used for the measurement of the $\bar{\mathrm{p}}\mathrm{p}$ total cross-section.

The incoming beam was defined by the coincidence B of the signals from three thin (0.5 mm) scintillation counters, B0, B1 and B2 (only B1 is shown in the figure). B2 had a diameter of 1 cm and was placed in front of the target. B0 was placed in front of the degrader at the first focus F_1, 20 m upstream of the target. The time-of-flight between B0 and B1 eliminated the small (less that 0.1%) contamination of pions (and decay muons) produced in the degrader. The beam focusing was continuously monitored by two multi-wire chambers PC1 and PC2.

A liquid hydrogen target (LHT) was used, which was emptied for background measurements. The target consisted of two cells (the first one had 8.33$\pm$0.04 cm length and 3.5 cm diameter, the second one 1.17$\pm$0.03 cm length and 5 cm diameter), which could be filled and emptied independently. The temperature was continuously monitored.

A box of scintillation counters S1-S5 surrounded the target except for holes at the top and for the entrance and exit beam-windows. The box covered 90% of the solid angle around the target.

The transmitted beam was measured in thin scintillation counters in air light guides: a circular one, T, and three overlapping concentric annular ones, A1-A3. The latter extended up to an external radius of 10.8 cm; rings were chosen to minimise $\bar{\mathrm{p}}$ annihilation in the array. The signals from these detectors were added electronically to form a set of four transmission rates B$\cdot$T$_i$ (T$_1$ = T, T$_2$ = T+A1, etc.) corresponding to different maximum values of the momentum-transfer square $|t|$. The efficiency of counter T was monitored using the E1 and E2 counters.

The angular range between the backward hole of the target veto counters and the transmission array was covered by two annular counters (S6 and S7). The S$_i$ counters recorded predominantly events with annihilation into charged pions and the OR of the signals from all of them (S) was used to derive a second set of transmission rates B$\cdot\bar{\mathrm{S}}\cdot$T$_i$, with a slope in $|t|$ dominated by elastic scattering.

At each incoming antiproton momentum, the two sets of transmission rates were corrected for accidental coincidences and vetoing, for energy losses in the targets, and for residual hydrogen gas present in the empty target. The partial cross-sections obtained from both sets were corrected for Coulomb–nuclear interference and single Coulomb scattering. The linear extrapolation to $|t| = 0$ gave two measurements of the total cross-section which turned out to be in very good agreement.

$\sigma_{\mathrm{tot}}(\bar{\mathrm{p}}\mathrm{p})$ measurements

PS172 measured the $\bar{\mathrm{p}}\mathrm{p}$ total cross-section using the traditional transmission technique at 29 $\bar{\mathrm{p}}$ momenta between 388 and 596.8 MeV/c [77] and at 45 $\bar{\mathrm{p}}$ momenta between 221.9 and 413.2 MeV/c [78], in few days of data taking. The different momenta were obtained using extracted $\bar{\mathrm{p}}$ beams of 388, 599, 352, and 432 MeV/c, and carbon degraders of different thicknesses in F1.

The experimental set-up for the higher momenta measurements is shown schematically in Fig. 2.6; for the lower-momentum measurements, some small changes were introduced.

The quoted normalisation error is $\pm 0.7\%$ at higher energies (long target), and $\pm 0.9\%$ at low energies (short target). At momenta below $285\,\mathrm{MeV}/c$, the correction for straggling and nuclear attenuation in the apparatus became relevant and, at the lowest momenta, the error on the correction was larger than the statistical error.

ρ measurements

The ρ parameter defined as ratio of real to imaginary part of the elastic scattering amplitude was determined in dedicated measurements of the $\bar{\mathrm{p}}\mathrm{p}$ elastic scattering differential cross-section at small angles, in the Coulomb-nuclear interference region. Data were taken at five momenta (233, 272, 550, 757, and $1077\,\mathrm{MeV}/c$ $\bar{\mathrm{p}}$ momenta at the target centre) under two different running conditions.

The lower energy measurements at $233\,\mathrm{MeV}/c$ and at $272\,\mathrm{MeV}/c$ [79] were performed with a dedicated set-up, similar to that used for the σ_{tot} measurements and shown in Fig. 2.6. For these data the set of annular transmission counters behind the target was replaced by a set of four multi-wire proportional chambers (PC3, PC4, PC5 and PC6). The "short" liquid hydrogen target was used. Scattered $\bar{\mathrm{p}}$'s were detected by a counter (R), placed behind the last wire chamber. This counter was made up by four partly overlapping rectangular scintillation counters, and had a square hole of $6 \times 6\ \mathrm{cm}^2$ for the outgoing beam.

The trigger for elastic events consisted in a first level trigger (given by the coincidence B0·B1·R) and in a second level trigger, which consisted of a software cut on the calculated distance between the coordinates measured in the last multi-wire chamber and the nominal beam axis. After the cut, the acceptance for events with a scattering angle of 6° was larger than 80%, and the trigger rate was reduced by a factor of 10 at $233\,\mathrm{MeV}/c$, giving a typical rate of 250 events per second. Events with trigger B0·B1 were also collected to determine the angular resolution for full and empty target runs and the angular acceptance of the elastic trigger.

In the analysis, the scattering angle was determined from the measured directions of the incoming and outgoing $\bar{\mathrm{p}}$ as obtained from the two sets of multi-wire proportional chambers. Events due to $\bar{\mathrm{p}}\mathrm{p}$ annihilation in the liquid hydrogen target were rejected by identifying the pions using the time-of-flight between B1 and R. For the data at $233\,\mathrm{MeV}/c$ the time-of-flight between B1 and S1-S5 was also used to reject annihilation events.

The momentum spread of the incoming beam, determined from the B0-B1 time-of-flight spectra, was smaller than $\pm$ $1.2\,\mathrm{MeV}/c$. The average momentum loss in the liquid hydrogen target was $10\,\mathrm{MeV}/c$ at $272\,\mathrm{MeV}/c$ and $14\,\mathrm{MeV}/c$ at $233\,\mathrm{MeV}/c$. Energy straggling calculations indicated that less than 0.5% of the antiprotons stopped before reaching the R-counters at both momenta, making negligible the effect on the measured angular distributions.

At these two low $\bar{\mathrm{p}}$ momenta, the experimental angular resolution was dominated by multiple scattering (25.7 mrad with target full at $272\,\mathrm{MeV}/c$); to fit the measured differential cross-section a "folding" procedure had to be applied. The elastic $\bar{\mathrm{p}}\mathrm{p}$ differential cross-section was published in the range where the acceptance was higher than 70% (54 points with $1.37 \times 10^{-3} < -t < 6.60 \times 10^{-3}\,\mathrm{GeV}$ and 69 points with $1.07 \times 10^{-3} < -t < 8.98 \times 10^{-3}\,\mathrm{GeV}$, at 233 and $272\,\mathrm{MeV}/c$ respectively); the statistical errors are less than 10%.

The data at $550\,\mathrm{MeV}/c$, and those at 757 and $1077\,\mathrm{MeV}/c$ [80], were collected during two separate runs, under somewhat different experimental conditions, in parallel with the measurement of the analysing power in $\bar{\mathrm{p}}\mathrm{C}$ elastic scattering $A_{\bar{\mathrm{p}}\mathrm{C}}$. The geometrical arrangement of the detectors was optimised for the $A_{\bar{\mathrm{p}}\mathrm{C}}$ measurements; in particular the "scattered" $\bar{\mathrm{p}}$ beam (either at 5° and 8°) was used. The Carbon scatterer was 5.2 g/cm^2 thick and the scattered beam intensity was between 300 and 1000 $\bar{\mathrm{p}}$/sec, depending on angle and extracted beam momentum (600.8, 800 and $1100\,\mathrm{MeV}/c$). The apparatus, shown in Fig. 2.7, was very similar to the one used for the low energy measurements. It consisted of the liquid hydrogen target (LHT), telescopes of multi-wire proportional chambers (PCs in the figure), and scintillation counters. It allowed to measure scattering events on either the liquid hydrogen target, or on a carbon target (C), and to extract the (eventual) $\bar{\mathrm{p}}$ beam polarisation from the azimuthal asymmetry of the events. The scintillator boxes S1-S5 and P1-P5 ensured the

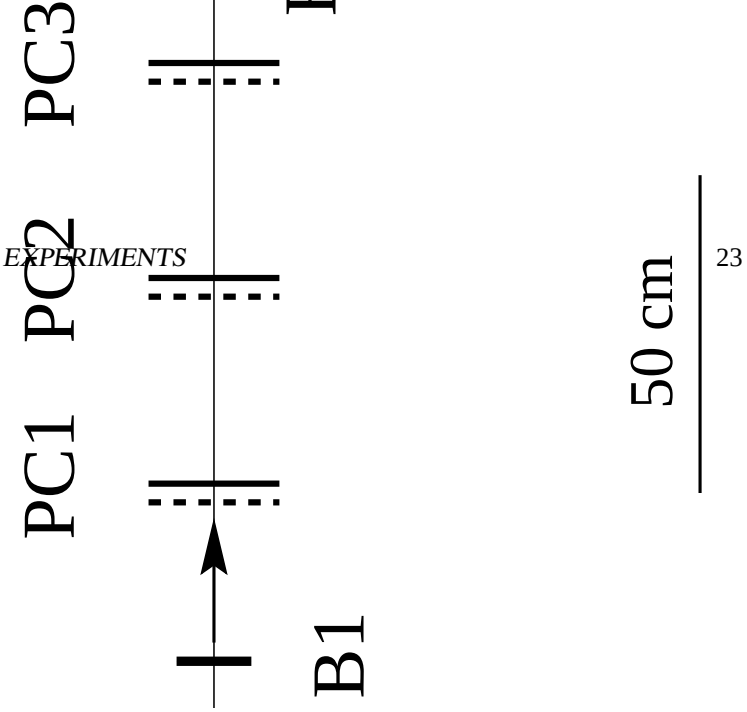

Figure 2.7: PS172: Schematic top view of the set-up used for the measurement of small angle $\bar{\mathrm{p}}\mathrm{p}$ elastic scattering differential cross-section at 757 and 1077 MeV/c.

scattering process on both targets to be elastic. The events on which the scattering took place on the liquid hydrogen target were used to extract ρ for the $\bar{\mathrm{p}}\mathrm{p}$ elastic scattering.

The differential cross-section was measured in the range $0.39\times10^{-3} < -t < 65.5\times10^{-3}\,\mathrm{GeV}$, $0.38\times10^{-3} < -t < 43.0\times10^{-3}\,\mathrm{GeV}$, and $0.60\times10^{-3} < -t < 80.7\times10^{-3}\,\mathrm{GeV}$, at 550, 757, and 1077 MeV/c respectively. The corresponding total detection and reconstruction efficiencies were estimated to a few per cent to be 75%, 89%, and 76% respectively. Also in this case, a "folding" procedure had to be applied to measure the ρ parameter.

Differential cross-section and analysing power in $\bar{\mathrm{p}}\mathrm{p}$ elastic scattering

The most important physics objective of PS172 was an energy scan of the differential cross-section and the analysing power of the two-body annihilation channels $\bar{\mathrm{p}}\mathrm{p}\to\pi^-\pi^+$ and $\bar{\mathrm{p}}\mathrm{p}\to\mathrm{K}^-\mathrm{K}^+$, with the aim of revealing the existence of $\bar{\mathrm{p}}\mathrm{p}$ s-channel resonances. A pentanol polarised target was used. Data have been published for 20 momenta between 360 MeV/c and 1550 MeV/c [81], and analysed in several papers (see e.g., Ref. [82–84]).

The same apparatus was also used to measure (in parallel) the same observables for the elastic $\bar{\mathrm{p}}\mathrm{p}$ reaction. The A_{0n} data are given for 15 momenta, between 497 MeV/c and 1550 MeV/c [85]. Differential cross-section data for the $\bar{\mathrm{p}}\mathrm{p}\to\bar{\mathrm{p}}\mathrm{p}$ reaction are given at 13 momenta, down to 679 MeV/c [86]: at lower momenta absorption of the outgoing particles in the target material led to large systematic uncertainties and the results were not published.

The experimental apparatus is sketched in Fig. 2.8. The pentanol target was a cylinder, 3 cm long and 1 cm diameter, with a hydrogen content corresponding to 3.7 cm of liquid hydrogen. The transverse proton polarisation, typically 75% $\pm$ 4%, was reversed every few hours. The target was placed in the nose of a cryostat, keeping the target temperature below 1 K, and in a locally homogeneous field of 2.5 T, provided by a C-shaped dipole magnet (M in the figure). A liquid hydrogen and "dummy" target, made of Teflon, were also used for absolute normalisation and to determine the background.

The beam signal was given by the coincidence of three scintillation counter (B0, S1, and S2 or S3), and the incoming particle trajectories were measured by two multi-wire proportional chambers (the J and C chambers).

The scattered and recoil particles were detected by the multi-wire proportional chambers J, C, and either R or L. The J and C chambers were operated in a high magnetic field region; their positions were chosen to optimise the measurement of the outgoing particle momenta from the deflection in the field of the dipole magnet. An array of trigger scintillation counters placed around the R and

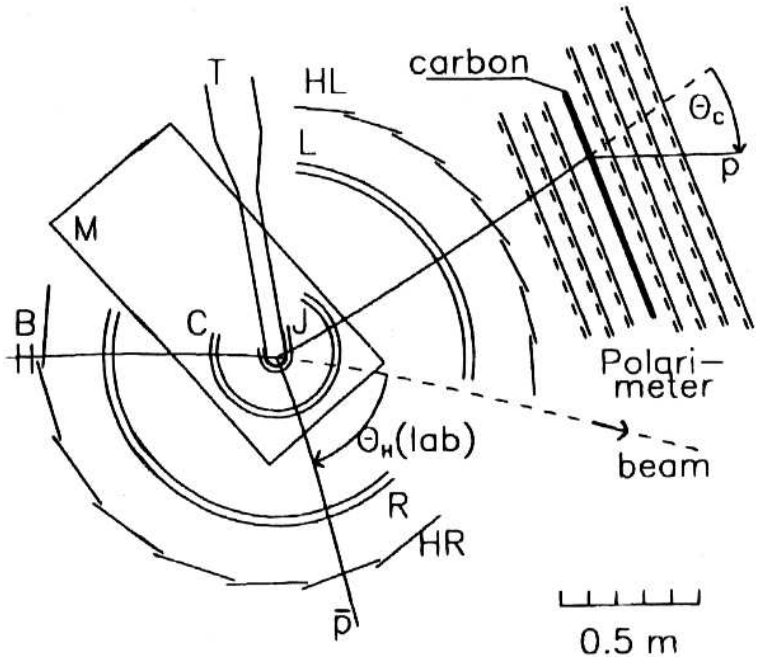

Figure 2.8: PS172: Schematic side view of the set-up used for the measurement of the $\bar{\mathrm{p}}\mathrm{p}$ elastic scattering differential cross-section and analysing power.

L chambers completed the set-up. The R and L chambers and the scintillation counters could be rotated around the magnet axis according to the beam deflection in the magnetic field.

The background due to scattering on quasi-free target nucleons was substantially reduced using only events with both recoil and scattered particle detected. In the PS172 case, this request reduced the geometrical acceptance both in the scattering angle ϑ_{cm} and in the azimuthal angle φ. The acceptance, given by the minimal energy needed by the final particles to traverse the target and the detectors, was $-0.28 < \cos\vartheta_{\mathrm{cm}} < 0.28$ at $497\,\mathrm{MeV}/c$ and $-0.84 < \cos\vartheta_{\mathrm{cm}} < 0.80$ at $1550\,\mathrm{MeV}/c$; only events with $|\varphi| < 6^\circ$ and 15° were used for the $\mathrm{d}\sigma/\mathrm{d}\Omega$ and A_{0n} measurements respectively.

Corrections above 10% had to be applied to take into account the background subtraction, the chamber inefficiencies, and the absorption of the secondary particles; all these points are relevant for the differential cross-section measurement. The quoted systematic errors are about 10% in the differential cross-section and 4.5% in the analysing power.

In parallel to the A_{0n} measurements, the depolarisation parameter D_{0n0n} was measured [87] using a standard polarimeter with a Carbon slab (shown in Fig. 2.8) as analyser for the proton polarisation. The polarimeter was built by a variable number (typically 6) of 1 cm thick C plates and seven MWPC (three upstream and four downstream of the carbon plates), each with horizontal and vertical wires.

The polarimeter was positioned to analyse the polarisation of recoil protons coming from $\bar{\mathrm{p}}\mathrm{p}$ elastic scattering in the polarised target, in the angular range in which the proton is detected by the J, C and R chambers[2]. From the left-right asymmetries in pC elastic scattering, measured for two different orientations of the transverse spin of the polarised target protons, it is possible to extract the spin correlation parameter D_{0n0n}. This measurement was severely limited in statistics: the $\bar{\mathrm{p}}$ was

[2]The original idea of analysing the scattered $\bar{\mathrm{p}}$ (which would have lead to the measurement of the spin transfer parameter K_{n00n}) was abandoned since the $\bar{\mathrm{p}}\mathrm{C}$ elastic scattering analysing power turned out to be small.

scattered in the backward hemisphere where the cross-section is small, and the measurement had to be performed in the one or two days allocated at each momentum for the measurement of A_{0n} in $\bar{\mathrm{p}}\mathrm{p}\rightarrow\pi^-\pi^+$, $\mathrm{K}^-\mathrm{K}^+$, $\bar{\mathrm{p}}\mathrm{p}$.

2.3.2 Experiment PS173

The experiment PS173 was set up to measure with good precision cross sections for antiproton-proton scattering in the low-energy domain. Total and the annihilation cross-sections, as well as differential elastic and charge-exchange cross-sections were determined in the range from 180 MeV/c to 600 MeV/c.

The experiment used the same C2 beam line designed for PS172, and, during the runs, the apparatus was located in the focus F2 (see Fig. 2.5). The degrader placed in the first focus F_1 provided a fine momentum scan (in 5 and 10 MeV/c steps). The beam momentum was measured by time-of-flight between the F_1 focus and the beam detectors positioned at F_2.

Fig. 2.9 shows the projection of the apparatus in the horizontal plane. Details can be found in Ref. [88].

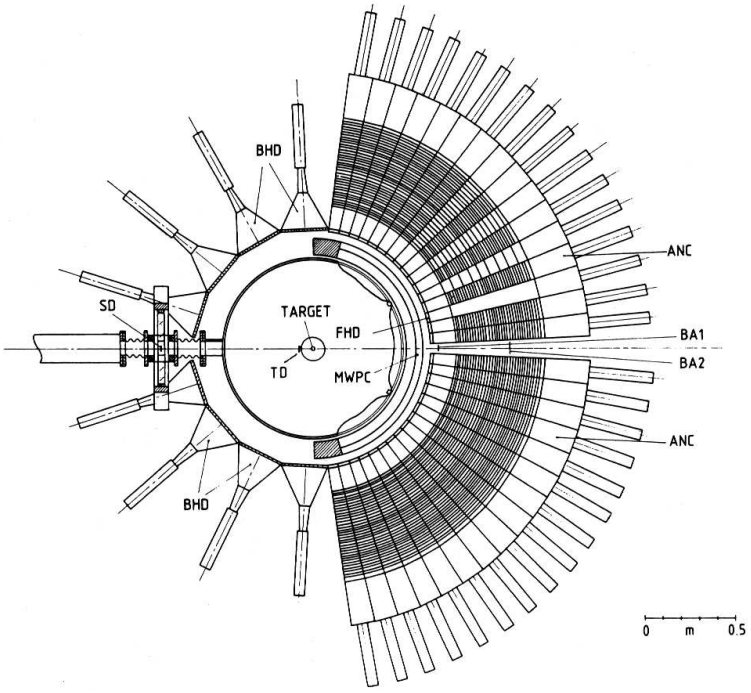

put(20,-5)

Figure 2.9: Schematic view of the horizontal plane of the PS173 experiment apparatus.

The beam impinged on a liquid-hydrogen target placed in the centre of the 1 m diameter vacuum tank with 1 cm thick aluminium walls. The incoming $\bar{\mathrm{p}}$ was identify by a coincidence between a scintillation counter F1 placed in the first focus, close to the degrader, and two thin (50 $\mu\mathrm{m}$) scintillators placed in front of the target (SD and TD); the dimensions of SD and TD were chosen to define a beam with $\pm 1^\circ$ divergence and a 5 mm diameter spot size at the target position.

Two target cells of different thickness (a vertical cylinder, 2 cm in diameter, and a 7 mm thick planar disk, respectively) filled with liquid hydrogen were used, depending on the beam momentum. Data collected with empty targets were used for background measurements.

Two 3 mm thick scintillator detectors (BA1 and BA2), located on the beam axis downstream from the target, were used in some measurements to veto antiprotons that did not interact strongly

in the target. These detectors were also used for the measurement of the total cross-section.

In the horizontal plane of the forward hemisphere, a cylindrical multi-wire proportional chamber (MWPC) with two wire planes was located in front of a thin window. It measured charged scattered particles with a resolution between 0.2 and 0.3° in the scattering angle. The MWPC covered scattering angles up to 75° in the horizontal plane and $\pm 15°$ (full acceptance $\pm 10°$) in the vertical direction.

In the same plane, the apparatus was completed by a scintillator hodoscope (FHD, forward hodoscope) and a calorimeter-like detector array (ANC, antineutron calorimeter). The FHD consisted of 32 pieces of plastic scintillators ($200 \times 50 \times 3\,\mathrm{mm}^3$), positioned 66 cm from the target, and was used for particle identification by energy loss and time-of-flight measurements. The ANC consisted of 32 modules; each module contained 50 slabs of $6\,\mathrm{mm}$ thick plastic scintillator and 50 plates of 4 mm thick iron, with a total thickness of 2.5 absorption lengths for $1.5\,\mathrm{GeV}/c$ antineutrons. The ANC was used to detect and identify $\bar{\mathrm{n}}$ annihilating in it; the $\bar{\mathrm{n}}$-γ separation was done using time-of-flight and energy-loss measurements.

Charged mesons from antiproton annihilation were detected by the FHD and an upper, a lower, and a backward plastic scintillator hodoscope (UHD, LHD, and BHD) surrounding the vacuum tank. The solid angle covered by the hodoscopes was 73% of 4π. 126 lead glass blocks above and below the scattering chamber (not shown in the figure) detected the gamma-rays from π^0 decays.

$\sigma_{\mathrm{ann}}(\bar{\mathrm{p}}\mathrm{p})$ measurement

PS173 measured the $\bar{\mathrm{p}}$ annihilation cross-section $\sigma_{\mathrm{ann}}(\bar{\mathrm{p}}\mathrm{p})$ at 53 incident $\bar{\mathrm{p}}$ momenta between 180 and $590\,\mathrm{MeV}/c$ [89, 90]. The extracted beam momenta were 605, 547, 527, 467, 397, 305, 243, and $190\,\mathrm{MeV}/c$; the intermediate momenta were obtained using the Carbon degrader or a varying number of $200\,\mu\mathrm{m}$ thick polyethylene foils (for momenta below $300\,\mathrm{MeV}/c$) located in F_1.

The incoming beam was defined by the coincidence F1·SD·TD and the beam profile was monitored by the MWPC. Both liquid hydrogen targets were used, in different momentum ranges.

The charged mesons produced by $\bar{\mathrm{p}}$ annihilation in the target were detected in the hodoscopes. The gamma-rays from π^0 decays were converted to electron–positron pairs in the wall of the vacuum tank with the average probability of 6%, and were then detected by the same hodoscopes. Annihilation channels with neutral particles only in the final state were detected if at least one gamma-ray was converted in the region covered by the hodoscopes. Events with $\bar{\mathrm{p}}$ elastically scattered into the FHD were eliminated by TDC–ADC correlation. The "reaction" trigger required a "beam" signal, no signal in the beam veto-counter BA1, and at least one hit in the hodoscopes.

The effect of beam instabilities on the measured annihilation cross-section was evaluated to be 0.6% (point-to point systematic error); after all corrections, the precision of the beam-flux measurement was estimated to be 1%. A correction to the cross-section was applied to account for $\bar{\mathrm{p}}$ elastic scattering at large angles followed by $\bar{\mathrm{p}}$ annihilation in the target; this correction is larger than the statistical error only below $300\,\mathrm{MeV}/c$ (where the corresponding estimated systematic error becomes not negligible). The corrections to the annihilation cross-section due to the overall charged-meson acceptance and to the all-neutral channels detection efficiency (evaluated at $297\,\mathrm{MeV}/c$) were estimated to be $10.4 \pm 1.0\%$ and $3.0 \pm 1.1\%$, respectively. Further systematic errors were due to the uncertainty about the target thickness ($\pm 1\%$ and $\pm 4\%$ for the thick and the thin target, respectively) and the density of the liquid hydrogen ($\pm 0.7\%$). Summarising: the point-to-point systematic errors due to beam instabilities and $\bar{\mathrm{p}}$ elastic scattering followed by $\bar{\mathrm{p}}$ annihilation in the target range from 0.5 to $6.1\,\mathrm{mb}$. The overall normalisation errors are 2.2% and 4.4% for the thick and the thin target, respectively.

$\bar{\mathrm{p}}\mathrm{p}$ elastic differential cross-section measurement

Results have been published at 181, 287, 505, and $590\,\mathrm{MeV}/c$ [91, 92]. The p and $\bar{\mathrm{p}}$ were detected in the FHD and in the MWPC. Forward $\bar{\mathrm{p}}$ detected in the FHD were identified by time-of-flight

and energy loss. At large scattering angles, the $\bar{\mathrm{p}}$ annihilated in the target and pions coming from annihilation were detected in the hodoscopes; the p was identified by the coincidence of a signal in the FHD and a pion signal in one of the four hodoscopes. At intermediate angles, both p and $\bar{\mathrm{p}}$ came out of the target and could be detected in the FHD and the MWPC, giving a clear angular-correlation signal. In this case, the $\bar{\mathrm{p}}$ was identified by the detection of its annihilation products in the slabs of either the ANC or the FHD next to the FHD-slab in which the $\bar{\mathrm{p}}$ was detected.

The scattering angle was measured from the coordinates of the hit in the MWPC and the geometrical centre of the target. The beam axis was determined and monitored with an accuracy of $\pm 0.3^{\circ}$. The angular resolution due to beam divergence, uncertainty in the reaction vertex in the target, and spatial resolution of MWPC, was estimated to be better than 1° over the full angular range. Multiple scattering was evaluated to be negligible for the published data.

Corrections for MWPC efficiency (98 to 99%) and geometrical acceptance were applied.

ρ measurement

The ρ parameter was determined at 181, 219, 239, 261, 287, 505, and 590 MeV/c [92, 93], by measuring the forward differential elastic cross-section and using the Coulomb-nuclear interference method. The beam momenta were obtained by using directly the extracted $\bar{\mathrm{p}}$ beam (202, 309, and 609 MeV/c) or by degrading its momenta to the desired value.

In the data analysis, corrections were applied for the FHD acceptance; the probability of $\bar{\mathrm{p}}$ absorption in the window of the vacuum chamber and in MWPC was evaluated to be 0.15 to 2.5%, depending on beam energy and scattering angle.

To measure ρ, only data at angles outside the multiple Coulomb scattering region were used at all momenta (40 to 50 points), so that this effect did not need to be considered. In the differential cross-section fit, three free parameters were used (ρ, $\sigma_{\mathrm{tot}}(\bar{\mathrm{p}}\mathrm{p})$, and the slope b of the nuclear amplitude); results were given for all of them.

$\bar{\mathrm{p}}\mathrm{p}$ charge-exchange differential cross-section

The $\bar{\mathrm{p}}\mathrm{p}$ differential charge-exchange cross-section was measured [94] at four $\bar{\mathrm{p}}$ momenta, 590, 505 (degraded beam), 287, and 183 MeV/c, by measuring the angular distribution of the antineutrons with the ANC calorimeter.

In the analysis, the $\bar{\mathrm{n}}$ were defined asking for a hit with the correct TOF in the ANC and no early $\pi^{\pm}/\mathrm{K}^{\pm}$ or $\bar{\mathrm{p}}$ signal in the FHD. If any other hodoscope was fired, the signal had to be compatible with pions from $\bar{\mathrm{n}}$ annihilation in the ANC. This cut had to eliminate events with a $\bar{\mathrm{p}}$ scattered at large angle and annihilated in the vacuum-tank wall, since a π could also not be detected in the FHD or MWPC sector corresponding to the fired ANC module. To reject events with the $\bar{\mathrm{p}}$ going through the gap of two FHD modules, it was required to have no MWPC hit within ± 8 mm from the calculated $\bar{\mathrm{n}}$ trajectory.

The $\bar{\mathrm{n}}$ scattering angle was measured with a precision ranging from $\pm 4.4^{\circ}$ (forward direction, first module) to $\pm 2.7^{\circ}$ if only one ANC module fired; for the less than 35% of the events in which two or more ANC modules fired, the angular resolution was not affected appreciably. To avoid edge effects, the vertical acceptance was restricted to 75% of the geometrical height of the calorimeters. The TOF separation between γ and $\bar{\mathrm{n}}$ was considered sufficient to neglect γ contamination in the $\bar{\mathrm{n}}$ sample.

The n detection efficiency of the ANC was sufficiently low to assume pure $\bar{\mathrm{n}}$ detection, since in the kinematic region in which both n and $\bar{\mathrm{n}}$ could be detected less than 5% of coincidences with the correct correlation angle were found. This assumption could have been a source of systematic error in the backward hemisphere where neutrons largely outnumber antineutrons. The detection efficiency of the $\bar{\mathrm{n}}$ in the ANC was estimated to be 98 ± 2%. Module-to-module variations of about 10% were found and corrected for. The quoted overall normalisation error is 5%, due to the uncertainty in

the $\bar{n}$ detection efficiency and to uncertainties in the cuts for background reduction. At the smallest angle, a systematic error of 5% due to $\bar{p}$ annihilation in the beam veto counters was estimated.

2.3.3 Experiment PS201

The aim of the second generation LEAR experiment PS201 (OBELIX) was the study of meson spectroscopy, as well as low-energy $\bar{p}$ and $\bar{n}$ annihilation on nucleons and nuclei to investigate nuclear dynamics effects.

A detailed description of the experimental apparatus can be found in [95]. It consisted of a magnetic spectrometer (shown in Fig. 2.10) covering a solid angle of about 3π, a cylindrical target located at the centre of the spectrometer, and a thin detector (about 80 mm of scintillator), placed closed to the beam pipe window, to measure the incoming $\bar{p}$ beam.

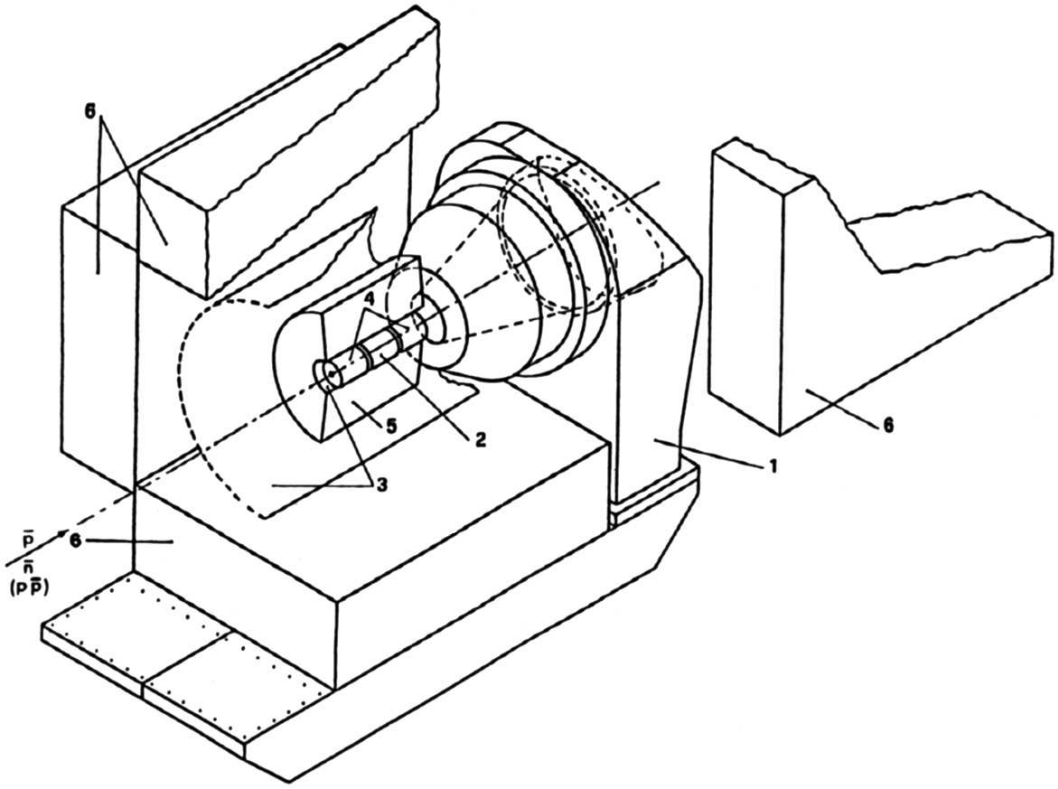

Figure 2.10: Schematic view of the PS201 experiment set-up. The numbers indicate the main components of the apparatus: the Open Axial Field magnet (1), the SPC (2, 4), the TOF (3), the AFSJet (5), the HARGD (6).

The spectrometer consisted of the Open Axial Field magnet, whose magnetic field was about 0.6 T in an open volume of about 3 m^3, and of four sub-detectors arranged inside and around the magnet:

- spiral projection chambers (SPC): an imaging vertex detector with three-dimensional readout for charged tracks and X-ray detection. This detector allows to take data with a large fraction of P-wave annihilation.
- a time-of-flight system (TOF): two coaxial barrels of plastic scintillators consisting of 30 (84) slabs positioned at a distance of 18 cm (136 cm) from the beam axis; a time resolution of

$1\,\mathrm{ns}$ FWHM is achieved. This device provides information about multiplicity and topology of annihilation events; it was used in the first level trigger.

- a jet drift chamber (AFSJet, axial field spectrometer jet chamber): it was used for tracking and particle identification by $\mathrm{d}E/\mathrm{d}x$ measurement. The chamber was split into two half-cylinders (160 cm in diameter, 140 cm long) with a total of 3280 wires.
- a high-angular-resolution gamma detector (HARGD), consisting of four modules made by layers of 3×4 m^2 lead converter foils enclosed by planes of limited streamer tubes.

The target could be filled with different gases at different pressures or liquids, according to the measurements to be performed.

Several measurements of the $\bar{\mathrm{p}}\mathrm{p}$ and $\bar{\mathrm{n}}\mathrm{p}$ integrated cross-sections were performed. These measurements extend the existing data-base down to very low energies (about 1 MeV). The experimental techniques are described in the following.

$\sigma_{\mathbf{ann}}(\bar{\mathbf{p}}\mathbf{p})$ measurement

The $\bar{\mathrm{p}}\mathrm{p}$ annihilation cross-section was measured by PS201 at 14 incoming $\bar{\mathrm{p}}$ momenta in the range 37.6 to 174.4 MeV/c [96, 97].

The data were taken using an extracted $\bar{\mathrm{p}}$ beam with 105 and 201 MeV/c, in two different data taking periods using the same procedure. The beam was degraded in mylar sheets before entering the gaseous hydrogen target (75 cm length and 30 cm diameter) whose pressure could be varied to allow the incident $\bar{\mathrm{p}}$ beam to stop near or upon the end window of the target tank. Using no degrader or mylar sheets, 9 different $\bar{\mathrm{p}}$ momenta at the entrance of the target were selected. For the data of Ref. [96], 5 more bins in the incoming $\bar{\mathrm{p}}$ momentum were obtained by dividing the target along the beam axis in several fiducial regions.

The $\bar{\mathrm{p}}\mathrm{p}$ annihilation cross-section into charged particles was measured by counting the number N_{ev} of annihilation events in flight within a fiducial volume inside the target, and the number $N_{\bar{\mathrm{p}}}$ of $\bar{\mathrm{p}}$ not interacting in the target and annihilating, at rest, near or in the end wall of the target tank. To measure $N_{\bar{\mathrm{p}}}$, a scintillator disc positioned close to the end wall of the target tank was used, together with the TOF system. The number $\bar{\mathrm{p}}$'s crossing the fiducial volume, corrected for the efficiency of the counting system, was used as incident beam rate to extract the annihilation cross-section.

For $\bar{\mathrm{p}}\mathrm{p}$ annihilating in flight, the coordinates of the annihilation point were measured with an uncertainty of 1 cm using the tracking system of the spectrometers ; the annihilation time relative to the beam detectors was measured with a total uncertainty of 1 ns by the TOF system detecting the charged annihilation products. The correlation between the vertex coordinate of the reconstructed annihilation point along the beam axis and the annihilation time was used to determine the incident beam momentum (in good agreement with Monte-Carlo calculation) and to reject in-flight annihilation events of $\bar{\mathrm{p}}$ with momentum in the low-energy tail of the distribution (3σ cut). Only annihilation events inside cylindric fiducial volumes at a suitable distance from the entrance mylar window of the target were considered.

Corrections were applied to take into account several effects, like annihilation detection efficiency, all-neutral annihilation channels, background due to annihilation on the target walls whose vertex was (wrongly) reconstructed inside the fiducial volume, the cut on the correlation between the reconstructed annihilation point and the annihilation time, and the efficiency of the beam counting system.

The overall normalisation error (to be added to the quoted systematic error) was estimated to be 3.4% [96] and 2% [97]; it is mainly due to the corrections for the apparatus efficiency and for all-neutral annihilation, and to the uncertainty in the target density. The quoted systematic errors on $\beta\,\sigma_{\mathrm{ann}}$ range from about 1.2% at 174.4 MeV/c to 14% at 37.6 MeV/c, to be compared with statistical errors between 3.8 and 1.9%.

The $\bar{\mathrm{n}}$ beam

To perform measurements with low energy $\bar{\mathrm{n}}$'s, the OBELIX collaboration put into operation a facility for the production of a collimated $\bar{\mathrm{n}}$ beam [98–100]. The $\bar{\mathrm{n}}$ beam was produced via the charge-exchange reaction $\bar{\mathrm{p}}\mathrm{p} \rightarrow \bar{\mathrm{n}}\mathrm{n}$ on a liquid H_2 target, a technique already used at AGS by T. Armstrong et al. [101] to produce $\bar{\mathrm{n}}$ beams of momenta between 100 and 500 MeV/c, and at LEAR by experiment PS178 [102].

In PS201, the "$\bar{\mathrm{n}}$ production target" was a 40 cm long liquid hydrogen target, positioned 2 m upstream of the centre of the main detector, on the nominal $\bar{\mathrm{p}}$ axis. The target thickness was chosen as to stop the $\bar{\mathrm{p}}$ beam (incident momentum 406 MeV/c) in the target. Charge-exchange events in the production target were selected asking no signal in the veto box of scintillators surrounding the target. The veto box could detect charged particles produced in $\bar{\mathrm{p}}$ interaction in the target, and γ's produced in annihilation into neutral particles and converted in a 5 mm thick lead shields wrapping the target. The $\bar{\mathrm{n}}$ produced by charge-exchange in the forward direction were collimated using a suitable shaped lead shield. The resulting $\bar{\mathrm{n}}$ beam had an intensity of 3 to 5×10^{-5} $\bar{\mathrm{n}}$/ $\bar{\mathrm{p}}$, and momenta between 50 and 400 MeV/c.

Because of the structure of the apparatus, the $\bar{\mathrm{n}}$ beam could not be tagged by detecting the associated n, thus the momentum of each $\bar{\mathrm{n}}$ was unknown. For $\bar{\mathrm{n}}$'s annihilating in the reaction target, the annihilation point and time were measured; with an iterative procedure, the $\bar{\mathrm{n}}$ momentum could be estimated from the $\bar{\mathrm{p}}$ and $\bar{\mathrm{n}}$ time-of-flight, with an error ranging from about 2 MeV/c at 50 MeV/c to about 18 MeV/c at 400 MeV/c.

The $\bar{\mathrm{n}}$ flux was monitored by $\bar{\mathrm{n}}$ annihilating in a nuclear target, 30 cm downstream the reaction target, or a $\bar{\mathrm{n}}$ detector put at the end of the apparatus. The $\bar{\mathrm{n}}$ beam intensity was evaluated by the measured $\bar{\mathrm{p}}$ flux through Monte-Carlo simulation.

$\sigma_{\mathrm{tot}}(\bar{\mathrm{n}}\mathrm{p})$ measurement

The $\bar{\mathrm{n}}\mathrm{p}$ total cross-section has been measured at 18 $\bar{\mathrm{n}}$ momenta between 54 and 380 MeV/c using the transmission technique in a thick target [100]. The reaction target was a 25 cm long liquid hydrogen target, sitting in the centre of the spectrometer. For $\bar{\mathrm{n}}$ annihilating into charged mesons, the annihilation vertex was reconstructed. The $\bar{\mathrm{n}}$ momentum was evaluated from the time of flight of the charged particles produced in the annihilation and from the annihilation position. The annihilation data were then grouped into 18 sets, corresponding to different $\bar{\mathrm{n}}$ momentum bins, 10 to 20 MeV/c wide, according to the momentum resolution. In each bin the total cross-section was evaluated from the measured z distribution (where z is the depth in the target along the beam axis) of the annihilating $\bar{\mathrm{n}}$, inside a fiducial region with a frustum of cone shape of small aperture (about 1.3^o). The position of the cone was defined taking into account beam misalignments. Corrections due to annihilation events occurring after scattering were estimated with a dedicated Monte-Carlo to be 2 to 5% (at the lowest momentum).

The quoted systematic errors are between 10 and 26 mb (less than 10% at the higher momenta and about 5% at 60 MeV/c); the statistical errors are of the same order at higher momenta and about twice at the lower momenta.

$\sigma_{\mathrm{ann}}(\bar{\mathrm{n}}\mathrm{p})$ measurement

The cross-section for $\bar{\mathrm{n}}\mathrm{p}$ annihilation was measured at 18 $\bar{\mathrm{n}}$ momenta between 50 and 400 MeV/c. The data are not yet published; information can be found in a Thesis [103] or in Conference proceedings [99, 104, 105].

The cross-section was extracted from the number of annihilation events in the liquid hydrogen reaction target. The statistical errors are small, and the systematic error is about 10%, mainly due to the uncertainties in determination of the $\bar{\mathrm{n}}$ flux.

2.3.4 Experiment PS198

Experiment PS198 has measured differential cross-section and analysing power in $\bar{\mathrm{p}}\mathrm{p}$ elastic scattering at 439, 544, and 697 MeV/c [106, 107] in the full angular range. The measurements were performed using a solid polarised proton target, and a one-arm magnetic spectrometer to select elastically scattered $\bar{\mathrm{p}}$.

The experimental set-up is sketched in Fig. 2.11. The incoming beam with an intensity of a few

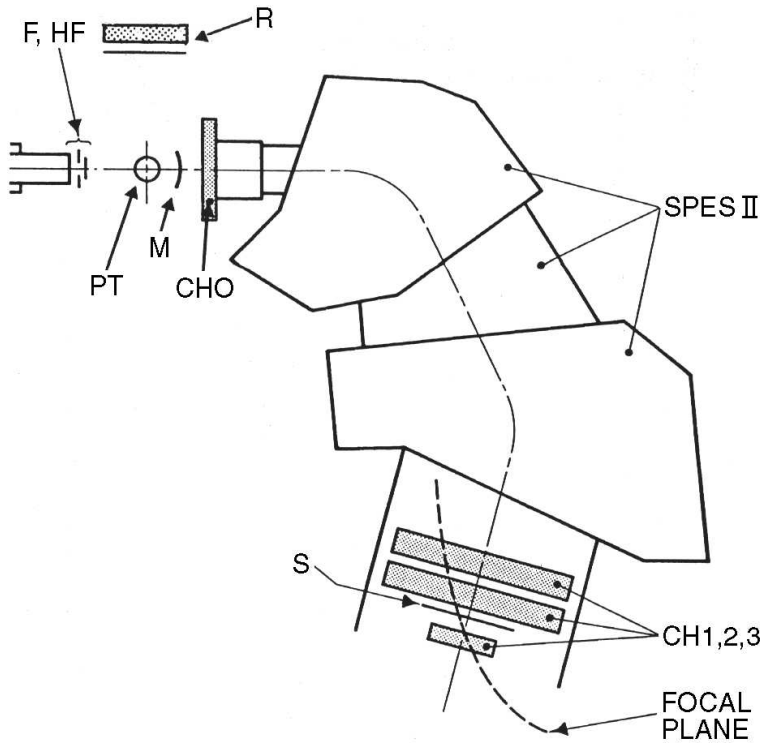

Figure 2.11: Schematic top view of the PS198 experiment set-up.

times 10^5 $\bar{\mathrm{p}}$/sec was monitored by the scintillation counter F, 0.3 mm thick, and by the "antihalo" scintillation counter HF, 0.5 mm thick and with a circular hole of 12 mm diameter. Additional monitoring was performed with the scintillation counter M, placed downstream of the target, outside the acceptance of the spectrometer.

The polarised target consisted of a 5 mm thick slab of pentanol and was operated in the frozen-spin mode. The 0.7 T vertical magnetic field needed to hold the proton polarisation was produced by a superconducting split-coil magnet. The polarisation ranged between 68% and 85% and was measured with an error of $\pm$4%.

The forward final particle (the $\bar{\mathrm{p}}$ for $\vartheta_{\mathrm{cm}} < 90^\circ$, the p for $\vartheta_{\mathrm{cm}} > 90^\circ$) was detected and its momentum analysed with the magnetic spectrometer SPESII [108]. To cover the full angular range, the spectrometer was rotated and set at the chosen scattering angles. The detection system of the spectrometer consisted of four MWPC (CH0-CH3), all of them with horizontal and vertical wires, and of a scintillation counter S. Protons and antiprotons were discriminated from the other particles (mainly π) produced by $\bar{\mathrm{p}}$ interactions in the target by means of time-of-flight, measured by F and S. Using this technique, the complete reaction kinematics was reconstructed, and antiprotons scattering off free protons of the target could be distinguished from those scattered off quasi-free target nucleons, on the basis of the reconstructed missing mass. Around $\vartheta_{\mathrm{cm}} = 90^\circ$, where the energy of

the detected particle was minimal, the angular and energy straggling deteriorated the missing mass resolution. To improve the signal to background ratio in this angular region and to check the background evaluation, a detector R, consisting of scintillator slabs and a MWPC, was added to detect the recoil particle, thus improving considerably the kinematic reconstruction.

The systematic error in the differential cross-section (5%, included in the quoted error) is due to background, acceptance, efficiency, and absorption evaluation. The quoted error does not include the overall normalisation error of 10%. The total systematic error in A_{0n} is of the order of 8%, the major contribution being the uncertainty about the target polarisation.

2.3.5 Experiment PS199

Experiment PS199 was proposed to measure spin effects in the charge-exchange reaction $\bar{\mathrm{p}}\mathrm{p} \to \bar{\mathrm{n}}\mathrm{n}$ at low energy, in particular the analysing power A_{0n} and the polarisation transfer parameter D_{0n0n}, using a solid-pentanol polarised target. The differential cross-section was also extracted from the same data and from the calibration data collected using a liquid hydrogen target at one $\bar{\mathrm{p}}$ momentum ($693\,\mathrm{MeV}/c$).

The experimental apparatus is shown in Fig. 2.12. The incoming $\bar{\mathrm{p}}$'s were detected by two small

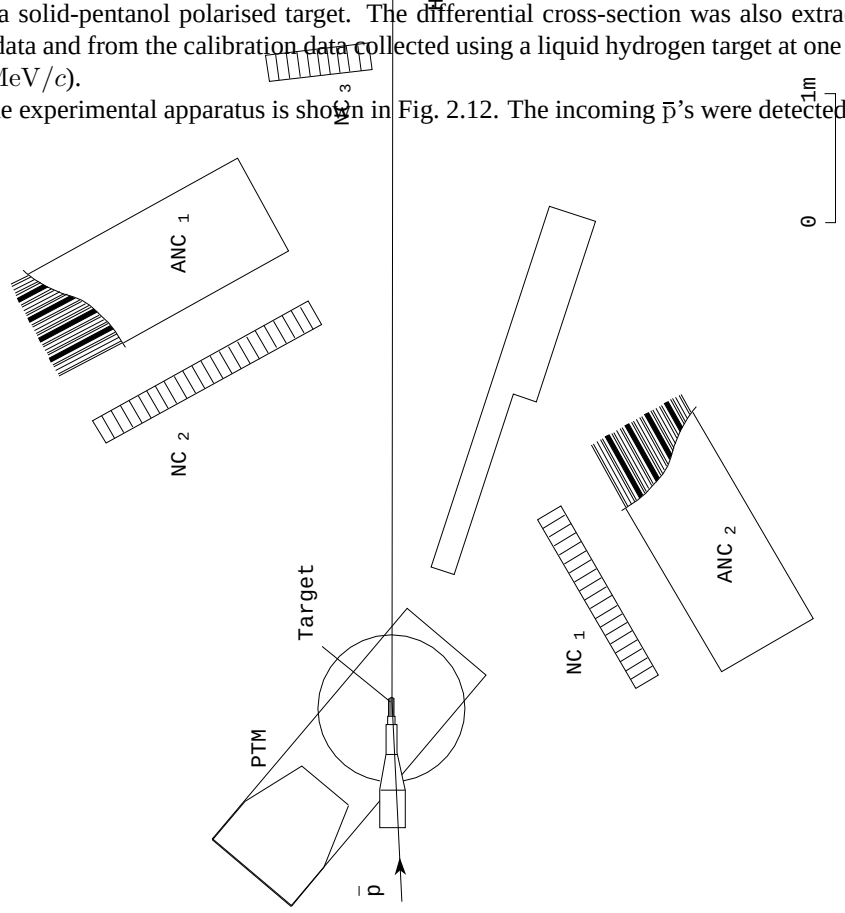

Figure 2.12: Top view of the experiment PS199 set-up.

scintillation counters (not shown in the figure). The beam direction in the horizontal plane (indicated by the continuous line in the figure) was monitored by the scintillation counter hodoscope HB.

The pentanol polarised target (PT) had 12 cm length and 1.8 cm diameter, and was operated in the frozen-spin mode. During data taking, its polarisation was about 75%. To reduce systematic effects, the spin orientation was reversed typically after four one-hour spills. For calibration purposes, the polarised target could be replaced by a liquid hydrogen target, 12 cm length and 3.2 cm diameter. The background from charge-exchange events on the bound nucleons of the polarised target was

evaluated using data collected with a dummy target (DT), having the same mass and density as the PT but all H atoms replaced by F atoms. The considerable amount of material in the target caused a large energy loss of the $\bar{\mathrm{p}}$ beam in the target: at $905\,\mathrm{MeV}/c$ extracted beam momentum, the mean reaction momentum was $875\,\mathrm{MeV}/c$ and the total range was about $40\,\mathrm{MeV}/c$. A scintillator veto box surrounded the target and rejected at the trigger level annihilation and elastic scattering events, as well as non-interacting $\bar{\mathrm{p}}$'s. The azimuthal acceptance was limited to $\pm 15^\circ$ by the polarised target magnet (PTM) coils.

The neutron detectors NC_1, NC_2 and NC_3 were made of vertical plastic scintillator bars [109]. Each bar (8 cm wide and 20 cm thick) was viewed at its end by two photo-multipliers (PM); the coincidence between the two PMs defined a bar hit. In the off-line analysis, the n candidates were identified by requiring one bar (or at most two adjacent bars) be hit in one NC hodoscope. The neutron coordinates were given by the bar number in the horizontal plane. The vertical coordinate was given by the difference between the time measured by the top and the bottom PM of each bar; it was determined with a precision of 3.7 cm. The neutron time-of-flight was given by the mean of the TOFs of all the PMs of the hit bars. Only neutron bars showing a stable behaviour (monitored with a laser system during all data taking) were considered.

The antineutron detectors (ANC_1 and ANC_2) were designed to have good efficiency and an excellent n/$\bar{\mathrm{n}}$ separation. The $\bar{\mathrm{n}}$'s were identified by reconstructing the trajectories of the charged products of their annihilation. The geometry of the $\bar{\mathrm{n}}$ detectors was chosen to have a maximum antineutron annihilation rate on relatively thick absorbers, which were sandwiched by tracking detectors to reconstruct the trajectories of charged particles. An antineutron-annihilation event was identified in the off-line analysis looking for a "star" pattern in the detectors. With Monte-Carlo events, the resolution in the transverse coordinates of the annihilation point was estimated to be somewhat smaller than 1 cm, and about 2 cm in the z-coordinate.

Each ANC [110] was built up using 5 identical basic units, the "modules", separated by 4 iron slabs, 30 mm thick, which made up most of the mass of the detector. The distance between the iron slabs was 190 mm. Each "module" was made of four planes of vertical Limited Streamer Tubes (LST) with one plane of scintillation counters in between, and was closed by two 6.35 mm thick Al walls. The LST planes were used to reconstruct the trajectories of the charged particles produced in the $\bar{\mathrm{n}}$ annihilation. Each plane had an active surface of 166×200 cm^2 and was equipped with 192 strips to measure the horizontal coordinates and 160 strips for the vertical coordinates. The planes were made up with PVC eight-tube chambers filled with a 30:70 Ar-iso$\mathrm{C_4H_{10}}$ gas mixture at atmospheric pressure.

The scintillation counter planes were hodoscopes of six vertical scintillator slabs 10 mm thick, 33 cm wide, and 166 cm long. Each slab was viewed by two PMs and a scintillation counter hit was given by the mean-time coincidence of the two PMs.

In the off-line analysis, the time-of-flight of the antineutron was computed from the mean of the TOFs of the scintillation counters of the two modules sandwiching the absorber where the vertex of the annihilation 'star' was reconstructed. A TOF cut allowed the rejection of γ and π produced in the target.

At the trigger level, a $\bar{\mathrm{n}}$ signal was defined as at least two fired counters in one ANC.

Measurement of A_{0n} and $\mathrm{d}\sigma/\mathrm{d}\Omega$

A_{0n} was measured at 8 $\bar{\mathrm{p}}$ momenta between 546 and $1287\,\mathrm{MeV}/c$, during two short runs in 1989 and 1990 [111–114].

The useful charge-exchange events were characterised by a neutron detected in one neutron counter and an antineutron seen by the corresponding $\bar{\mathrm{n}}$ detector (NC_1-ANC_1 and NC_2-ANC_2 for the forward and backward angular range respectively). The requirement to detect both particles in the final state implied that very forward and very backward scattering events could not be measured. Only at $875\,\mathrm{MeV}/c$ incident $\bar{\mathrm{p}}$ momentum, a measurement was done over a broad angular range detecting only the $\bar{\mathrm{n}}$ [114].

All events with a valid beam signal, with no signal from the veto box surrounding the target, with at least one bar hit in a NC and with a $\bar{\mathrm{n}}$ signal in the corresponding ANC were recorded on tape.

The data collected for the A_{0n} measurement were also used to extract the $\bar{\mathrm{p}}\mathrm{p} \to \bar{\mathrm{n}}\mathrm{n}$ differential cross-section at all $\bar{\mathrm{p}}$ momenta but $1000\,\mathrm{MeV}/c$ [115]. This was possible thanks to a calibration method for the ANC detectors [116] which gave the $\bar{\mathrm{n}}$ detection efficiency with an error of few percent. The quoted overall normalisation error of about 10% was mainly due to the uncertainty in the polarised target length.

Using the calibration data collected with a liquid hydrogen target, the differential cross-section was measured at $693\,\mathrm{MeV}/c$ over a wider angular range [111].

Measurement of D_{0n0n}

The D_{0n0n} parameter was measured at 546 and $875\,\mathrm{MeV}/c$ [117, 118], with two similar experimental set-ups. As in the case of A_{0n}, the measurement of D_{0n0n} was performed detecting both the n and the $\bar{\mathrm{n}}$. D_{0n0n} was then measured by analysing the polarisation of the final-state neutrons. The apparatus used for the measurement at $875\,\mathrm{MeV}/c$ is shown in Fig. 2.13 and is very similar to the one used to measure A_{0n}: the polarised target and the n and $\bar{\mathrm{n}}$ detectors are the same, they are only differently arranged.

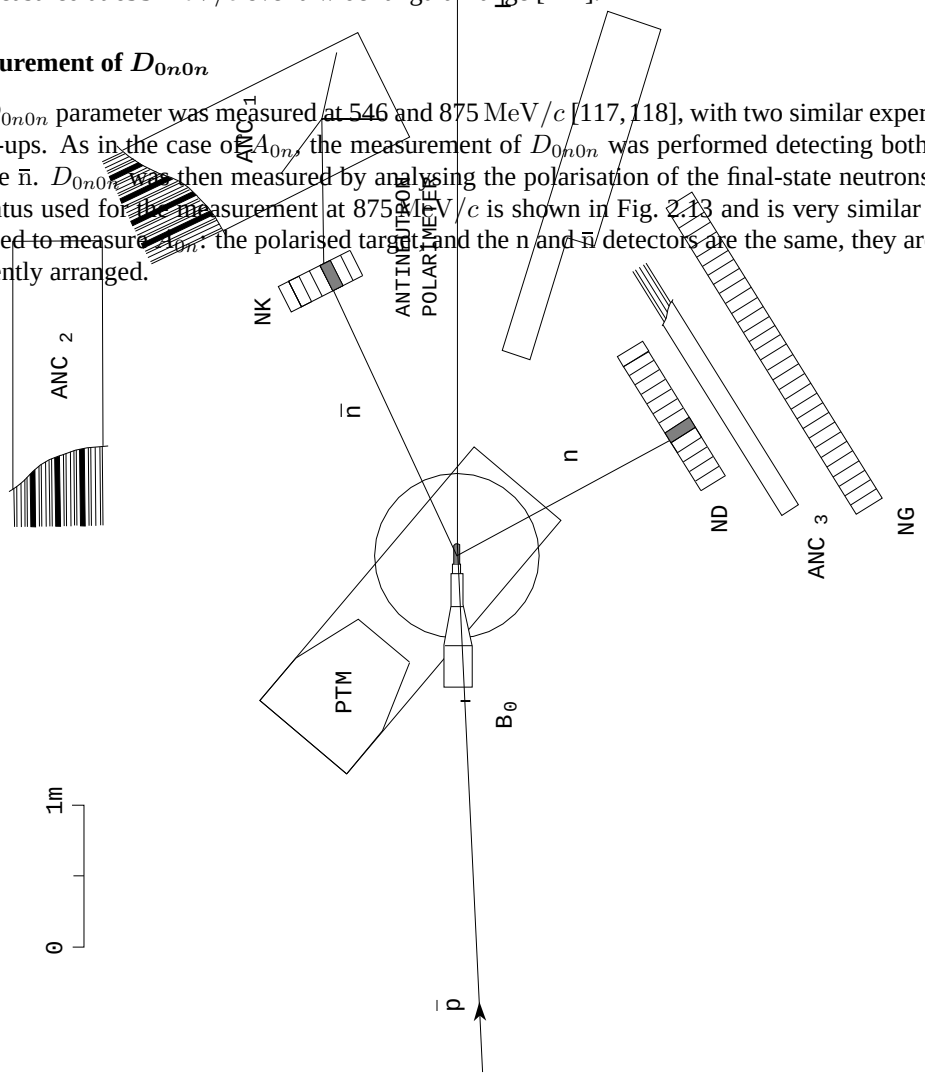

Figure 2.13: Top view of the experiment PS199 set-up used for the measurement of D_{0n0n}.

The data were collected in a about 10 days run at each energy, almost equally divided among PT spin up, PT spin down, and DT data.

The relevant detectors for the D_{0n0n} measurement were the $\bar{\mathrm{n}}$ counter ANC_1 and neutron hodoscopes ND and NG which made up the neutron polarimeter; ANC_3 was a LST module, used in the off-line analysis to reject events with charged particles produced in ND. ANC_2 was used to measure in parallel A_{0n} and $\mathrm{d}\sigma/\mathrm{d}\Omega$ in the backward hemisphere [114]. The useful events for the D_{0n0n}

measurement were those with an $\bar{\mathrm{n}}$ produced by charge-exchange on a free hydrogen of the polarised target and detected in ANC_1, and the associated n interacting elastically on a hydrogen nucleus of the counter ND and then detected by NG. The polarisation of the n produced in the charge-exchange reaction could thus be measured from the left-right asymmetry of the scattered neutrons, since the analysing power of the np elastic scattering reaction is known. Only a small percentage of the sample (10%) were events in which the neutron was elastically scattered off a proton in ND. They were selected using all three measured quantities, namely the n scattering angle, the time-of-flight of the scattered particle and the energy T_p released in ND. A precise energy calibration of each neutron-counter bar was performed before, during and after the run measuring the ADC spectra of the 4.4 MeV γ-rays from an Am/Be neutron source and the ADC spectra of cosmic ray muons crossing the hodoscopes. The stability of the counters during data-taking was monitored using a system based on a N_2 laser. The effective analysing power of the n polarimeter was estimated with a Monte-Carlo program which took into account all the interactions of neutrons in the scintillator, and using previous measurements for a similar polarimeter.

To eliminate the systematic errors due to the non-uniform efficiency of the NG counter, and to possible geometrical effects, D_{0n0n} was extracted using an estimator which did not require a uniform efficiency of the polarimeter, it only required the detection efficiency to be stable during the data taking.

Using the same data, a measurement of the product of the $\bar{\mathrm{n}}\mathrm{p}$ analysing power times the spin parameter K_{n00n} was performed at $875\,\mathrm{MeV}/c$ [119].

2.3.6 Experiment PS206

The objective of PS206 [120, 121] was to accurately measure at a few energies the differential cross-section of the charge-exchange reaction $\bar{\mathrm{p}}\mathrm{p} \rightarrow \bar{\mathrm{n}}\mathrm{n}$. It was proposed and performed by a large fraction of the PS199 Collaboration, using much of the detectors and the experimental method of that experiment, with a few notable differences. A dedicated liquid hydrogen target was built for this experiment, the $\bar{\mathrm{p}}\mathrm{p} \rightarrow \bar{\mathrm{n}}\mathrm{n}$ differential cross-section was measured from the $\bar{\mathrm{n}}$'s angular distribution alone, and the associated neutrons were detected only over a smaller angular range, to determine the efficiency of the $\bar{\mathrm{n}}$ detectors.

The measurements were performed at two extracted $\bar{\mathrm{p}}$ momenta, $612\,\mathrm{MeV}/c$ and $1206\,\mathrm{MeV}/c$. The layout of the experiment for the measurements at $612\,\mathrm{MeV}/c$ is shown in Fig. 2.14. For the measurement at $1206\,\mathrm{MeV}/c$ a slightly different arrangement of the detectors was adopted.

The antineutron detectors ANC_1 and ANC_2 were used to measure the angular distribution in the forward region; ANC_3 detected both n and $\bar{\mathrm{n}}$ in the backward hemisphere. Thus almost all the angular range was covered, extending down to the forward direction $\theta = 0$. The continuous line in Fig. 2.14 indicates the $\bar{\mathrm{p}}$ beam direction, the dashed line the direction of $\bar{\mathrm{n}}$'s produced at zero degree in the target. The incoming $\bar{\mathrm{p}}$'s were defined by two scintillation counters B_0 (50×70 cm^2) and B_1 (a 1 cm diameter, 5 mm thick). The total beam flux was measured by B_0, while the coincidence $\mathrm{B}_0 \times \mathrm{B}_1$ defined the beam entering the target. Three multi-wire proportional chambers (PBC_1, PBC_2, and PBC_3) monitored the beam direction and position. A C-shaped magnet (MN) was used to sweep the $\bar{\mathrm{p}}$ leaving the target away from the 0° direction, allowing to measure the differential cross-section in the very forward region. The scintillation counter hodoscope HB monitored the beam direction in the horizontal plane. The beam momenta at the target centre were 601.5 and $1202\,\mathrm{MeV}/c$, with a total spread of about 14 and $5\,\mathrm{MeV}/c$ in the two cases. The 1 σ beam divergence, 6.8 mrad in both planes at $601.5\,\mathrm{MeV}/c$ and 3.3 mrad at $1202\,\mathrm{MeV}/c$, was dominated by multiple scattering.

The liquid hydrogen target (LHT), 10.61 cm long and 3 cm diameter, could be filled and emptied in a few minutes; inside the target, a diode measured its temperature in order to monitor the filling operations and to evaluate the residual hydrogen density in the "empty" target.

To reject annihilation and elastic events at the trigger level, the target was surrounded by a scintillation counter box on all sides, except that of the incoming beam. The forward and the two lateral counters ensured that no trigger caused by charged particles in the ANCs was accepted. The upper

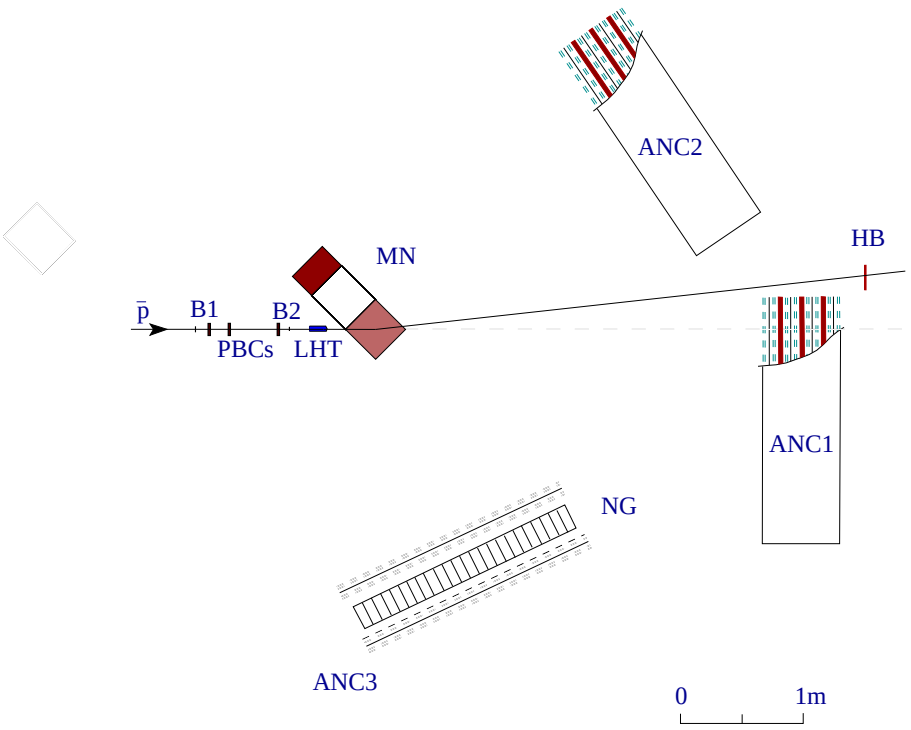

Figure 2.14: Top view of the experiment PS206 set-up.

and lower vetoes were made up of four layers of scintillator, interleaved with a total of 1 radiation lengths of lead to reject annihilation events into neutrals.

The $\bar{\mathrm{n}}$ detectors ANC_1 and ANC_2 were essentially the same which had already been used in experiment PS199. Each detector was made up by three identical units, a unit consisting of a 3 cm thick iron slab, sandwiched between two modules of four planes of limited streamer tubes (LST) and one plane of scintillation counters, already described in Sect. 2.3.5.

ANC_3 was a new counter, designed to detect with reasonable efficiency both neutrons and antineutrons, and which could thus be used both for calibration purposes and to measure the $\bar{\mathrm{n}}$ angular distribution in the backward hemisphere. ANC_3 consisted of a neutron counter (NG) sandwiched by two modules, identical to those making up ANC_1 and ANC_2. The neutron counter was a hodoscope of 27 vertical scintillator bars, 8 cm wide and 20 cm thick; the bar heights range from 110 to 130 cm. The bars were viewed from each end by a photomultiplier; time and amplitude information was recorded. A system based on a N_2 laser had been used during all runs to monitor the NG bars as well as the ANC scintillation counters.

For the measurement at $1202\,\mathrm{MeV}/c$, the antineutron detectors ANC_1 and ANC_2 were put at about 6 m away from the target in order to separate, on the basis of the measured time-of-flight, $\bar{\mathrm{n}}$'s produced in the $\bar{\mathrm{p}}\mathrm{p} \to \bar{\mathrm{n}}\mathrm{n}$ reaction from π^0 and γ coming from $\bar{\mathrm{p}}\mathrm{p}$ annihilation in the target, much in the same way as at the low-energy measurement.

For the first time, large samples of data were collected for the charge-exchange reaction. For background evaluation, data were taken alternating full target (FT) and empty target (ET) runs. With the full target about 75×10^6 events at $601.5\,\mathrm{MeV}/c$ and 17×10^6 events at $1202\,\mathrm{MeV}/c$ were collected, corresponding to a useful beam of 38×10^9 and 21.5×10^9 $\bar{\mathrm{p}}$ respectively; the statistics with empty target were 5×10^6 and 3×10^6 events on tape and 8.7×10^9 and 15.6×10^9 incoming $\bar{\mathrm{p}}$ at $601.5\,\mathrm{MeV}/c$ and $1202\,\mathrm{MeV}/c$ respectively.

The measurement of the $\bar{\mathrm{p}}\mathrm{p} \to \bar{\mathrm{n}}\mathrm{n}$ charge-exchange differential cross-section required the measurement of the $\bar{\mathrm{n}}$ angular distribution, and the measurement of the $\bar{\mathrm{n}}$ detection efficiency. To identify the $\bar{\mathrm{n}}$'s, one looked at "star" topologies in the ANC detectors, much in the same way as in PS199. As compared to PS199, the $\bar{\mathrm{n}}$ definition had been further improved in two ways:

- a "sphericity" cut was applied to the "star" topology, to distinguish an $\bar{\mathrm{n}}$ annihilation star (the distribution of secondaries in ANC is almost isotropic) from γ-stars (the corresponding e^+ and e^- tracks are almost collinear) or π-stars. The γ-stars or π-stars could have been produced by pions from an undetected $\bar{\mathrm{n}}$ annihilation in the ANC and might result in a false $\bar{\mathrm{n}}$-star, far from the $\bar{\mathrm{n}}$-annihilation point.
- To improve the measurement of the $\bar{\mathrm{n}}$ time-of-flight, a more restricted definition was introduced, which used the tracks belonging to the star topology to identify the scintillators that should have fired. Only scintillators crossed by these tracks were taken into account, and the measured $\bar{\mathrm{n}}$ TOF was defined as the average of the "good" scintillator TOFs. Further TOF cuts were applied to reject cross-talk events between ANC_1 and ANC_2.

To evaluate the ANC efficiency for $\bar{\mathrm{n}}$'s, PS206 applied the same procedure already adopted by PS199, relying on the "associate particle" method. A detailed investigation of many systematic effects, the improved layout of the experiment, and the much larger data sample available for the analysis allowed to reduce the error of the method by almost a factor of three, as compared to PS199. A precision in the absolute normalisation of 2% and 4% at $601.5\,\mathrm{MeV}/c$ and $1202\,\mathrm{MeV}/c$ respectively is quoted, while over most of the angular range the point-to-point error is lower than 1%.

2.3.7 Experiment PS185

The aim of this experiment was to study how strangeness is produced, by studying hyperon–antihyperon final states. The cross-section, angular distribution and final-state polarisation were measured. The last runs, PS185/3, benefited from a polarised proton target, as described in the proposal [122]; its

data are still being analysed at the time we finish this review. They include the spin transfer from proton to Λ and to $\overline{\Lambda}$.

The data on strangeness-exchange scattering have been published in Refs. [123–129]. Results on *CP* tests can be found in Ref. [130]. The collaboration also took data on $K\overline{K}$ channels [131].

A schematic view of the set-up is shown in Fig. 2.3.7. The antiproton beam was sent on a C-CH_2

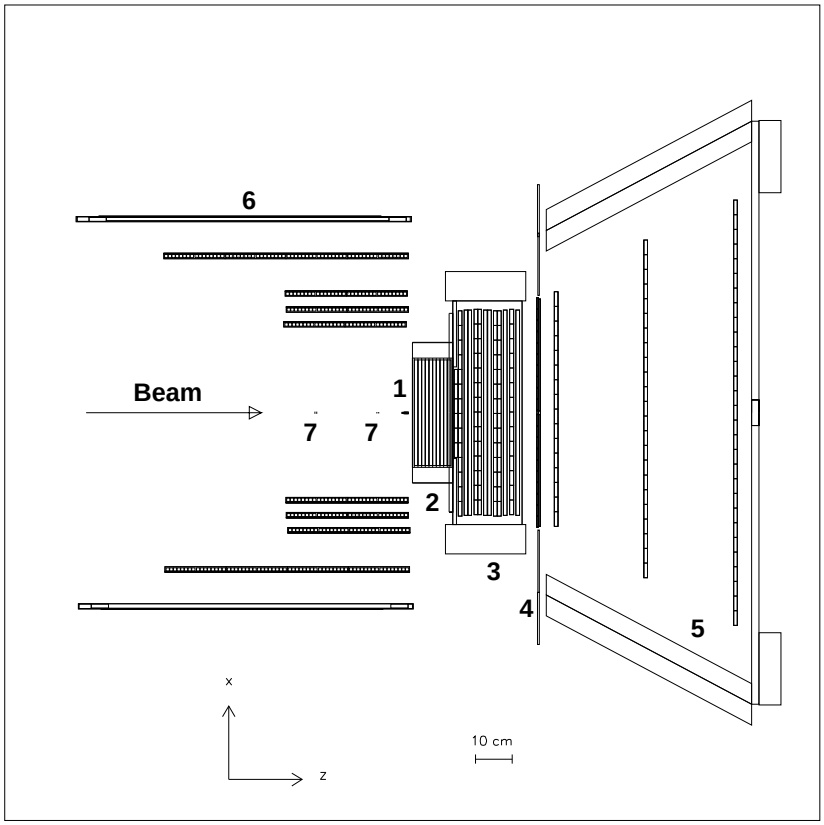

Figure 2.15: Overview of the PS185 detector at LEAR. 1:target, 2: multi-wire proportional chambers, 3: drift chambers, 4: hodoscope, 5: solenoid with drift chambers, 6: limited streamer tubes, 7: silicon microstrips.

target which was thick, to obtain high luminosity, and segmented to provide a good determination of the reaction vertex.

The target was divided into five modules, each with a thickness of 2.5 mm. Four target cells were built of polyethylene (CH_2) (high proton density). This structure allowed fine momentum scales in $800\,\mathrm{keV}/c$ bins. In order to control the Carbon background of the other modules, one cell consisted of pure Carbon.

The detection system included tracking chambers, multi-wire proportional chambers and drift chambers and allowed the reconstruction of the charged-particle tracks. Within the LEAR range ($p_{\overline{\mathrm{p}}} \leq 2\,\mathrm{GeV}/c$) the hyperons are always emitted into a forward cone. In fact, also the decay proton (or antiprotons) are confined within a limited forward cone ($\leq 42^\circ$), fully within the acceptance of the tracking system and of the triggering hodoscope. The charge of each particle was determined from a set of three additional drift chambers inside a magnetic field of typically $B = 0.09$ T. The hodoscope was used to reduce the background, in particular from neutral kaon decays. The limited streamer tubes were not necessary to study the $\overline{\mathrm{p}}\mathrm{p} \to \overline{\Lambda}\Lambda$ reaction, but were used for $K\overline{K}$ final states or to measure $\overline{\Lambda}\Lambda$ production on carbon.

The Λ hyperon was identified by its dominant $p\pi^-$ decay mode (about 64%), which produced a characteristic V^0 signature in the detector. In principle, the reaction $\bar{p}p \to \overline{\Lambda}\Lambda$ is fully identified from the complete reconstruction of the $p\pi^-\bar{p}\pi^+$ final state.

Thanks to parity violation, the decay $\Lambda \to p\pi^-$ is not isotropic in the Λ rest frame, but correlated to its spin. The proton is emitted preferentially parallel to the Λ spin, and the antiproton oppositeto the $\overline{\Lambda}$ spin. The distribution is of the type $I(\vartheta) \propto 1 + \alpha P \cos\vartheta$, where P is the (anti)-hyperon polarisation, and $\alpha = \pm 0.642 \pm 0.013$. So measuring the proton and pion momentum with high statistics gives the polarisation of the outgoing Λ.

As for other hyperons, Σ^0 was identified through its $\Lambda\gamma$ decay, which has almost 100% branching ratio. The photon needs not be measured as long as the precision on charged-particle tracking is sufficient. The charged hyperons were reconstructed through the decays $\Sigma^+ \to p\pi^0$ ($\sim 52\%$), $\Sigma^+ \to n\pi^+$ ($\sim 48\%$) and $\Sigma^- \to n\pi^0$ ($\sim 99.85\%$) and their antibaryon analogues.

2.3.8 Experiment E760 at Fermilab

Experiment E760, at the Fermilab Antiproton Accumulator ring, was devoted to high resolution studies of charmonium states formed in $\bar{p}p$ annihilation. The $\bar{p}p$ forward elastic scattering parameters between 3.7 and 6.2 GeV/c have also been measured [132], using an apparatus incorporated in the luminosity monitor of the experiment. The monitor was designed to perform precision measurements of the $\bar{p}p$ differential cross-section in the very small t region by measuring the recoil protons, to extract the luminosity from the shape of the differential cross-section, with a systematic error of a few percent. The analysis of the shape of the small angle differential cross-section provided also precise values for the ρ parameter.

Details on the apparatus, shown in Fig. 2.16, can be found in Ref. [132] and [133]. The circu-

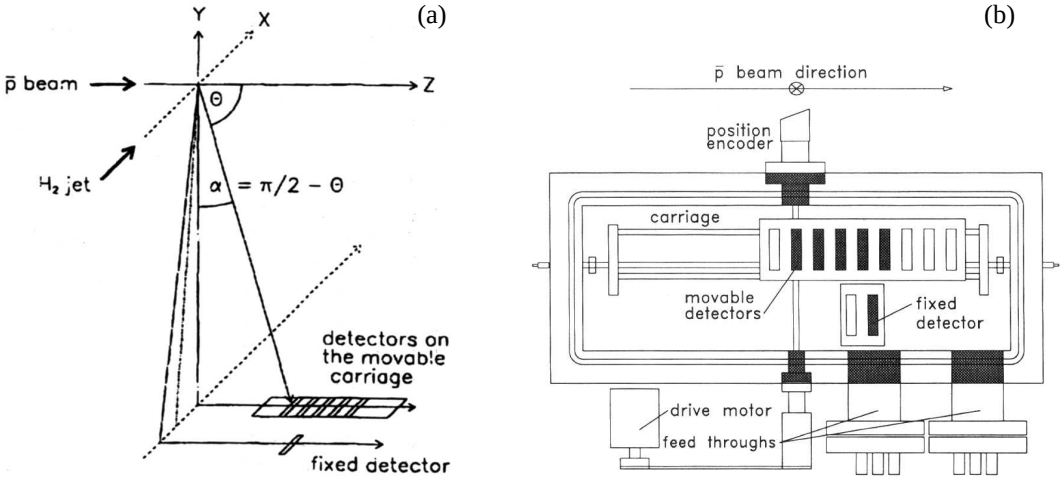

Figure 2.16: Experiment E760: schematic view of the apparatus for detecting recoil protons (a), and top view of the solid-state detectors set-up (b).

lating $\bar{p}$ beam (typically 4×10^{11} $\bar{p}$, about 8 mm diameter) intersected an internal H_2 gas jet target (typical density 3.5×10^{13} protons/cm^2, 7 mm diameter). The solid-state detectors measuring the recoil protons of the $\bar{p}p$ elastic scattering events were placed in a pan (shown in figure 2.16(b)) located at the bottom of a 150 cm long tapered vacuum chamber suspended vertically from the beam pipe. The detector system consisted of one fixed detector for luminosity monitoring positioned at an angle $\alpha = 90^\circ - \theta = 3.547^\circ$ (where θ is the recoil angle), and five detectors with an active

area of about 1×5 cm^2. The latter were located on a carriage which could be moved in a direction parallel to the beam. The "movable" detectors were positioned about 1° apart along a line parallel to the beam, and typically covered the recoil angle range $\alpha = 1.1^\circ$ to 5°. At $5\,\mathrm{GeV}/c$ this angular range corresponds to $-t$ ranging from 0.0009 to 0.019 GeV and to recoil proton energies between 0.4 and 11 MeV. The energy calibration of the detectors was performed using a ^{244}Cm alpha source; the energy resolution of the different detectors ranged between 60 and 110 keV and was found to be reproducible to within 0.2%.

The basic points of the measurements were to measure in each solid state detector the spectrum of the kinetic energy distribution of the recoil protons, subtract the background, and evaluate the mean value of the recoil energy, and thus α and t. Only at $-t < 0.003\,\mathrm{GeV}$, the recoil angle had to be determined from the known distance between the detector and another detector placed at larger $-t$ values. Then, the relative differential cross-section was extracted from the number of detected protons corrected for the slightly different solid angles seen by each detector, and normalised to the fixed detector counts.

The error on the recoil angle was estimated to be less than $\pm 0.006^\circ$. The systematic error due to the uncertainties in the values of the relative areas of the different detectors (less that 0.1%) was also taken into account in extracting the $\bar{\mathrm{p}}\mathrm{p}$ forward elastic scattering parameters.

The angular distribution was measured at six incident $\bar{\mathrm{p}}$ momenta between 3.70 and 6.23 GeV/c, corresponding to the masses of charmonium resonances. To perform the scanning over the width of the charmonium resonances, the beam momentum variations were always less than $75\,\mathrm{MeV}/c$, and were considered negligible for the $\bar{\mathrm{p}}\mathrm{p}$ forward elastic scattering parameters measurements. Also, the perturbation caused by the resonances on the elastic scattering parameters are expected to be completely negligible because the cross-section for the reaction $\bar{\mathrm{p}}\mathrm{p} \to (\mathrm{c}\bar{\mathrm{c}})_\mathrm{R} \to \bar{\mathrm{p}}\mathrm{p}$ is known to be by 5 to 7 orders of magnitude smaller than the $\bar{\mathrm{p}}\mathrm{p}$ elastic scattering cross-section.

The data were fitted considering as free parameters σ_tot, the slope b, and ρ; because of the large correlation between the parameters, a fit was also performed which used for σ_tot the best estimate from the world data in the region of interest. In the two cases, the systematic errors on ρ were estimated to be 0.004 and 0.005 respectively. Correspondingly, the total error on ρ ranged between 0.007 and 0.024 and between 0.007 and 0.012.

2.4 Experiments on $\bar{\mathrm{p}}\mathrm{p}$ and $\bar{\mathrm{p}}\mathrm{d}$ atoms

2.4.1 Pre-LEAR experiments

The motivation to search for X-rays from $\bar{\mathrm{p}}\mathrm{p}$ atoms came from three different sources or "traditions". These traditions and the results of early experiments [134–136] had a significant impact on the experimental techniques chosen at LEAR. It seems therefore adequate to spend a few sentences on the "pre-history" of protonium atoms.

One of the roots of the experimental searches for the X-ray spectrum of antiprotonic hydrogen goes back to the discovery of heavy antiprotonic atoms by the group of Backenstoss, Bamberger, Koch and Lynen [137]. Pionic and kaonic atoms were studied extensively at that time, and the same experimental techniques proved to be useful for antiprotonic atoms, too. The good resolution of solid state detectors allowed to determine line shifts and broadenings due to strong interactions. But the resulting strong interaction parameters were influenced by the nuclear environment. The demand to determine the "free" $\bar{\mathrm{p}}\mathrm{p}$ scattering length required the use of H_2 as target.

Studies of antiproton–proton annihilation at rest in bubble chamber experiments [138] motivated also the study of $\bar{\mathrm{p}}\mathrm{p}$ atoms. From data on $\bar{\mathrm{p}}\mathrm{p}$ annihilation into $\mathrm{K}\overline{\mathrm{K}}$, it had been deduced that most antiprotons annihilate from S-wave orbitals of $\bar{\mathrm{p}}\mathrm{p}$ atoms and that the contributions of P-states should be negligible. The dominance of S-wave capture was explained as cascade effect [139, 140]. S-wave dominance was later challenged by Kalogeropoulos and his coworkers, who argued in favour of very large P-wave contributions to $\bar{\mathrm{p}}\mathrm{p}$ [141] and $\bar{\mathrm{p}}\mathrm{d}$ [142] annihilation. A deeper understanding of the atomic cascade seemed necessary.

Last not least, the Lamb-shift experiments on muonic helium by Zavattini and collaborators [143] had a significant impact. These experiments focused the attention on the importance of cascade processes and on the need to minimise the interaction of light exotic atoms with neighbouring molecules. Indeed, no muonic lines had been observed after stopping muons in liquid hydrogen [144] but Bailey and collaborators did see lines from pionic hydrogen when stopping pions in hydrogen gas [145].

The early experiments on antiprotonic hydrogen confirmed the idea that low-density targets are mandatory for a successful search for radiative traditions of $\bar{\mathrm{p}}\mathrm{p}$ atoms. Two experiments which used a liquid [135] or a high-density H_2 gas [136] target and solid state detectors failed to observe $\bar{\mathrm{p}}\mathrm{p}$ atomic X-rays. It required the use of a low-density gas target to observe at least the *Balmer* series of $\bar{\mathrm{p}}\mathrm{p}$ [134] and $\bar{\mathrm{p}}\mathrm{d}$ [146] atoms and thus to establish the formation and observability of protonium atoms. The low stop rate of the low-density target was compensated by use of a cylindrical multi-wire proportional chamber with large solid angle for X-ray detection. The Balmer series was observed with a yield of $(6 \pm 3)\%$ per annihilation but no K X-rays were found. The result thus confirmed the large annihilation probability of the 2P protonium states, predicted by Kaufmann and Pilkuhn [147].

When LEAR came into operation three experiments were proposed, all three using H_2 gas at low density. In this section we discuss experimental techniques; physics results will be presented in Chapter 5.

2.4.2 PS171: The Asterix experiment

The ASTERIX (**A**ntiproton **ST**op **E**xperiment with t**R**igger on **I**nitial **X**-rays) experiment was designed to study $\bar{\mathrm{p}}\mathrm{p}$ annihilation from P-wave orbitals of protonium atoms formed by stopping antiprotons in H_2 gas. The main emphasis of the experiment was ($\mathrm{q}\bar{\mathrm{q}}$) spectroscopy and the search for glueballs, hybrids, baryonia and other boson resonances [148]. However, the detector was also designed to contribute to the physics of the protonium atom [149]. The detector is fully described in [150]. Physics results on protonium are published in [151–154]. Results on antiproton annihilation from P-states of the protonium atom can be found in [155–166].

Protonium spectroscopy relied on the central detector of a general-purpose particle spectrometer with cylindrical proportional chambers and a homogeneous 0.8T magnetic field. Fig. 2.17 shows the central components of the detector.

Antiprotons with an incident momentum of $105\,\mathrm{MeV}/c$ were moderated by passing through the LEAR exit window, a variable air gap, and a $50\,\mu\mathrm{m}$ entrance scintillator which identified incoming antiprotons, and then entered a H_2 target at standard temperature and pressure (STP). At the end of the target, a thick scintillator was mounted to facilitate beam tuning. The distance between the thin entrance (T2) and the exit (T4) counter was $72\,\mathrm{cm}$. Two further beam defining counters (T1,T3) were used only in the initial phase of the experiment. For $105\,\mathrm{MeV}/c$ antiproton beam momentum, the residual range of antiprotons entering the target led to a well localised stop distribution in the centre of the H_2 target.

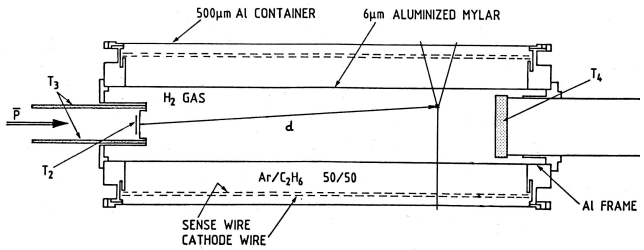

Figure 2.17: The central drift chamber of the Asterix experiment and the antiproton defining scintillators.

The H_2 target was surrounded by a X-ray drift chamber (XDC) and separated from it by a thin

$(6\,\mu\mathrm{m})$ aluminised mylar cylinder of $16\,\mathrm{cm}$ diameter. The mylar cylinder was held at a voltage of $-10\,\mathrm{kV}$ and acted as cathode. The XDC was continuously flushed with an (50:50) argon-ethane-gas mixture; likewise the H_2 gas was exchanged continuously to minimise a possible Argon contamination from the XDC gas diffusing through the mylar foil. A slight overpressure of 1 mbar on the H_2 side (controlled to better than 0.1 mbar) stretched the mylar foil to a perfect cylindrical shape.

The 90 anode wires (Ni-Cr, $32\,\mu\mathrm{m}$ diameter, $1.5\,\mathrm{k}\Omega/\mathrm{m}$) were kept at ground potential, 270 field wires (Cu-Be, $100\,\mu\mathrm{m}$ diameter) at $-2.1\,\mathrm{kV}$ shaped the electric field in 90 "cells" into which the XDC was segmented. An outer Al container provided the mechanical stability of the construction. Each XDC cell was defined by five field wires and one sense wire collecting the charge deposited along a road from the mylar cylinder to the cell. Due to the presence of the 0.8 Tesla magnetic field, the roads were curved. Hence charges, deposited along a straight track originating from the target centre, were collected at different sense wires.

The readout of the XDC was based on the UA1 central detector electronics which recorded the pulse-height history on each wire as a function of time (in $32\,\mathrm{ns}$ time bins and for a time period of $4\,\mu\mathrm{s}$). The sense wires were read out on both ends; from the drift time and the signal ratio on the two wire ends, the conversion point of X-rays could be reconstructed in space. The XDC had, for the measured stop distribution, a large solid angle (90% of 4π), a high detection efficiency even for low X-ray energies (30% for the L_α line at $1.74\,\mathrm{keV}$) but only a rather modest energy resolution of 25% at $5.5\,\mathrm{keV}$.

The XDC allowed an efficient discrimination of X-rays against the dominating background from charged particles, see Fig. 2.18. Charged particles ionise the counter gas all along their path. In

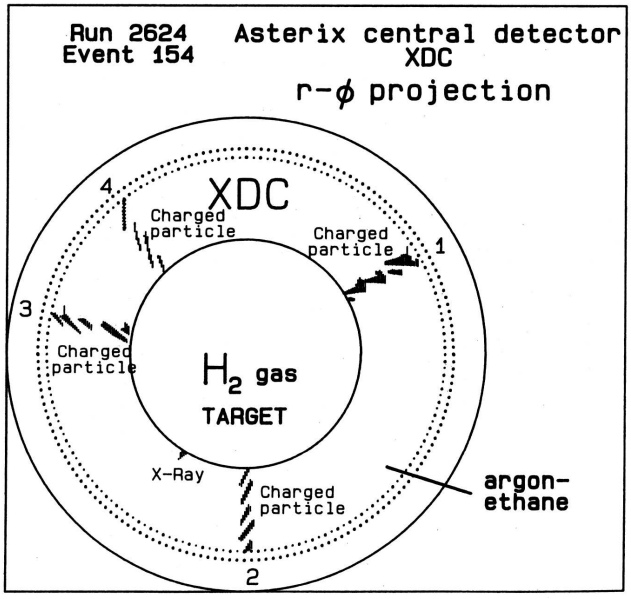

Figure 2.18: Antiproton-proton annihilation into four charged particles preceded by an X-ray transition. Tracks of charged particles deposit energy along their path, X-rays only locally. The short penetration depth and the small energy indicate that a Balmer or Paschen X-ray is observed.

presence of the magnetic field, several cells show ionisation due to the effect of the Lorentz angle. X-rays loose their energy locally very close to the conversion point. A short pulse is detected in one cell while the neighbouring cells are free of charge. The localisation of the energy deposit can be used to define X-rays.

A special hard-wired trigger was designed to select events with isolated charge deposits in the

chamber and thus to enhance the fraction of events on tape with X-rays. A trigger on the absence of charged particles removed the background associated with charged particles.

2.4.3 PS174: The cold-gas experiment

The cold gas experiment used a gas target which provided the possibility to reduce the temperature or the pressure of the gas and to vary its density over a wide range, from 10 times to 1/8 times STP density. The target was filled with H_2, D_2 and He gas; in this report only the results using H_2 or D_2 are discussed.

Figure 2.19 shows the apparatus. Antiprotons entered (from left) through a Be window and a final thin scintillator providing sufficient light so that very slow antiprotons at the end of their range can be detected. The moderator thickness can be tuned by rotating a $50\,\mu\mathrm{m}$ thick mylar foil to optimise the stop distribution for detection of X-rays. The antiproton momenta were reduced in the course of time: 300, 200 and $105\,\mathrm{MeV}/c$ antiprotons were delivered to the experiment.

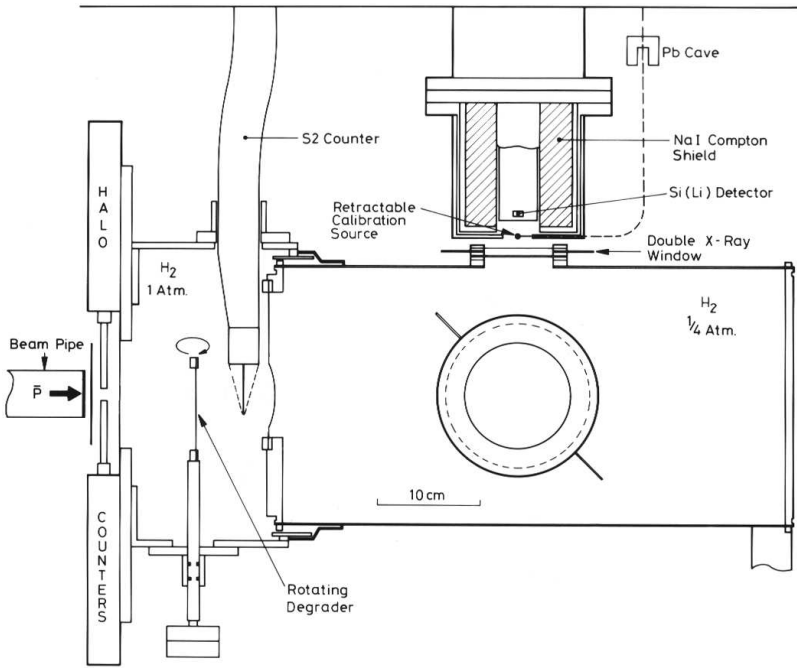

Figure 2.19: Apparatus used in experiment PS174. For part of data, a GSPC (not shown) viewed the target from the side.

Stopped antiprotons form antiprotonic hydrogen (or deuterium) atoms which emit X-rays. The volume in which antiprotons stopped was viewed at by Si(Li) detectors with excellent energy resolution (320 eV FWHM at 6.4 keV) but small solid angle, typically 10^{-3} of 4π. Si(Li)'s consist of solid material; high-energy γ–rays have a large probability to scatter off the detector material via Compton scattering. The kicked electron leaves ionisation in the detector thus producing a continuous background. This background can be reduced (but not eliminated) by surrounding the Si(Li) detector with a NaI(Tl) annulus as Compton shield vetoing scattered high-energy γ-rays.

With Si(Li) detectors, a high resolution can be achieved; their disadvantage is the small solid angle and the low background-rejection power. In a later stage, the PS174 collaboration used also two gas scintillation proportional detectors (GSPD). The main advantage of gas counters lies in their low mass, resulting in a low probability for Compton scattering. Energy deposits from charged particles

can easily be reduced by pulse shape analysis. On the other hand, gas counters have a limited energy resolution due to the smaller number of electron–ion pairs created; about 32 eV are needed for one pair leading to an expected resolution of 15% at 8 keV[3]. These electrons normally drift towards a wire where gas amplification occurs. The statistics of the gas amplification deteriorates the theoretical resolution in normal proportional counters, but this can be avoided: in the GSPD the primary electron cloud is drifted through a gas at a velocity that optical excitation of the gas takes place but no ionisation. The amount of light produced in this process is only limited by the experimental set up; the resolution is essentially given by the primary electron–ion pair statistics. Practically a resolution of 850 eV at 11 keV was reached. A detailed description of the GSPC can be found in [167]. The results on H_2 and D_2 are published in [168–170].

2.4.4 PS175 and PS207: the inverse cyclotron

In the inverse cyclotron experiment, a dense antiproton stop distribution was reached even at very low densities. The apparatus is shown in Fig. 2.20. Antiprotons were decelerated in a dedicated low-energy beam line with optimised emittance. The beam entered the H_2 chamber through a 12.5 μm thick Kapton window separating the beam line from the experiment, and passed through a thin scintillator and a set of mylar foils. The range of incoming particles was wound up in a focusing magnetic field. Two superconducting coils provided a field gradient exerting a force towards the symmetry plane and the actual equilibrium orbit. The antiprotons continued to loose energy in collisions with the H_2 gas, with decreasing cyclotron orbits and betatron oscillation amplitudes, until they came to rest. A large fraction ($\sim 90\%$) of the incoming antiproton flux was stopped in the target gas.

If a target density of, e.g., 30 mbar would have been chosen in the experiments above, beam straggling would have led to a stop distribution along the beam axis of 45cm; the beam would have grown to a transverse width of 65cm. The use of a cyclotron to decelerate antiprotons allowed a concentration of the stop distribution in a volume of about 100 cm^3. Later, in experiment PS207, a special low-energy beam line was built with very good emittance and the stop distribution was contained in a volume of about 1 cm^2 $\times$ 1.5 cm. The development of the inverse cyclotron and the performance which was reached was a major technical breakthrough which also had a considerable impact on the scientific program at PSI [171].

Three detectors were used in PS175 to detect X-rays two Si(Li) detectors and one X-ray drift chamber. The first Si(Li) was mounted in a guard-ring configuration to reduce background from Compton scattering and from annihilation products. Only the center area of the detector was used to collect X-rays while charge deposited in the outer guard ring vetoed the event. The low background allowed clear identification of X-rays from the Balmer series with high resolution (280 eV at 6.4 keV). The second Si(Li) had a larger sensitive area (300 mm^2) and less resolution (560 eV at 6.4 keV). Its main purpose was to search for the K_α transition.

The X-ray drift chamber had 16 anode wires and 16 cathodes strips and covered an active area of 16×16 cm^2. Off-line pulse shape analysis and the request for isolated ionisation clusters reduced the charged-particle background. A resolution of 11% (FWHM) at 9 keV was achieved.

The inverse cyclotron trap was used for a second series of experiments (PS207). Charged-coupled X-ray detectors with CCD pixel sizes of $(22\,\mu\mathrm{m})^2$ were used to detect the Balmer and Lyman series'. CCD's also allow a powerful background rejection, with no compromise in energy resolution (which was 320 eV at 9 keV). They need long readout times; many events had to be accumulated before readout took place. Hence they cannot be used for trigger purposes. In parallel, precision measurements on the energy profile of the Balmer series were carried out by use of two crystal spectrometers with a resolution of about 30 MeV. In the spherically bent quartz or silicon crystal, photons were reflected under the Bragg condition, and detected in CCD pixel detectors. An efficiency for X-ray detection and reconstruction of up to 10^{-6} was reached. The spectrometer is

[3]The creation of a number of ion pairs is not a completely random process since energy must be conserved. Therefore the theoretical resolution is better by a factor F, the Fano factor, than the above naive argument suggests.

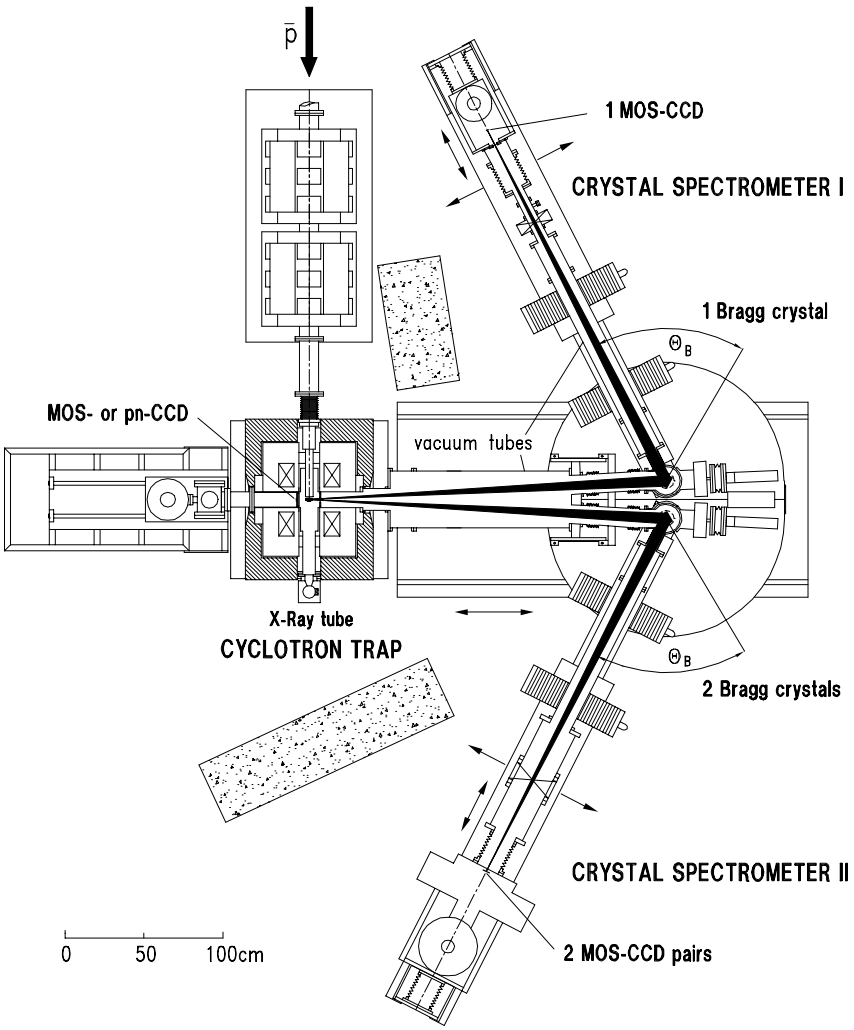

Figure 2.20: The inverse cyclotron in the setup for PS207. Si(Li) or CCD detectors counters view at the target center along the axis of the magnetic field provided by two superconducting coils. Scintillation counters determine the time at which annihilation took place. On the opposite side, a two-arm crystal spectrometer was set up, equipped with three Bragg crystals each reflecting to a separate CCD detector.

fully described in [172]. Results from experiment PS175 on antiprotonic hydrogen and deuterium are published in [173, 174], from experiment PS207 in [175–178].

Chapter 3

Theoretical background

In this chapter, we present the kinematics of nucleon–antinucleon elastic, charge-exchange and strangeness-exchange scattering. We define the various spin observables and list the relations among them. We briefly summarise the state of understanding of nucleon–antinucleon interaction when LEAR came into operation. The G-parity rule is derived, and potential models are briefly introduced. The role of strong interaction in antiprotonic hydrogen and deuterium is described and linked to very-low energy scattering.

3.1 Kinematics

3.1.1 Elastic scattering

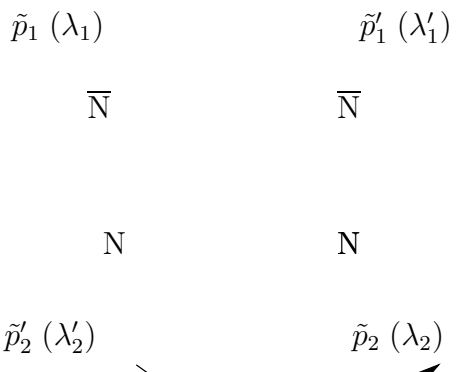

Figure 3.1: Kinematics of $\overline{\mathrm{N}}\mathrm{N}$ scattering, showing momenta and helicities of the incoming and outgoing particles.

The notations for the incoming and outgoing 4-momenta are summarised in Fig. 3.1. From the 4-momenta $\tilde{p}_i$ and $\tilde{n}_i$, one computes the Mandelstam variables

$$s = (\tilde{p}_1 + \tilde{p}_2)^2 \,, \quad t = (\tilde{p}'_1 - \tilde{p}_1)^2 \,, \quad u = (\tilde{p}'_2 - \tilde{p}_1)^2 \,, \tag{3.1}$$

which fulfil the relation $s + t + u = 4m^2$, where m is the nucleon mass.

In the centre-of-mass frame (c.m.), the values are

$$\tilde{p}_i = [E, \vec{p}_i] \,, \qquad \tilde{p}'_i = [E, \vec{p}'_i] \,, \tag{3.2}$$

with $\vec{p}_2 = -\vec{p}_1$, $\vec{p}'_2 = -\vec{p}'_1$, $\vec{p}_1^{\,2} = \vec{p}_2^{\,\prime 2} = p^2$, and

$$s = 4E^2 = 4(p^2 + m^2) \,, \qquad t = -2p^2(1 - \cos\vartheta_{\mathrm{cm}}) \,, \tag{3.3}$$

where $\vartheta_{\rm cm} = (\hat{p}_1, \hat{p}'_1)$ is the scattering angle. In the laboratory frame where the initial proton is at rest,

$$s = 2m^2 + 2mE_{\rm lab} = 2m^2 + 2m\sqrt{m^2 + p_{\rm lab}^2}\,. \tag{3.4}$$

The relation between the c.m. energy $\sqrt{s}$ and the momentum $p_{\rm lab}$ is illustrated in Fig. 3.2. Eq. (3.4)

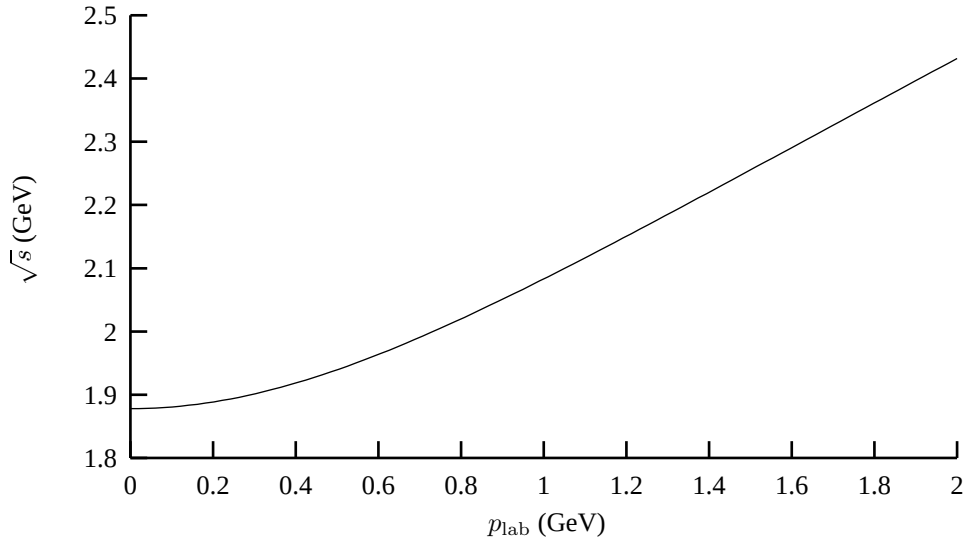

Figure 3.2: Relation between the invariant mass of the initial state and the momentum of the incoming antiproton.

can be inverted into the useful relations

$$E_{\rm lab} = \frac{s - 2m^2}{2m}\,, \qquad p_{\rm lab} = \frac{\sqrt{s(s-4m^2)}}{2m}\,. \tag{3.5}$$

The relation between the angle and momentum of a particle in the final state can be obtained by writing energy-momentum conservation as $\tilde{p}'_2 = \tilde{p}_1 + \tilde{p}_2 - \tilde{p}'_1$ and squaring. One obtains

$$m - \sqrt{m^2 + p_1'^2} + \sqrt{\frac{s-4m^2}{s}}\, p'_1 \cos\vartheta_1 = 0\,. \tag{3.6}$$

Thus, for given s in a given plane, the momentum $\vec{p}'_1 = \{p'_1, \cos\vartheta_1\}$ of the scattered antiproton draws an ellipse passing through the origin, as shown in Fig. 3.3. In particular, *i)* any acute angle $0 < \vartheta_1 < \pi/2$ is possible; *ii)* there is only one value of the momentum p'_1 associated with any given ϑ_1 in this interval. The momentum p'_1 experiences values between 0 and $p_{\rm lab}$. The eccentricity of this ellipse is $2m/\sqrt{s}$.

3.1.2 Charge and strangeness exchange

At very low energy, one should account for the neutron-to-proton mass difference when describing the charge-exchange reactions. The strangeness-exchange reactions involves hyperon masses in the final state. We shall restrict ourselves to equal masses in the final state. The generalisation to, e.g., $\overline{\rm p}{\rm p} \to \overline{\Sigma}^0\Lambda$ is straightforward.

In units where the proton mass is set to $m = 1$, the masses of interest are: $m({\rm n}) = 1.00138$, $m(\Lambda) = 1.189$, $m(\Sigma^+) = 1.268$ and $m(\Sigma^-) = 1.276$ [179].

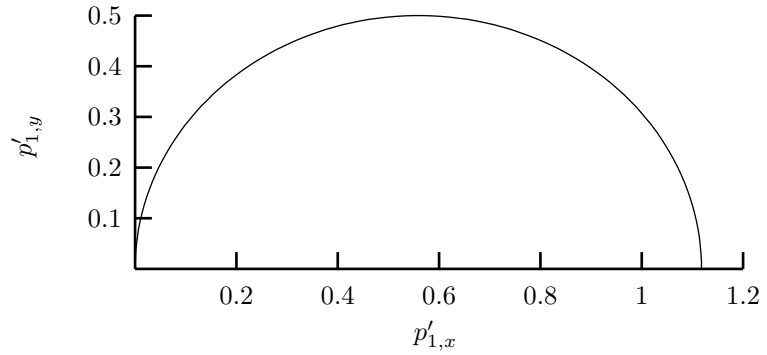

Figure 3.3: Ellipse drawn by the momentum $\vec{p}_1'$ of the scattered antiproton for given s in a given half-plane. The figure corresponds to $s = 5$ in units where $m = 1$.

The threshold for the reaction $m + m \to M + M$ is $s = 4M^2$ if $M > m$. This corresponds to $p_{\rm lab} = 98.7$, 1435.3, 1853.1, and 1898.9 MeV/c, for $\overline{\rm p}{\rm p} \to \overline{\rm n}{\rm n}$, $\overline{\Lambda}\Lambda$, $\overline{\Sigma}^-\Sigma^+$ and $\overline{\Sigma}^+\Sigma^-$, respectively.

In such a reaction $m + m \to M + M$, the momentum p_2 of one of the final state particle runs between the extreme values

$$p = \frac{\sqrt{s}}{4m}\left[\sqrt{s - 4m^2} \pm \sqrt{s - 4M^2}\right] . \tag{3.7}$$

In a given plane, $\vec{p}_2$ draws an ellipse, still with eccentricity $2m/\sqrt{s}$. The origin is outside if $M > m$, as shown in Fig. 3.4. The polar equation of the ellipse is

$$\cos\vartheta_1 = \frac{\sqrt{M^2 + p_1'^2} - m}{p_1'\sqrt{(s - 4m^2)/s}} \cdot \tag{3.8}$$

Thus, as compared to the elastic case, there are two major differences:

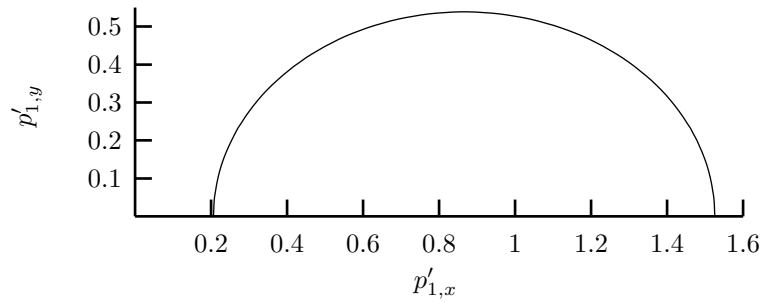

Figure 3.4: Ellipse drawn by the momentum $\vec{p}_1'$ of the outgoing $\overline{\Lambda}$, for given s in a given half-plane. The figure corresponds to $s = 6$ in units where $m = 1$ and $M = 1.1$.

i) the range of scattering angle is restricted to $(0, \vartheta_{\rm M})$, where

$$\cos\vartheta_{\rm M} = \sqrt{\frac{s(M^2-m^2)}{M^2(s-4m^2)}}\,, \qquad \sin\vartheta_{\rm M} = \sqrt{\frac{m^2(s-4M^2)}{M^2(s-4m^2)}}\,. \tag{3.9}$$

The relation between the maximal angle $\vartheta_{\rm M}$ and the incident momentum $p_{\rm lab}$ is illustrated in Fig. 3.5.

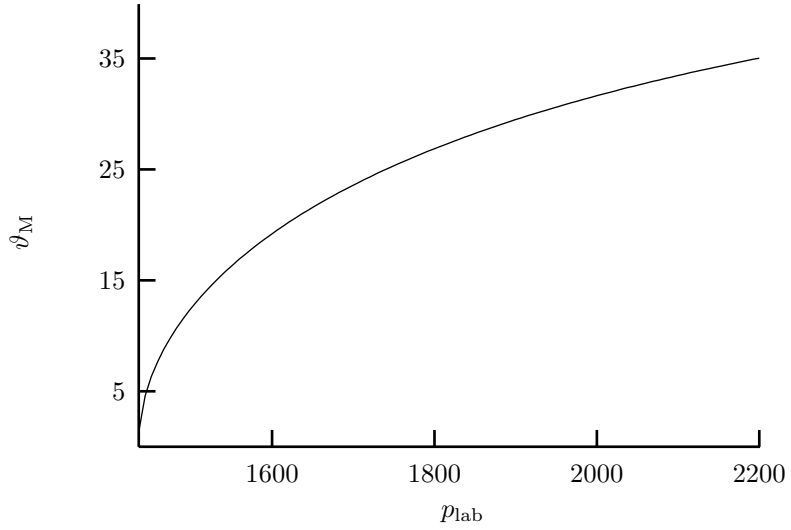

Figure 3.5: Relation between the maximal scattering angle (in degrees) and the incident momentum (in MeV/c) for the reaction $\bar{\rm p}{\rm p} \to \overline{\Lambda}\Lambda$.

ii) for a given angle $0 < \vartheta < \vartheta_{\rm M}$, there are two possible values of the final-state momentum p_2.

3.2 Amplitudes and observables

3.2.1 Isospin formalism

In the limit where the neutron-to-proton mass difference can be neglected, as well as Coulomb corrections, the $\overline{\rm N}{\rm N}$ system obeys isospin symmetry: antiproton–neutron (or c.c.) is pure isospin $I = 1$, while $\bar{\rm p}{\rm p}$ and $\bar{\rm n}{\rm n}$, with $I_3 = 0$, are combinations of $I = 1$ and $I = 0$, namely

$$|\,\bar{\rm p}{\rm p}\rangle = \frac{|\,I=1\rangle + |\,I=0\rangle}{\sqrt{2}}\,, \qquad |\,\bar{\rm n}{\rm n}\rangle = \frac{|\,I=1\rangle - |\,I=0\rangle}{\sqrt{2}}\,, \tag{3.10}$$

so that the elastic and charge-exchange amplitudes are given by

$$\mathcal{T}(\bar{\rm p}{\rm p} \to \bar{\rm p}{\rm p}) = \frac{1}{2}\left(\mathcal{T}^1_{\overline{\rm N}{\rm N}} + \mathcal{T}^0_{\overline{\rm N}{\rm N}}\right)\,, \quad \mathcal{T}(\bar{\rm p}{\rm p} \to \bar{\rm n}{\rm n}) = \frac{1}{2}\left(\mathcal{T}^1_{\overline{\rm N}{\rm N}} - \mathcal{T}^0_{\overline{\rm N}{\rm N}}\right)\,. \tag{3.11}$$

Otherwise, the $\bar{\rm p}{\rm n} \to \bar{\rm p}{\rm n}$, $\bar{\rm p}{\rm p} \to \bar{\rm p}{\rm p}$ and $\bar{\rm p}{\rm p} \to \bar{\rm n}{\rm n}$ scattering processes should be treated in a formalism where proton and neutron are different particles.

Note that the relative sign in the above equations is a matter of convention. The choice adopted here differs from the current way of writing a SU(n) singlet as $|\,0\rangle \propto {\rm u}\bar{\rm u} + {\rm d}\bar{\rm d} + {\rm s}\bar{\rm s} + \cdots$. For a comprehensive discussion of isospin wave-functions for antiparticles, see, e.g., Ref. [180].

3.2.2 Spin amplitudes, elastic case

The description of the reaction $\overline{\mathrm{N}}\mathrm{N} \to \overline{\mathrm{Y}}\mathrm{Y}'$, where Y and Y′ are spin-1/2 baryons, involves 16 helicity amplitudes. Those are $\mathcal{T}_{\pm\pm\pm\pm} = \mathcal{T}(\lambda_1, \lambda_2; \lambda'_1, \lambda'_2)$, if one uses the notations of Fig. 3.1.

In the elastic case $\bar{\mathrm{p}}\mathrm{p} \to \bar{\mathrm{p}}\mathrm{p}$, symmetry considerations reduce this number to 5 amplitudes, as for the well-studied cross-channel reaction $\mathrm{pp} \to \mathrm{pp}$. They can be chosen as

$$\begin{aligned}
\mathcal{T}_1 &= \mathcal{T}_{++++} \,, \\
\mathcal{T}_2 &= \mathcal{T}_{++--} \,, \\
\mathcal{T}_3 &= \mathcal{T}_{+-+-} \,, \\
\mathcal{T}_4 &= \mathcal{T}_{+--+} \,, \\
\mathcal{T}_5 &= \mathcal{T}_{+---} \,.
\end{aligned} \tag{3.12}$$

There are many other sets of amplitudes, which are linear combinations of these $\mathcal{T}_i$. One of them is proposed by Lehar et al. [181]

$$\begin{aligned}
a &= (\ \ \mathcal{T}_1 + \mathcal{T}_2 + \mathcal{T}_3 - \mathcal{T}_4)\,(\ \cos\vartheta_{\mathrm{cm}})/2 - 2\mathcal{T}_5 \sin\vartheta_{\mathrm{cm}} \,, \\
b &= (\ \ \mathcal{T}_1 - \mathcal{T}_2 + \mathcal{T}_3 + \mathcal{T}_4)\,/2 \,, \\
c &= (-\mathcal{T}_1 + \mathcal{T}_2 + \mathcal{T}_3 + \mathcal{T}_4)\,/2 \,, \\
d &= (\ \ \mathcal{T}_1 + \mathcal{T}_2 - \mathcal{T}_3 + \mathcal{T}_4)\,/2 \,, \\
e &= (-\mathcal{T}_1 - \mathcal{T}_2 - \mathcal{T}_3 + \mathcal{T}_4)\,(i\sin\vartheta_{\mathrm{cm}})/2 + 2\mathcal{T}_5 \cos\vartheta_{\mathrm{cm}} \,.
\end{aligned} \tag{3.13}$$

In the forward direction, one should satisfy $\mathcal{T}_4 = \mathcal{T}_5 = 0$, i.e.,

$$e(0) = 0 \,, \qquad a(0) - b(0) = c(0) + d(0) \,. \tag{3.14}$$

The amplitudes a, b, … can be defined directly as [181]

$$\mathcal{T} = (a+b)I + (a-b)\vec{\sigma}_1.\hat{n}\,\vec{\sigma}_2.\hat{n} + (c+d)\vec{\sigma}_1.\hat{k}\,\vec{\sigma}_2.\hat{k} + (c-d)\vec{\sigma}_1.\hat{p}\,\vec{\sigma}_2.\hat{p} + e(\vec{\sigma}_1 + \vec{\sigma}_2).\hat{n} \,, \tag{3.15}$$

where the unit vectors are defined as

$$\hat{p} = \frac{\vec{p}_1 + \vec{p}\,'_1}{|\vec{p}_1 + \vec{p}\,'_1|} \,, \qquad \hat{k} = \frac{\vec{p}\,'_1 - \vec{p}_1}{|\vec{p}\,'_1 - \vec{p}_1|} \,, \qquad \hat{n} = \frac{\vec{p}_1 \times \vec{p}\,'_1}{|\vec{p}_1 \times \vec{p}\,'_1|} \,. \tag{3.16}$$

In the limit of exact isospin symmetry, parity, time-reversal and G-parity relations hold for each isospin channel, and thus a set of five amplitudes $\mathcal{T}_i$ or $\{a,\, b, \ldots\}$ can be introduced for each isospin state, $I = 0$ and $I = 1$.

The symmetry-violating amplitudes are discussed, e.g., in Ref. [182].

3.2.3 Observables, elastic case

The general formalism is described, e.g., in Ref. [181], where all possible beam and target polarisations are considered, as well as all possible spin measurements in the final state.

For $\bar{\mathrm{p}}\mathrm{p}$ scattering, the total integrated cross-section includes an elastic and a charge-exchange parts. At low energy, the remainder is the annihilation cross-section, i.e.,

$$\sigma_{\mathrm{tot}} = \sigma_{\mathrm{el}} + \sigma_{\mathrm{ce}} + \sigma_{\mathrm{ann}} \,. \tag{3.17}$$

For $\bar{\mathrm{p}}\mathrm{n}$ or $\bar{\mathrm{n}}\mathrm{p}$ scattering, we simply have

$$\sigma_{\mathrm{tot}} = \sigma_{\mathrm{el}} + \sigma_{\mathrm{ann}} \,. \tag{3.18}$$

The total cross-section $\sigma_{\rm tot}$ is related to the forward amplitude ($\vartheta_{\rm cm} = 0$) by the optical theorem. It reads [181], in terms of the polarisation $\vec{P}_{\rm t}$ of the target and $\vec{P}_{\rm b}$ of the beam,

$$\begin{aligned}
\sigma_{\rm tot} &= \sigma_{0,\rm tot} + \sigma_{1,\rm tot}\, \vec{P}_{\rm t}.\vec{P}_{\rm b} + \sigma_{2,\rm tot}\, \vec{P}_{\rm t}.\hat{p}\, \vec{P}_{\rm b}.\hat{p}\ , \\
\sigma_{0,\rm tot} &= \frac{2\pi}{p}\, \mathcal{I}{\rm m}[a(0) + b(0)]\ , \\
\sigma_{1,\rm tot} &= \frac{2\pi}{p}\, \mathcal{I}{\rm m}[c(0) + d(0)]\ , \\
\sigma_{2,\rm tot} &= -\frac{4\pi}{p}\, \mathcal{I}{\rm m}[d(0)]\ ,
\end{aligned} \tag{3.19}$$

The observables measured in elastic and charge-exchange antiproton–proton scattering are restricted to the differential cross-section $I_0 = {\rm d}\sigma/{\rm d}\Omega$, the analysing power A_{000n}, sometimes abbreviated as A_{0n} or A_n, the depolarisation $D_{0n0n} = D_{nn}$, and some indirect information on the transfer of polarisation $K_{n00n} = K_{nn}$ for charge-exchange. These observables are given by

$$\begin{aligned}
I_0 &= |a|^2 + |b|^2 + |c|^2 + |d|^2 + |e|^2\ , \\
I_0 A_n &= 2\,{\rm Re}(a^* e)\ , \\
I_0 D_{nn} &= |a|^2 + |b|^2 - |c|^2 - |d|^2 + |e|^2\ , \\
I_0 K_{nn} &= |a|^2 - |b|^2 + |c|^2 - |d|^2 + |e|^2\ .
\end{aligned} \tag{3.20}$$

More observables can be deduced from the formulas displayed in (3.28) for $\bar{\rm p}{\rm p} \to \overline{\Lambda}\Lambda$, using the prescription given below in Eq. (3.26).

The analysing power A_n measures the azimuthal dependence of the angular distribution

$$d(\vartheta_{\rm cm}, \varphi_{\rm cm}) \propto I_0(1 + A_n P_{2,n} \cos\varphi_{\rm cm})\ . \tag{3.21}$$

D_{nn} reflects how much of the initial polarisation of the proton target normal to the scattering plane remains in the recoil nucleon, and K_{nn}, how much is transferred to the scattered antinucleon, namely

$$P'_{2,n} = A_n + D_{nn} P_{2,n}\ , \qquad P'_{1,n} = A_n + K_{nn} P_{2,n}\ , \tag{3.22}$$

if $\vec{P}_i$ denotes the polarisation the $i^{\rm th}$ particle (with the usual convention 1 = beam, 2 = target, $1'$ = scattered, $2'$ = recoil).

3.2.4 Spin amplitudes for charge exchange

At high energy, the neutron-to-proton mass difference can be neglected, and the spin observables are given by the same expressions as for the elastic case. The only difference lies in the isospin combinations (3.11) used for the amplitudes.

If one analyses experiments close to the threshold, or if one suspects for any other reason that isospin symmetry might be violated, then one should introduce a sixth amplitude and use the formalism given in the next subsection.

3.2.5 Spin amplitudes for strangeness exchange

The case of unequal masses in the final state, as for $\bar{\rm p}{\rm p} \to \overline{\Sigma}^0\Lambda$ + c.c. is rather straightforward. The data for this channel are, however, too meager to deserve a detailed formalism. We shall thus restrict ourselves here to reactions of the type $m + m \to M + M$. As compared to the elastic case, time-reversal invariance is lost, and six amplitudes are needed, instead of five.

A recent discussion of the $\bar{\rm p}{\rm p} \to \overline{\Lambda}\Lambda$ spin formalism has been done in Refs. [183, 184], where references to earlier works can be found.

At each energy and angle, the transition matrix can be decomposed into [181, 185]

$$\begin{aligned}\mathcal{T} =&(a'+b')I + (a'-b')\vec{\sigma}_1.\hat{n}\,\vec{\sigma}_2.\hat{n} + (c'+d')\vec{\sigma}_1.\hat{k}'\,\vec{\sigma}_2.\hat{k}' \\ &+ (c'-d')\vec{\sigma}_1.\hat{p}'\,\vec{\sigma}_2.\hat{p}' + e'(\vec{\sigma}_1+\vec{\sigma}_2).\hat{n} + g'(\vec{\sigma}_1.\hat{k}'\,\vec{\sigma}_2.\hat{p}' + \vec{\sigma}_1.\hat{p}'\,\vec{\sigma}_2.\hat{k}')\ ,\end{aligned} \tag{3.23}$$

where the kinematical unit-vectors are defined from the momentum $\vec{p}_1$ of $\bar{\mathrm{p}}$ and $\vec{p}_1'$ of $\overline{\Lambda}$

$$\hat{p}' = \frac{\vec{p}_1}{|\vec{p}_1|}\ , \qquad \hat{n} = \frac{\vec{p}_1\times\vec{p}_1'}{|\vec{p}_1\times\vec{p}_1'|}\ , \qquad \hat{k}' = \hat{n}\times\hat{p}'\ , \tag{3.24}$$

and are adapted to describe the final-state spins. Since

$$\hat{p} = \hat{p}'\cos(\vartheta_{\rm cm}/2) - \hat{k}'\sin(\vartheta_{\rm cm}/2)\ , \qquad \hat{k} = \hat{p}'\sin(\vartheta_{\rm cm}/2) + \hat{k}'\cos(\vartheta_{\rm cm}/2)\ , \tag{3.25}$$

the elastic amplitudes (3.15) correspond to the special case $a'=a$, $b'=b$, $c'=c$, $e'=e$, and

$$d' = d\cos\vartheta_{\rm cm}\ , \qquad g' = d\sin\vartheta_{\rm cm}\ . \tag{3.26}$$

3.2.6 Spin observables for strangeness production

The rank-1 and rank-2 observables are defined (to an overall factor) as

$$\begin{aligned} I_0 &= \mathrm{Tr}[\mathcal{T}\mathcal{T}^\dagger]\ , \\ P_nI_0 &= \mathrm{Tr}[\vec{\sigma}_1.\hat{n}\mathcal{T}\mathcal{T}^\dagger]\ , \\ A_nI_0 &= \mathrm{Tr}[\mathcal{T}\vec{\sigma}_2.\hat{n}\mathcal{T}^\dagger]\ , \\ C_{ij}I_0 &= \mathrm{Tr}[\vec{\sigma}_1.\hat{\imath}\,\vec{\sigma}_2.\hat{\jmath}\mathcal{T}\mathcal{T}^\dagger]\ , \\ D_{ij}I_0 &= \mathrm{Tr}[\vec{\sigma}_2.\hat{\imath}\mathcal{T}\vec{\sigma}_2.\hat{\jmath}\mathcal{T}^\dagger]\ , \\ K_{ij}I_0 &= \mathrm{Tr}[\vec{\sigma}_1.\hat{\imath}\mathcal{T}\vec{\sigma}_2.\hat{\jmath}\mathcal{T}^\dagger]\ , \end{aligned} \tag{3.27}$$

corresponding to differential cross-section, polarisation, analysing power, spin correlation in the final state, baryon depolarisation and baryon-to-antibaryon polarisation transfer, respectively.

More explicitly, in terms of the amplitudes

$$\begin{aligned} I_0 &= |a'|^2 + |b'|^2 + |c'|^2 + |d'|^2 + |e'|^2 + |g'|^2\ , \\ P_nI_0 &= 2\,\mathrm{Re}(a'e'^*) + 2\,\mathrm{Im}(d'g'^*)\ , \\ A_nI_0 &= 2\,\mathrm{Re}(a'e'^*) - 2\,\mathrm{Im}(d'g'^*), \\ C_{nn}I_0 &= |a'|^2 - |b'|^2 - |c'|^2 + |d'|^2 + |e'|^2 + |g'|^2\ , \\ C_{xx}I_0 &= -2\,\mathrm{Re}(a'd'^* + b'c'^*) - 2\,\mathrm{Im}(g'e'^*)\ , \\ C_{zz}I_0 &= 2\,\mathrm{Re}(a'd'^* - b'c'^*) + 2\,\mathrm{Im}(g'e'^*)\ , \\ C_{xz}I_0 &= -2\,\mathrm{Re}(a'g'^*) - 2\,\mathrm{Im}(e'd'^*)\ , \\ D_{nn}I_0 &= |a'|^2 + |b'|^2 - |c'|^2 - |d'|^2 + |e'|^2 - |g'|^2\ , \\ D_{xx}I_0 &= 2\,\mathrm{Re}(a'b'^* + c'd'^*)\ , \\ D_{zz}I_0 &= 2\,\mathrm{Re}(a'b'^* - c'd'^*)\ , \\ D_{xz}I_0 &= 2\,\mathrm{Re}(c'g'^*) + 2\,\mathrm{Im}(b'e'^*)\ , \\ K_{nn}I_0 &= |a'|^2 - |b'|^2 + |'c|^2 - |d'|^2 + |e'|^2 - |g'|^2\ , \\ K_{xx}I_0 &= -2\,\mathrm{Re}(a'c'^* + b'd'^*)\ , \\ K_{zz}I_0 &= -2\,\mathrm{Re}(a'c'^* - b'd'^*)\ , \\ K_{xz}I_0 &= -2\,\mathrm{Re}(b'g'^*) + 2\,\mathrm{Im}(e'c'^*)\ . \end{aligned} \tag{3.28}$$

To project out the spins of the particles, we follow here the usual convention that for $\overline{\Lambda}$, the axes $\{\hat{x}, \hat{n}, \hat{z}\}$ coincide with $\{\hat{k}, \hat{n}, \hat{p}\}$, while for p or Λ, the axes $\{\hat{x}, \hat{n}, \hat{z}\}$ coincide with $\{-\hat{k}, \hat{n}, -\hat{p}\}$.

In principle (i.e., with enough statistics), a polarised target gives access to some rank-3 observables, of the type:

$$C_{0\alpha ij} I_0 = \mathrm{Tr}[\vec{\sigma}_1.\hat{\imath}\,\vec{\sigma}_2.\hat{\jmath}\,\mathcal{T}\,\vec{\sigma}_2.\hat{\alpha}\,\mathcal{T}^\dagger] \,. \tag{3.29}$$

For instance,

$$\begin{aligned} C_{0nzz} I_0 &= \quad 2\,\mathrm{Re}(d' e'^*) - 2\,\mathrm{Im}(a' g'^*) \,, \\ C_{0nxx} I_0 &= -2\,\mathrm{Re}(d' e'^*) + 2\,\mathrm{Im}(a' g'^*) \,, \\ C_{0nzx} I_0 &= -2\,\mathrm{Re}(g' e'^*) - 2\,\mathrm{Im}(a' c'^* + b' d'^*) \,, \end{aligned} \tag{3.30}$$

C_{0nnn} being equal to A_n.

3.2.7 Constraints on observables

Each spin observable X or Y is typically normalised to $-1 \leq X \leq +1$. However, the allowed domain for a pair (X, Y) of observables is usually smaller than the unit square ($|X| \leq 1,\ |Y| \leq 1$). Inequalities can be derived, which restrict the domain. They are, of course, automatically fulfilled in any theoretical model, where the amplitudes a', b', ... are first calculated and then used to compute the observables. However, these inequalities represent non-trivial constraints when the observables are extracted from data. Similar relations have been written for other reactions, for instance photoproduction of vector mesons off nucleons [186].

We just list a few examples below. For a more comprehensive list, and a possible derivation, see Ref. [183].

i) Linear relations:

$$\begin{aligned} 2|A_n| - C_{nn} &\leq 1 \,, \\ I_0(1 - C_{nn} + C_{xx} + C_{zz}) &\geq 0 \,. \end{aligned} \tag{3.31}$$

Note that the second relation is nothing but the spin-singlet fraction,

$$F_0 = \frac{1}{4}(1 + C_{xx} - C_{yy} + C_{zz}) = \frac{1}{2I_0}|b' - c'|^2 \,, \tag{3.32}$$

being positive. The normalisation is such that $F_0 = 1/4$ in absence of any spin-dependent interaction.

ii) Quadratic relations:

$$\begin{aligned} C_{zz}^2 + D_{nn}^2 &\leq 1 \,, \\ \left(\frac{D_{nn} - K_{nn}}{2}\right)^2 + (2F_0 - 1)^2 &\leq 1 \,, \end{aligned} \tag{3.33}$$

the latter relating $D_{nn}, K_{nn}, C_{nn}, C_{xx}$ and C_{zz}. As a consequence, $D_{nn} = K_{nn}$ in both limits of a pure spin-singlet ($F_0 = 1$) or pure spin-triplet ($F_0 = 0$) reaction.

3.3 Possibility of reconstructing the amplitudes from the data

3.3.1 General considerations

Extracting the amplitudes from data is a rather delicate subject. Consider first the case of spinless particles. Measuring the differential cross-section at a given energy provides $|f|^2$, where f is the scattering amplitude. There are difficulties to access to the phase from the angular distribution [187], even if one uses elastic unitarity globally or under the form of a partial wave expansion,

$$f = \sum_\ell (2\ell + 1) \frac{\exp(2i\delta_\ell) - 1}{2ik} P_\ell(\cos\vartheta) \,, \tag{3.34}$$

where δ_ℓ is real and the expansion finite. The absolute phase of f can sometimes be derived, for instance from its interference in the extreme-forward region with the Coulomb amplitude.

More severe difficulties occur in case of inelasticity (δ_ℓ parameters, now complex) or particles with spin (several amplitudes involved). Low-energy $\overline{\rm N}$N scattering cumulates both handicaps.

The case of two amplitudes is very much documented, as it corresponds to πN scattering or its crossed reaction $\overline{\rm N}$N $\to \pi\pi$. The angular distribution gives $I_0 = |f|^2 + |g|^2$ and the polarisation (or analysing power) $P_n = 2\,\mathcal{R}{\rm e}(fg^*)/I_0$. If the latter is extreme ($P_n = \pm 1$) , $f = \pm g$ is implied. In general, the value of this parameter is not maximal, and several choices might be considered. For instance, $P_n = 0$ can be achieved with $f = 0$, or $g = 0$, or more generally with $f \propto ig$. In short, reconstructing the amplitudes from the data becomes easier in situations where some spin parameters are extreme.

Still a few common-sense considerations hold. One cannot determine unambiguously five or ten complex amplitudes from the measurement of just two or three observables. It took a long time to achieve the "tour de force" of reconstructing the five amplitudes in the NN case. See, e.g., Ref. [188]. Several subtle measurements were required, with beam and target both polarised.

Now, the $\overline{\rm N}$N case looks by far more difficult than the NN one. First, there is no Pauli principle to remove every second partial wave. Second, the phase-shifts are complex already at threshold (or, equivalently, the partial-wave S-matrix contains both a real phase and an inelasticity parameter). Moreover, there are much fewer data than in the NN case. So there is no hope to achieve an unambiguous amplitude or even phase-shift analysis.

Still, integrated cross-sections are now available in a wide range of energy. For the elastic $\bar{\rm p}{\rm p} \to \bar{\rm p}{\rm p}$ and the charge-exchange reaction $\bar{\rm p}{\rm p} \to \bar{\rm n}{\rm n}$, we also have detailed angular distributions and polarisations, as well as some indication on the depolarisation parameter. For $\bar{\rm n}{\rm p}$ or $\bar{\rm p}{\rm n}$ scattering, we are restricted to the integrated cross-sections. Several observables have been measured for hyperon pair production.

It remains that one can always fit the data within some models which summarise the best of our knowledge on the physics of the $\overline{\rm N}$N interaction and contain several free parameters. In these circumstances, the resulting amplitudes and the corresponding complex phase-shifts are compatible with the data. Such analyses are thus often quoted for comparison with the data, and they provide a possible extrapolation for observables which have not yet been measured. Of course, it is more delicate to appreciate to which extent a set of amplitudes obtained by tuning a specific model can be considered as unique.

3.3.2 Elastic or charge-exchange case

Let us examine more precisely here what can be learned from the data on elastic $\bar{\rm p}{\rm p}$ or charge-exchange. As it will be seen in the next chapter, the only observables which have been measured consist of the differential cross-section $I_0 = {\rm d}\sigma/{\rm d}\Omega$, the analysing power A_n (sometimes called polarisation) and the depolarisation D_{nn}. Though a lot of physics can be extracted (pion coupling, early onset of P-waves, etc.), we are far from envisaging a full reconstruction of the five amplitudes.

For the ease of discussion, let us replace Lehar's amplitudes (3.15) a and e by their normalised sum and difference, namely

$$\{a, e\} \to \{\tilde{a} = (a+e)/\sqrt{2},\ \tilde{e} = (a-e)\sqrt{2}\}, \tag{3.35}$$

and omit the tilde mark in this subsection. These new a and e correspond to transversity amplitudes [181]. The available observables read

$$\begin{aligned} I_0 &= |a|^2 + |b|^2 + |c|^2 + |d|^2 + |e|^2\ , \\ I_0 A_n &= |a|^2 - |e|^2\ , \\ I_0 D_{nn} &= |a|^2 + |b|^2 - |c|^2 - |d|^2 + |e|^2\ , \end{aligned} \tag{3.36}$$

this defining a possible normalisation. In the optimal cases, i.e., at energies and angles where these three observables are measured, one can at best extract from the data the quantities

$$|a|^2 + |b|^2/2 \,, \qquad |e|^2 + |b|^2/2 \,, \qquad |c|^2 + |d|^2 \,, \tag{3.37}$$

or linear combinations. Improving the accuracy on A_n or D_{nn} will not enable one to disentangle $|c|^2$ from $|d|^2$, for instance, unless it is found that $|c|^2 + |d|^2 = 0$, which would imply $c = d = 0$.

3.3.3 Hyperon-pair production

We restrict ourselves here to the $\overline{\Lambda}\Lambda$ case, as channels involving a Σ or a $\overline{\Sigma}$ do not benefit of the same amount of data on spin observables. Would the question of statistics be disregarded, the situation would be different from the $\overline{\mathrm{N}}\mathrm{N}$ case, with the risk of having too many observables, and thus the problem of compatibility among those observables.

As pointed out in Ref. [184], experiments carried out with a transversally polarised target lead to many rank-2 observables (correlations in the final state, transfer from p to Λ or to $\overline{\Lambda}$), and even some rank-3 observables. There are enough relations to fix a', b', c', d', e' and g', to an overall phase.

3.4 General properties of the $\overline{\mathrm{N}}\mathrm{N}$ interaction

The best known particle–antiparticle system consists of an electron e^- and a positron e^+, which is described by comparison with the two-electron system. In this latter case, the interaction is known to be mediated by the exchange of a photon, as pictured in Fig. 3.6. This diagram is then iterated

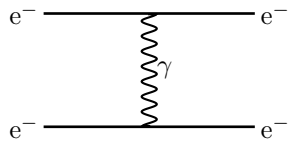

Figure 3.6: One-photon exchange, the driving mechanism for $\mathrm{e}^-\mathrm{e}^-$ interaction.

in the Schrödinger equation or in some more elaborate relativistic equation, and supplemented by small higher-order corrections.

The C-conjugation rule states that, since the exchanged photon has $C = -1$, the corresponding diagram for $\mathrm{e}^+\mathrm{e}^-$ changes sign. In other words, the repulsive $1/r$ potential becomes an attractive $V \propto -1/r$ for the electron–positron case. This is, however, not the only change. At the same lowest order, there is the annihilation diagram of Fig. 3.7, centre. The two particles merge into a virtual photon which then decays back to $\mathrm{e}^+\mathrm{e}^-$. This is a contact interaction. Another annihilation diagram is shown in Fig. 3.7, right. It corresponds to the feed-back into the $\mathrm{e}^+\mathrm{e}^-$ amplitude of the annihilation processes $\mathrm{e}^+\mathrm{e}^- \to n\gamma$, pictured here for $n = 2$. This annihilation part is however, a small correction, due to its short range $(2m_\mathrm{e})^{-1}$, where m_e is the mass of the electron. For instance, the positronium atom has well-defined levels. The S-wave levels eventually decay into photons, but with a lifetime which is much larger than the classical period of rotation. States with angular momentum $\ell \geq 1$ are practically stable with respect to annihilation. They decay by ordinary radiative transitions to lower states.

At first sight, this dynamics is easily translated for the $\overline{\mathrm{N}}\mathrm{N}$ system, with electrons, positrons and photons being replaced by nucleons, antinucleons and pions, respectively. More attraction is expected in $\overline{\mathrm{N}}\mathrm{N}$ than in $\mathrm{N}\mathrm{N}$ leading to speculations on "Baryonium" states, the analogues of positronium atoms.

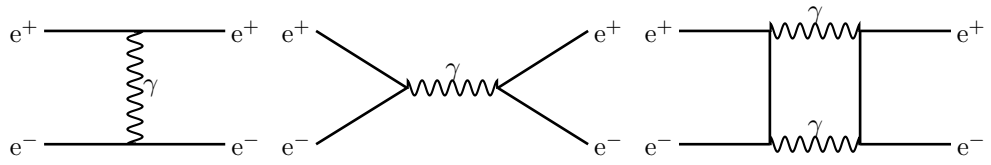

Figure 3.7: Basic mechanisms for $\mathrm{e^+e^-}$ interaction: Elastic photon-exchange (left), virtual annihilation into one-photon (centre), annihilation into two-photons (right). (What is pictured is not annihilation itself, but its feed-back on the $\mathrm{e^+e^-}$ amplitude.)

This is, however, far from being that simple. A minor complication comes from isospin or, say, the existence of two nucleons. As will be seen in Sec. 3.5, the C-conjugation rule has to be rewritten with the G-parity operator. More serious is the strength of the coupling constant, and the variety of mesons. The NN interaction cannot be reduced to one-pion-exchange: multiple exchanges, as well as the exchange of heavier meson resonances should be introduced. Moreover, we do not know precisely the nature of the short-range NN forces. This difficulty is of course, translated into a similar uncertainty for the elastic part of the $\overline{\mathrm{N}}\mathrm{N}$ interaction. But the worse is still to come: annihilation cannot be handled as a short-range correction: its is a violent process, which takes place up to about $1\,\mathrm{fm}$ and presumably washes out the bound-state spectrum generated by the attractive real potential.

A possible way out is that the correspondence between electromagnetic- and strong-interaction physics should be stated at the quark level rather than at the nucleon level. Then electrons and photons of QED are replaced by quarks and gluons, respectively. This is certainly the right approach at high energy and high momentum-transfer. For our low-energy physics, one cannot elude the problem of confinement, and the many-body aspects: $\overline{\mathrm{N}}\mathrm{N}$ annihilation is not an elementary process, it is the analogue of a molecular-collision process in QED, with several possible final states.

We shall discuss below these aspects of the $\overline{\mathrm{N}}\mathrm{N}$ interaction and look what understanding was reached when LEAR came into operation.

3.5 The G-parity rule for amplitudes

It is well-known in quantum field theory that the same S-matrix describes the reaction $a+b \to c+d$ and its crossed reactions such as $a + \bar{c} \to \bar{b} + d$. However, the empirical knowledge of the direct reaction, in a kinematical domain $\{s > 4m^2,\, t < 0\}$ (for equal masses), does not give easy access to the domain $\{s < 0,\, t > 4m^2\}$, as no analytic continuation can be used reliably for such a huge jump.

Another point of view is adopted in the so-called "G-parity rule": one compare the $a+b \to c+d$ and $\bar{a} + b \to \bar{c} + d$ reactions in the *same* kinematical domain.

The G-parity $G = C\exp(-i\pi I_2)$ associates the C-conjugation with a rotation in isospin space, such that [180] $G|\,\mathrm{p}\rangle = |\,\overline{\mathrm{n}}\rangle$ and $G|\,\mathrm{n}\rangle = |\,\overline{\mathrm{p}}\rangle$, linking states with same isospin quantum numbers. Non-strange meson systems are eigenstates with $G = +1$ or $G = -1$. In particular, for a system of n pions, $G = (-1)^n$.

The mesons which contribute to the NN forces can also be exchanged between a nucleon and an antinucleon to build the long-range part of the $\overline{\mathrm{N}}\mathrm{N}$ interaction. The precise relation between the NN and $\overline{\mathrm{N}}\mathrm{N}$ amplitudes is the G-parity rule: in a given isospin state, $I = 0$ or $I = 1$, the contribution of the exchange of a meson or set of mesons μ to the $\overline{\mathrm{N}}\mathrm{N}$ amplitude differs from its NN analogue by a factor $G_\mu = \pm 1$, which is the G-parity of the meson system μ.

$$\mathcal{T}^I_{\mathrm{NN}} = \sum_\mu \mathcal{T}_\mu \quad \Longrightarrow \quad \mathcal{T}^I_{\overline{\mathrm{N}}\mathrm{N}} = \sum_\mu G_\mu \mathcal{T}_\mu \,. \tag{3.38}$$

Remarks are in order:

i) This rule links isospin eigenstates. It generalises the familiar "C-conjugation rule", which states that $\mathcal{T}(\mathrm{e^+e^-}) = -\mathcal{T}(\mathrm{e^+e^+})$ for the leading diagram, since the photon which is exchanged has $C = -1$. The C-conjugation rule links pp to $\bar{\mathrm{p}}\mathrm{p}$, np to $\bar{\mathrm{p}}\mathrm{n}$. The G-parity rule is nothing but an astute combination of the C-conjugation rule with isospin invariance.

ii) The G-parity rule is by no means restricted to the one-boson-exchange approximation, where only single, narrow mesons are involved. It works for instance for 2-pion exchange ladder or crossed diagrams, with or without excitation of nucleon resonances in the intermediate states.

The derivation of the G-parity rule can be elaborated as follows. Both amplitudes, $\mathcal{T}_1$ for NN and $\mathcal{T}_2$ for $\overline{\mathrm{N}}\mathrm{N}$ are formally written in terms of their t-channel content

$$\begin{aligned} \mathcal{T}_1 &= \langle \overline{\mathrm{N}}(-p_1)\mathrm{N}(p_2) \mid \mathcal{T} \mid \mathrm{N}(n_1)\overline{\mathrm{N}}(-n_2)\rangle \,, \\ \mathcal{T}_2 &= \langle \mathrm{N}(-p_1)\overline{\mathrm{N}}(p_2) \mid \mathcal{T} \mid \mathrm{N}(n_1)\overline{\mathrm{N}}(-n_2)\rangle \,. \end{aligned} \tag{3.39}$$

The kinematics is defined in Fig. 3.1. Since strong interactions are invariant under G-parity, $\mathcal{T} = G\mathcal{T}G$, each amplitude can be split into two parts, with $G = +1$ or $G = -1$ in the t-channel, without interference between them

$$\mathcal{T}_i = \mathcal{T}_i{}^+ + \mathcal{T}_i{}- \,. \tag{3.40}$$

In particular

$$\mathcal{T}_1^{\pm} = \langle \overline{\mathrm{N}}(-p_1)\mathrm{N}(p_2) \mid G\mathcal{T}G \mid \mathrm{N}(n_1)\overline{\mathrm{N}}(-n_2)\rangle \,. \tag{3.41}$$

The first G, acting on the left, transforms the bra into the desired $\langle \mathrm{N}(-p_1)\overline{\mathrm{N}}(p_2) \mid$, while the second G can be replaced by its eigenvalue $\pm$, with the desired result $\mathcal{T}_1^{\pm} = \pm\mathcal{T}_2^{\pm}$.

The G-parity rule is rather general, and reflects basic symmetries of strong interactions. This is why the rule is first formulated in terms of scattering amplitudes. In the particular case where the amplitude is generated from a potential, the rule implies that the potential mediated by a meson (or set of mesons) of G-parity $G_\mu = \pm 1$ is multiplied by G_μ when translated from NN to $\overline{\mathrm{N}}\mathrm{N}$, in a given isospin state I. For instance, the one-pion-exchange potential changes sign when going from NN and $\overline{\mathrm{N}}\mathrm{N}$, and so does its Born approximation when its generates an amplitude. Its first iteration (second term in the Born expansion) is identical for NN and $\overline{\mathrm{N}}\mathrm{N}$, the next iteration flips its sign, etc.

As we shall see along this review, the G-parity rule (3.38) induces dramatic changes in the long-range potential. First, the $\overline{\mathrm{N}}\mathrm{N}$ potential is on the average more attractive than the NN one. This is important for understanding the observed cross-sections and the speculations about possible $\overline{\mathrm{N}}\mathrm{N}$ bound states and resonances. Secondly, the spin and isospin dependence is different: the more pronounced effects are expected in the $I = 0$ channel, and affect mainly the tensor component of the potential.

3.6 Potential models

The G-parity rule is the starting point of phenomenological studies of low-energy $\overline{\mathrm{N}}\mathrm{N}$ interaction based on potential models. Schematically, one starts from a realistic NN potential, apply the G-parity rule to its meson-exchange tail, and replace the short-range NN core by a complex short-range part to account both for the short range elastic forces and for the strong annihilation component.

Potentials models are very useful tools

i) to get a hint on the strength and range of annihilation

ii) to test the role of various components of the interaction (π-exchange, ρ-exchange, absorption, etc.) in various observables

iii) to make quantitative comparisons with NN interaction

iv) to use information on the "elementary" $\overline{\mathrm{N}}\mathrm{N}$ interaction for studying antinucleon–nucleus interaction.

It should remain clear, however, that there is no fundamental reason for believing that the $\overline{\mathrm{N}}\mathrm{N}$ interaction should reduce to a potential, especially if this potential is restricted to be local and energy independent.

Any microscopic derivation of the absorption potential from the internal quark structure gives, indeed, a kernel that is *i)* separable rather than local and ii) highly sensitive to the difference between the incoming energy and the location of the main thresholds (e.g., the threshold for two vector mesons and a pseudoscalar). See, for instance, [189].

3.6.1 Current NN potentials

From the 50's to the 70's, a rather successful description of the NN interaction was achieved with "semi-phenomenological" potentials. They consist of a long-range part which include meson exchanges and a short-range part which describes empirically the observed repulsion with a few parameters. These potentials have been tuned to reproduce the NN scattering data with good accuracy and used in nuclear-structure calculations. For a review, see, e.g., [190].

3.6.2 Pion-exchange and more elaborate nucleon–nucleon potentials

There are several reviews on the meson-exchange approach to the NN interaction. We thus refer to the literature [190–192] for a detailed survey and restrict ourselves here to what is necessary for extrapolating to the $\overline{\mathrm{N}}\mathrm{N}$ case.

Following Yukawa, the exchange of a particle of mass μ leads to a potential of range $\hbar c/\mu c^2$ (hereafter simplified into μ^{-1}), namely

$$V(r) \propto \frac{\exp(-\mu r)}{r} \,, \tag{3.42}$$

when spin and isospin complications are omitted. In momentum space, the one-pion-exchange (OPE) potential reads

$$V_{\mathrm{OPE}} = \frac{g^2}{\vec{q}^{\,2} + \mu^2} \cdot \tag{3.43}$$

In the actual situation, the pion is pseudoscalar and isovectorial, and gives a characteristic spin and isospin dependence. The OPE potential is an operator acting on isospin state and Dirac spinor of each nucleon

$$V_{\mathrm{OPE}} \propto \gamma_5^{(1)} \gamma_5^{(2)} \vec{\tau}_1.\vec{\tau}_2 \, \frac{1}{\vec{q}^{\,2} + \mu^2} \,, \tag{3.44}$$

where $\vec{\tau}_i$ is the isospin operator for nucleon (i) and $\vec{q} = \vec{p}_2 - \vec{p}_1$ is the momentum transfer. After non-relativistic reduction, one obtains in position space a combination of spin–spin and tensor potentials, namely

$$\begin{aligned} V_{\mathrm{OPE}} &= \left(V_{\mathrm{SS}}\, \vec{\sigma}_1.\vec{\sigma}_2 + V_{\mathrm{T}}\, S_{12}\right) \vec{\tau}_1.\vec{\tau}_2 \,, \\ V_{\mathrm{SS}} &= \frac{g^2}{4\pi} \frac{\mu^2}{4m^2} \frac{\exp(-\mu r)}{r} \,, \\ V_{\mathrm{T}} &= \frac{g^2}{4\pi} \frac{\mu^2}{4m^2} \frac{\exp(-\mu r)}{r} \left(1 + \frac{3}{\mu r} + \frac{3}{\mu^2 r^2}\right) \,, \end{aligned} \tag{3.45}$$

where the tensor operator is

$$S_{12} = 3\, \vec{\sigma}_1.\hat{r}\; \vec{\sigma}_2.\hat{r} - \vec{\sigma}_1.\vec{\sigma}_2 \,, \tag{3.46}$$

and the isospin coefficient

$$\begin{aligned} \vec{\tau}_1.\vec{\tau}_2 &= \;\; 1 \quad \text{for} \quad I = 1 \,, \\ \vec{\tau}_1.\vec{\tau}_2 &= -3 \quad \text{for} \quad I = 0 \,. \end{aligned} \tag{3.47}$$

This potential V_{OPE} successfully explains the peripheral NN phase-shifts at low energy, as well as the quadrupole deformation of the deuteron. Now, some departures from the simple OPE model are

seen in NN phase-shifts of lower angular-momentum ℓ, or in peripheral partial-waves when energy increases. This indicates the need for additional terms that have a range shorter than OPE.

A first improvement consists of allowing the nucleons to exchange mesons with larger mass and new quantum numbers, leading to additional potentials that have a shorter range and exhibit new kinds of spin–isospin dependence. Strictly speaking, one should distinguish the one-boson-exchange models (OBEM) with a direct parametrisation of the scattering *amplitude* in terms of t-channel poles

$$M_{\rm OBEM} = \sum_i \frac{g_i}{\vec{q}^{\,2} + \mu_i^2} \,, \tag{3.48}$$

from the one-boson-exchange potentials (OBEP) where these exchanges are written for the *potential*

$$V = \sum_i g_i \frac{\exp(-\mu_i r)}{r} \,, \tag{3.49}$$

and thus are iterated in the Schrödinger equation. Eqs. (3.48) and (3.49) should be understood with spin and isospin factors which are specific for each type of mesons, and play an important role. One needs for instance vector mesons to generate spin–orbit forces for $I = 1$ and to cancel the tensor part of OPEP at short distances in the isospin $I = 0$ channel. The existence of vector mesons was in fact anticipated by scrutinising NN scattering data and their spin dependence [1, 193].

These OBE models were elaborated in the 60's and 70's, typically. In the 50's and 60's, there were attempts to construct a field theory of nuclear forces, in analogy with QED, but based on the Yukawa coupling $g\gamma_5$ of the pseudoscalar pion field to the nucleons. This turned out eventually unsuccessful, but the studies revealed the role of two-pion exchange (TPE) in the intermediate range attraction. This is why all modern NN potentials include TPE contributions explicitly.

In fact, ρ or σ[1] exchanges are already part of TPE, ρ and σ being resonances of the $\pi\pi$ system. Also, since TPE includes the box (ladder) diagram of Fig. 3.8 with nucleons in the intermediate

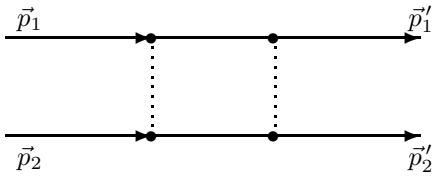

Figure 3.8: Box diagram, part of the two-pion-exchange contribution to NN interaction.

states, it is natural to account for these ladder or crossed diagrams where one or two Δ or N^* are excited. All these contributions to TPE are incorporated, without double counting, in the dispersion-theoretical calculation whose formalism was written down by Amati et al. [194, 195] and later on used to compute the medium-range NN potential [190, 191].

In the approach based on dispersion relations, one has given up the idea of an expansion in powers of the pion–nucleon coupling constant g. In particular, TPE contains diagrams where the exchanged pions rescatter several times with each others or with the nucleons. Instead, one achieves an expansion according to the range of the various contributions: OPE provides the tail of the potential and TPE the medium part. This gives a good description of the NN phase-shifts with $\ell > 1$ at low energy.

In potentials designed for practical purpose, the short-range part of the NN interaction is described empirically by cutting off meson exchanges at distances $r \lesssim 1\,\mathrm{fm}$ and adding a phenomenological core to account for the observed repulsion. This is the basis of the Paris, Bonn and others

[1] In the early literature on nuclear forces, ϵ or σ denotes a scalar and isoscalar meson exchanged between the nucleons. Today the amplitude for two pions in a scalar and isoscalar state below ~ 1.2 GeV is often designated as σ. If it has to be identified with an actual meson, then it should be renamed f_0.

semi-phenomenological potentials [191, 192] that are widely used for nuclear-physics calculations. Some potentials have been updated regularly to reach better accuracy [196].

In early studies of the NN interaction, the short-range repulsion was attributed to the exchange of heavy vectors mesons. It is now explained by the direct interaction of the quarks which build up the nucleons. There is an abundant literature on this subject [197, 198] and one can say that a semi-quantitative understanding of the short-range NN potential has been achieved. There are two major mechanisms: the exclusion principle between quarks and the chromomagnetic interaction.

To summarise, we have in hand potentials describing very accurately NN scattering and the deuteron properties which can be applied to nuclear systems. However, the theoretical ground is uncomfortably split into two parts. The Yukawa picture accounts for the long-range part in terms of nucleons and pions, while the short-range part is described directly at the quark level. A synthesis is badly needed. One should in principle derive microscopically the Yukawa model out of QCD, to end with a unified picture in terms of quarks. Alternatively, one could reformulate QCD at low energy in terms of pions and solitons. One attempt is the Skyrmion model. However, the bosonisation of QCD remains to be demonstrated rigorously.

More promising, perhaps, is the approach with effective Lagrangians which incorporate the basic symmetries of QCD. Applications to the NN interaction have already been done, and there is already a rich literature on the subject, which can be traced back from Refs. [199–205]

3.6.3 Long-range nucleon–antinucleon potential

Once the long-range NN potential is described in terms of exchange of mesons or set of mesons, schematically

$$V^I(\mathrm{NN}) = \sum_m V_m \ , \tag{3.50}$$

there is no difficulty in writing down the $\overline{\mathrm{N}}\mathrm{N}$ analogue

$$V^I(\overline{\mathrm{N}}\mathrm{N}) = \sum_m G_m V_m \ , \tag{3.51}$$

except that G_m should be clearly identified. For instance, the ω-exchange contribution is sometimes thought as a resummation of many contributions of mass 0.8 GeV or higher. If this is $\pi\rho$, the conclusions are not changed as this system has the same G-parity -1 as ω. If this is part of four-pion exchange, then the translation from NN to $\overline{\mathrm{N}}\mathrm{N}$ is misleading.

Sometimes the boson-exchange NN potential is regularised à la Pauli–Villars [206], i.e.,

$$\frac{1}{q^2+\mu^2} \to \frac{1}{q^2+\mu^2} - \frac{1}{q^2+\Lambda^2} \ , \tag{3.52}$$

the short-range term elegantly conspiring to parametrise a realistic core in terms of elementary Yukawa functions. Nothing guarantees that for the short-range interaction, the same regularising term should be applied to $\overline{\mathrm{N}}\mathrm{N}$, using the G-parity factor. In absence of a microscopic derivation, the G-parity content of the core is simply unknown.

The translation of NN forces toward the $\overline{\mathrm{N}}\mathrm{N}$ system has been performed by several authors, including Fermi and Yang [207], and Ball and Chew [208], the latter been motivated by the first measurements of antiproton cross sections. The potentials by Gourdin et al. [209], Bryan and Philips [210], Dover and Richard [211], Kohno and Weise [212], just to mention a few examples, will be discussed shortly.

3.6.4 Spin–isospin dependence of the long-range potential

We now discuss the spin and isospin dependence of the long-range $\overline{\mathrm{N}}\mathrm{N}$ potential. For simplicity, we shall often adopt the language of the one-boson-exchange approximation, but most of the analysis remains valid in more elaborated models.

Consider any J^P exchange. Thanks to the exchange degeneracy of the meson spectrum, there are always two mesons, one with $I = 0$ and another with $I = 1$, with same C-conjugation (for the $I_3 = 0$ states) and different G-parity. For instance, the vector-meson exchange contribution to NN being

$$V_{\rm V} = V_\omega + \vec{\tau}_1 \cdot \vec{\tau}_2 V_\rho \ , \tag{3.53}$$

it reads

$$\begin{aligned} V_{\rm V}^{I=0} &= V_\omega - 3V_\rho \ , \\ V_{\rm V}^{I=1} &= V_\omega + \ \ V_\rho \ . \end{aligned} \tag{3.54}$$

Coherences appear in the isospin $I = 1$ channel. Now, if one looks at the cumulated effect of scalar, vector and pseudoscalar exchanges, the most pronounced coherence occurs in the spin–orbit potential, as seen in Table 3.1. It is well known, indeed, that protons experience strong spin–orbit forces when scattered on protons or on nuclei. The spin–spin component of the NN interaction is less visible, since the Pauli principle forbids the existence of the triplet state if the singlet is allowed, or vice-versa.

exch.	NN $I=0$				NN $I=1$				$\overline{\rm N}$N $I=0$				$\overline{\rm N}$N $I=1$			
meson	C	SS	LS	T	C	SS	LS	T	C	SS	LS	T	C	SS	LS	T
π	0	–	0	–	0	+	0	+	0	+	0	+	0	–	0	–
η	0	+	0	+	0	+	0	+	0	+	0	+	0	+	0	+
ρ	–	–	+	+	+	+	–	–	–	–	+	+	+	+	–	–
ω	+	+	–	–	+	+	–	–	–	–	+	+	–	–	+	+
a_0	+	0	+	0	–	0	–	0	–	0	–	0	+	0	+	0
σ	–	0	–	0	–	0	–	0	–	0	–	0	–	0	–	0

Table 3.1: Sign of meson-exchange contributions to central (C), spin-spin (SS), spin-orbit (LS) and tensor (T) components of the NN and $\overline{\rm N}$N potentials.

In the $\overline{\rm N}$N case, Eq. (3.54) becomes

$$\begin{aligned} V_{\rm V}^{I=0} &= -V_\omega - 3V_\rho \ , \\ V_{\rm V}^{I=1} &= -V_\omega + \ \ V_\rho \ . \end{aligned} \tag{3.55}$$

Coherences now take place in the $I = 0$ channel, with a larger strength. From Table 3.1, the most pronounced effect occur in the tensor component [213]. This has many consequences on the phenomenology of $\overline{\rm N}$N interaction in potential models: spin effects in elastic or charge-exchange scattering, spin effects in specific reactions such as $\bar{\rm p}{\rm p} \to \overline{\Lambda}\Lambda$ or $\bar{\rm p}{\rm p} \to {\rm K}^-{\rm K}^+$, distortion of the protonium wave function, enhancement of some branching ratios, etc. We shall come back very often on possible signatures of this strong tensor interaction.

A quantitative illustration of these coherences is provided in Fig. 3.9 and 3.10 below. We use the static version of the Paris potential, and display the NN and $\overline{\rm N}$N spin–orbit and tensor potentials for both $I = 0$ and $I = 1$ isospin. In Fig. 3.9, one sees the large spin–orbit component of the proton–proton potential, with $I = 1$. In Fig. 3.10, one notices the large and positive tensor potential for $\overline{\rm N}$N in isospin $I = 0$ states.

Testing tensor forces in scattering experiments require delicate measurements. If one would treat tensor forces at first order in DWBA[2] starting from central forces only, there would be no polarisation. In actual calculations, tensor forces produce polarisation from their second and higher order contributions, but polarisation alone cannot distinguish current models with strong tensor force

[2]Distorted-wave Born approximation

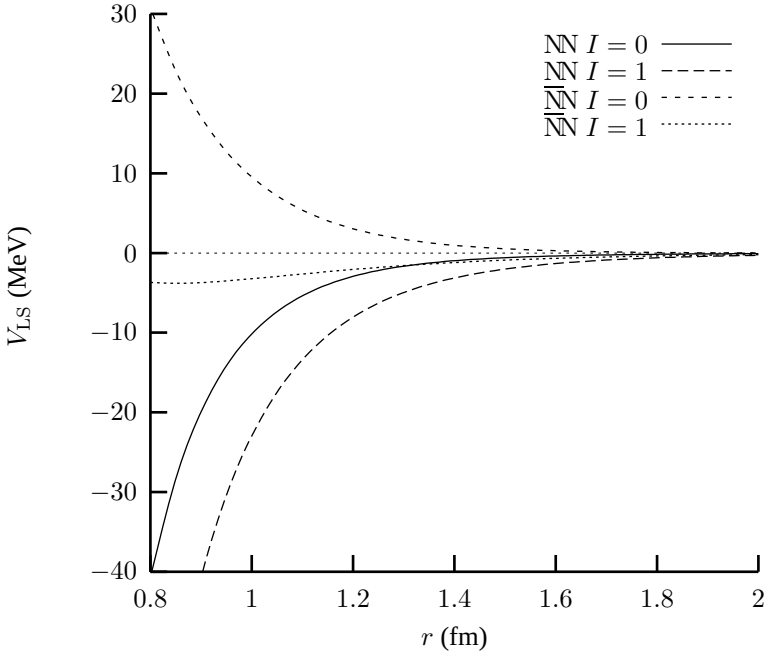

Figure 3.9: Comparison of the NN and $\overline{\rm N}$N spin–orbit potentials in the Paris model.

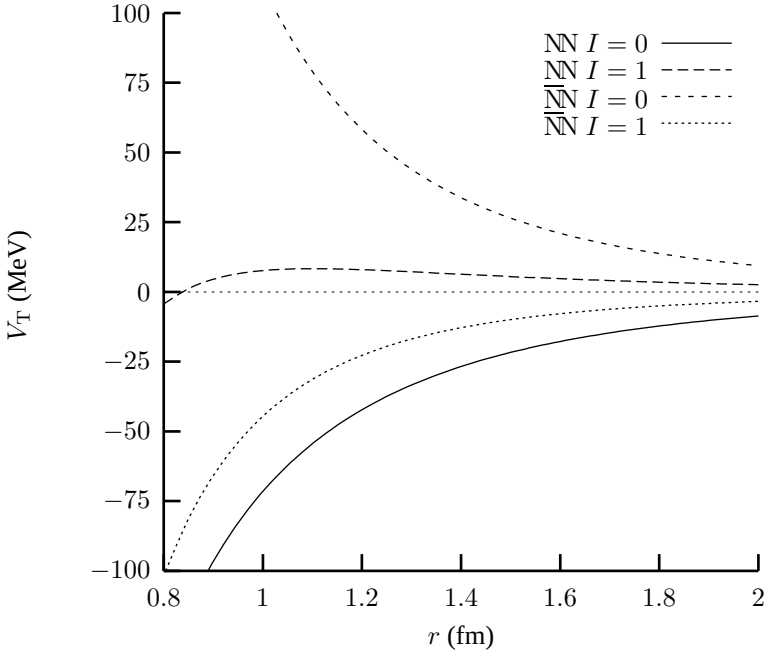

Figure 3.10: Comparison of the NN and $\overline{\rm N}$N tensor potentials in the Paris model.

and weak spin-orbit from possible alternative models with weak tensor forces and moderate spin-orbit potential. The best tests rely on observables to which tensor forces contribute already at first order. As the tensor operator S_{12} involves two spin operators (see Eq. (3.46) of Chap. 3), these observables are of rank 2. An example is the transfer of longitudinal polarisation [214].

In this latter paper [214], it was shown that the spin-dependence of the long-range potential, when blindly associated with a spin-independent optical potential, produces substantial spin effects in $\overline{\mathrm{N}}\mathrm{N}$ scattering. The question is to which extent scattering experiments can test this spin dependence unambiguously and give information on the spin dependence of short-range forces.

3.7 Strangeness-exchange reactions

When $\overline{\Lambda}\Lambda$ or other hyperon–antihyperon pairs are produced near threshold, a nuclear-physics approach seems justified, where the reaction is described by exchange of strange mesons, in the same way as the charge-exchange reaction $\bar{\mathrm{p}}\mathrm{p} \to \bar{\mathrm{n}}\mathrm{n}$ is mediated by charged mesons. This corresponds to the diagram of Fig. 3.11.

As mentioned earlier, the pseudoscalar character of the pion gives a specific spin dependence in the charge-exchange reaction $\bar{\mathrm{p}}\mathrm{p} \to \bar{\mathrm{n}}\mathrm{n}$. A similar pattern can thus be expected for $\bar{\mathrm{p}}\mathrm{p} \to \overline{\Lambda}\Lambda$. However, the K^* is closer in range to K than ρ to π, and thus the corrections due to vector and higher exchanges could be more important in $\bar{\mathrm{p}}\mathrm{p} \to \overline{\Lambda}\Lambda$ than in $\bar{\mathrm{p}}\mathrm{p} \to \bar{\mathrm{n}}\mathrm{n}$.

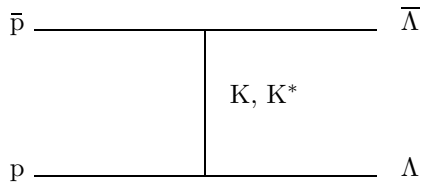

Figure 3.11: Meson-exchange diagram for $\bar{\mathrm{p}}\mathrm{p} \to \overline{\Lambda}\Lambda$.

Since K or K^* mesons are relatively heavy, the production of hyperons is a rather short-range process and, instead of summing over all possible kaon excitations in the t-channel, one might think of a simple quark process, as pictured in Fig. 3.12: a pair of ordinary quarks annihilate and a pair of strange quarks is created. Gluons are not shown, but are crucial to actually generate the process.

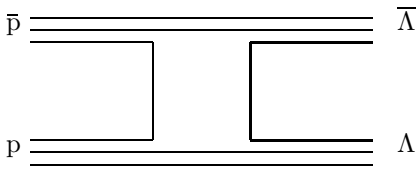

Figure 3.12: Quark pair and creation for $\bar{\mathrm{p}}\mathrm{p} \to \overline{\Lambda}\Lambda$. The strange quarks or antiquarks are shown with thick lines.

While PS185 was taking data and seeking further spin observables, new ideas were developed, motivated by experiments on the structure functions of the nucleon. A $\mathrm{s}\bar{\mathrm{s}}$ pair might be extracted from the nucleon or antinucleon sea instead of being created during the reaction, as schematically pictured in Fig.3.13. This point of view was proposed in particular by Ellis et al. [215], who pointed out that a similar mechanism would produce an abundant violation of the OZI[3] rule in annihilation.

[3]Okubo–Zweig–Iizuka, see, e.g., Ref. [216] for references

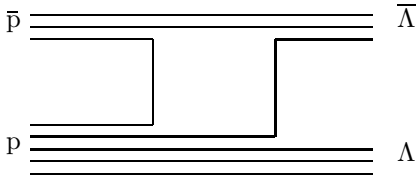

Figure 3.13: Possible sea-quark contribution to $\bar{p}p \to \overline{\Lambda}\Lambda$.The strange quarks or antiquarks are shown with thick lines.

The channel $\overline{\Sigma}^0\Lambda$ forces an isospin $I = 1$ initial state, unlike $\overline{\Lambda}\Lambda$ which filters $I = 0$. In a naive quark model, the spin of Λ is carried by the s quark, which is associated with a spin 0 (ud) diquark, while the spin of a Σ is opposite to that of its constituent s quark.

The final states $\overline{\Sigma}^+\Sigma^-$ and $\overline{\Sigma}^-\Sigma^+$ bear essential differences. In a Yukawa-exchange or Regge-exchange language, the production of the latter can be understood in terms of a neutral kaon in the t-channel, and thus its cross section should be of the same order of magnitude as for $\overline{\Lambda}\Lambda$ or $\overline{\Sigma}^0\Lambda$. The production of $\overline{\Sigma}^+\Sigma^-$ requires exotic exchanges, namely mesonic systems with one unit of strangeness and two units of charge. It is thus expected to be suppressed. This was clearly seen in pre-LEAR data (for Refs., see, e.g., the bibliography in Ref. [129]). The same difference can be seen in the quark-diagram approach: $\overline{\Lambda}\Lambda$, $\overline{\Sigma}^0\Lambda$ or $\overline{\Sigma}^-\Sigma^+$ can be reached by annihilating a single $u\bar{u}$ or $d\bar{d}$ pair replaced by a $s\bar{s}$ one. For the final state $\overline{\Sigma}^+\Sigma^-$, the simple quark diagram of Fig. 3.12 does not operate: one needs more pairs created or annihilated.

3.8 Phenomenological description of annihilation

Only the long-range part of the $\overline{N}N$ interaction can be translated from its NN analogue. It remains to include short-range elastic forces and annihilation. We review here the different approaches and the salient results obtained in early models. More refined studies incorporating the LEAR results will be presented in Chap. 6.

3.8.1 The range of annihilation and early optical models

Before antiprotons were produced and their cross-sections first measured, in the years 1955–56, one would probably have guessed that the $\bar{p}p$ interaction is mostly elastic, with a small correction due to annihilation, as in the e^+e^- case. Why such a (wrong) prediction? The elastic forces have a range given by the inverse pion mass and thus act up to a few fermis, while annihilation was expected to have a very short-range, the inverse nucleon mass, i.e., about 0.1 fm, as the range of e^+e^- annihilation is the inverse electron mass.

A typical annihilation diagram, representing $\overline{N}N \to \pi\pi$ is shown in Fig. 3.14 (left), as well as its contribution to the $\overline{N}N$ amplitude (right). This amplitude has an imaginary part, because the sum of the meson masses is smaller than the centre-of-mass energy $\sqrt{s}$. There are two baryons in the t-channel, of invariant mass larger than $2m$, thus the range is $r \leq (2m)^{-1} \simeq 0.1\,\text{fm}$. The same result holds for intermediate states with a larger number of mesons. For a more rigorous discussion of the range of annihilation, see, e.g., Ref. [217].

The striking surprise was [7] that the total antiproton cross-section on matter is very large (as compared to the proton one), and that more than half of this cross-section is due to annihilation. This annihilation cross-section σ_{ann} cannot be understood from a simple S-wave correction. It requires angular-momentum $\ell > 0$ contributions.

The simplest phenomenological method to describe these data consists of supplementing the meson-exchange potential (regularised at short-distance) by an empirical complex potential, which

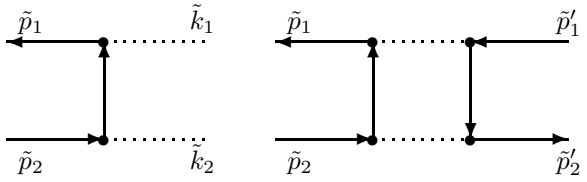

Figure 3.14: Simplest annihilation diagram in an old-fashioned hadronic approach: the nucleon and the antinucleon and transformed into a two-pion state by exchange of two nucleons. Shown are the basic process (left) and its contribution to the $\overline{\mathrm{N}}\mathrm{N}$ amplitude (right).

represent the sum of $\overline{\mathrm{N}}\mathrm{N}\to\overline{\mathrm{N}}\mathrm{N}$ diagrams with meson intermediate states, and other short-range processes.

The method of optical models is very successful in nuclear physics [218]. The idea, when studying a specific reaction, say $a + A \to a + A$, consists of not wasting time and computer resources to try to parametrise each open channel such as $a + A \to a' + A^*$ or $a + A \to b + B$, where A^* stands for an excited level and B another nucleus with different quantum numbers. What matters, for the reaction of interest [218], is that the presence of these channels strongly distorts the incoming $a + A$ wave. An empirical potential reproducing this distortion provides a realistic picture of the scattering process.

Early attempts to describe $\overline{\mathrm{N}}\mathrm{N}$ annihilation by an optical model were proposed by Ball et al. [208], Gourdin et al. [209], etc. A rather celebrated model, remaining a reference for later studies, is the potential developed by Bryan and Phillips [210]. The starting point is the $\mathrm{N}\mathrm{N}$ potential of Bryan and Scott with includes several one-boson-exchange contributions. The short-range $\overline{\mathrm{N}}\mathrm{N}$ interaction is parametrised as

$$W(r) = \frac{V_\mathrm{R} - iV_\mathrm{I}}{1 + \exp(a(r - R))} \cdot \tag{3.56}$$

An impressively large strength is required to fit the data, in both variants BP1 and BP2 of the model, as seen in Table 3.2. Independent of the precise value of the parameter a, the Bryan–Philips (and earlier) fits imply that the annihilation potential should be important up to about 1 fm. An illustration is provided in Fig. 3.15, whose drawing is inspired by Ref. [219]. The annihilation potential, chosen as the renowned Bryan–Philips model (static version), is compared to the spin–spin and tensor components of the one-pion exchange potential. One clearly needs something like $r \gtrsim 1.5\,\mathrm{fm}$ to become sure that the annihilation potential is negligible.

If one reduces the range of the absorptive potential $W(r)$ in the Bryan–Philips model, then the fit to the cross-section quickly deteriorates. In particular, one cannot account for the ratio of annihilation to elastic cross-sections, nor for the smallness of the charge-exchange cross-section. Remember that in a naive model with one-pion-exchange only, treated in the Born approximation, the charge-exchange process will be four times larger than the elastic cross-section, due to to the favourable isospin factors! One needs large corrections due to higher-order iterations, exchange of heavier mesons, and absorption, to restore the proper hierarchy of cross-sections.

To summarise, the relatively long-range character of the imaginary potential, needed to reproduce the observed integrated cross-sections, is the most striking feature of these optical-model fits.

Later on, a strong support to a large value of the annihilation range came from the detailed study of protonium annihilation. With a zero-range absorption, annihilation at rest would be restricted to S-waves. The observation of the $\pi^0\pi^0$ decay of protonium [141] gave the first indication for P-wave annihilation at rest. It was followed by the observation of several other channels with a clear signature of P-wave annihilation. Globally, P-states of protonium have an annihilation width much larger than their radiative decay to S-states.

Many years after the pioneering experiments on antiproton annihilation and the first phenomenological analyses, we understand better what is underneath: the finite size of the nucleon (and antin-

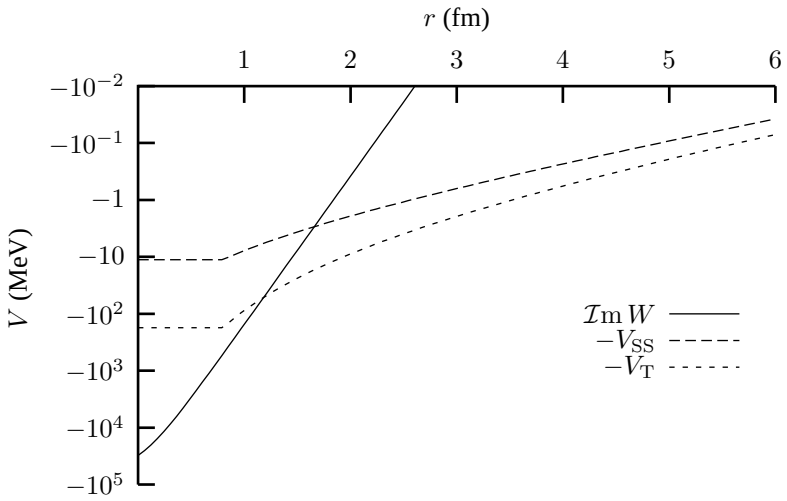

Figure 3.15: Comparison of the imaginary optical potential $W(r)$, corresponding to the fit of Ref. [210], with the spin–spin and tensor components of the pion-exchange potential.

ucleon), eventually due to its composite structure.

3.8.2 Phenomenology of optical models

Shortly before LEAR came into operation, Dover and Richard [211] revisited the Bryan–Phillips model. The long-range is a slightly simplified version of the Paris potential, which includes two-pion exchange and excitation of πN resonances in the intermediate states. The potential is cut-off at short distances and supplemented by an empirical Wood–Saxon core of the same type, see Eq. (3.56). This corresponds to models DR1 and DR2 [220] in Table 3.2. A similar procedure was used by Kohno and Weise [212] (model KW) and others [221].

Though every microscopic derivation of the optical potential leads to an interaction that is strongly non-local and energy-dependent, most phenomenological models use a local ansatz, for simplicity. The real and the imaginary parts of the isoscalar and isovector components in the core (3.56) are chosen to be identical. The possibility of adding some spin or isospin dependence is discussed in Chap. 6.

The values of a, R and $V_{\rm I}$ adopted by Bryan and Philips [210] (BP), Dover, Richard and Sainio [211, 220] (DR) and Kohno and Weise [212] (KW) are summarised in Table 3.2. The parameters

Table 3.2: Comparison of the imaginary potentials of several optical-model fits of $\overline{\rm N}$N scattering

model	Ref.	a (fm^{-1})	R (fm)	$V_{\rm I}$ (GeV)
BP1	[210]	6	0	62
BP2	[210]	6	0	8.3
DR1	[211]	5	0	20
DR2	[220]	5	0.8	0.5
KW	[212]	5	0.55	1.6

look rather different, but the imaginary potentials almost coincide in the region of interest, near

$1\,\mathrm{fm}$. The comparison of the above imaginary potentials is made in Fig. 3.16. Also shown here is the average imaginary potential of Ref. [222],

$$\mathcal{I}\mathrm{m}\,V = -\frac{1}{2}\left[w_0 \exp(-(\alpha_0 r)^2) + w_1 \exp(-(\alpha_1 r)^2)\right], \tag{3.57}$$

with $w_0 = 3$ GeV, $w_1 = 0.6$ GeV, $\alpha_0 = 1.80$ fm^{-1} and $\alpha_1 = 1.47$ fm^{-1}. Note that in Ref. [222], the absorptive potential is allowed to be isospin dependent. It is found that data suggest a somewhat stronger absorption for isospin $I = 0$ than for $I = 1$. This presumably explains why in Fig. 3.16, this $\bar{\mathrm{p}}\mathrm{p}$ absorptive potential is slightly weaker than the others, if the full strength is needed in one isospin channel only.

In Fig. 3.16, we observe at a different scale the same phenomenon of surface interaction as in low-energy heavy-ion collisions, where the scattering is entirely determined by the nuclear potential in a very small interval of the distance between the two ions. Similarly, the low-energy $\overline{\mathrm{N}}\mathrm{N}$ data are not sensitive to the value of the absorptive potential at very small distances. What really matters is the strength of annihilation near $1\,\mathrm{fm}$. This correlation between the range and the strength of the imaginary potential was noticed in Ref. [222].

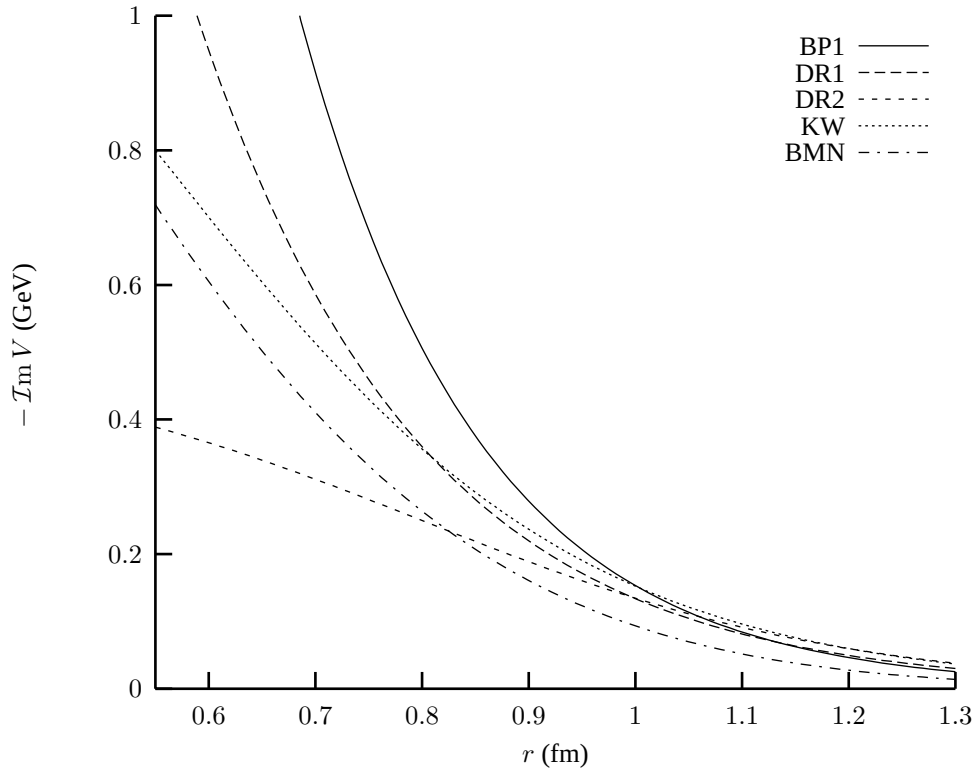

Figure 3.16: Comparison of various imaginary potentials used for describing $\overline{\mathrm{N}}\mathrm{N}$ annihilation. We restrict ourselves here to local models, Bryan–Philips (BP1), Dover–Richard (DR1 and DR2), and Kohno–Weise (KW), Bydzovsky et al. (BMN).

Note that the values of the parameters V_{R} in different models cannot be compared independently of the cut-off procedure which is adopted for the short-range of the meson-exchange potential. It was noticed in Ref. [211] that increasing the attraction allows one to use smaller values of V_{I} and tends to slightly improve the overall fit of integrated cross-sections. This illustrates the mechanism

proposed by Shapiro [29] for annihilation: the attractive potential focuses the wave function toward the region where absorption acts.

3.8.3 Boundary condition models

In practice, the method consists of a phenomenological prescription for the logarithmic derivative of the radial wave function in each partial wave, at a distance $r = R$. Then the long-range behaviour, given by a homogeneous second-order equation, is entirely determined by the knowledge of $R\mathrm{d}u(r)/\mathrm{d}r|_{r=R}$.

A boundary-condition model was used, for instance, by Lomon et al. [223], to account for the short-range repulsion of the NN potential. Years later, a microscopic interpretation was proposed by Jaffe and Low [224]. The boundary condition achieves a transition between the inner part of the wave function, described in terms of quarks, and the outer part, which is accounts for the relative motion of two well separated hadrons.

In the $\overline{\mathrm{N}}\mathrm{N}$ case, the inner part of the wave function contains the rich dynamics of multiquark states $(\mathrm{q}^n\bar{\mathrm{q}}^n)$. Thus the boundary-condition models are not too far from those by Dorokhov [225] and Roberts [226], who later extended this approach to strangeness-exchange [227]. These authors describe $\overline{\mathrm{N}}\mathrm{N}$ scattering as a superposition of broad s-channel resonances.

A simple boundary-condition model was used by Ball and Chew [208], but in practice, when combined with WKB approximation, it led to discontinuous inelasticity parameters, as a function of energy. It was sufficient, however, to account for the large magnitude of the observed cross sections. This method has been regularly revisited. The boundary condition model was used in particular by Kaufmann and Pilkuhn [147], and Dalkarov and Myhrer [228].

3.8.4 Coupled-channel models

Here the various annihilation channels are mimicked by a few coupled channels. Usually, no diagonal term is introduced in these new channels, i.e., the interaction among mesons is neglected. Annihilation manifests itself as a coupling between the main channel (nucleon–antinucleon) and the mesonic channels [229–232].

A reasonable description of scattering data has been obtained by various groups. It is interesting that the transition operators V_i from $\overline{\mathrm{N}}\mathrm{N}$ to the mesonic channels can be chosen as relatively short-ranged. As explained, e.g., by Liu and Tabakin [229], the contribution of a mesonic channel to the optical potential can be derived from the coupled equations

$$\begin{aligned}(2m + T_{\overline{\mathrm{N}}\mathrm{N}} + V_{11} - \sqrt{s})\Psi_1 &= -V_{12}\Psi_2 \ , \\ (2\mu + T_\mu + V_{22} - \sqrt{s})\Psi_2 &= -V_{21}\Psi_1 \ .\end{aligned} \tag{3.58}$$

Solving formally the second equation as

$$\Psi_2 = -(2\mu + T_\mu + V_{22} - \sqrt{s})^{-1}\, V_{21}\Psi_1 \ , \tag{3.59}$$

and inserting the result into the first equation gives an effective potential

$$V_{\mathrm{eff}} = V_{11} - V_{21}\,(2\mu + T_\mu + V_{22} - \sqrt{s})^{-1}\, V_{21} \ , \tag{3.60}$$

which is highly non local, as it contains the kinetic operator T_μ of the meson sector and and explicit dependence upon the energy $\sqrt{s}$. In other words, the meson propagator can be appreciably extended, and tend to spread the annihilation region.

Usually, the channels that are introduced represent an average over many channels with comparable phase-space. There are more specific models, with a few explicit physical channels, such as $\bar{\mathrm{p}}\mathrm{p}\to\pi^-\pi^+$, $\mathrm{K}^-\mathrm{K}^+$, and either fictitious channels or an optical model to account for the rest of annihilation [232]. That way, not only $\overline{\mathrm{N}}\mathrm{N}$ observables can be studied, but also those of the specific reactions such as $\bar{\mathrm{p}}\mathrm{p}\to\pi^-\pi^+$ or $\bar{\mathrm{p}}\mathrm{p}\to\mathrm{K}^-\mathrm{K}^+$.

3.8.5 Microscopic derivation of the absorptive potential

In principle, the optical potential can be entirely determined once one knows the transition amplitude from $\overline{\mathrm{N}}\mathrm{N}$ to every possible mesonic channel. A prototype calculation was given by Ihle et al. [189], who simply assumed that annihilation is dominated by rearrangement diagrams, and neglected most of the interaction between the three mesons in the final states. They ended with an annihilation potential which is not too far from being realistic and at least exhibits the appropriate range.

Note that optical potentials obtained in explicit models are far from being local. With simple Gaussian wave functions for the quark distribution inside hadrons, one usually ends with a separable operator [233, 234]. For simplicity, empirical optical potentials are parametrised in term of local operators. The energy dependence which is sometimes introduced reflects the need for non-local corrections.

In the above references, and others, for instance, Ref. [235], annihilation is described at the quark level. The baryon-exchange process is used in Ref. [236]. The short-range character of the potential is somewhat hidden by large form-factor corrections. Baryon-exchange diagrams were also advocated by the Paris group to motivate the parametrisation of their short-range potential [237].

Note also a series of papers by the Bonn group [232, 236, 238] where a fraction of the annihilation is taken from the assumed dynamical mechanisms, and the rest of annihilation is treated phenomenologically.

3.8.6 Annihilation range revisited

Many debates arose about the range of annihilation. Let us quote for instance our late friend I.S. Shapiro in the discussion following the talk by one of us [239] at the Mainz Conference [39]:

> *The value of the annihilation range (that is equal in order of magnitude to the Compton length of the annihilating baryons) is not a question for discussion. It is a general statement following from the analytical properties of the amplitudes in quantum field theory... It does not matter how the annihilating objects are constructed from their constituents...*

The arguments based on the analytical properties of Feynman graphs (See, e.g., Refs. [217, 240]) cannot be challenged. However, as addressed at Erice [54] by Brodsky [241] and Shapiro [240], and also at Mainz [239, 242], there is a semantic question about what is meant by "annihilation" and on how to get proper guidance from the comparison with QED.

If the rule links nucleons to electrons, and mesons to photons, then what we call "$\overline{\mathrm{N}}\mathrm{N}$ annihilation" is comparable to $\mathrm{e}^+\mathrm{e}^- \to$ photons, and should, indeed, be of very short range, about $m^{-1} \sim 0.1$ fm, as already said.

However, nucleons are composite, as well as mesons. At the quark level, the analogy with positronium annihilation into photons is not relevant anymore for the so-called "annihilation" into ordinary mesons. In the language of atomic collisions, most of the transitions from baryon–antibaryon to mesons are *not* "annihilation" reactions, they are *rearrangements*, with sometimes partial annihilation.

This distinction can be made more clearly by considering muonium ($\mu^+\mathrm{e}^-$) and antimuonium ($\mu^-\mathrm{e}^+$) scattering. The process

$$(\mu^+\mathrm{e}^-) + (\mu^-\mathrm{e}^+) \to (\mu^+\mu^-) + (\mathrm{e}^+\mathrm{e}^-)\,, \tag{3.61}$$

which is energetically possible even at rest, is simply governed by the spatial overlap of the initial and final-state wave-functions. It has nothing to do with annihilation.

Now, the process

$$(\mu^+\mathrm{e}^-) + (\mu^-\mathrm{e}^+) \to \gamma\text{'s} + (\mu^+\mu^-)\,, \tag{3.62}$$

requires the initial electrons on the top of each other, and thus is of shorter range. Note that the muons can be a little separated, of the order of the $(\mu^+\mu^-)$ Bohr radius.

Finally, the (rare) reaction

$$(\mu^+ \mathrm{e}^-) + (\mu^- \mathrm{e}^+) \rightarrow \gamma\text{'s} \,, \tag{3.63}$$

corresponds to a complete annihilation. It implies μ^+ very close to μ^- and e^+ very close to e^-, and thus a perfect overlap of the initial atoms. Is is extremely short ranged at the atomic scale. As noted by Shapiro [240] on a basis of a calculation by Brodsky [241], one also ends with a very short range if one starts with the rearrangement process (3.61) and imposes eventual annihilation of both $(\mu^+\mu^-)$ and $(\mathrm{e}^+\mathrm{e}^-)$ atoms in the final state. What matters is the final state one considers.

Similarly, $\overline{\mathrm{N}}\mathrm{N} \rightarrow$ pions "annihilation" might proceed by rearrangement of the initial quarks and antiquarks into meson resonances, as pictured in Fig. 3.17. In the harmonic oscillator model, one

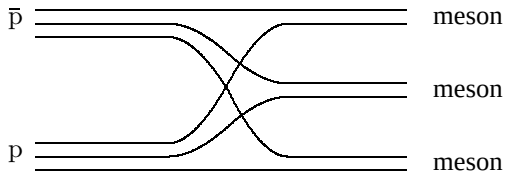

Figure 3.17: Possible diagram for "annihilation" into ordinary mesons.

can write down simple expressions for the transition amplitude [233], and realise that the crucial parameter is the size of the mesons, i.e., their ability to make a "bridge" to pick up a quark in the nucleon and an antiquark in the antinucleon. (The size of the baryons governs the spatial spread of the mesons in the final state.)

Now, processes like $\overline{\mathrm{N}}\mathrm{N} \rightarrow \mathrm{K}^+\mathrm{K}^-$ (see Fig. 3.18) should be of shorter range, since some of the initial constituents have to disappear. It is often proposed that a fraction of annihilation events into

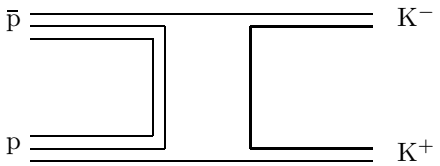

Figure 3.18: Possible diagram for the transition to $\mathrm{K}^+\mathrm{K}^-$.

pions proceed with at least one quark–antiquark pair merging into gluons.

The extreme case corresponds to $\overline{\mathrm{N}}\mathrm{N} \rightarrow \phi\phi$, studied by the JETSET collaboration [243]. This is genuine "complete" annihilation, and should be of very short range. It corresponds to the diagram of Fig. 3.19.

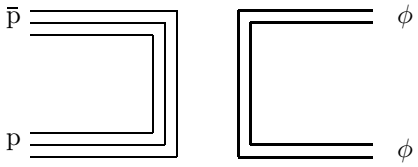

Figure 3.19: Possible diagram for annihilation into $\phi\phi$.

It would be interesting to test somehow that final states with or without strangeness have different ranges, and, perhaps, behave differently when extrapolated from $\overline{\rm N}$N annihilation to annihilation in nuclei [244].

A detailed study of annihilation is beyond the scope of the present paper. What matters to $\overline{\rm N}$N$\to\overline{\rm N}$N scattering process are the global properties of annihilation, which most likely occur via quark rearrangements, and are governed by the size of the mesons. It is not surprising therefore that most parametrised potential models suggest an annihilation radius of the order of $1\,{\rm fm}$.

3.9 Possibility of quasi-nuclear bound states

The ${\rm N}{\rm N}$ interaction is rather weak: phase-shifts are small, and there is only one bound state with a very small binding energy $E\sim 2\,{\rm MeV}$. The attraction provided by σ-exchange is partly compensated by the repulsion due to ω-exchange. In the $\overline{\rm N}$N case, the potential induced by ω-exchange flips sign since $G(\omega)=-1$, leading to a coherent attraction. Thus the $\overline{\rm N}$N potential is likely to support a rich spectrum of bound states and resonances.

The first explicit calculations were performed in the 60's, in the "bootstrap" approach to strong interactions [245]. In this very appealing, and unfortunately unsuccessful theory, hadrons are built out of hadrons interacting through hadron exchanges. In an approximation to the full bootstrap picture, one has tried to describe mesons as $\overline{\rm N}$N states, and this was not too successful, as analysed for instance by Ball, Scotti and Wong [246]. In fact, the $\overline{\rm N}$N potential is isospin dependent, due to its strong isovector-exchange (π, ρ exchange in particular), and the $\overline{\rm N}$N model fails in accounting for the observed degeneracy of the meson spectrum (exchange degeneracy in the Regge-pole language): except in the pseudoscalar sector and perhaps in the scalar sector, isospin $I=0$ and $I=1$ mesons have nearly the same mass.

Shapiro and collaborators [29] came back to the $\overline{\rm N}$N model of mesons, but with a different point of view. In their approach, $\overline{\rm N}$N states do not refer to ordinary mesons such as ρ or ω, but to new mesons lying near the $\overline{\rm N}$N threshold and strongly coupled to the $\overline{\rm N}$N channel. These states are called " quasi-nuclear $\overline{\rm N}$N bound or resonant states", or " nuclear baryonia". Such states can be seen in radiative or pionic transition from atomic protonium, or, for these above the threshold, as resonances in $\overline{\rm N}$N cross sections. A review of the work of the Russian school can be found in [29].

Further calculations of the $\overline{\rm N}$N spectrum were performed by other groups, in particular by Dover et al. A comprehensive review can be found in [30], and a comparison with other approaches to baryonium (string models of quarks, multiquarks), in [247]. See also [248].

While early calculations tend to give $\overline{\rm N}$N states in almost every low partial wave, the spectra displayed in [30] show clear selection rules: the most favourable channels are those with isospin $I=0$ and natural parity $P=(-1)^J$, i.e., the coupled $\ell=J-1$ and $\ell=J+1$ partial waves, where tensor forces act at best.

The role of tensor forces was emphasised in [213]. In the case of deuteron, tensor forces are crucial to achieve binding, but the quadrupole distortion remains moderate, with typically a D-wave percentage of 5 or 6%. In $I=0$ baryonium, we are far from the dominance of the lowest angular momentum, $\ell=J-1$, based on centrifugal-barrier arguments. We have a coherent mixture of the two partial waves, in a combination $|\,\alpha_J\rangle$ corresponding to an eigenstate of the tensor operator with eigenvalue $S_{12}=-4$, while the orthogonal combination $|\,\beta_J\rangle$ experiences a repulsion, with $S_{12}=2$. They are

$$\begin{aligned} |\,\alpha_J\rangle &= \quad\sqrt{\frac{J+1}{2J+1}}|\,J-1\rangle+\sqrt{\frac{J}{2J+1}}|\,J+1\rangle\,,\\ |\,\beta_J\rangle &= -\sqrt{\frac{J}{2J+1}}|\,J-1\rangle+\sqrt{\frac{J+1}{2J+1}}|\,J+1\rangle\,. \end{aligned} \tag{3.64}$$

(This basis is also relevant for discussing spin effects for annihilation into two pseudoscalar mesons.)

So far, annihilation is neglected, or treated as a perturbation. This is clearly not justified, even so one can argue that the $I=0$, natural parity states have a wave function with a large radius. A

calculation of the spectrum with the full $\overline{\mathrm{N}}\mathrm{N}$ potential, including the imaginary part, was performed by Myhrer and Thomas [249]. They use the Bryan–Phillips potential [210], and found that the nice spectrum of bound states produced by the real part is completely washed out when the annihilation part is switched on. Widths exceed several hundreds of MeV, typically, and thus $\overline{\mathrm{N}}\mathrm{N}$ states cannot account for the narrow structures that were claimed to be found at that time.

The conclusions of Myhrer and Thomas might be attenuated in several ways. Firstly, the brute-force annihilation they used can be replaced by imaginary potentials that are slightly weaker, and have a slightly shorter range, but still fit total cross-sections. Secondly, non-local effects, or energy-dependent effects can be significant. For instance, in any microscopic derivation of optical potential, channels with vector mesons are found to contribute significantly. When one looks at possible baryonia below the $\overline{\mathrm{N}}\mathrm{N}$ threshold, these channels are suppressed by simple phase-space considerations, and one is left with an absorption that is weaker than the one governing the scattering experiments. See, e.g., [250, 251]. In these references, it is remarked that if there are baryonia below the threshold, a fraction (with the largest range) of $\overline{\mathrm{N}}\mathrm{N}$ annihilation at rest goes through baryonium plus pion, and due to the lack of phase-space, this component of annihilation does not act on baryonium itself.

Explicit calculations of the $\overline{\mathrm{N}}\mathrm{N}$ spectrum with these refinements lead, indeed, to conclusions more moderate that these of Myhrer and Thomas. Most states are washed out by annihilation, but some moderately broad (50 MeV typically) structures survive, near the threshold and in some specific channels. See, for instance, Ref. [252].

Similar calculations have been carried out for $\overline{\mathrm{N}}\mathrm{N}$ resonances, i.e., baryonia above the threshold. Here, absorption corresponds to the actual annihilation. Moreover, elastic decay (into $\overline{\mathrm{N}}\mathrm{N}$) is sufficient to produce a large width as soon as one goes above threshold. Some plots are given in [247], where it is clear that the elastic width becomes very large as soon the resonance move above the threshold: narrow structures of $\overline{\mathrm{N}}\mathrm{N}$ type cannot exist for a centre-of-mass energy greater than 10 or $20\,\mathrm{MeV}$ above the threshold.

3.10 Colour chemistry

At the time when several candidates for baryonium were proposed, the quasi-nuclear approach, inspired by the deuteron described as a NN bound state, was seriously challenged by a direct quark picture. We define here baryonium as a meson with preferential coupling to baryon–antibaryon channels, and let theory propose either a quasi-nuclear model of baryonium or a multiquark picture.

Among the first contributions to multiquark spectroscopy, there is an interesting remark by Jaffe [253] that $\mathrm{q}^2\bar{\mathrm{q}}^2$ S-wave are not that high in the spectrum, and might even challenge P-wave $(\mathrm{q}\bar{\mathrm{q}})$ to describe scalar or tensor mesons. The debate is still open, and even more confused by the possible contributions of gluonia, hybrids or $(\mathrm{s}\bar{\mathrm{s}})$ configurations in these sectors, with many mixing scenarios.

It was then pointed out [254] that orbital excitations of these states, of the type (q^2)—$(\bar{\mathrm{q}}^2)$, have preferential coupling to $\overline{\mathrm{N}}\mathrm{N}$. Indeed, simple rearrangement into two $(\mathrm{q}\bar{\mathrm{q}})$ is suppressed by the orbital barrier, while the string can break into an additional $\mathrm{q}\bar{\mathrm{q}}$ pair, leading to (q^3) and $(\bar{\mathrm{q}}^3)$.

Chan H.M. and collaborators [255, 256] went a little further and speculated about possible internal excitations of the colour degree of freedom. When the diquark is in a colour $\bar{3}$ state, they obtained a so-called "true" baryonium, basically similar to the orbital resonances of Jaffe. However, if the diquark carries a colour 6 state (and the antidiquark a colour $\bar{6}$), then the "mock-baryonium", which still hardly decays into mesons, is also reluctant to decay into N and $\overline{\mathrm{N}}$, and thus is likely to be very narrow (a few MeV, perhaps).

This "colour chemistry" was rather fascinating. A problem, however, is that the clustering into diquarks is postulated instead of being established by a dynamical calculation. An analogous situation existed for orbital excitations of baryons: the equality of Regge slopes for meson and baryon trajectories is natural once one accepts that excited baryons consist of a quark and a diquark, the latter behaving as a colour $\bar{3}$ antiquark. The dynamical clustering of two of the three quarks in excited baryons was not shown before 1985 [257]. Diquark clustering is even more questionable for sextet

than for triplet states. If confinement has anything to do with colour, one naively expects forces to depend on the colour configuration. See, e.g., Ref. [258] for a discussion on mock-baryonium.

3.11 Introduction to antiprotonic hydrogen and deuterium

The lowest momenta for $\bar{\mathrm{p}}\mathrm{p}$ scattering are obtained by stopping antiprotons in hydrogen, by forming antiprotonic hydrogen atoms (called protonium) and by deducing from X-ray transitions the proton-antiproton scattering lengths. Protonium atoms possess several features in common with the well-known positronium atoms and the name "protonium" had been chosen to emphasise this similarity. Both systems consist of a particle and its antiparticle. In both cases, the constituents are intrinsically stable, but annihilate each on the other. Essential features of both positronium and protonium atoms can be understood from the *Bohr* formula. The energy levels E_n and classical radii r_n are functions of the principal quantum number n. The energy levels are proportional to the reduced mass m_{r}, which is the combination $m_1 m_2/(m_1+m_2)$ of the constituent masses m_i and is equal to $m_{\mathrm{p}}/2$ in case of protonium. The radii are inversely proportional to m_{r}:

$$E_n = -\frac{1}{2} m_{\mathrm{r}} c^2 \left(\frac{\alpha}{n}\right)^2 , \qquad r_n = \frac{\hbar c}{m_{\mathrm{r}} c^2} \frac{n^2}{\alpha} \cdot \tag{3.65}$$

Here, $\alpha = 1/137.036$ is the fine structure constant, and $\hbar c = 197.33\,\mathrm{MeV.\,fm}$. The first Bohr radius r_1 is often denoted as a_0 in the literature; we use a_0 for the S-wave scattering length. More specifically, for $\bar{\mathrm{p}}\mathrm{p}$ and $\bar{\mathrm{p}}\mathrm{d}$ atoms,

$$E_n(\bar{\mathrm{p}}\mathrm{p}) = -12.491\ \frac{1}{n^2}\,\mathrm{keV} , \qquad r_n(\bar{\mathrm{p}}\mathrm{p}) = 57.6\ n^2\,\mathrm{fm} , \tag{3.66}$$

$$E_n(\bar{\mathrm{p}}\mathrm{d}) = -16.653\ \frac{1}{n^2}\,\mathrm{keV} , \qquad r_n(\bar{\mathrm{p}}\mathrm{d}) = 43.2\ n^2\,\mathrm{fm} . \tag{3.67}$$

Corrections due to QED and relativistic effects have to be applied to find the true electromagnetic binding energies. They have been calculated to be

$$E(n,\ell) = E_n \left[1 + \left(\frac{\alpha}{n}\right)^2 \left(\frac{m_{\mathrm{r}}}{2(m_1+m_2)} - \frac{3}{4} + \frac{n}{\ell+1/2}(1+a_v+a_{lj})\right)\right] , \tag{3.68}$$

by Barmo *et al.* [259]. The values of a_v and a_{lj} are tabulated in this reference. The most important correction is due to vacuum polarisation which increases the binding energy of the $\bar{\mathrm{p}}\mathrm{p}$ atom by $42\,\mathrm{eV}$. The finite size of the proton makes a shift into the opposite direction, of $-3.2\,\mathrm{eV}$. In $\bar{\mathrm{p}}\mathrm{d}$ atoms, the vacuum polarisation of $67\,\mathrm{eV}$ is partly compensated by the finite size effect of $-48\,\mathrm{eV}$. The corrections were reevaluated recently [260]; in Table 3.3 we give final QED transition energies relevant for this review.

The QED fine-structure splittings of the 2P states are very small, of the order 100 meV. Strong interaction effects are – as we shall see – of the same order of magnitude. The level splittings of the higher-n levels are even smaller and not resolvable with present-day techniques. The transition energies listed in Table 3.3 are calculated using mean 3D-level energies, weighted with their statistical frequencies.

Figure 3.20 shows the energy levels of protonium and some radiative transitions. Of particular importance are transitions to the 1S ground state, often called *Lyman* series or K-line series. The $2\mathrm{P} \to 1\mathrm{S}$ transition is named Lyman-α or K_α line; its expected energy without corrections due to strong interactions is $9.406\,\mathrm{keV}$. The $3\mathrm{P} \to 1\mathrm{S}$ transition is called Lyman-β or K_β line, and its energy is $1.737\,\mathrm{keV}$ higher. The $4\mathrm{P} \to 1\mathrm{S}$ transition – the Lyman-γ or K_γ line – carries $2.345\,\mathrm{keV}$ more energy than the K_α line. The $n\mathrm{D} \to 2\mathrm{P}$ transitions are called *Balmer* series or L-series, with Greek suffixes $\alpha, \beta, \gamma, \delta, \ldots \infty$ to characterise individual lines. The *Paschen* series or M-series feeding the 3D levels has energies from $0.608\,\mathrm{keV}$ (M_α) to $1.389\,\mathrm{keV}$ (M_∞). Transitions of type

Table 3.3: QED transition energies in $\bar{\mathrm{p}}\mathrm{p}$ and $\bar{\mathrm{p}}\mathrm{d}$ atoms

$\bar{\mathrm{p}}\mathrm{p}$		$\bar{\mathrm{p}}\mathrm{d}$	
$2\mathrm{P}\rightarrow 1^3\mathrm{S}_1$	9405.7 eV	$2\mathrm{P}\rightarrow 1^4\mathrm{S}_{3/2}$	12505 eV
$2\mathrm{P}\rightarrow 1^1\mathrm{S}_0$	9405.7 eV	$2\mathrm{P}\rightarrow 1^2\mathrm{S}_{1/2}$	12505 eV
$3\mathrm{D}\rightarrow 2^3\mathrm{P}_2$	1736.79 eV	$3\mathrm{D}\rightarrow 2^4\mathrm{P}_{5/2}$	2316.48 eV
$3\mathrm{D}\rightarrow 2^3\mathrm{P}_1$	1736.85 eV	$3\mathrm{D}\rightarrow 2^4\mathrm{P}_{3/2}$	2316.38 eV
$3\mathrm{D}\rightarrow 2^3\mathrm{P}_0$	1737.00 eV	$3\mathrm{D}\rightarrow 2^4\mathrm{P}_{1/2}$	2316.46 eV
$3\mathrm{D}\rightarrow 2^1\mathrm{P}_1$	1736.70 eV	$3\mathrm{D}\rightarrow 2^2\mathrm{P}_{3/2}$	2316.52 eV
		$3\mathrm{D}\rightarrow 2^2\mathrm{P}_{1/2}$	2316.52 eV

$(n,\, \ell = n-1) \rightarrow (n-1,\, \ell = n-2)$ are called circular transitions. They take place between two atomic states with circular classical orbits. Transitions between states with smaller angular momenta are called parallel transitions. They play no significant role in the experiments which are described later in this review.

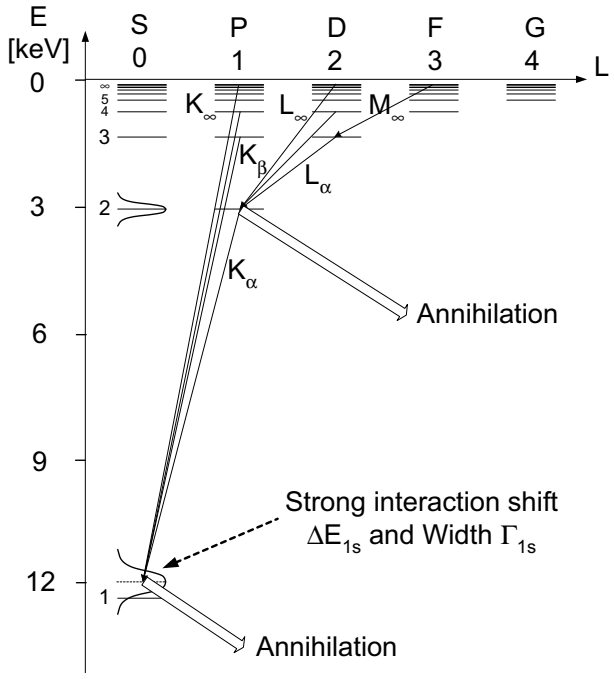

Figure 3.20: Energy levels of antiprotonic hydrogen atoms showing the definition of K, L, M series. Effects due to strong interactions are also indicated.

Of course, experiments on $\bar{\mathrm{p}}\mathrm{p}$ and $\bar{\mathrm{p}}\mathrm{d}$ atoms are carried out not to study quantum electrodynamics but strong interaction effects. Before discussing results it is useful to estimate the magnitude which we might expect for these effects. Strong interactions – given, e.g., by the widths of the $\Delta(1232)$ or the $\rho(770)$ – have a typical strength of 100–150 MeV. The pion mass μ_π appears as a natural scale parameter. In $\bar{\mathrm{p}}\mathrm{p}$ atoms, strong interactions are smaller due to the large volume of the $\bar{\mathrm{p}}\mathrm{p}$ atom. We

may expect hadronic shifts and half-widths to be of the order

$$\Delta E \sim \frac{1}{2}\Gamma \sim \frac{\mu_\pi}{n^3}\left(\frac{a_{\rm hadr}}{r_1}\right)^{2\ell+1} , \tag{3.69}$$

where $a_{\rm hadr} \sim 1\,{\rm fm}$ and r_1 is the first Bohr radius. The wave functions of atomic states have a tail

$$\Psi_n \propto \exp\left(-\sqrt{-2m_{\rm r}E_n}r/\hbar\right) , \tag{3.70}$$

i.e., extends in a volume that grows as n^3. This is why the density at short distances has a n^{-3} dependence, which will be made precise in Sec. 3.12.

In Table 3.4 we list the expected size of strong interaction parameters for the S-wave ground states, for the 2P states and for the 3D states, and a comparison with the radiative widths Γ_X, whose expression will be given below. We show the imaginary part of the energy shift, $\mathcal{I}{\rm m}(\Delta{\rm E}) = \Gamma/2$; the real part is expected to be of similar magnitude. The energy shift and width of the 1S states are directly measurable. A direct measurement of the 2P level width is not possible with conventional techniques like solid state detectors; the expected shifts and widths are, however, within the range of modern X-raydiffraction spectrometers. Strong interaction effects in the 3D and other $\ell \geq 2$ states are unmeasurably small, even when ${}^3{\rm D}_1$–${}^3{\rm S}_1$ mixing is taken into account [261]. This is why, once all relativistic and electromagnetic corrections are taken into account, the measured change of energy ϵ of photon transitions is identified with the shift of the lowest state in the transition, namely

$$\epsilon = -\Delta E . \tag{3.71}$$

The values given in Table (3.4) show that for P-levels of $\bar{\rm p}{\rm p}$ atoms, annihilation is expected to be more likely than emission of X rays by two orders of magnitude! In addition, collisions of the $\bar{\rm p}{\rm p}$ atom with neighbouring molecules will lead to premature annihilation reducing the yield of X-rayseven further. These two effects made experimental searches for ${\rm K}_\alpha$ radiation extremely difficult. The difficulties were only overcome when LEAR came into operation.

Table 3.4: Expected hadronic and radiative widths in $\bar{\rm p}{\rm p}$ atoms

Hadronic width			Radiative width
$\Gamma_{1{\rm S}}/2$	$\sim$	700 eV	stable
$\Gamma_{2{\rm P}}/2$	$\sim$	30 meV	$\Gamma_{\rm X} = 0.379\,{\rm meV}$
$\Gamma_{3{\rm D}}/2$	$\sim$	2 μeV	$\Gamma_{\rm X} = 38.9\,\mu{\rm eV}$

The width of the 2P levels can also be measured indirectly. The total intensity feeding one of the 2P levels is larger than the intensity of Lyman-α radiation. Protonium atoms in the 2P levels mostly annihilate instead of emitting ${\rm K}_\alpha$ radiation to the 1S ground state. The intensity balance of radiative transition and annihilation width can be determined from the yield $Y({\rm K}_\alpha)$ of ${\rm K}_\alpha$ radiation compared to the yield $Y({\rm L}_{\rm tot})$ with which the 2P levels are populated. This ratio is related to the radiative width Γ_X of the 2P fine structure levels and their annihilation widths $\Gamma({}^{2s+1}{\rm P}_J)$:

$$\begin{aligned} r &= \frac{Y({\rm K}_\alpha)}{Y({\rm L}_{\rm tot})} \\ &= \frac{\Gamma_X}{12}\left[\frac{3}{\Gamma_X+\Gamma({}^1{\rm P}_1)} + \frac{1}{\Gamma_X+\Gamma({}^3{\rm P}_0)} + \frac{3}{\Gamma_X+\Gamma({}^3{\rm P}_1)} + \frac{5}{\Gamma_X+\Gamma({}^3{\rm P}_2)}\right] . \end{aligned} \tag{3.72}$$

The equation assumes that the fine-structure levels are populated statistically. If the P-levels all have identical widths, the summation yields

$$Y({\rm K}_\alpha)/Y({\rm L}_{\rm tot}) = r' = \Gamma_X/(\overline{\Gamma}_{2{\rm P}} + \Gamma_X) , \tag{3.73}$$

from which $\overline{\Gamma}_{2\mathrm{P}}$ can be deduced. In both relations (3.72) and (3.73), it is tacitly assumed that parallel transitions $n\mathrm{P} \to 2\mathrm{S}$ do not contribute to $Y(\mathrm{L_{tot}})$. This assumption is justified by the preference of the protonium cascade to populate circular orbits.

3.12 Quantum mechanics of protonium

In this Section, we review how to calculate the properties of protonium in a given potential model. Some results hold beyond this particular framework. The energy shifts and widths can be computed with simple tools, like the Trueman formula. However, the microscopic calculation of branching ratios requires the knowledge of the wave function at short distances. One should thus solve accurately the wave equation with a superposition of long-range Coulombic and short-range nuclear potentials. The corrections due to relativity and QED and these due to strong interactions are essentially additive and thus can be computed independently. This is why we may use the Schrödinger framework to estimate the effect of strong interactions.

3.12.1 Results on pure Coulomb systems

Before introducing strong-interaction corrections at short distances, we recall here some useful results on pure Coulomb bound states.

Scaling

Any Coulomb problem with a reduced mass m_{r} and coupling e^2 in the potential $-e^2/r$ can be reduced to the case where $\hbar = 2m_{\mathrm{r}} = e^2 = 1$, for which the radial equation reads

$$u''_{n,\ell}(r) + \left[\frac{\ell(\ell+1)}{r^2} + E_n - \frac{1}{r}\right] u_{n,\ell}(r) = 0 \,, \tag{3.74}$$

with $E_n = -1/(4n^2)$. In the actual problem, the energy scale is $2m_{\mathrm{r}}e^4/\hbar^2$ and the unit of distance is $\hbar^2/(2m_{\mathrm{r}}e^2)$.

The radial wave function is defined as usual from the wave function by

$$\Psi_{n,\ell,m}(\vec{r}) = \frac{u_{n,\ell}(r)}{r}\, Y_\ell^m(\vartheta,\varphi) \,. \tag{3.75}$$

The normalised S-state wave function of principal quantum number n are given by

$$u_{n,0} = \frac{r\mathcal{L}(n-1,1,r/n)}{\sqrt{2n^5}}\, \exp\left(-\frac{r}{2n}\right) \,, \tag{3.76}$$

where $\mathcal{L}$ denotes a Laguerre polynomial.

The normalised P states are

$$u_{n,1} = \frac{r^2\mathcal{L}(n-2,3,r/n)}{\sqrt{2n^7(n^2-1)}}\, \exp\left(-\frac{r}{2n}\right) \,. \tag{3.77}$$

Radiative widths

De-excitation of highly-excited protonium states formed in vacuum occurs via radiative transitions. They populate preferentially "circular" states with maximum angular momentum $\ell = n-1$, since the angular momentum changes by one unit only, $\ell_f = \ell_i \pm 1$, while the transition probability increases with the energy difference ΔE_{if} between initial and final state:

$$\Gamma_{\mathrm{rad}} = \frac{4\alpha}{3\hbar}\frac{1}{m_p^2}\left(\Delta E_{if}\right)^3 \left(R_{n_i}^{n_f}\right)^2 \,, \tag{3.78}$$

with

$$R_{n_i}^{n_f} = \int_0^\infty u_{n_i,\ell_i}(r) u_{n_f,\ell_f}(r)\, r\, \mathrm{d}r \ . \tag{3.79}$$

Radiative transitions from high n, ℓ states are very slow; from the $n = 30$ level, the cascade time is of the order of μs.

Value at the origin

For S-states, Eqs. (3.75) and (3.76) imply

$$|\Psi_{n,0}(0)|^2 = \frac{|u'_{n,0}(0)|^2}{4\pi} = \frac{1}{8\pi n^3} \ . \tag{3.80}$$

For P states, the analogue is the second derivative of $u_{n,1}$, with the result

$$\left|u''_{n,1}(0)\right|^2 = \frac{n^2-1}{18n^5} \ . \tag{3.81}$$

Thus the annihilation widths are expected to scale as with principal quantum number according to

$$\begin{aligned} \Gamma_{n\mathrm{S}} &= \frac{1}{n^3}\Gamma_{1\mathrm{S}} \ , \\ \Gamma_{n\mathrm{P}} &= \frac{32}{3}\left(\frac{1}{n^3} - \frac{1}{n^5}\right)\Gamma_{2\mathrm{P}} \ . \end{aligned} \tag{3.82}$$

Eq. (3.80) can be derived from the Schwinger rule, which states that $u'_{n,0}(0)^2$ is proportional to the expectation value of the derivative of the potential [262]. Here, this derivative is $1/r^2$, and its expectation value is linked by the Feynmann–Hellmann theorem to the ℓ-dependence of the binding energy, $\langle r^{-2}\rangle \propto (\partial E_{n,\ell}/\partial\ell)_{\ell=0}$. For P-states, the derivation of Eq. (3.81) is a little more laborious.

Nodal structure

The structure of radial excitations is important, as annihilation often occurs from nP states with $n > 2$ rather than from 2P or from nS states with $n > 1$ rather than from the 1S ground state.

In a confining potential such as the harmonic oscillator $Kr^2/2$, the binding energy E_n increases with the number of nodes n and dominates the behaviour of the radial wave function u_n at short distances. In units where $K/2 = 2m_\mathrm{r}/\hbar^2 = 1$, the radial equation of S-states,

$$u''_n + (E_n - r^2)\, u_n = 0 \ , \tag{3.83}$$

gives energies $E_n = 3 + 2n$ and wave functions $u_n \propto \sin((3+2n)^{1/2} r)$ at large n and small r, i.e., more and more oscillations closer and closer to the origin as n increases.

The situation is different in the Coulomb case[4]. In Eq. (3.74), the binding energy $E_n = -1/(4n^2)$ becomes negligible compared to the Coulomb potential at short distances as n increases. For $\ell = 0$, the ground state $u_{1\mathrm{S}} \propto r\exp(-r/2)$ is nodeless and peaks at the Bohr radius which in our temporary units is $r_1 = 2$. The first excitation $u_{2\mathrm{S}} \propto r(4-r)\exp(-r/4)$ has a node at $b_2 = 4$, this ensuring the orthogonality with $u_{1\mathrm{S}}$. The first node b_n of $u_{n\mathrm{S}}$ should move to smaller r as n increases, from general principles. It quickly converges towards its $n \to \infty$ limit, which is $b_\infty \simeq 3.67$, corresponding to the first zero of a Bessel function that is solution of

$$u''_\infty(r) + u_\infty(r)/r = 0, \qquad u_\infty(0) = 0 \ . \tag{3.84}$$

This is illustrated in Fig. 3.21.

[4]We thank André Martin for an enlightening discussion on this point.

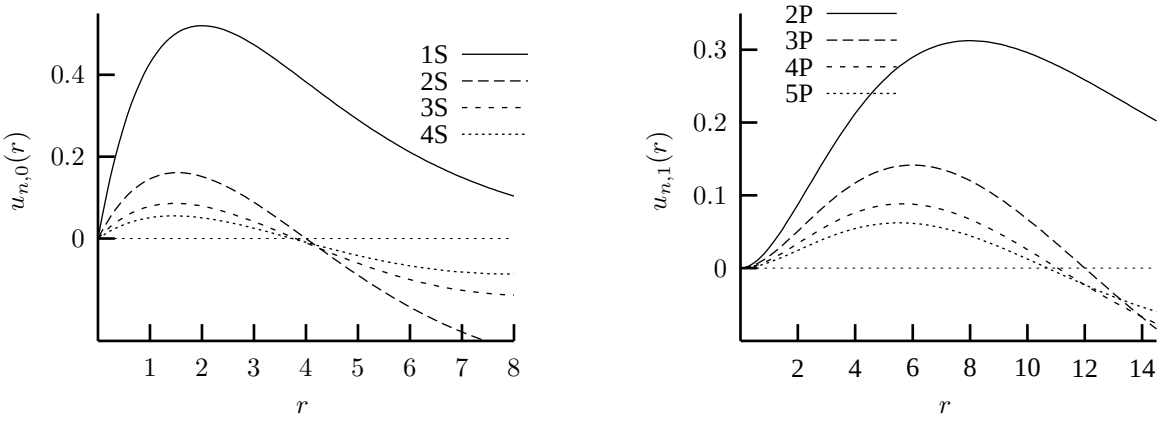

Figure 3.21: Radial wave functions $u_{n,0}(r)$ for $n = 1$ to $n = 4$ (left), and $u_{n,1}(r)$ for $n = 2$ to $n = 5$ (right). Natural units are used, so that the Bohr radius $r_1 \sim 50\,\mathrm{fm}$ corresponds to $r_1 = 2$.

For P states, $u_{2\mathrm{P}} \propto r^2 \exp(-r/4)$ is nodeless and peaks at $r = 8$. The first radial excitation, $u_{3\mathrm{P}} \propto r^2(r-12)\exp(-r/4)$ has a node at $b_3 = 12$. The first node moves to $b_4 \simeq 11.06$ for $n = 4$, then to $b_5 \simeq 10.71$, and quickly reaches its asymptotic value $b_\infty \simeq 10.18$, this again corresponding to a zero of a Bessel function. The first P-states are shown in Fig. 3.21.

In short, at small distances the radial functions exhibit a universal shape as n increases, besides the overall normalisation factor corresponding to $u'_{n,0}(0)$ and $u''_{n,1}(0)$. In particular, the nodes never reach the region of small r where one-pion-exchange and other strong interaction effects take place. We thus expect annihilation rates to exhibit a universal n^{-3} behaviour, and thus the branching ratios to be independent of n.

3.12.2 Hadronic widths and shifts

Simple Trueman formula

We have to study the changes that undergoes the solution of the radial equation

$$u''(r) - \frac{l(l+1)}{r^2}u(r) + 2m_{\mathrm{r}}(E-V)u(r) = 0\,, \tag{3.85}$$

where the pure Coulomb potential $V^{\mathrm{c}} = -\alpha/r$ is replaced by the total potential $V = V^{\mathrm{c}} + V^{\mathrm{n}}$ with a nuclear piece V^{n}. For protonium the reduced mass is $m_{\mathrm{r}} = m_{\mathrm{p}}/2$. One typically gets shifts of the order of $1\,\mathrm{keV}$ for the 1S level, small compared to the Bohr energy $E^{\mathrm{c}} = -12.49\ \mathrm{keV}$. This does not mean, however, that V^{n} can be treated perturbatively. A first order estimate,

$$\Delta E \equiv E - E^{\mathrm{c}} = \int_0^\infty u_{\mathrm{c}}(r)^2 V^{\mathrm{n}}\,\mathrm{d}r\,, \tag{3.86}$$

would overestimate $|\Delta E|$ by orders of magnitude! In the limit of a hard core of radius a, the integration (3.86) gives an infinite shift when one uses the undistorted wave function $u_{\mathrm{c}}(r)$ but vanishes exactly when $u_{\mathrm{c}}(r)$ is replaced by the "true" wave function $u(r)$, which vanishes for $r < a$.

The ordinary expansion in terms of powers of the additional potential is not applicable here. What is appropriate is the "radius perturbation theory" [263, 264], where the expansion parameter is the ratio a/r_1 of the scattering length a in the nuclear potential V^{n} to the Bohr radius r_1 of the atom. At first order, one gets the famous Trueman formula [263, 265], which reads

$$\Delta E = \frac{2\pi}{m_{\mathrm{r}}}\,|\Psi_{\mathrm{c}}(0)|^2\,\frac{a}{r_1}\,, \tag{3.87}$$

for S-wave states. There is an analogue for P-waves, where the first derivative of the radial wave function $\mathrm{d}u_\mathrm{c}(r)/\mathrm{d}r|_{r=0} = \sqrt{4\pi}\Psi_\mathrm{c}(0)$ is replaced by the second derivative and a by the scattering volume. A poor-man derivation is as follows. At zero energy, the nuclear potential is equivalent to a hard core of radius a, where a is the scattering length, first supposed to be real and positive and later on allowed to be negative or complex. The two radial wave-functions $u_\mathrm{c}(r)$ (pure Coulomb) and $u(r)$ (total) are submitted to the same equation with different boundary conditions

$$\begin{aligned} {u_\mathrm{c}}'' - \frac{l(l+1)}{r^2}u_\mathrm{c} + 2m_\mathrm{r}(E^\mathrm{c} - V^\mathrm{c})u_\mathrm{c} = 0\,, \qquad & u_\mathrm{c}(0) = u_\mathrm{c}(\infty) = 0\,, \\ u\ '' - \frac{l(l+1)}{r^2}u\ + 2m_\mathrm{r}(E\ - V^\mathrm{c})u\ = 0\,, \qquad & u\ (a) = u\ (\infty) = 0\,. \end{aligned} \tag{3.88}$$

For $r > a$, $u{u_\mathrm{c}}'' - u''u_\mathrm{c} = 2m_\mathrm{r}(\Delta E)uu_\mathrm{c}$, hence

$$\Delta E = \frac{1}{2m_\mathrm{r}} \frac{[u{u_\mathrm{c}}' - u'u_\mathrm{c}]_a^\infty}{\int_a^\infty uu_\mathrm{c}\mathrm{d}r}\,. \tag{3.89}$$

In first approximation, the denominator is equal to 1; $u'(a) = 2r_1^{-3/2}$ if one accepts that $u(r)$, at large distances, is nothing but $u_\mathrm{c}(r)$ translated by a (see Fig. 3.22); $u_\mathrm{c}'(a) = 2ar_1^{-3/2} + O(a^2/r_1^2)$. Then one gets the desired formula.

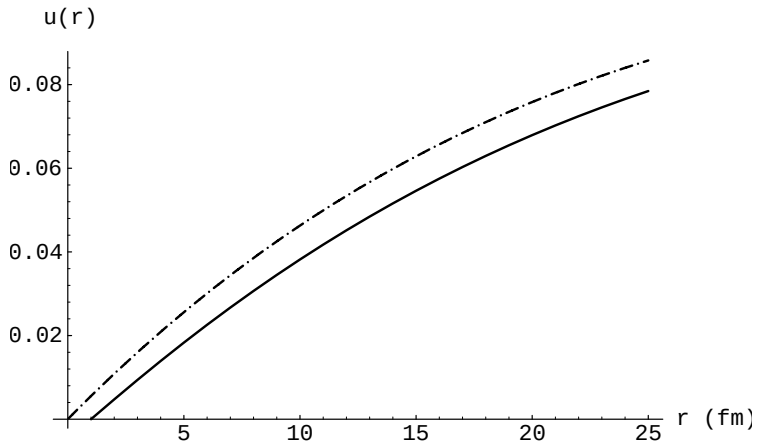

Figure 3.22: Comparison of the 1S radial wave functions with a pure Coulomb potential (u_c) and a Coulomb potential added to a hard core of radius $a = 1\,\mathrm{fm}$.

Improved Trueman formula

A more rigorous derivation makes use of the low-energy expansion of the scattering amplitude for $V = V^\mathrm{c} + V^\mathrm{n}$ and introduces the binding energy as a pole in this amplitude. This results into the more accurate formula

$$\Delta E = E_{n,\ell} - E^\mathrm{c}_{n,\ell} = -E^\mathrm{c}_{n,\ell}\left(\frac{4}{n}\right)\frac{a_\ell^\mathrm{sc}}{r_1^{2\ell+1}}\alpha_{n,\ell}\left(1 - \frac{a_\ell^\mathrm{sc}}{r_1^{2\ell+1}}\,\beta_{n,\ell} + \cdots\right)\,, \tag{3.90}$$

where

$$\alpha_{n,0} = 1\,, \qquad \alpha_{n,\ell} = \prod_{s=1}^{\ell}\left(\frac{1}{s^2} - \frac{1}{n^2}\right) \quad (\ell > 0)\,, \tag{3.91}$$

and the $\beta_{n,\ell}$ are numerical coefficients. For S and P waves, they take the values

$$\beta_{n,0} = 2\left(\log n + \frac{1}{n} - \Psi(n)\right) , \qquad \beta_{n,1} = \alpha_{n,1}\beta_{n,0} - \frac{4}{n^3} , \tag{3.92}$$

Ψ being the digamma function [266].

In Eq. 3.90, $a_\ell^{\rm sc}$ is the *Coulomb corrected* scattering length (volume, ...) for angular momentum ℓ. It is defined as usual from the low-energy expansion of the reaction matrix K as a function of the c.m. momentum p as

$$K^{-1}(p) = -\frac{1}{a_\ell} + \frac{\rho_\ell\, p^2}{2} + \cdots \tag{3.93}$$

Unlike the case of a short-range interaction, where $K^{-1} = p^{2\ell+1}\cot\delta_\ell(p)$, the Coulomb-corrected reaction matrix is defined as

$$K^{-1}(p) = p^{2\ell+1} g_\ell(\eta)\left[C_0^2(\eta)\cot\delta_\ell^{\rm sc}(p) + 2\eta h(\eta)\right] , \tag{3.94}$$

where $\eta = -1/(pr_1)$ is the Coulomb parameter, $\delta_\ell^{\rm sc}$ the Coulomb-corrected phase-shift (measuring the matching of the radial wave-function to the regular and irregular asymptotic Coulomb wave-functions), and

$$\begin{aligned} &g_0(\eta) = 1 , \\ &g_\ell(\eta) = \left[\frac{1}{(2\ell+1)!!}\right]^2 \prod_{s=1}^{\ell}\left(1+\frac{\eta^2}{s^2}\right) \quad (\ell = 1, 2\ldots) , \\ &C_0^2(\eta) = \frac{2\pi\eta}{\exp(2\pi\eta)-1} , \\ &h(\eta) = \frac{\Psi(i\eta) + \Psi(-i\eta) - \log(\eta^2)}{2} . \end{aligned} \tag{3.95}$$

Equation (3.90) gives the protonium energy level shifts as a function of the $\bar{\rm p}$p scattering length (or volume). See, e.g., [265, 267]

For illustration, we display in Fig. 3.23 the results obtained for a hard-core potential. Natural units are used, so the shift ΔE has to be compared to the unperturbed $E_1 = -1/4$, and a core of radius $1\,{\rm fm}$ corresponds to $a \simeq 0.04$ if the Bohr radius is $r_1 = 2$. The naive estimate is $a/2$ is improved into $a^{\rm c}/2$, in terms of the Coulomb corrected scattering length. The exact result is easily obtained: the energy is such that the Coulomb wave function with proper vanishing at large distance has a node at the border of the core.

In presence of Coulomb interaction, the S-wave scattering length is also related to the annihilation cross section at low energy by

$$p^2\sigma_{\rm ann}^{\rm sc}({\rm S\text{-}wave}) = \frac{8\pi^2}{1-\exp(2\pi\eta)}\,\frac{\mathcal{I}{\rm m}(-a_0^{\rm sc}/r_1)}{|1+ipw(\eta)a_0^{\rm sc}|^2} , \tag{3.96}$$

where $w(\eta) = C_0^2(\eta) - 2i\eta h(\eta)$.

Antiproton-proton interactions are known to have contributions from P-waves even at very low energies. This contribution can be obtained by replacing the scattering length $a_0^{\rm sc}$ by $a_1^{\rm sc}(1+\eta^2)p^2$ where $a_1^{\rm sc}$ is the corresponding P-wave spin averaged scattering volume [268]:

$$p^2\sigma_{\rm ann}^{\rm sc}({\rm P\text{-}wave}) = 24\pi^2\,\frac{1+1/\eta^2}{1-\exp(2\pi\eta)}\,\frac{\mathcal{I}{\rm m}(-a_1^{\rm sc}/r_1^3)}{|1-pw(\eta)(1+1/\eta^2)\,\mathcal{I}{\rm m}\,a_1^{\rm sc}/r_1^3|^2} . \tag{3.97}$$

There is some confusion in the literature about the validity of the Trueman formula, with a tentative clarification in a survey by Carbonell *et al.* [265]. We first note a lack of unified conventions for defining a, E, and ΔE. Secondly, there are claims for the Trueman formula being inaccurate.

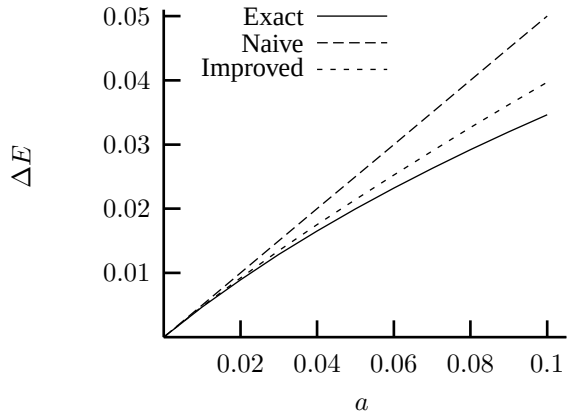

Figure 3.23: Comparison of the naive Trueman formula (3.87), the Coulomb-corrected formula (3.90) and the exact calculation for a hard core of radius a. Natural units are used.

The problem comes in fact from the Coulomb corrections to the scattering length, which are often omitted or badly computed. In particular, some popular prescriptions for calculating $a_\ell^{\rm sc} - a_\ell$ turn out to be inadequate [265]. In fact, once the Coulomb corrected scattering length $a_\ell^{\rm sc}$ is properly computed, the Trueman formula (3.90) turns out to be very precise.

Pathological cases

The most famous exception would be a situation where a nuclear bound state lies very close to the threshold. The scattering length becomes large and radius perturbation theory diverges. A first analysis of this situation is based on a potential [242, 269]

$$V(\lambda) = V^{\rm c} + \lambda V^{\rm n}, \tag{3.98}$$

where $V^{\rm c} = -\alpha/r$ is the usual Coulomb term and $V^{\rm n}$ the strong-interaction potential assumed to be real and attractive. Note that Zel'dovich's work [269] was inspired by a problem encountered in solid state physics.

For small values of the strength λ, the Coulomb spectrum is slightly shifted downwards. When λ approaches the critical value λ_0 for which $\lambda V^{\rm n}$ supports a bound state, there is a sudden change: the former atomic 1S state, in the keV range, becomes a nuclear state with binding energy in MeV or even tens or hundreds of MeV. The former 2S state quickly becomes what looks like a modified 1S state, with a node at short distance. Atomic spectroscopy shows a repulsive energy shift ΔE associated with an attractive potential! The observation of a positive value of $\Delta E_{1\rm S}$ may be the consequence of the strong binding force leading to nuclear bound states in the ${}^1{\rm S}_0$ and ${}^3{\rm S}_1$ partial waves!

In the transition region near λ_0, the spectrum is completely disorganised. If λ is further increased, the scattering length $a(\lambda)$ becomes negative again. Another sharp transition occurs at λ_1 for which $\lambda V^{\rm n}$ starts supporting a second bound state. This is illustrated in Fig. 3.24. It corresponds to a Wood–Saxon potential of depth $-V$ and radius $a = 0.04$ in natural units, i.e., about $1\,{\rm fm}$ for protonium.

In the actual situation, the short-range part includes a strong annihilation potential and mixes $\bar{\rm n}{\rm n}$ to $\bar{\rm p}{\rm p}$ in the wave function, so that the pattern is more involved than in the above models. Still, oscillations are seen in the protonium wave function at short distances [270], reminiscent of the nodes one gets with one-channel, real potentials.

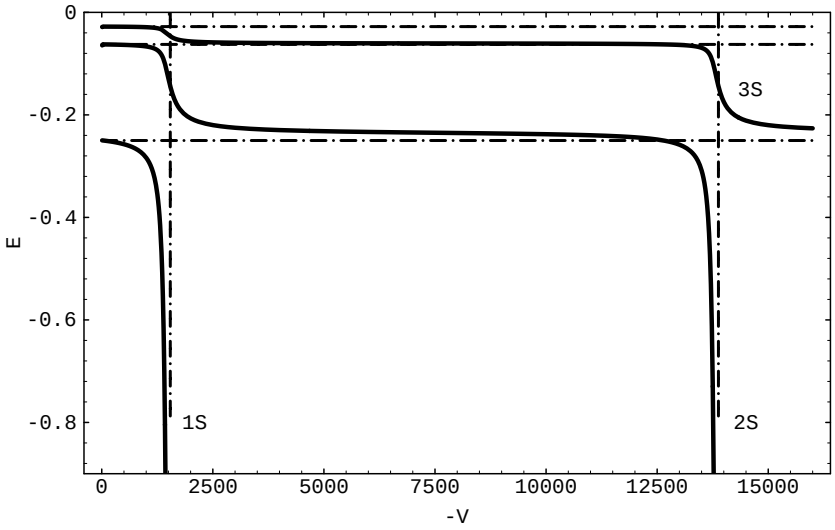

Figure 3.24: Energy levels of an atom for a Coulomb potential modified by a square-well of radius $a = 0.04$ and increasing depth V. Natural units are used, with the unperturbed 1S energy is $-1/4$ and the Bohr radius $r_1 = 2$. Also shown are the unperturbed levels 1S, 2S and 3S, and the critical value of the strength V for binding one or two S-states in the square well.

The role of absorption on the Zel'dovich–Shapiro rearrangement of atomic levels has been carefully studied by Gal et al. [271], who used an optical potential

$$V^{\rm n} \propto -(b_{\rm r} + ib_{\rm i})\varrho(r) \ , \tag{3.99}$$

where $\varrho(r)$ is a typical nuclear density. For very small $b_{\rm i}$, the rearrangement persists, though the real part of the energy changes less rapidly than in Fig. 3.24, which corresponds to $b_{\rm i} = 0$. When $b_{\rm i}$ increases, the rearrangement disappears: the nS level is "shaken" when $g_{\rm r}$ passes near its critical value, but the nS energy remains in the region of the unperturbed nS. In short, the "atomic" and the "nuclear" spectra become independent.

The numerical analysis of Ref. [271] has been checked analytically by Raina and Richard [272], who used a model where the Coulomb potential is supplemented by a point interaction. When the strength $g_{\rm r} - ig_{\rm i}$ of the point interaction is real, or when $g_{\rm i}$ is very weak, then the spectrum reproduces the Zel'dovich effect of Fig. 3.24, with however, only one nuclear bound state. For larger $g_{\rm i}$, the atomic spectrum, as a function of $g_{\rm r}$ is given is Fig. 3.25. The nuclear state, instead of being generated from the atomic spectrum as in Fig. 3.24, is disconnected [272].

Direct numerical estimate of the complex shift

Another approach to ΔE consists of solving directly Eq. (3.85) with appropriate numerical algorithms. One should only care that $V^{\rm c}$ and $V^{\rm n}$ require different meshes in the discretisation. A direct numerical method looks a little heavy if ΔE only is needed. However, it also provides the values of $u(r)$, and it is easily generalisable to the case of coupled equations. The first coupling one has to consider comes from charge exchange. Strong interactions contains a $\bar{\rm p}{\rm p} \to \bar{\rm n}{\rm n}$ component, and this results into the following equations [147], written here for ${}^1{\rm S}_0$.

$$\Psi = \frac{u(r)}{r}|\,\bar{\rm p}{\rm p}\rangle + \frac{w(r)}{r}|\,\bar{\rm n}{\rm n}\rangle \ , \tag{3.100}$$

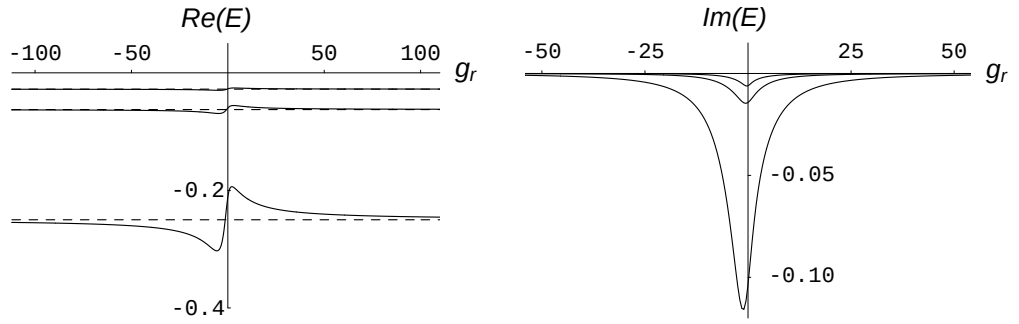

Figure 3.25: First levels of the atomic spectrum in a model with Coulomb potential and point interaction of strength $g_{\rm r} + ig_{\rm i}$, as a function of $g_{\rm r}$, for $g_{\rm i} = 5$.

$$\begin{aligned} u'' + 2m_{\rm r}\left[E + \frac{\alpha}{r} + V_{\bar{\rm p}{\rm p}}\right] u &= 2m_{\rm r} V_{\rm ce} w \,, \\ w'' + 2m_{\rm r}\left[E - 2\delta m + V_{\bar{\rm n}{\rm n}}\right] w &= 2m_{\rm r} V_{\rm ce} u \,, \end{aligned} \tag{3.101}$$

where $\delta m = m_{\rm n} - m_{\rm p}$ is the neutron-to-proton mass difference, and the nuclear potentials are $V_{\bar{\rm p}{\rm p}} = V_{\bar{\rm n}{\rm n}} = (V_0 + V_1)/2$ and $V_{\rm ce} = (V_1 - V_0)/2$ in terms of the potentials in isospin eigenstates. For $^1{\rm P}_1$ and $^3{\rm P}_0$ one gets the same equations with an orbital barrier $2/r^2$. For $^3{\rm S}_1$ and $^3{\rm P}_2$, one should also account for orbital mixing due to tensor forces and there are altogether four coupled equations.

Several authors have calculated the complex energy shifts of protonium, using a variety of realistic optical potentials. We reproduce in Table 3.5 part of the compilation by Carbonell *et al.* [265], for the Dover–Richard and Kohno–Weise potentials introduced earlier in this chapter.

A few comments are in order:

1. The calculated widths are of the order of magnitude expected from the very simple ansatz in Eq. (3.69).

2. There is reasonable agreement among the models and also, as we shall see in Chapter 6, with data.

3. The effect of orbital mixing (S–D or P–F mixing) is not dramatic.

The complex energy shifts is essentially equivalent to the (Coulomb corrected) scattering length or volume. Table 3.6 displays a partial compilation of scattering lengths.

Simple (i.e., not adjusted to the recent LEAR data) potential models tend to give similar predictions, which are in reasonable agreement with the protonium data, *via* the Trueman formula. Early potential models, such as BP, DR1,DR2 or KW in Table 3.6 had an isospin-independent annihilation. This seems sufficient to reproduce the main features of $\bar{\rm p}{\rm p}$ and $\bar{\rm p}{\rm p} \to \bar{\rm n}{\rm n}$ data. The work of [222,273] also include the constraint from $\bar{\rm n}{\rm p}$ absorption at low energy [274].

Spin-dependence of 2P shifts

The strong spin dependence of the $\overline{\rm N}{\rm N}$ interaction is responsible for the differences in Table 3.5 between the $^1{\rm P}_1$, $^3{\rm P}_0$, $^3{\rm P}_1$ and $^3{\rm P}_2$ energy shifts. There are also noticeable differences for the widths which can be understood in a simple semi-classical picture.

In Fig. 3.26 are shown the effective potentials (including the centrifugal barrier) for $^1{\rm P}_1$ and $^3{\rm P}_0$. It is clearly seen that tunnelling towards the annihilation region through the centrifugal barrier is much easier in the latter case.

Table 3.5: Energy shift and half-width, and ratio of $I = 1$ to $I = 0$ widths for the lowest states of protonium, as calculated from the Dover–Richard and Kohno–Weise potentials.

State	Units	Model	$\mathcal{R}\mathrm{e}(\Delta\mathrm{E})$	$\Gamma/2$	Γ_1/Γ_0	State	Units	Model	$\mathcal{R}\mathrm{e}(\Delta\mathrm{E})$	$\Gamma/2$	Γ_1/Γ_0
		DR1	0.54	0.51	0.68			DR1	–26	13	0.96
$1^1\mathrm{S}_0$	keV	DR2	0.58	0.52	0.80	$2^1\mathrm{P}_1$	meV	DR2	–24	14	0.61
		KW	0.50	0.63	0.68			KW	–29	13	0.82
		DR1	68	66	0.68			DR1	–74	57	0.03
$2^1\mathrm{S}_0$	eV	DR2	73	67	0.80	$2^3\mathrm{P}_0$	meV	DR2	–62	40	0.05
		KW	65	78	0.68			KW	–69	48	0.03
		DR1	0.77	0.45	0.79			DR1	36	10	9.4
$1^3\mathrm{SD}_1$	keV	DR2	0.82	0.46	0.79	$2^3\mathrm{P}_1$	meV	DR2	36	8.8	6.5
		KW	0.78	0.49	0.90			KW	29	11	9.7
								DR1	–4.8	15	0.63
						$2^3\mathrm{PF}_2$	meV	DR2	–5.9	16	0.66
								KW	–8.5	18	0.43

Table 3.6: Comparison of $\bar{\mathrm{p}}\mathrm{p}$ scattering lengths, computed from early potentials models: static Bryan–Phillips (BP), Dover, Richard and Sainio (DR1,DR2), Kohno and Weise (KW), Bydzovsky, Mach and Nichitiu (BMN), and from simple or more refined analyses of scattering data.

State	Source	Ref.	$\mathcal{R}\mathrm{e}(a_{\mathrm{sc}})$ (fm)	$\mathcal{I}\mathrm{m}(a_{\mathrm{sc}})$ (fm)
$^1\mathrm{S}_0$	pot. BP	[210]	1.10	-0.72
$^1\mathrm{S}_0$	pot. DR1	[265]	0.62	-0.63
$^1\mathrm{S}_0$	pot. DR2	[265]	0.68	-0.68
$^1\mathrm{S}_0$	pot. KW	[265]	0.57	-0.77
$^3\mathrm{SD}_1$	pot. BP	[210]	0.68	-0.85
$^3\mathrm{SD}_1$	pot. DR1	[265]	0.91	-0.57
$^3\mathrm{SD}_1$	pot. DR2	[265]	0.98	-0.59
$^3\mathrm{SD}_1$	pot. KW	[265]	0.92	-0.63
Average	pot. BMN	[222]	0.82	-0.67
Average	Eff. range exp.	[275]	0.1	-0.7
Average	Eff. range exp.	[273]	0.4	-0.6
Average	Eff. range exp.	[276]	0.6	-0.7
Average	Fit scatt. data	[277]	0.52	-0.56

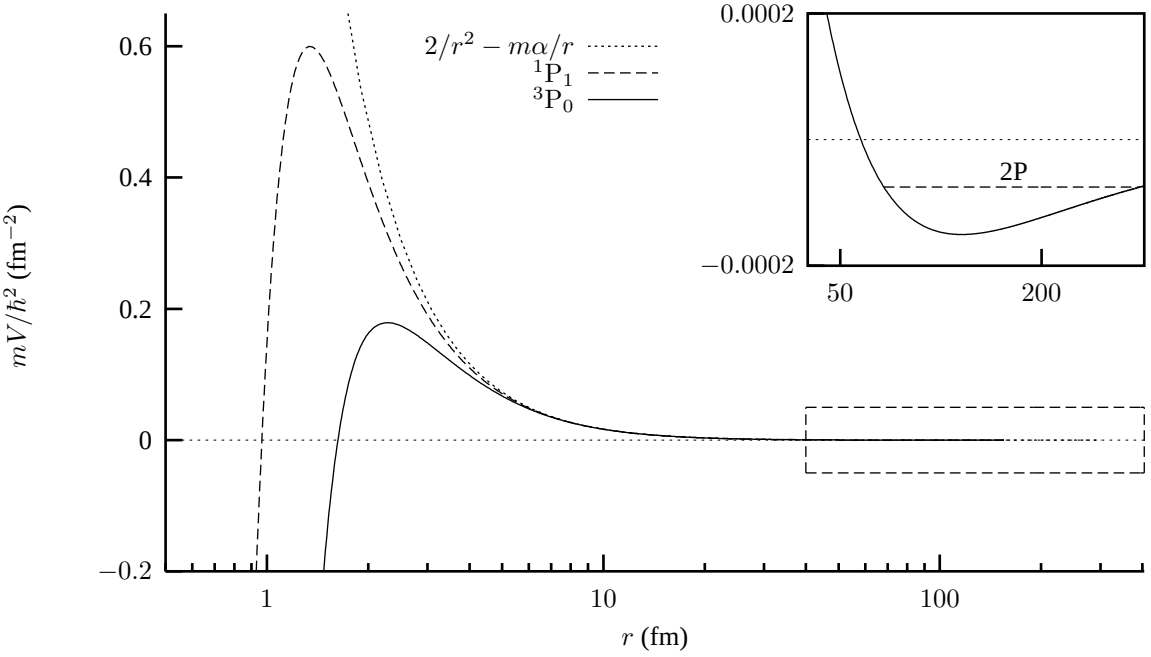

Figure 3.26: The P-wave effective radial potential is the sum of the Coulomb contribution and the centrifugal term (dotted line). It is supplemented by the $\bar{\mathrm{p}}\mathrm{p}$ strong potential (average of $I = 0$ and $I = 1$) shown here for the $^3\mathrm{P}_0$ (solid line) and $^1\mathrm{P}_1$ (dashed line) partial-waves. We use the Paris model, but the effect is largely model-independent, since dominated by pion-exchange. Annihilation proceeds by tunnelling between the Coulomb attractive tail (magnified in the insert) and the short-range region. The height and width of the barrier depends dramatically on the quantum numbers.

3.12.3 Isospin mixing

Optical potentials include an isovector part, in particular pion exchange, leading to isospin mixing in the protonium wave functions at small distances.

The isospin content, as defined in Eq. (3.100), can be recombined into

$$\Psi = u_1 |\, I = 1\rangle + u_0 |\, I = 0\rangle \;, \tag{3.102}$$

with

$$u_1 = \frac{u(r) + w(r)}{\sqrt{2}} \;, \qquad u_0 = \frac{u(r) - w(r)}{\sqrt{2}} \;. \tag{3.103}$$

Assuming an overall normalisation

$$\int_0^\infty \left(|u_0(r)|^2 + |u_1(r)|^2 \right) \mathrm{d}r = 1 \;, \tag{3.104}$$

the annihilation width in isospin I can be computed as

$$\Gamma_I = -2 \int_0^\infty \mathcal{I}\mathrm{m}\, V_I(r)\, |u_I(r)|^2 \, \mathrm{d}r \;. \tag{3.105}$$

This was done by Kaufmann and Pilkhun [147], Richard and Sainio [220], Gutsche et al. [278], and others. Carbonell *et al.* [265] have estimated the ratio of the integrated isovector to isoscalar annihilation widths Γ_1/Γ_0 with various potentials. Their results are reproduced in Table 3.5.

The differences between the $I = 0$ and $I = 1$ components of the $^3\mathrm{P}_0$ width can be understood from Fig. 3.27. The meson exchange potential is attractive for $I = 0$ and repulsive for $I = 1$. So the tunnelling from the Coulomb attraction to the annihilation region is much easier for $I = 0$ than for $I = 1$.

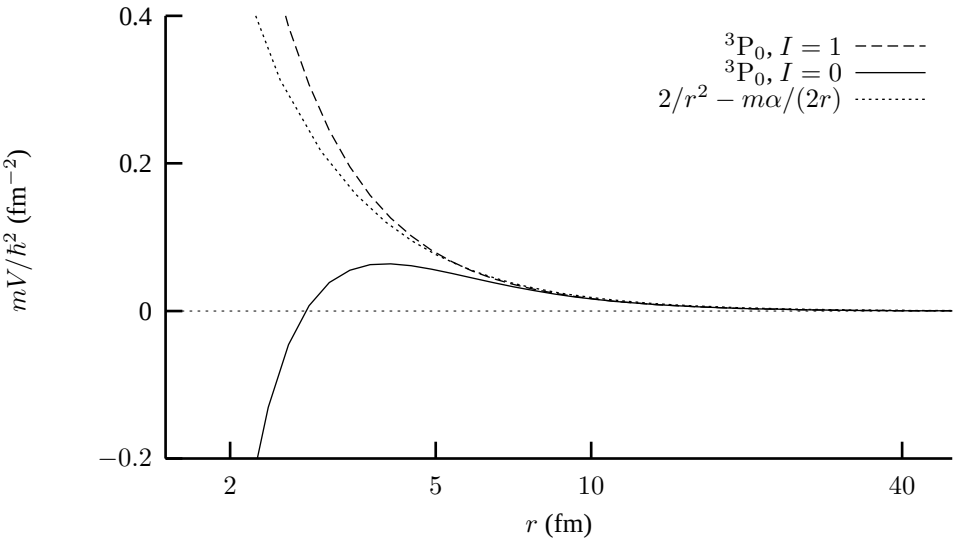

Figure 3.27: Effective radial potential, sum of the Coulomb, centrifugal and strong-interaction contributions, for the $I = 0$ and $I = 1$ components of the $^3\mathrm{P}_0$ partial wave. The dotted line is obtained when strong interaction is switched off. The Paris model is used, but the isospin dependence is largely model-independent, since dominated by one-pion exchange. Note that the Coulomb potential has also off-diagonal components in this isospin basis.

Remarks are in order:

1. Isospin mixing ($\bar{\mathrm{n}}\mathrm{n}$ admixture) has no significant impact on the complex energy shift. But very important effects are predicted for the wave function, and hence for the annihilation properties.

2. The isospin-mixing effects are particularly large for two levels, the $2^3\mathrm{P}_0$ state which is predicted to be an almost pure isoscalar state, and the $2^3\mathrm{P}_1$ state which is dominantly of isovector character.

Chapter 4

Antinucleon–nucleon scattering data

In this chapter we highlight the salient features of scattering data. We do not attempt to collect all pieces of the available experimental information, nor even to list all relevant references in the bibliography. One can refer for instance to the papers by Timmermans et al. [279], and Pignone et al. [277], which contain a comprehensive bibliography (we shall comment the corresponding analyses in Chapter 6). Most pre-LEAR data are reviewed in the 1984 compilation by the High-Energy Reactions Analysis Group [280]. There have been $\overline{\mathrm{N}}\mathrm{N}$ scattering experiments performed at KEK, BNL, FNAL and CERN. Some results of these experiments will be presented in the next sections, together with the results of the LEAR experiments. Their technical aspects were described in Chapter 2.

4.1 Integrated cross-sections

4.1.1 $\bar{\mathrm{p}}\mathrm{p}$ cross-sections

Some representative measurements of the $\bar{\mathrm{p}}\mathrm{p}$ total, annihilation, elastic, and charge-exchange integrated cross-sections are shown in Fig. 4.1 as a function of the $\bar{\mathrm{p}}$ incident momentum.

The data are from:

- Total cross-section:
  - Experiment PS172 [77, 78]. The systematic and statistical errors are added quadratically; in addition there is an overall normalisation error of 0.7 to 0.9% at higher $\bar{\mathrm{p}}$ momenta.
  - Experiment PS173 [92, 93]. Systematic errors were not quoted separately; the data are from the ρ-parameter measurement.
  - Hamilton et al. [281] (BNL AGS). The quoted absolute normalisation uncertainty is 1.5%; the relative difference with the PS172 data [77] is about 3.4%.
  - Ganguli et al. [282] (CERN PS). The systematic errors, estimated to 2 mb, have not been added.

  Among the data sets which are not shown one may mention:
  - Nakamura et al. [283] (KEK), in agreement with Hamilton et al. [281] data. The relative difference with the PS172 data [77] is about 4.3%.
  - Chaloupka et al. [284] (CERN PS, a bubble chamber experiment), in agreement with Hamilton et al. [281], plus evidence for the S meson.

- Annihilation cross-section:
  - Experiment PS173 [90]. The systematic and statistical errors are added quadratically; the quoted overall normalisation error varied from 2.2 to 4.4%. A correction for annihilation in all-neutral channels (+3.0%$\pm$1.1% at 297 MeV/c) was applied.

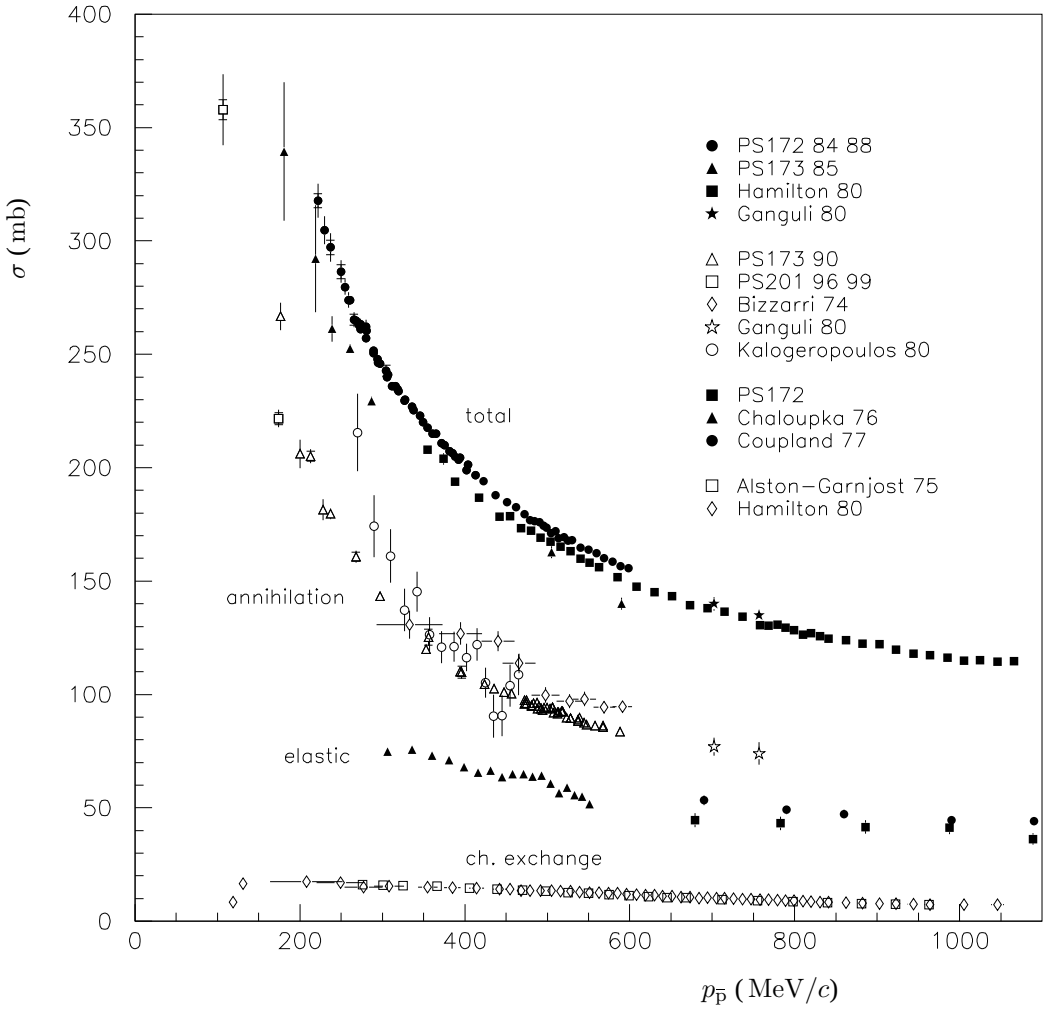

Figure 4.1: Representative $\bar{p}p$ total, annihilation, elastic, and charge-exchange cross-section data versus the incoming antiproton momentum.

- Experiment PS201 [96,97]. The systematic and statistical errors are added quadratically; for the two sets of data the quoted normalisation errors are 3.2 and 2% respectively.

- Bizzarri et al. [285] (CERN PS, a bubble chamber experiment). The values were extracted from $\bar{p}d$ annihilation data, looking for events with even or 0 prongs (i.e., charged mesons) in the final state, without corrections for "shadowing" nor charge-exchange events. The contribution of the charge-exchange cross-section was estimated to be about 9%.

- Ganguli et al. [282]. The data were obtained from their total cross-section measurements, subtracting the interpolated measurements of the elastic and charge-exchange cross-section from Coupland et al. [286] and Alston-Garnjost et al. [287].

- Kalogeropoulos–Tzanakos [288] (BNL). The values were extracted from $\bar{p}d$ annihilation data, looking for events with even or 0 prongs in the final state, without corrections for "shadowing" nor charge-exchange events.

Other data exist, but are not shown in the figure:

- Chaloupka et al. [284];

- Brando et al. [289] (BNL AGS). They measured several points from 308 to 591 MeV/c; the normalisation is from previous published data;

- Hamilton et al. [281]. They measured several points at closely spaced $\bar{\mathrm{p}}$ momenta in the range 355 to 1066 MeV/c; the measured annihilation cross-sections into charged particles are not corrected for background from large angle $\bar{\mathrm{p}}\mathrm{p}$ elastic scattering and neutral interactions in the veto box.

- Elastic cross-section:

  - Experiment PS172 [86]. The integrated elastic $\bar{\mathrm{p}}\mathrm{p}$ cross-sections were estimated by fitting the differential cross-section data with Legendre Polynomials; the quoted normalisation error is about 10%.

  - Chaloupka et al. [284].

  - Coupland et al. [286]. The measurement was obtained from the Eisenhandler et al. [290] differential cross-section data; the quoted normalisation error is 4%.

- Charge-exchange cross-section:

  - Alston-Garnjost et al. [287] (BNL AGS). The quoted systematic error varies from 5% (higher momenta) to 10% and it is mainly due to the absorption correction.

  - Hamilton et al. [291] (BNL AGS). The quoted systematic error varies from 3% (higher momenta) to 5%. The point to point uncertainty is less than 1%. For the two lowest momentum points large uncertainties exist in the mean interaction momentum.

  Not shown in the figure are the data from Cutts et al. [292], in agreement with the other measurements, but probably with large systematic errors.

Comments on those integrated cross-sections are in order:

i) The total cross-section shows the $1/k^2$ behaviour, typical of diffraction.

ii) The cross-sections are large. This is due to the long-range interaction. A simple black disk would be restricted by its own size ($2\pi(\hbar/m_\pi\, c)^2 \simeq$120 mb).

iii) The annihilation cross-section σ_{ann} is larger than the elastic one, σ_{el}. A black disk would give comparable σ_{ann} and σ_{el}, a result reminiscent from the Babinet theorem in optics. Again, we have a combined effect of the strong absorption, and of long-range forces [29]: the latter focuses the wave function towards the short-distance region where the former act. This is tentatively realized in optical models with real and imaginary components, and in some boundary-condition models, to be discussed in the next chapter.

iv) As mentioned in section 3.8, the integrated cross-sections can be reproduced in potential models provided the annihilation potential is strong enough up to $0.8 - 1\,\mathrm{fm}$. If the range is smaller one can obtain the correct values at one energy by adjusting the strength of $\mathcal{I}\mathrm{m}\, V$, but the energy dependence of the cross-section will not be reproduced.

v) The charge-exchange cross-section provides the strongest constraint on the strength of the potential. Since $\sigma_{\mathrm{ce}} = |\mathcal{T}_{I=0} - \mathcal{T}_{I=1}|^2$ a dramatic cancellation occurs, and the cross-section is only due to the tail of π- and ρ-exchange. With isovector-exchange only, the two isospin amplitudes would have opposite signs, and thus add coherently, leading to a charge-exchange cross-section four times larger than the elastic one! Such a coherence presumably holds for the high partial-waves, which are dominated by one-pion exchange. To get a small cross-section, one needs an effective cancellation between the $I = 1$ and $I = 0$ amplitudes in the low partial waves. This reflects that annihilation is almost isospin blind. This is probably not accidental. As there are many contributions to short-range annihilation, the equality of the two isospin amplitudes should reflect a kind of symmetry.

vi) Structures have been sometimes seen when scanning the cross-sections as a function of the incoming energy $\sqrt{s}$, and tentatively interpreted as $\overline{\mathrm{N}}\mathrm{N}$ or $\mathrm{qq}\bar{\mathrm{q}}\bar{\mathrm{q}}$ type of baryonium. They are not confirmed by the most recent measurements. The most famous baryonium candidate was the S(1936),

searched for with detailed cross-section scans around an incident $\bar{\mathrm{p}}$ momentum of 500 MeV/c. The latest experiments did not confirm the original observations (for a review see [293]).

vii) As experiments have been done with unpolarised beams and targets, or with at most a polarised target, no information on $\Delta\sigma_{\mathrm{L}} = \sigma_{\rightleftarrows} - \sigma_{\rightrightarrows}$ nor on $\Delta\sigma_{\mathrm{T}} = \sigma_{\uparrow\downarrow} - \sigma_{\uparrow\uparrow}$ exists. If one of these $\Delta\sigma$ is large, one could use a polarised proton target to filter one spin component, and possibly get a polarised $\bar{\mathrm{p}}$ beam [71].

The low energy data of the $\bar{\mathrm{p}}\mathrm{p}$ total and annihilation cross-sections are shown in Fig. 4.2(a). Figure 4.2(b) shows the behaviour of $\beta\,\sigma$. To be noticed, the very fast rise of the annihilation cross-

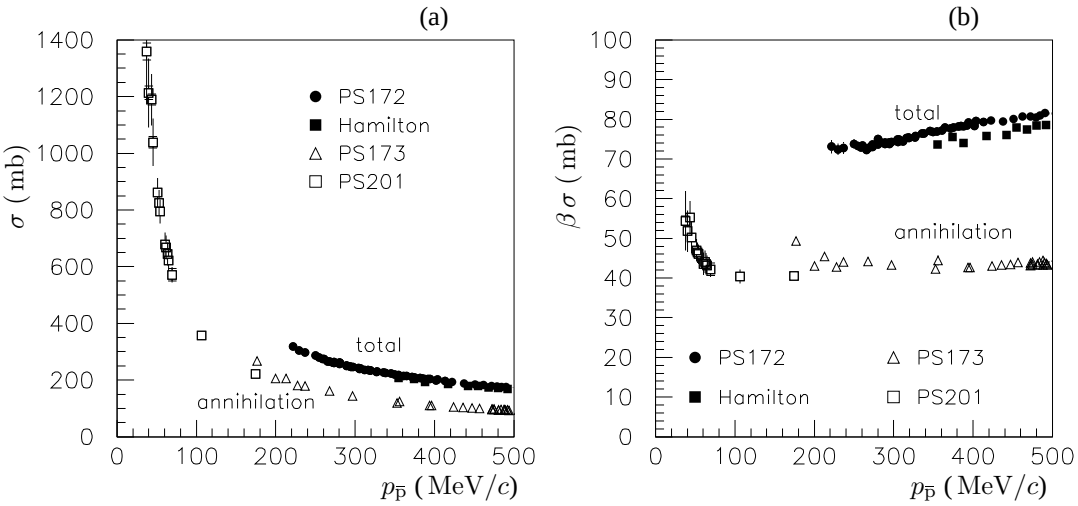

Figure 4.2: $\bar{\mathrm{p}}\mathrm{p}$ total and annihilation cross-section data (a) and the corresponding $\beta\,\sigma$ values (b) versus the incoming antiproton momentum.

section for momenta smaller than 100 MeV/c. From general principles [294] it was known that the total reaction cross-section near threshold in a hadronic system with Coulomb attraction should have exhibited a $1/v^2$ behaviour, v being the velocity of the incident particle. Figure 4.2(b) shows the behaviour of $\beta\,\sigma$: the very low momentum PS201 data indeed show very clearly the breakdown of the $1/v$ law and the onset of this new regime, and agree with the theoretical expectation [295].

4.1.2 $\bar{\mathrm{n}}\mathrm{p}$ and $\bar{\mathrm{p}}\mathrm{n}$ cross-sections

For obvious experimental reasons, the data are much poorer in the $I = 1$ sector, corresponding to $\bar{\mathrm{p}}\mathrm{n}$ or $\bar{\mathrm{n}}\mathrm{p}$ scattering.

Very few data exist in the $\bar{\mathrm{p}}\mathrm{n}$ channel, from the pre-LEAR period. They are extracted from $\bar{\mathrm{p}}\mathrm{d}$ measurements with bubble chambers. In Fig. 4.3, the $\bar{\mathrm{p}}\mathrm{n}$ data from:

- Bizzarri et al. [285] (The values were extracted from $\bar{\mathrm{p}}\mathrm{d}$ annihilation data, looking for events with an odd number of prongs in the final state.)

- Kalogeropoulos-Tzanakos [288] (The same technique was used.)

are compared with the $\bar{\mathrm{n}}\mathrm{p}$ annihilation cross-section from PS201 [103].

The $\bar{\mathrm{n}}\mathrm{p}$ total and annihilation (no elastic data exist) cross-sections are shown in Fig. 4.4 (a) and (b) as a function of the $\bar{\mathrm{n}}$ incident momenta. The data are from:

- Total cross-section:

  - Experiment PS201 [100]. The systematic and statistical errors are added quadratically; no normalisation error is quoted.

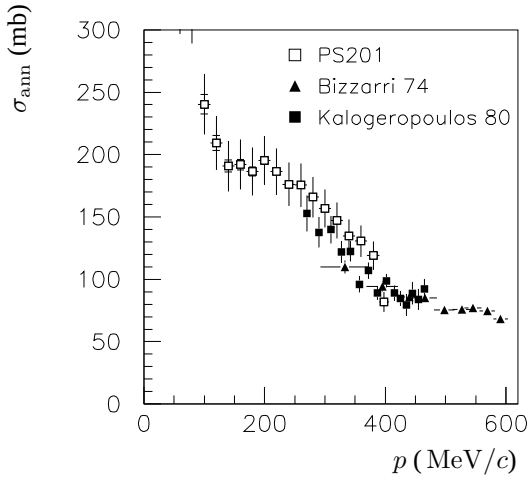

Figure 4.3: The $\bar{\rm n}{\rm p}$ (open points) and the $\bar{\rm p}{\rm n}$ (closed points) annihilation cross-sections versus the incoming antinucleon momentum.

- Armstrong et al. [101]. The total $\bar{\rm n}{\rm p}$ cross-section was measured using the transmission method. The $\bar{\rm n}$ were produced by $\bar{\rm p}{\rm p}$ charge-exchange reaction on scintillation counters. The systematic and statistical errors added quadratically in the figure.

- Annihilation cross-section:

  - Experiment PS201 [103] The systematic and statistical errors are added quadratically; the quoted normalisation errors are about 10%.

  - Armstrong et al. [101]. The annihilation cross-section was obtained from the total cross-section by subtracting the elastic cross-section, evaluated using a parametrisation from the potential model of Ref. [211].

While the $\bar{\rm n}{\rm p}$ total cross-section data from PS201 and Armstrong et al. are in fair agreement, the more precise annihilation cross-section data do not agree, and in the low momentum end ($\sim 100\,{\rm MeV}/c$) the PS201 data suggest rather low values. The different behaviour of the data is even more apparent in Fig. 4.5, where the quantities $\beta\,\sigma_{\rm tot}$ and $\beta\,\sigma_{\rm ann}$ are plotted: while the $\beta\,\sigma_{\rm ann}$ data of Armstrong et al. are consistent with a constant value of about $40\,{\rm mb}$, similar to the $\bar{\rm p}{\rm p}$ case, the more precise PS201 data show a strong decrease at small momentum, and deviate from the $1/v$ law.

The authors of Ref. [100] were not able to describe both their $\sigma_{\rm tot}$ and $\sigma_{\rm el}$ data with an effective-range-expansion technique. While the fits give good results when applied to either set of data, no parameters could be found to fit simultaneously the two sets. They interpret this situation as being due to an anomalous energy behaviour of $\sigma_{\rm el}(\bar{\rm n}{\rm p}) = \sigma_{\rm tot}(\bar{\rm n}{\rm p}) - \sigma_{\rm ann}(\bar{\rm n}{\rm p})$, which shows a profound dip in the momentum range 60 to $90\,{\rm MeV}/c$. They tentatively relate this anomaly to the presence of a near-threshold resonance, and have proposed a new set of measurements of the elastic $\bar{\rm p}{\rm p}$ cross-section at the CERN Antiproton Decelerator [296].

4.1.3 Comparison of $\bar{\rm p}{\rm p}$ and $\bar{\rm n}{\rm p}$ cross-sections

All available $\bar{\rm n}{\rm p}$ cross-section data are compared with the corresponding $\bar{\rm p}{\rm p}$ data in Fig. 4.6: in (a) and (b), the $\bar{\rm p}{\rm p}$ total cross-section results are from experiment PS172 [77,78], and the corresponding $\bar{\rm n}{\rm p}$ data from experiment PS201 [100] and from Armstrong et al. [101], respectively; in (c) and (d), the $\bar{\rm p}{\rm p}$ annihilation cross-section from experiment PS173 [90] and PS201 [96,97] are compared with the $\bar{\rm n}{\rm p}$ annihilation cross-section data from experiment PS201 [103].

The rough equality of the $\bar{\rm p}{\rm p}$ and $\bar{\rm n}{\rm p}$ cross-sections, like the smallness of the $\bar{\rm p}{\rm p} \to \bar{\rm n}{\rm n}$ cross-section, hints at the fact that annihilation is almost isospin independent. A closer look at the total

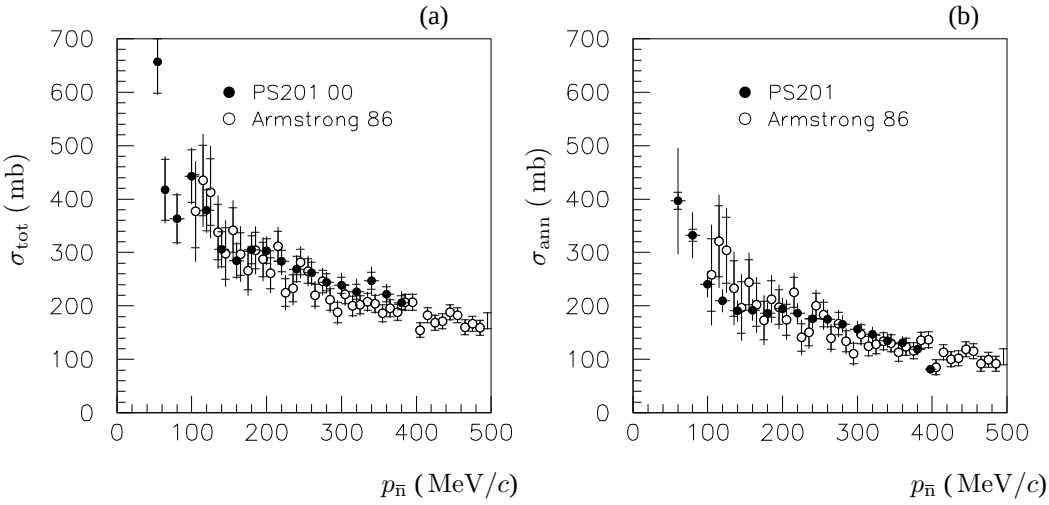

Figure 4.4: The $\bar{\rm n}$p total (a) and annihilation (b) cross-sections $\sigma_{\rm tot}$ and $\sigma_{\rm ann}$ versus the incoming antineutron momentum.

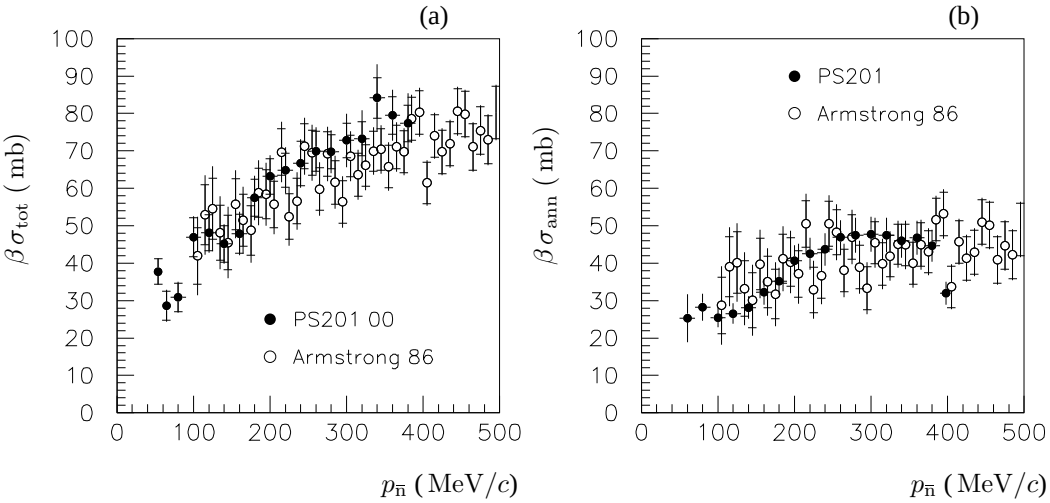

Figure 4.5: The $\bar{\rm n}$p $\beta\sigma_{\rm tot}$ (a) and $\beta\sigma_{\rm ann}$ (b) measured values versus the incoming antineutron momentum.

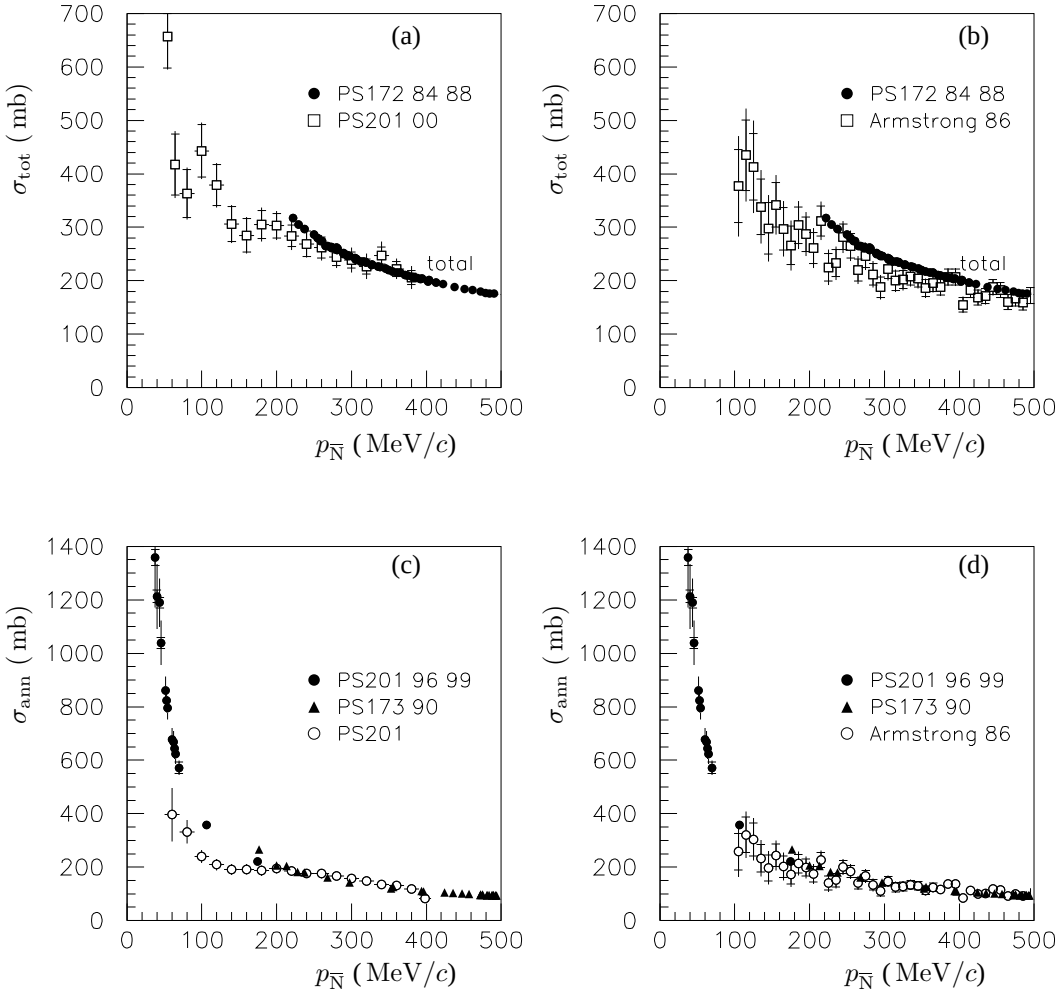

Figure 4.6: Comparison between the $\bar{\rm p}$p (black points) and the $\bar{\rm n}$p (open points) total (a and b) and annihilation (c and d) cross-sections.

cross-sections suggests somewhat smaller values for the $\bar{\mathrm{n}}\mathrm{p}$ cross-section, although, in the overlap region with the $\bar{\mathrm{p}}\mathrm{p}$ measurements, the effect seems to be smaller for the PS201 data.

In the case of annihilation data, while there is essentially equality between the Armstrong et al. $\bar{\mathrm{n}}\mathrm{p}$ data and the $\bar{\mathrm{p}}\mathrm{p}$ data, a strong effect is visible in the low momentum region of the PS201 data, around 100 MeV/c. In this region the $\bar{\mathrm{n}}\mathrm{p}$ annihilation cross-section is measured to be only 2/3 of the corresponding $\bar{\mathrm{p}}\mathrm{p}$ cross-section. It has to be mentioned that data from $\bar{\mathrm{p}}$-nucleus experiments also suggest that the $\bar{\mathrm{p}}\mathrm{n}$ annihilation cross-section is appreciably weaker than the $\bar{\mathrm{p}}\mathrm{p}$ one [297, 298].

4.2 $\bar{\mathrm{p}}\mathrm{p}$ elastic scattering differential cross-sections

Many precise measurements existed for the $\bar{\mathrm{p}}\mathrm{p}$ elastic scattering differential cross-section even before LEAR entered into operation, but mostly at momenta of about 600 MeV/c or larger. For this reason only one experiment (PS173) was proposed at LEAR to measure the $\bar{\mathrm{p}}\mathrm{p}$ differential cross-section, and it was especially designed to measure at incident momenta lower than 600 MeV/c. Also the experiments PS172 and PS198 produced $\bar{\mathrm{p}}\mathrm{p}$ elastic scattering differential cross-section data, but they were obtained while measuring, with a polarised target, the analysing power A_{0n}. As a consequence, some of the most precise data are still non-LEAR data.

4.2.1 Shape

Figure 4.7 shows a collection of data from many experiments, extending from the lowest momentum (181 MeV/c) to 1400 MeV/c. Almost the entire angular range is covered by each measurement. The two low-energy data sets are from experiment PS173 [91, 92]; at 287 MeV/c they are compared with the pp data of Batty et al. [299] (open points). The PS173 data at 505 MeV/c are compared with the Sakamoto et al. data [300] at $504.7\,\mathrm{MeV}/c$ (open points). The data at 439 MeV/c are from experiment PS198 [107], as well as the data at 697 MeV/c [106], which are compared with the data at 679 MeV/c [86] from experiment PS172 (closed points). The data at 790 and 990 MeV/c are from Eisenhandler et al. [290]. Data from Sakamoto et al. and from Eisenhandler et al. exist also at many other values of the incident $\bar{\mathrm{p}}$ momentum.

The sharp rise of the cross-section in the forward direction, visible in the data at the two lowest energies, is due to Coulomb scattering, and will be discussed in the next section.

Even the low energy $\bar{\mathrm{p}}\mathrm{p}$ data show a strong angular dependence, not present in the pp case. For comparison, the data at 287 MeV/c (about 50 MeV kinetic energy) are plotted together with the corresponding pp data at the same energy. The pp data are essentially isotropic, corresponding to S-wave scattering, while the $\bar{\mathrm{p}}\mathrm{p}$ data show a strong P-wave component.

Some insight into the behaviour of the elastic scattering differential cross-section can be obtained by neglecting the spin and performing a simplified partial wave analysis, as in Ref. [91, 301]. This analysis is possible only at low energy, where few partial waves are present; in Ref. [91, 301] only data at incident $\bar{\mathrm{p}}$ momenta less than 300 MeV/c were used. Important results of this analysis are that

- the S-wave elastic cross-section is suppressed (η_0, the absorption coefficient, is about 0.5): on the contrary, the S-wave inelastic cross-section is close to its geometrical limit;
- the P-wave is large, and is present even at the lowest measured momentum (181 MeV/c).

The question whether the relative strength of the P-wave is only due to the suppression of the S-wave has been discussed in the literature. The general understanding is that one observes a strong P-wave enhancement, as a direct consequence of the nuclear interaction, and not necessarily related to the strong S-wave annihilation. For the authors of Ref. [240, 302], the main reason for this enhancement is the existence of near-threshold bound or resonance states, due to the strong attractive nuclear forces between N and $\overline{\mathrm{N}}$. Indeed, switching off the annihilation, the P-wave contribution to the $\bar{\mathrm{p}}\mathrm{p}$ elastic scattering is even larger than in the presence of annihilation. This result was obtained

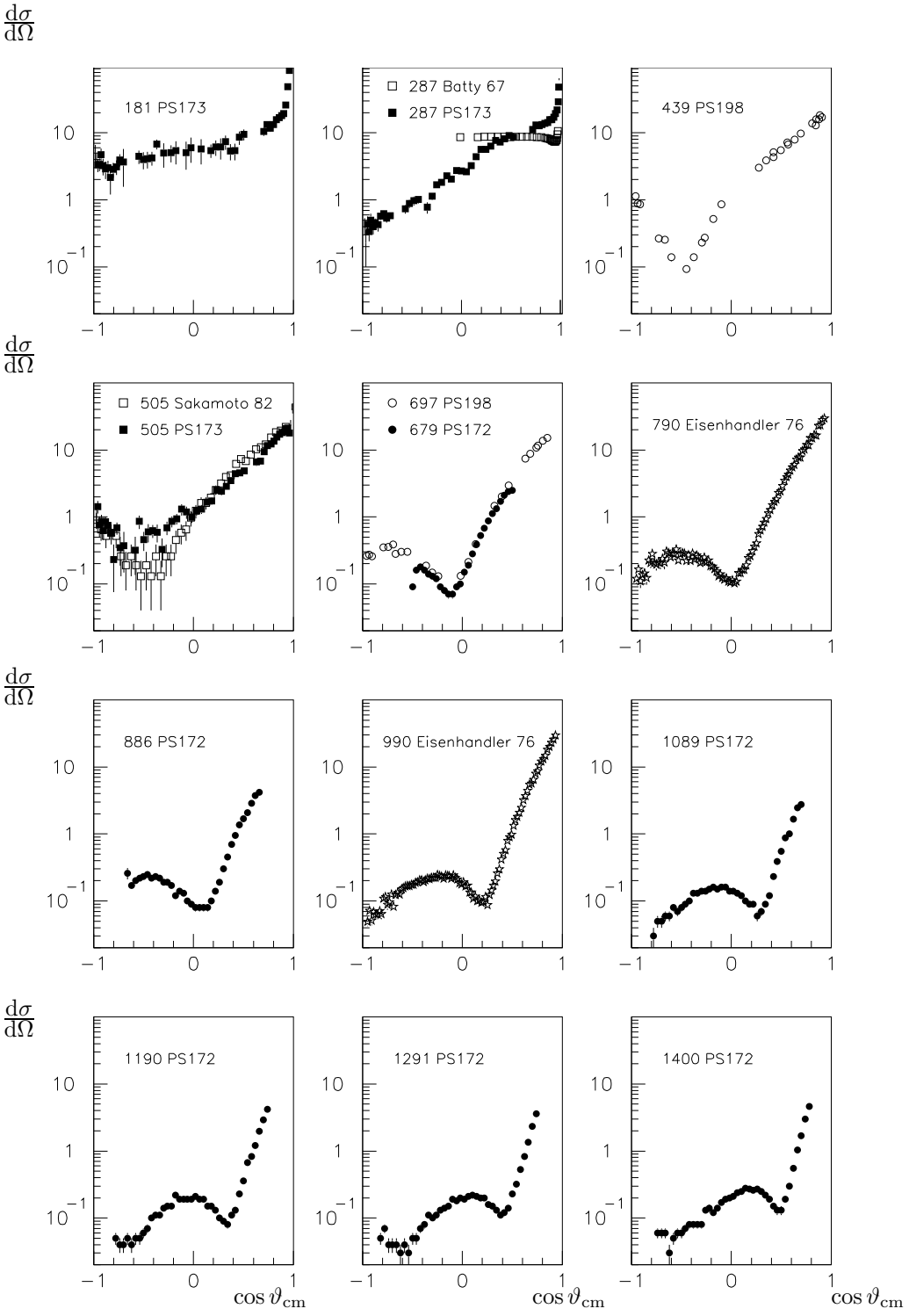

Figure 4.7: $\bar{\mathrm{p}}\mathrm{p}$ elastic differential cross-section data in mb/sr as a function of $\cos\vartheta_{\mathrm{cm}}$ at several values of the incident $\bar{\mathrm{p}}$momentum (from 181 to 1400 MeV/c).

both using a unitary coupled-channel model, and an optical model. It seems therefore reasonable to conclude that the P-wave enhancement is a consequence of the strong $\overline{\mathrm{N}}\mathrm{N}$ meson-exchange potential. This fact was first emphasised qualitatively by Dalkarov [228], a long time before the appearance of the LEAR data.

The strong P-wave enhancement at low energy is considered as one of the main results obtained by the scattering experiments at LEAR. It has also been observed in charge-exchange scattering, as it will be seen later. Moreover, the annihilation of protonium from P-states is very large, as well as the P-wave contribution to $\bar{\mathrm{p}}\mathrm{p}$ annihilation in flight.

In the higher momentum range (above 800 MeV/c), the shape of the elastic cross-section is essentially due to diffraction. It is the shadow of the strong absorption of the incoming wave which is caused by annihilation. Due to isospin factors ($\vec{\tau}_1.\vec{\tau}_2 = +1$ for $I = 1$ and $\vec{\tau}_1.\vec{\tau}_2 = -3$ for $I = 0$) the π-exchange contribution is partially suppressed in the $\bar{\mathrm{p}}\mathrm{p}$ elastic channel ($\mathcal{T}_{I=0} + \mathcal{T}_{I=1}$). The situation is different at low momenta, where a strong anti-shrinkage of the forward peak is observed. This effect is clearly visible in Fig. 4.8, where differential cross-section data at a few energies are plotted as a function of $-t$. Parametrising the forward cross-section as $\exp(bt)$ the b-

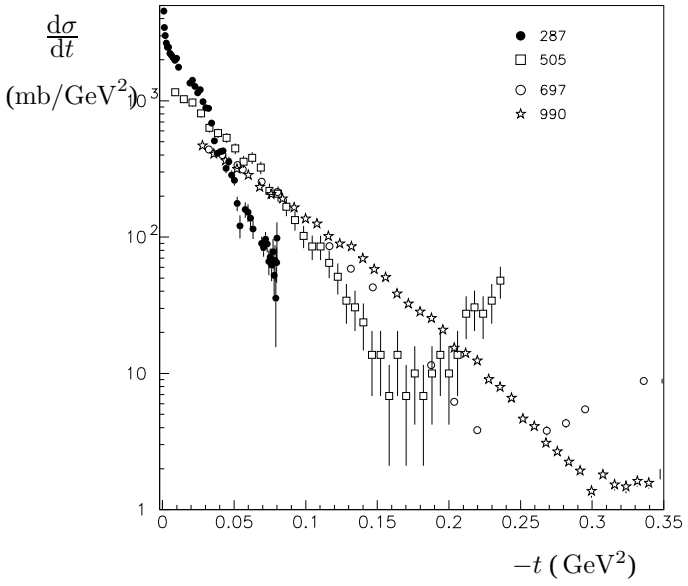

Figure 4.8: The $\bar{\mathrm{p}}\mathrm{p}$ elastic differential cross-section $\mathrm{d}\sigma/\mathrm{d}t$ as a function of $-t$ at four incoming $\bar{\mathrm{p}}$ momenta between 287 and 990 MeV/c.

values shown in Fig. 4.9 are obtained, which clearly exhibit a strong rise at low energy. This fact has been interpreted [228] as a consequence of the strong attraction of the long range $\overline{\mathrm{N}}\mathrm{N}$ meson-exchange potential, which pulls the $\overline{\mathrm{N}}\mathrm{N}$ wave function into the annihilation region. The net effect is that the effective absorption radius $R_{\mathrm{eff}} = 2\hbar c b^{1/2}$ is larger than the annihilation radius, as defined in optical potential models (section 3.8). As a consequence, at low energy the forward slope of the elastic differential cross-section, as well as its energy dependence, are given by the meson-exchange potential, and the $\overline{\mathrm{N}}\mathrm{N}$ scattering is not diffractive [60].

As a final comment, we note that some of the data are not compatible with each other. This is a known problem, discussed repeatedly in the literature, and sometimes a matter of debate when it comes to use a data base to extract information on the parameters of the various $\overline{\mathrm{N}}\mathrm{N}$ models. Figures 4.11 and 4.10 exhibit two typical situations faced by the community: the first one is "easily" solved by introducing a renormalisation factor, but the second one (see also [277]) is clearly a

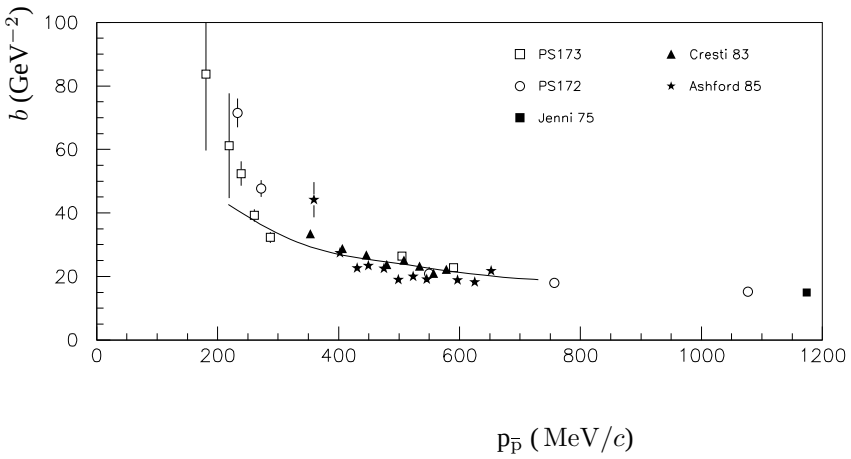

Figure 4.9: Best-fitted slope values b for the differential cross-section $\bar{\mathrm{p}}\mathrm{p} \rightarrow \bar{\mathrm{p}}\mathrm{p}$ in the forward region, as a function of the incident $\bar{\mathrm{p}}$ momentum. The data are from Ref. [79, 80, 93, 303–305]. The curve is the calculation of the optical model of Ref. [228].

problem.

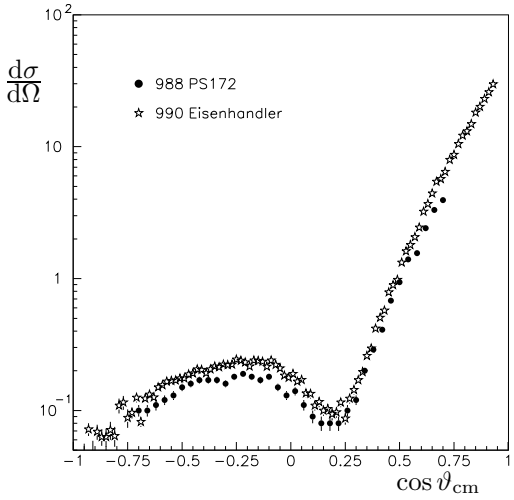

Figure 4.10: $\bar{\mathrm{p}}\mathrm{p}$ elastic differential cross-section at about $990\,\mathrm{MeV}/c$; the data are from PS172 (closed circles) and from Eisenhandler et al. (stars).

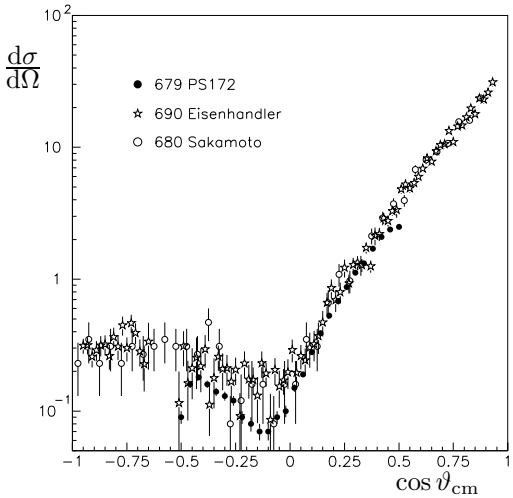

Figure 4.11: $\bar{\mathrm{p}}\mathrm{p}$ elastic differential cross-section in the range $679 - 690\,\mathrm{MeV}/c$; the data are from PS172 (closed circles), Eisenhandler et al. (stars), and Sakamoto et al. (open circles).

4.2.2 Extraction of ρ

In the extreme forward region ($\vartheta \simeq 0$), the shape of the $\bar{\mathrm{p}}\mathrm{p}$ differential cross-section reflects the interference of the strong amplitude $\mathcal{T}_{\mathrm{S}}$ with the Coulomb one $\mathcal{T}_{\mathrm{C}}$. Since the latter is known, we get access to the so-called "ρ" parameter, which is defined as

$$\rho(s) = \mathcal{R}\mathrm{e}\,\mathcal{T}_{\mathrm{S}}/\,\mathcal{I}\mathrm{m}\,\mathcal{T}_{\mathrm{S}}\ , \tag{4.1}$$

In Eq. 4.1 it is assumed that only the non-spin flip part of the strong amplitude contributes to the interference with Coulomb amplitude. The strong amplitude is usually parametrised as an exponential

$$f(t) = \frac{\sigma_{tot}}{4\pi}(i+\rho)\exp(bt/2)\ , \tag{4.2}$$

where b, the slope of the diffraction peak, is of the order of $20\,\mathrm{GeV}^{-2}$ around $600\,\mathrm{MeV}/c$, as seen in Fig. 4.9. The Coulomb amplitude is well known from the literature. A more refined treatment would require a spin dependence of the strong amplitudes, which can only be provided by a model or a phase-shift analysis, as stressed, e.g., in Ref. [279, 306].

Usually b and ρ are extracted from a fit to the data. In some cases the fit is also used to estimate values for the total cross-section.

The results of scattering experiments at CERN, Brookhaven, and FNAL are plotted in Fig. 4.12. The data are from

- PS172: points at 233 and $272\,\mathrm{MeV}/c$ [79], and 550, 757, and $1077\,\mathrm{MeV}/c$ [80].

- PS173: 7 points between 181 and $590\,\mathrm{MeV}/c$ [93]; σ_{tot} is also extracted from the data.

- Ashford et al. (BNL): 11 points between 359 and $652\,\mathrm{MeV}/c$ [305].

- Cresti et al. (CERN PS): 8 points between 353.3 and $578.3\,\mathrm{MeV}/c$ [304].

- Iwasaki et al. (KEK): 6 points between 430 and 687 MeV/c [307].

- Jenni et al. (CERN PS): 6 points between 1.174 and 2.607 GeV/c [303].

E760 (FNAL): 6 points between 3.70 and 6.23 GeV/c [132]; σ_{tot} fixed.

The point at $p_{\bar{\mathrm{p}}} = 0$ comes from the measurement of the $\bar{\mathrm{p}}\mathrm{p}$ atomic 1S state: as explained in Chapter 5, it is given by the ratio of the shift to the width of the protonium 1S level, which numerically turns out to be smaller than -1.

The rapid change of ρ from about 0 for momenta larger than 200 MeV/c to less than -1 at $p_{\bar{\mathrm{p}}} = 0$ is usually interpreted in terms of the strong P-wave enhancement already mentioned in Sec. 4.2.1, and S- and P-wave interference effects [308].

As one can see, there is an intriguing structure near 200 MeV/c. Several authors have computed the effect of the nearby $\bar{\mathrm{p}}\mathrm{p} \to \bar{\mathrm{n}}\mathrm{n}$ threshold, and concluded it is negligible and could not be responsible for the structure (see, e.g., Ref. [309]). Others have tried to explain the bump in terms of an $\overline{\mathrm{N}}\mathrm{N}$ state below threshold (see, e.g., Ref. [310]).

Three remarks however should be made:

i) there is some disagreement between the data;

ii) as already pointed out, if there is any spin dependence in the amplitude (and this is likely to occur), it should be accounted for when extracting ρ;

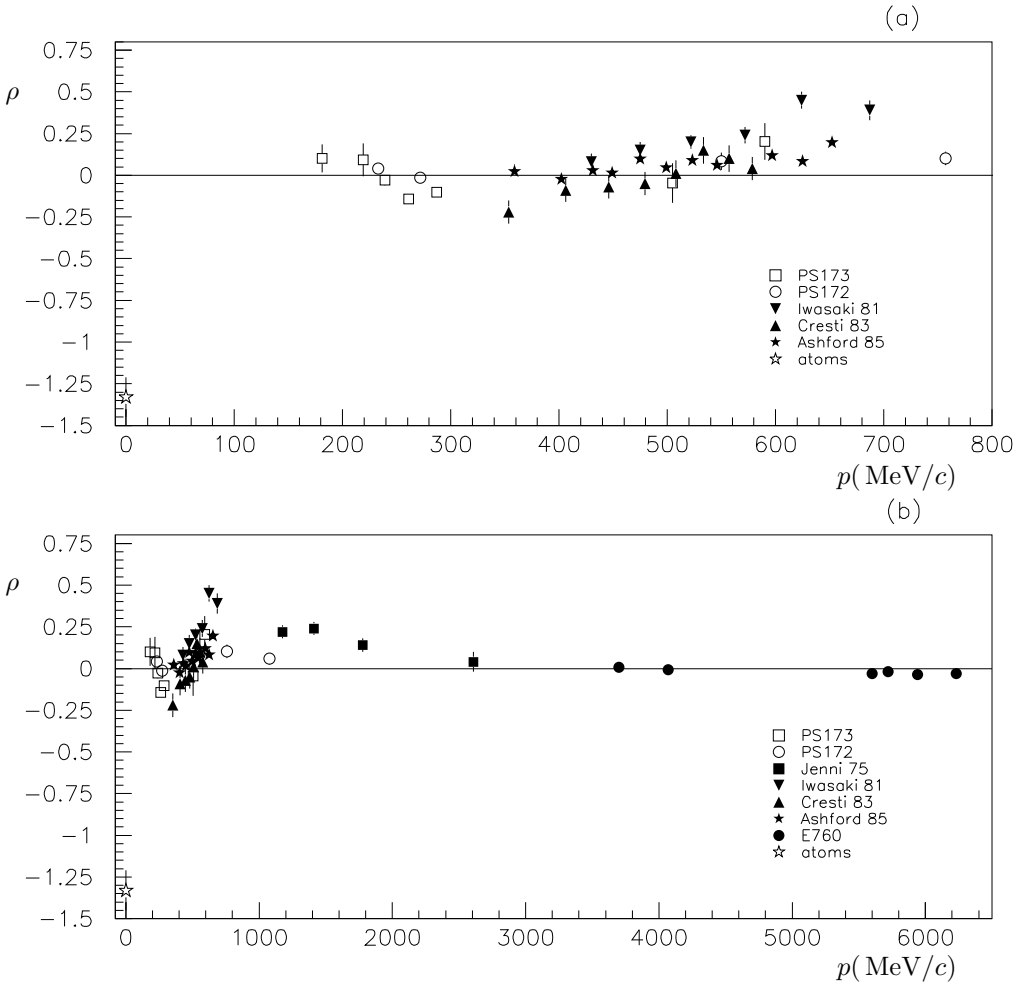

Figure 4.12: The ρ parameter as a function of the $\bar{\mathrm{p}}$ momentum in MeV/c.

iii) in Eq. 4.1 it is assumed that $\mathcal{R}\mathrm{e}\,\mathcal{T}_{\mathrm{S}}$ and $\mathcal{I}\mathrm{m}\,\mathcal{T}_{\mathrm{S}}$ have the same t-dependence;

iv) the unfolding of the experimental measuring errors or the effects of multiple scattering is a delicate procedure and the assessment of the systematic errors is not straightforward.

4.3 $\bar{\mathrm{p}}\mathrm{p}$ charge-exchange differential cross-section

The charge-exchange reaction is an instructive observatory of the subtle interplay between long-range Yukawa-type of forces, and the strong short-range absorption [311, 312]. Data were taken at LEAR, by the PS173, PS199, and PS206 collaborations, and also at BNL and KEK. Very much like in the $\bar{\mathrm{p}}\mathrm{p}$ elastic reaction, the data from the LEAR experiment (PS173) are the data at the lowest incident momentum.

4.3.1 Shape

Typical data from various experiments are shown in Fig. 4.13, as a function of $\cos\vartheta_{\mathrm{cm}}$. The data are from:

- PS173: closed squares at 181, 228, 240, 262, 300, 470, 499, 550 and 595 MeV/c. The data are from the HEPDATA Reaction Data Database [313]: the incident momenta bins differ slightly from those given in [94];

- Nakamura et al. (KEK): open circles at 392.4, 490.1, 591.2, 689.0, 780.5 MeV/c [314];

- Kohno et al. (CERN PS): open stars at 696 MeV/c [315];

- Colebourne et al. (CERN PS): closed triangles at 1130 MeV/c [316];

- Banerjee et al. (CERN PS): open squares at 760 MeV/c [317];

Bogdanski et al. (CERN PS): open triangles at 730 MeV/c [318];

PS199: closed stars at 693 MeV/c [111] and at 546 and 767 MeV/c [115].

Even at momenta as low as $p_{\bar{\mathrm{p}}} = 181\,\mathrm{MeV}/c$, the differential cross-section in Fig. 4.13 exhibits several structures. This is not surprising. The smallness of the integrated charge-exchange cross-section is due to a strong cancellation of the low partial waves in the combination $\mathcal{T}_{\mathrm{ce}} \propto \mathcal{T}_{I=1} - \mathcal{T}_{I=0}$. Then the high partial waves have a more important weight in the charge-exchange than in the other isospin channels.

The most interesting structure shown by the $\bar{\mathrm{p}}\mathrm{p} \to \bar{\mathrm{n}}\mathrm{n}$ differential cross-section data is the sharp peak in the forward direction, followed by a dip-bump structure. These features can be seen best in Fig. 4.14, which shows the recent measurement at LEAR by experiment PS206 at 601 MeV/c [121]. This experiment has provided at two momenta (601 and 1202 MeV/c) the most precise measurements, extending down to $t = 0$, and has allowed for the first time to measure accurately the shape of the forward peak. Very much like the forward peak of the $\mathrm{np} \to \mathrm{pn}$ reaction, this structure is interpreted as a manifestation of the nearby pion pole, which must contribute to the scattering amplitude with the Born term

$$\frac{1}{s}\, g^2_{\pi\mathrm{NN}}\, \frac{t}{t-\mu^2_\pi}, \tag{4.3}$$

where s and t are the Mandelstam variables, and $g^2_{\pi\mathrm{NN}} \simeq 14$ is the charged pion nucleon coupling constant.

Applying the Chew extrapolation method, the PS206 data have been used to extract $g^2_{\pi\mathrm{NN}}$. The value of this fundamental constant has been a matter of debate over the past fifteen years. A reanalysis of the NN data and a whole set of new experiments suggest a value of $g^2_{\pi\mathrm{NN}}$ of 13.6 [319], about 5% lower than the "standard" value. The value of $g^2_{\pi\mathrm{NN}}$ is important for our world: if it would be too small, the deuteron would be unbound and no nuclei would have been formed. If it would be too

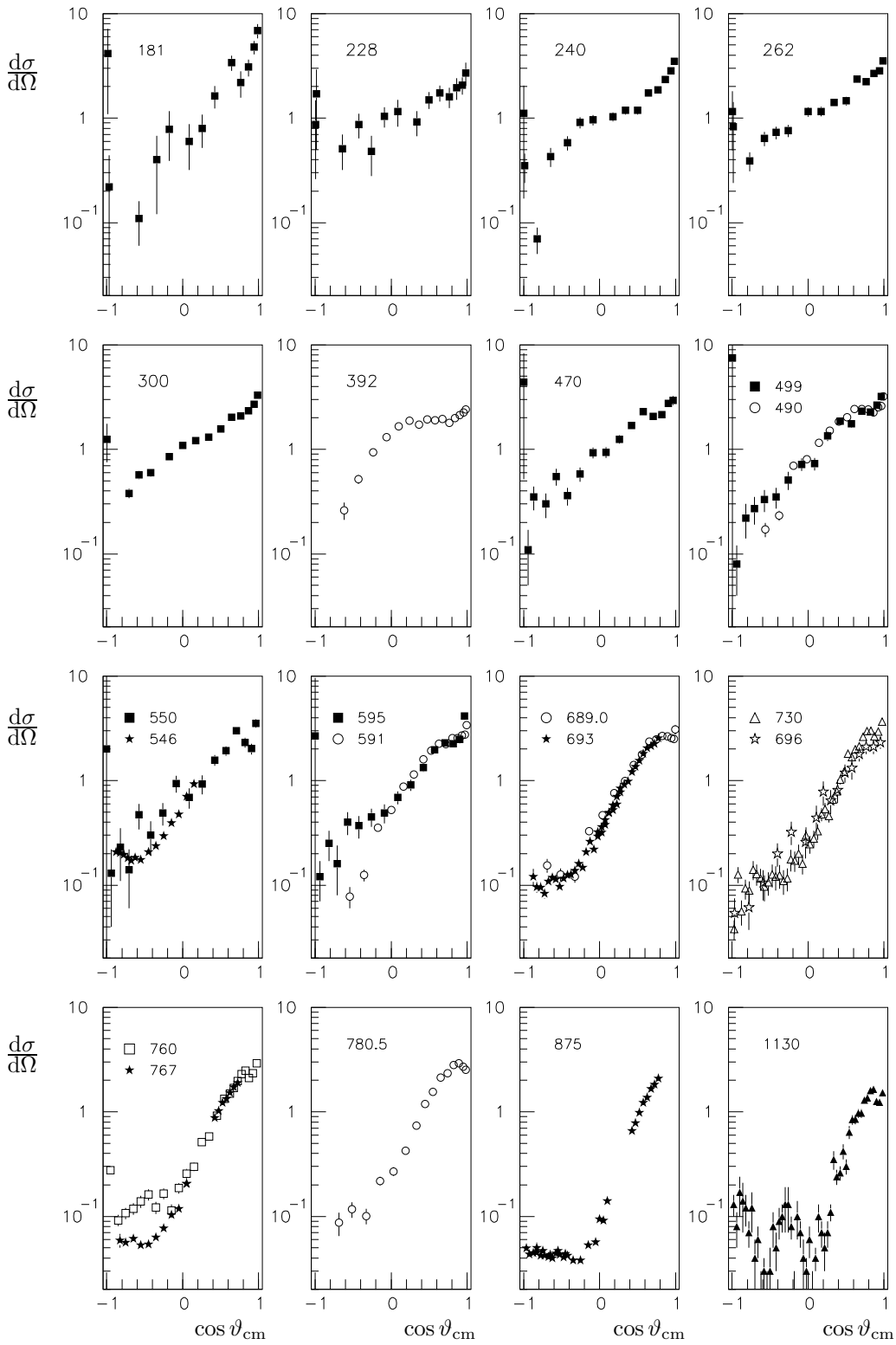

Figure 4.13: $\bar{\mathrm{p}}\mathrm{p}$ charge-exchange differential cross-section data in mb/sr as a function of $\cos\vartheta_{\mathrm{cm}}$ at several values of the incident $\bar{\mathrm{p}}$ momentum (from 181 to 1130 MeV/c). The data are from experiment PS173 (closed squares), experiment PS199 (stars), and pre-LEAR experiments.

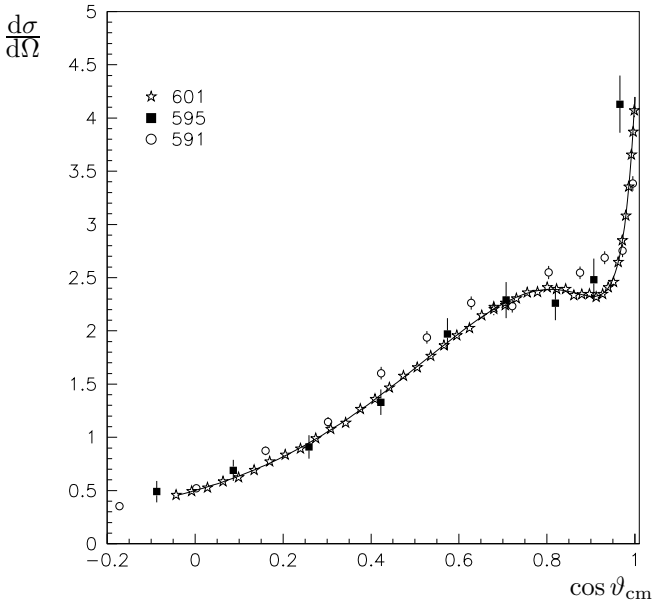

Figure 4.14: The $\bar{\mathrm{p}}\mathrm{p}$ charge-exchange differential cross-section at $601\,\mathrm{MeV}/c$from experiment PS206. Also shown are the measurements from PS173 and Nakamura et al. The curve is a fit to the PS206 data.

large, there would be no hydrogen-to-helium burning, and our sun would not shine [320]. The possibility to extract $g_{\pi\mathrm{NN}}$ from the $\bar{\mathrm{p}}\mathrm{p} \to \bar{\mathrm{n}}\mathrm{n}$ data was already suggested in 1967 by Phillips [321], and it was first realised by the Njimegen group, in a global fit of the $\overline{\mathrm{N}}\mathrm{N}$ data base [322]. In Ref. [323, 324] is was shown that $g_{\pi\mathrm{NN}}$ could be extracted with good precision from the data of a single experiment, in a model independent way by extrapolating the data to the pion pole. Like in the NN case, a "low" value for $g^2_{\pi\mathrm{NN}}$ was obtained, which has been a matter of concern and discussion [325].

Also interesting is the dip-bump structure in Fig. 4.14, which had already been seen in several previous experiments, and was known to depend on the energy: sometimes a simple shoulder, and sometimes a pronounced minimum. In the literature, several explanations of the dip-bump structure can be found:

i) according to Phillips [210, 321], the second maximum is a typical OPE effect, coming from a double-spin-flip amplitude;

ii) Shibata [219] ascribes the shape of the charge-exchange differential cross-section to π-exchange ($V_{\mathrm{SS}} + V_{\mathrm{T}}$) only; basically it is the same explanation;

iii) it turns out that the shape of the cross-section is also sensitive to the absorptive potential which accounts for the annihilation, and which interferes with the OPE amplitude.

Fits to the PS206 data with π-exchange only plus a smooth background [121, 323, 324] are excellent, as seen in Fig. 4.14. What the background is, it is still an open question. 2π-exchange and ρ-exchange surely contribute to it.

4.3.2 Exchange structure from the charge-exchange scattering data

The success of the simple fit described in the previous section to the small angle cross-section data rises the obvious question "is this all?", i.e., is annihilation plus OPEP enough to describe the $\overline{\mathrm{N}}\mathrm{N}$ scattering data?

The answer is no. In particular, as will be shown in Chapter 6, with such simple methods there is no way to reproduce A_{0n} data. But even for what concerns the differential cross-section data, overall

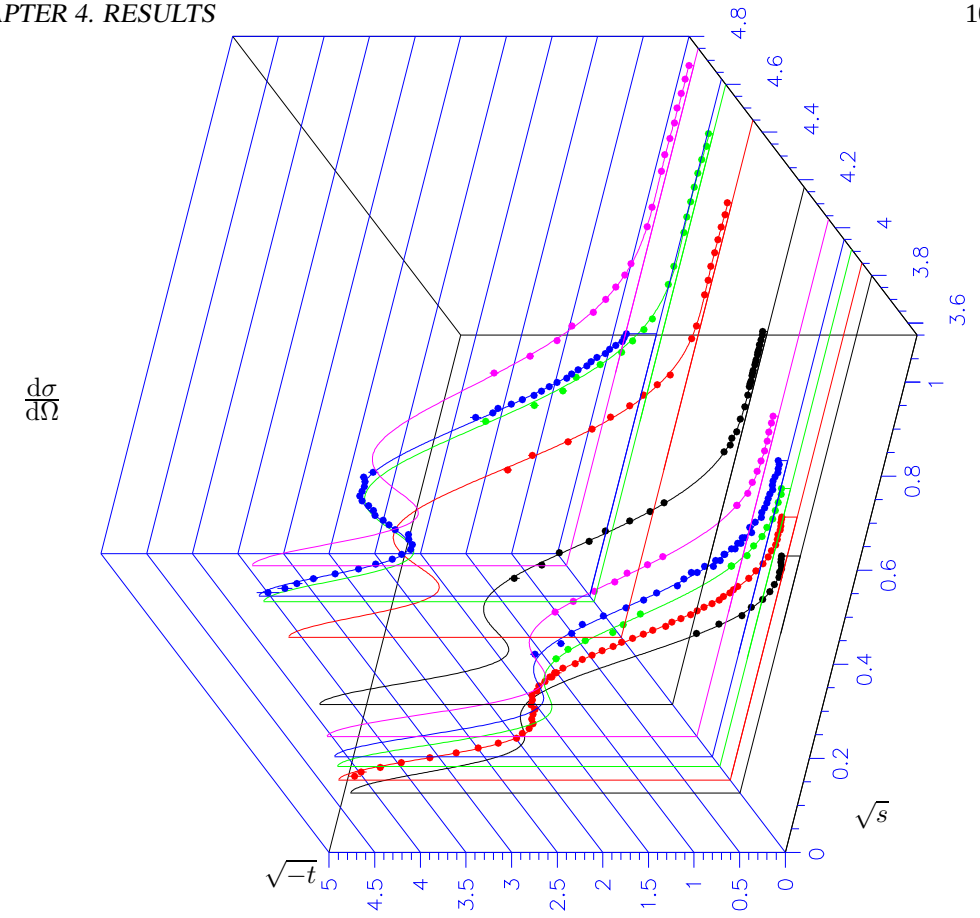

Figure 4.15: The $\bar{\mathrm{p}}\mathrm{p}$ charge-exchange differential cross-section data from PS199 and PS206. The fits, described in the text, assume the π -pole and the ρ -pole as the only singularities.

fits of the existing data at different energies seem to indicate the necessity of more structures in the amplitudes.

The effect of including 2π-exchange in the extrapolating function has been checked and the results presented at the last LEAP conferences [326, 327]. To take into account 2π-exchange a ρ-pole term has been introduced.

Removing the π and ρ singularities by multiplying the data by $(t-\mu_\pi^2)^2\,(t-\mu_\rho^2)^2$, excellent fits have been obtained to all the differential cross-section data from PS199 and PS206, at all energies and in all the t range (up to $1.15\,\mathrm{GeV}$), with smooth polynomials in t as can be seen in Fig. 4.15. On the contrary, the fits which had the pion as the only singularity did not give good results for the higher momenta PS199 data. This result has been interpreted by the authors as direct evidence for 2π-exchange in the $\bar{\mathrm{p}}\mathrm{p} \rightarrow \bar{\mathrm{n}}\mathrm{n}$ reaction. The comparison between the fits and the data from PS199 [111, 114, 115] and PS206 [120, 121] is shown in Fig. 4.15.

4.4 $\overline{\mathrm{N}}\mathrm{N}$ interaction radii from scattering data

An interesting analysis of the $\bar{\mathrm{p}}\mathrm{p}$ cross-sections at low energy was been performed by the Heidelberg group [219, 328], to describe in a model independent way the various interaction ranges. As shown, e.g., in Ref. [329], it is possible to derive from the potential in a straightforward way the interaction ranges. As an example, from the imaginary optical potential which simulates annihilation one can derive the "annihilation radius". If W is the strength of the absorption potential (negative), and ψ

the outgoing wave,

$$\psi(r,\theta) = \sum_l (2l+1) i^l R_l(r) P_l(\cos\theta) \,, \tag{4.4}$$

in the notation of Ref. [329], then

$$\sigma_{ann} = -\frac{2}{\hbar v} \int W |\psi|^2 d\Omega \,, \tag{4.5}$$

and the annihilation radius r_a can be defined as

$$\int_0^{r_a} W|\psi|^2 r^2 \mathrm{d}r = \int_{r_a}^{\infty} W|\psi|^2 r^2 \mathrm{d}r \,. \tag{4.6}$$

Similar expressions can be written for the other interaction ranges, starting from the corresponding potentials.

The Heidelberg group has fitted the parameters of various potentials to the low energy cross-section data of PS173 (elastic scattering and charge-exchange). In the context of an optical model, they have used different potentials, the real part, either a Wood-Saxon or a G-parity transformed OPE potential, to describe the meson-exchange potential, and an imaginary potential, again a Wood-Saxon or a Gaussian, to describe the annihilation. Good agreement with the data could be obtained with all these potentials, although the potentials, as always, could not be uniquely determined. Still, the interaction ranges evaluated from these various potentials agree remarkably with each other, so that the determination of these parameters seems really model-independent.

From the fitted parameters, an "annihilation radius" of about $1\,\mathrm{fm}$ was thus derived, as apparent from Fig. 4.16, which, as an example, shows the density probability $|R_1|^2\,(kr)^2$ and the annihilation probability $-W|R_1|^2\,(kr)^2$ computed for ${}^{13}P_1$ at $290\,\mathrm{MeV}/c$ [219]. The value obtained for

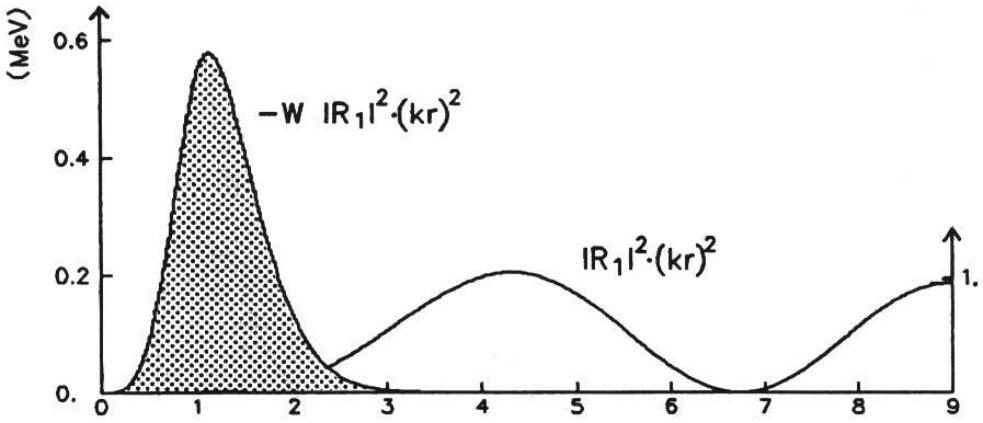

Figure 4.16: The squared wave function $|R_1|^2\,(kr)^2$ and the annihilation probability $-W|R_1|^2\,(kr)^2$ for ${}^{13}P_1$. R_1 is the radial wave function for the P_1 state.

r_a, about $1\,\mathrm{fm}$, is much larger than the Compton wave-length associated with baryon exchange ($\hbar/2m_Nc \simeq 0.1\,\mathrm{fm}$) which originally was proposed to account for annihilation. The size of the annihilation range has been a matter of debate for many years, as seen in Sec. 3.8.6.

A value of about $1\,\mathrm{fm}$ is also consistently derived for the annihilation radius using more elaborate potentials. Even from the Bonn potential, which uses small Compton wavelength exchanged baryons to derive the annihilation potential, one obtains consistently an annihilation radius around $1\,\mathrm{fm}$ [330, 331].

One can conclude that essentially in a model independent way the annihilation radius r_a is about $1\,\mathrm{fm}$. This result agrees with a simple picture where

$$\langle r_a^2 \rangle = 2\,\langle r_p^2 \rangle\,, \tag{4.7}$$

with r_p the proton (and antiproton) electromagnetic radius.

In the analysis of the Heidelberg group, the range of the real potential consistently turns out to be roughly twice as large as the annihilation radius, and practically equal to the corresponding range of the NN potential (essentially OPEP). This result is not surprising, since the G-parity transformation affects OPEP only slightly, and the cross-section data are not sensitive enough to underline the difference between the NN and the $\overline{\mathrm{N}}\mathrm{N}$ real potential.

As a final remark, it is interesting to remind that the range of the real potential for $\bar{\mathrm{p}}\mathrm{p}$ elastic is markedly smaller than the corresponding range for $\bar{\mathrm{p}}\mathrm{p}$ charge-exchange, hinting at the fact that OPE dominates this last reaction, while its contribution is partially cancelled in the elastic channel as already pointed out in Sect. 4.2.1: the charge-exchange potential is therefore the long-range OPEP, while the elastic $\bar{\mathrm{p}}\mathrm{p}$ potential is characterised by a medium-range.

4.5 Analysing power of $\bar{\mathrm{p}}\mathrm{p}$ elastic scattering

The analysing power A_{0n} has been measured at LEAR over most of the angular range by experiment PS172 [85] at fifteen momenta, ranging from 497 to $1550\,\mathrm{MeV}/c$, and the full angular range by experiment PS198 at 439, 544, and $697\,\mathrm{MeV}/c$ [106, 107]. Most of the data are shown in Fig. 4.17. A few nearby energies have been combined in a single plot. The agreement between the two sets of experimental data is good.

Some analysing power data were taken at the CERN PS [332], before LEAR entered into operation, but the error bars are almost an order of magnitude larger, as can be seen in the figure for the data at $910\,\mathrm{MeV}/c$ ("combined 0.88 and $0.95\,\mathrm{GeV}/c$ data").

Although the trend of the differential cross-section data is reminiscent of a diffractive phenomenon, and can be reproduced by simple optical models like the Frahn–Venter model [333], this is not the case for the analysing-power data. The A_{0n} pattern is reminiscent of diffraction, showing pronounced minima (sometimes going almost to zero) at the diffraction minima seen in the differential cross-section, but, as noticed by the authors [85] the analysing power data are not compatible with the simple optical models, especially in the backward hemisphere. As discussed in Chapter 6, much more sophisticated models are needed to reproduce these data.

4.6 $\bar{\mathrm{p}}\mathrm{p}$ charge-exchange analysing power

No pre-LEAR data existed for the analysing power of the $\bar{\mathrm{p}}\mathrm{p} \to \bar{\mathrm{n}}\mathrm{n}$ charge-exchange channel.

At LEAR, the PS199 experiment measured A_{0n} over most of the angular range at eight incident $\bar{\mathrm{p}}$ momenta, ranging from 546 to $1287\,\mathrm{MeV}/c$. The complete data set is shown in Fig. 4.18. The closed points are from Ref. [112, 113]; the open points at 875 and $546\,\mathrm{MeV}/c$ are independent measurements from Refs. [114] and [118], respectively.

The analysing power values do not exceed $\pm 20\%$, thus setting limits on the role of spin-orbit type of forces in this reaction.

At low energy the data exhibit a simple pattern, with a peak in the forward region and another in the backward region, but as the energy increases, a bump builds up in the central region.

Although some interesting analogies could be drawn between the $\mathrm{n}\mathrm{p} \to \mathrm{p}\mathrm{n}$ and the $\bar{\mathrm{p}}\mathrm{p} \to \bar{\mathrm{n}}\mathrm{n}$ data [327], it is fair to say that a simple physical explanation of the observed polarisation signal is still lacking, even at small t, where the π-exchange should be the dominating dynamical mechanism. A possible explanation is that, to first-order Born approximation, π-exchange does not contribute to A_{0n}. Polarisation is contributed by a spin-orbit $\vec{L}\cdot\vec{S}$ term generated either by a vector exchange (for instance ρ-exchange) or by iterated π-exchange.

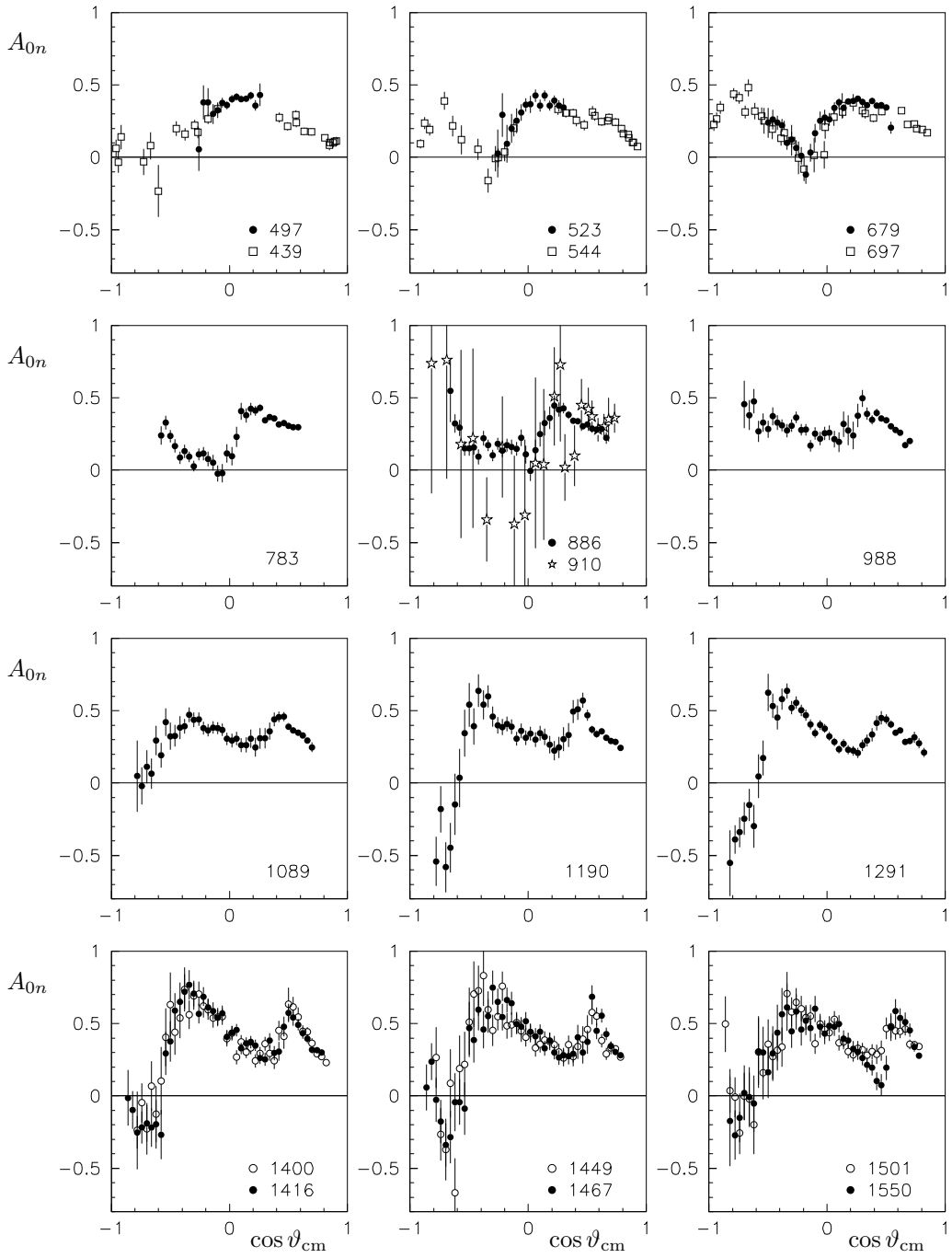

Figure 4.17: The analysing power A_{0n} as a function of $\cos\vartheta_{\rm cm}$ in the $\bar{\rm p}{\rm p}$ elastic channel, at several incident $\bar{\rm p}$ momenta, from 439 to 1550 MeV/c. The data are from experiment PS172 (open and closed circles), experiment PS198 (open squares) and from Ref. [332] (stars).

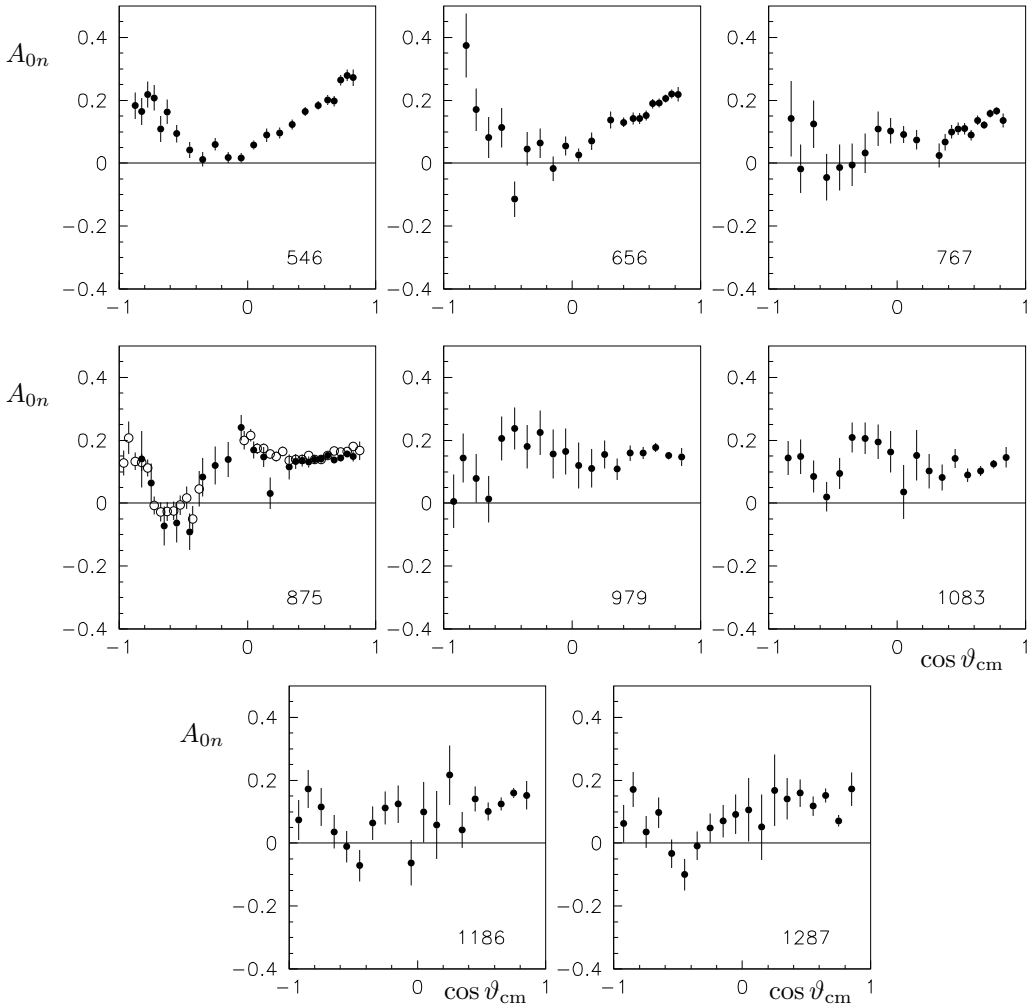

Figure 4.18: The analysing power A_{0n} as a function of $\cos\vartheta_{\rm cm}$ in the $\bar{\rm p}$p charge-exchange channel, from PS199, at several incoming $\bar{\rm p}$ momenta, from 546 to 1287 MeV/c.

4.7 Two spin correlation data

As byproduct of the A_{0n} measurement, the PS172 experiment at LEAR obtained some D_{0n0n} data for the $\bar{\mathrm{p}}\mathrm{p}$ elastic reaction, mostly in the central angular region [87]. The data were extracted from the measured polarisation of the scattered proton, by using a Carbon polarimeter, as described in Chapter 2.

Data were taken at 10 incoming $\bar{\mathrm{p}}$ momenta between 679 and 1501 MeV/c. In Fig. 4.19 they are plotted as a function of $\cos\vartheta_{\mathrm{cm}}$. In the figure, the point at 1416 MeV/c has been shifted (from $\cos\vartheta_{\mathrm{cm}} = -0.295$ to $\cos\vartheta_{\mathrm{cm}} = -0.3$). The error bars are large, but we note appreciable departures from $D_{0n0n} = 1$, indicating that the spin–spin forces are important.

The depolarisation parameter D_{0n0n} for the $\bar{\mathrm{p}}\mathrm{p} \to \bar{\mathrm{n}}\mathrm{n}$ reaction has been measured at 875 MeV/c [117] and 545 MeV/c [118]. This measurement was an important part of the PS199 program, and two relatively long runs were dedicated to it. D_{0n0n} was obtained from the measured polarisation of the scattered neutron. The measurement is difficult, and could be performed only in a limited angular range. The results, shown in Fig. 4.20, clearly indicate that D_{0n0n} is very different from 1, thus confirming the relevance of the tensor forces in the $\overline{\mathrm{N}}\mathrm{N}$ interaction. The same data are plotted as a

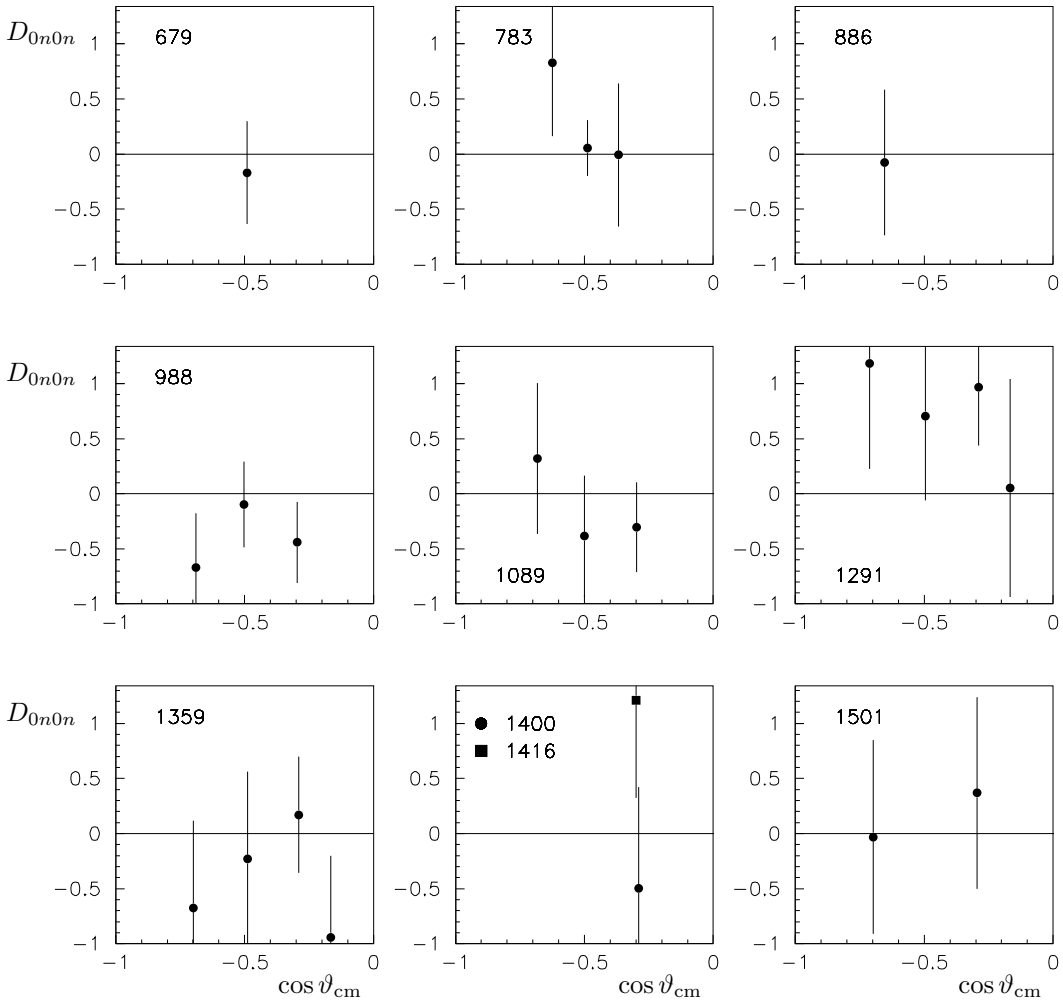

Figure 4.19: D_{0n0n} data from PS172 as a function of $\cos\vartheta_{\mathrm{cm}}$ in the $\bar{\mathrm{p}}\mathrm{p}$ elastic channel, at incident $\bar{\mathrm{p}}$ momenta from 679 to 1501 MeV/c.

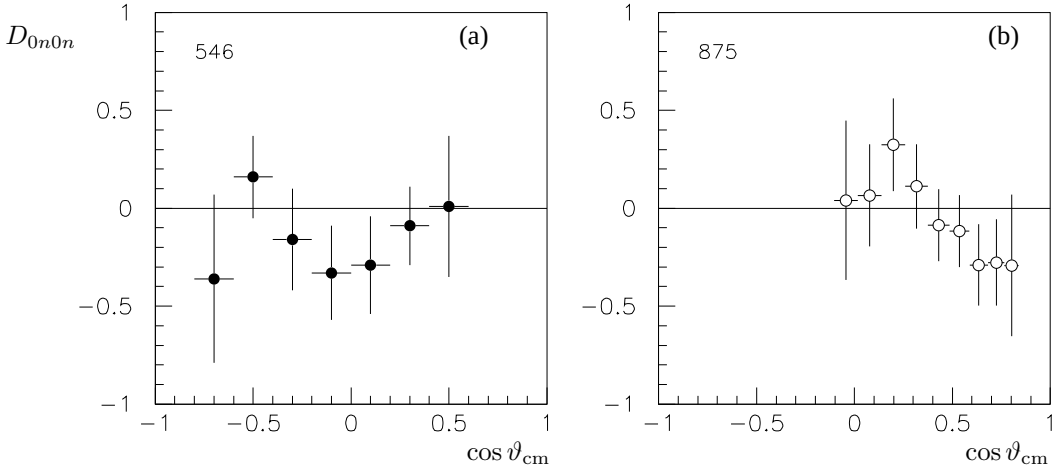

Figure 4.20: D_{0n0n} data for the $\bar{\rm p}{\rm p} \to \bar{\rm n}{\rm n}$ charge-exchange channel from PS199 vs $\cos\theta_{cm}$ at 545 MeV/c (a) at 875 MeV/c (b).

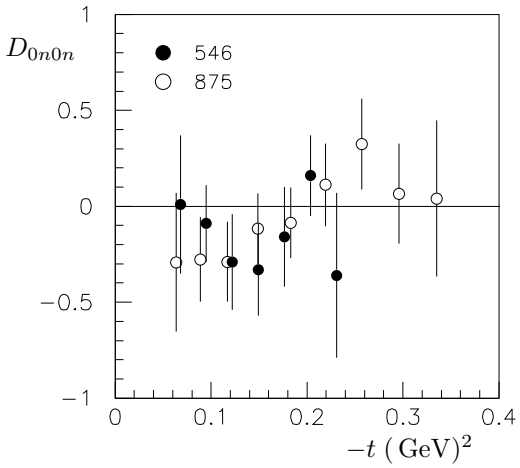

Figure 4.21: D_{0n0n} data for the $\bar{\rm p}{\rm p} \to \bar{\rm n}{\rm n}$ channel as a function of $-t$ from experiment PS199.

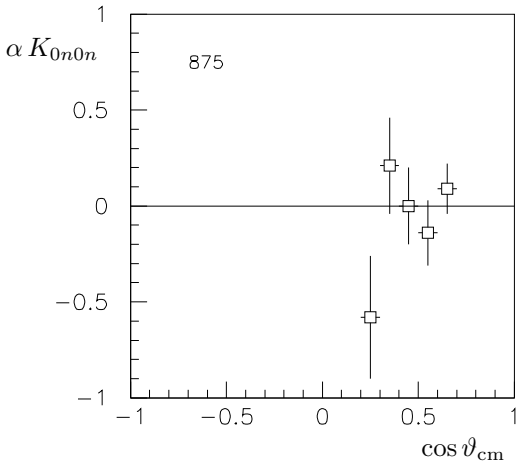

Figure 4.22: $\alpha\, K_{n00n}$ vs. $\cos\vartheta_{\rm cm}$ for the $\bar{\rm p}{\rm p} \to \bar{\rm n}{\rm n}$ channel at 875 MeV/c from experiment PS199.

function of $-t$ in Fig. 4.21. One notices a similar trend for D_{0n0n}, a small negative value (about -0.2) for $-t \leq 0.2$ GeV^2. The K_{n00n} parameter has also been measured for the charge-exchange reaction by PS199 at 875 MeV/c [119]. The measurement was done parasitically to the D_{0n0n} run, detecting the $\bar{\mathrm{n}}$ in the neutron polarimeter. Since the analysing power of the $\bar{\mathrm{n}}\mathrm{p}$ reaction is not known[1], the data shown in Fig. 4.22 are presented as $\alpha\, K_{n00n}$ where α is an unmeasured proportionality factor, related to the $\bar{\mathrm{n}}\mathrm{p}$ elastic scattering analysing power $A_{\bar{n}p}$ by the relation $A_{\bar{n}p} = \alpha\, q$ where q is the momentum transfer. The quantity α was estimated by PS172 from the measurement of the analysing power of the $\bar{\mathrm{p}}\mathrm{C}$ elastic scattering to be $0.61^{+0.18}_{-0.20}$, a value consistent with $\overline{\mathrm{N}}\mathrm{N}$ potential-model calculations. The data, plotted as a function of $\cos\vartheta_{\mathrm{cm}}$, are given in $(\,\mathrm{GeV}/c)^{-1}$.

4.8 Strangeness exchange reactions

4.8.1 Total cross sections for $\overline{\Lambda}\Lambda$ production

In Refs. [124, 130], the $\overline{\Lambda}\Lambda$ production is studied very close to the threshold at $s_0 = 4m_\Lambda^2$. The original motivation of the PS185 experiment was indeed to investigate the behaviour of the cross-section near threshold, to identify either a $(s - s_0)^{1/2}$ energy dependence, typical of S-wave, or $(s - s_0)^{3/2}$ given by a P-wave. See, e.g., Kilian's contribution at Tignes [336]. A gluon intermediate state associated with scalar diquarks suggests a $^3\mathrm{S}_1$ dominance, while current pair-creation models favour $^3\mathrm{P}_0$. This is discussed in several papers, for instance in Refs. [337, 338].

The PS185 data are summarised in Fig. 4.23, as a function of the c.m. excess energy $\epsilon = \sqrt{s} - 2M$, where M is the Λ mass. There is a sharp rise of the cross section starting at $1.434\,\mathrm{GeV}/c$. Above $1.5\,\mathrm{GeV}/c$, the measured cross section matches values obtained in earlier experiments, and listed in Ref. [124].

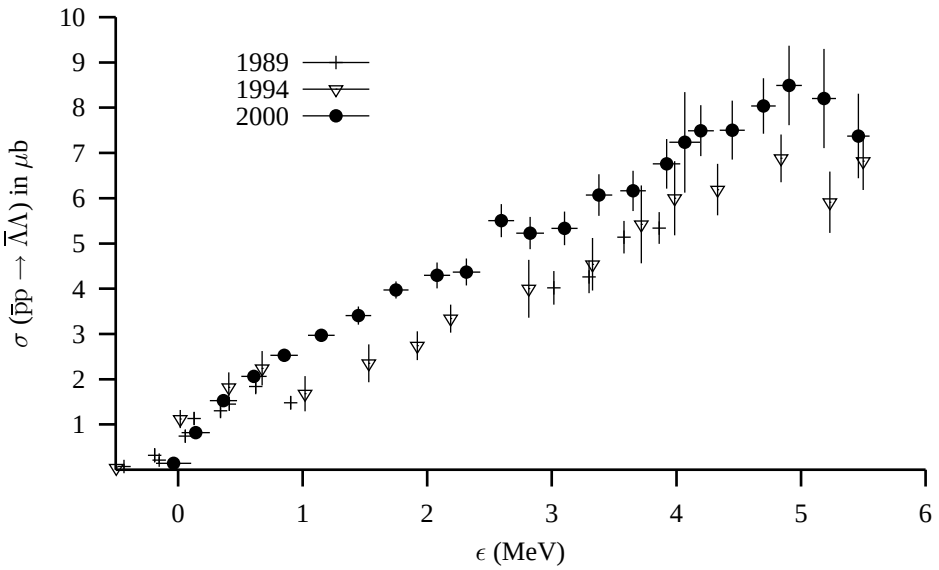

Figure 4.23: LEAR data on the $\bar{\mathrm{p}}\mathrm{p} \to \overline{\Lambda}\Lambda$ cross section at very low energy.

A puzzling structure occurred near $1\,\mathrm{MeV}$ excess energy in the 1989 data. It motivated further measurements in this threshold region. The data taken in 1994, also shown in Fig. 4.23, seemingly confirmed the structure near this momentum of $1438\,\mathrm{MeV}/c$. However more recent studies, reported

[1] A proposal from the PS199 Collaboration [334, 335] to measure the analysing power of $\bar{\mathrm{n}}\mathrm{p}$ elastic scattering by scattering $\bar{\mathrm{p}}$ on a polarised deuteron target was not accepted.

for instance at the LEAP98 Conference [339], indicated a smooth behaviour of the cross-section in this energy range. The final analysis of the low-energy region [340] confirmed this result, as can be clearly seen in Fig. 4.23.

A view at the cross section of the $\bar{\mathrm{p}}\mathrm{p} \to \overline{\Lambda}\Lambda$ reaction in a wider energy range is provided in Fig. 4.24.

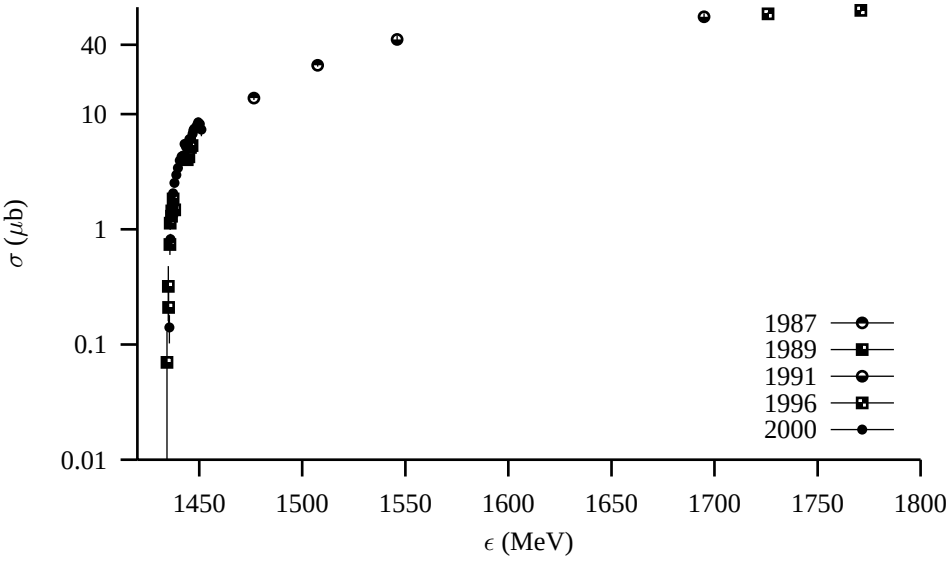

Figure 4.24: LEAR data on the $\bar{\mathrm{p}}\mathrm{p} \to \overline{\Lambda}\Lambda$ cross section at low energy.

4.8.2 Angular distribution for $\overline{\Lambda}\Lambda$ production

The angular distribution for $\overline{\Lambda}\Lambda$ production has been measured for several values of the antiproton momentum. Reference [130] displays the differential cross section at $p_{\mathrm{lab}} = 1476.5$ and $1507.5\,\mathrm{MeV}/c$. The results are reproduced in Fig. 4.25. Even at these low values of the excess energy, the distribution is far from being flat: there is an abundant contribution of P-wave scattering. This is confirmed in Ref. [124], where, for an excess energy of the order of $1\,\mathrm{MeV}$ or even lower, there is still a net asymmetry between forward and backward hemisphere in the c.m. frame.

The angular distribution has later been measured at higher energy, in particular at 1.726 and $1.771\,\mathrm{GeV}/c$ [127]. The results are shown in Fig. 4.26. The PS185 often displayed the cross section as a function of s and t in plots similar to that of Fig. 4.27. The plot emphasises that the forward peak does not start at a given angle, but at a particular value of t ($-t \simeq 0.4\,\mathrm{GeV}^2$, or $R \simeq 1/3\,\mathrm{fm}$).

4.8.3 Polarisation for $\overline{\Lambda}\Lambda$ production

The observed decay of Λ or $\overline{\Lambda}$ gives an indication on its polarisation and hence on the polarisation and spin correlation parameters of the $\bar{\mathrm{p}}\mathrm{p} \to \overline{\Lambda}\Lambda$ reaction.

In Ref. [130], the polarisation is measured at $1476.5\,\mathrm{MeV}/c$. The data are shown in Fig. 4.28. They include the polarisation of Λ, that of $\overline{\Lambda}$ and an average. There is a fair agreement between Λ and $\overline{\Lambda}$ polarisations.

A similar comparison has been made at $p_{\mathrm{lab}} = 1507.5\,\mathrm{MeV}/c$ [130]. See Fig. 4.29. There is now an better agreement on Λ and $\overline{\Lambda}$ polarisations. From now on, the data on polarisation will correspond to an average between Λ and $\overline{\Lambda}$.

There are also data on polarisation at very low energy [124].

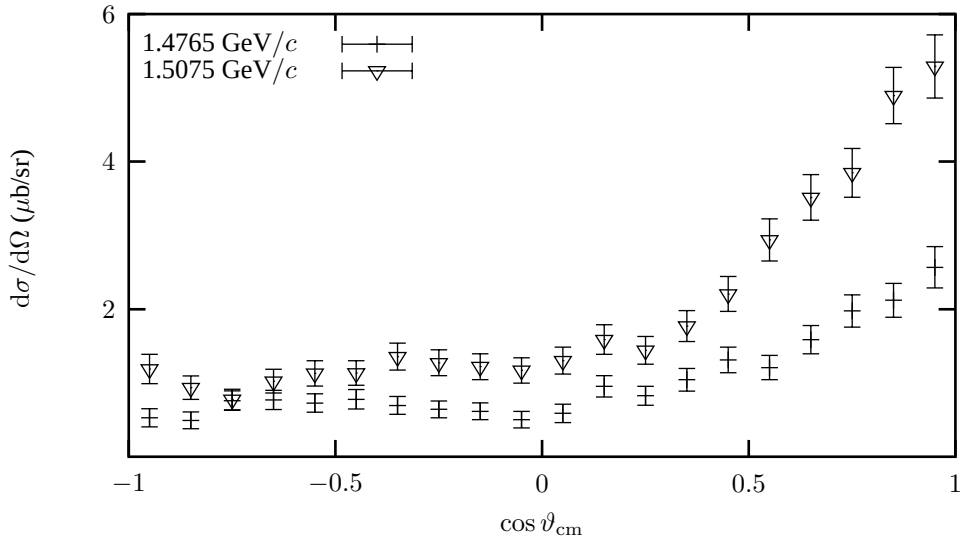

Figure 4.25: Differential cross section for $\bar{\mathrm{p}}\mathrm{p} \to \overline{\Lambda}\Lambda$ at 1476.5 and $1507.5\,\mathrm{MeV}/c$.

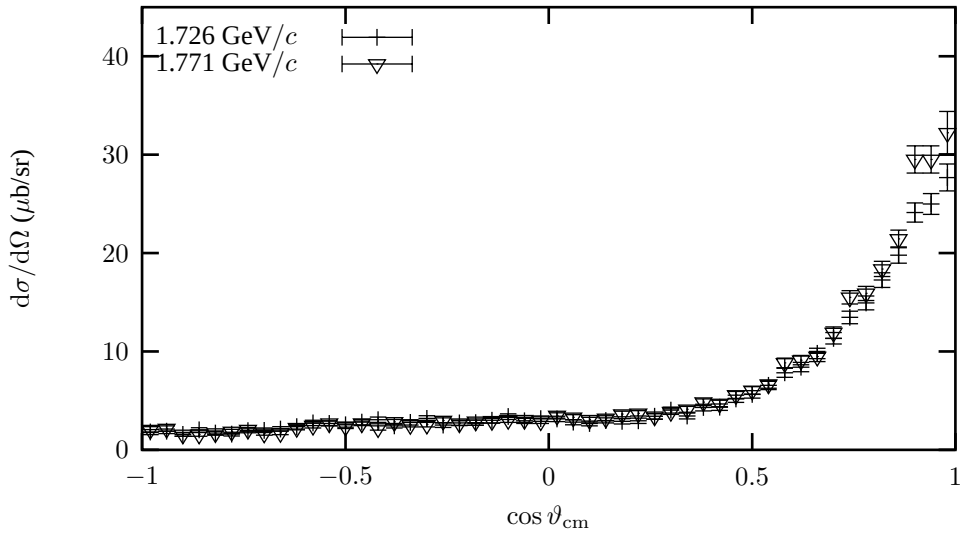

Figure 4.26: Differential cross section for $\bar{\mathrm{p}}\mathrm{p} \to \overline{\Lambda}\Lambda$ at 1726 and $1771\,\mathrm{MeV}/c$.

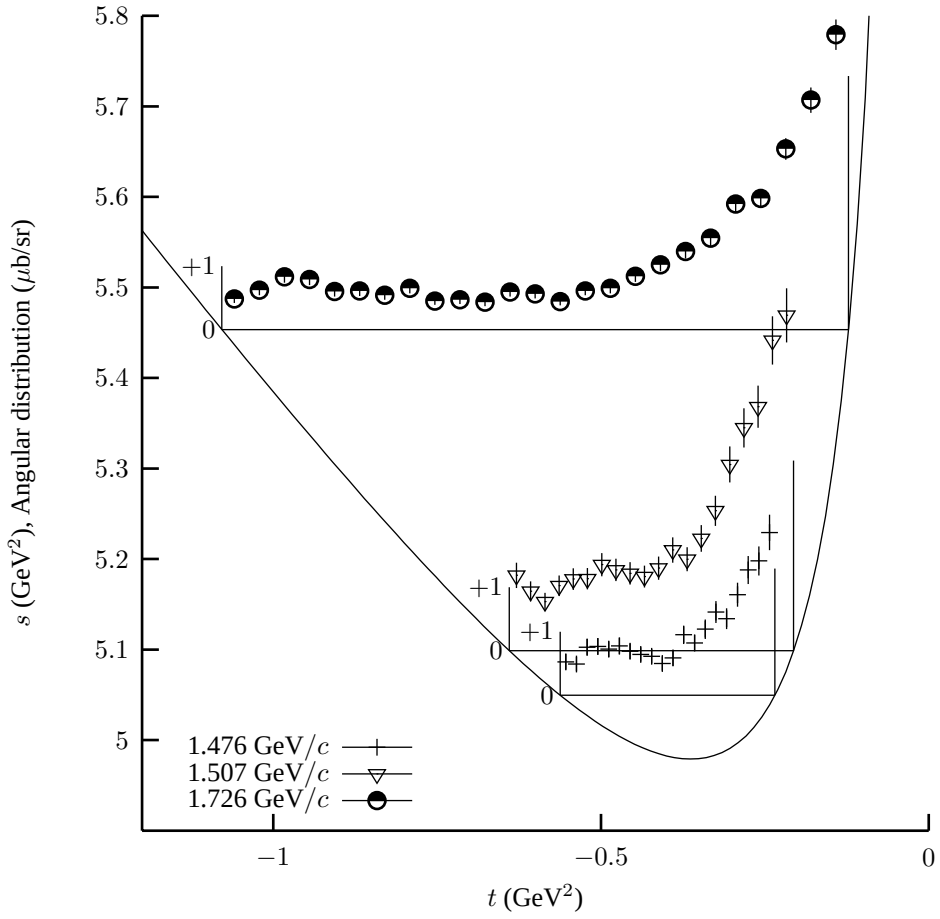

Figure 4.27: Differential cross section for $\bar{\mathrm{p}}\mathrm{p} \to \overline{\Lambda}\Lambda$ at various energies.

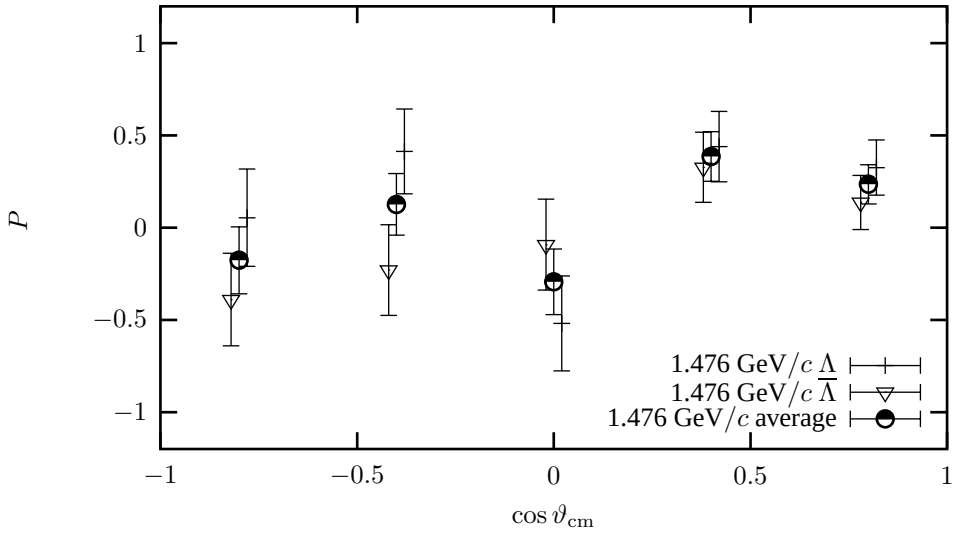

Figure 4.28: Polarisation for $\overline{\Lambda}\Lambda$ production at $p_{\mathrm{lab}} = 1476.5\,\mathrm{MeV}/c$.

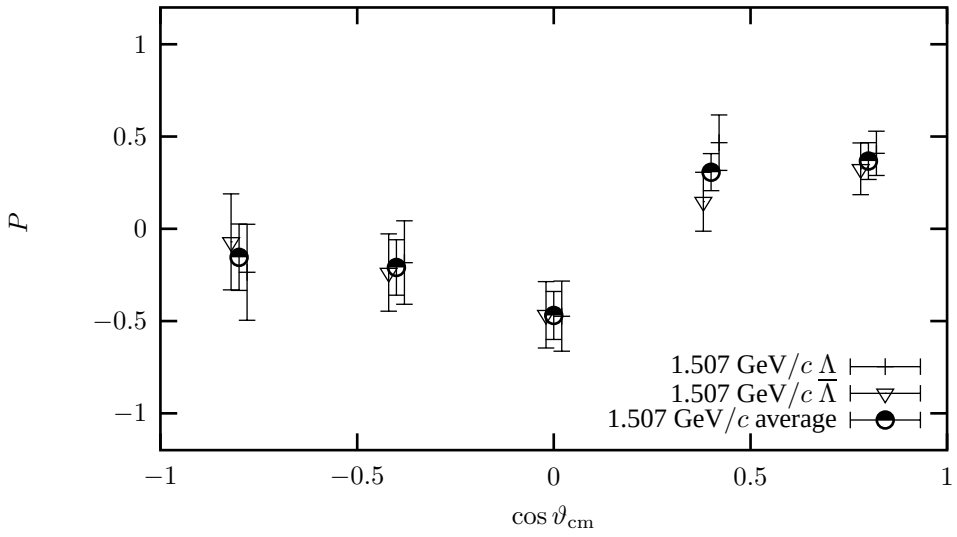

Figure 4.29: Polarisation for $\overline{\Lambda}\Lambda$ production at $p_{\mathrm{lab}} = 1507.5\,\mathrm{MeV}/c$.

Data on polarisation at higher energy, namely $p_{\rm lab} = 1.546$ and $1.691\,{\rm GeV}/c$ are given in Ref. [126] and reproduced below in Fig. 4.31. These corresponding to $p_{\rm lab} = 1.726$ and $1.771\,{\rm GeV}/c$ [127] are shown in Fig. 4.32. A summary of polarisation data at various energies as a function of t is given in Fig. 4.30.

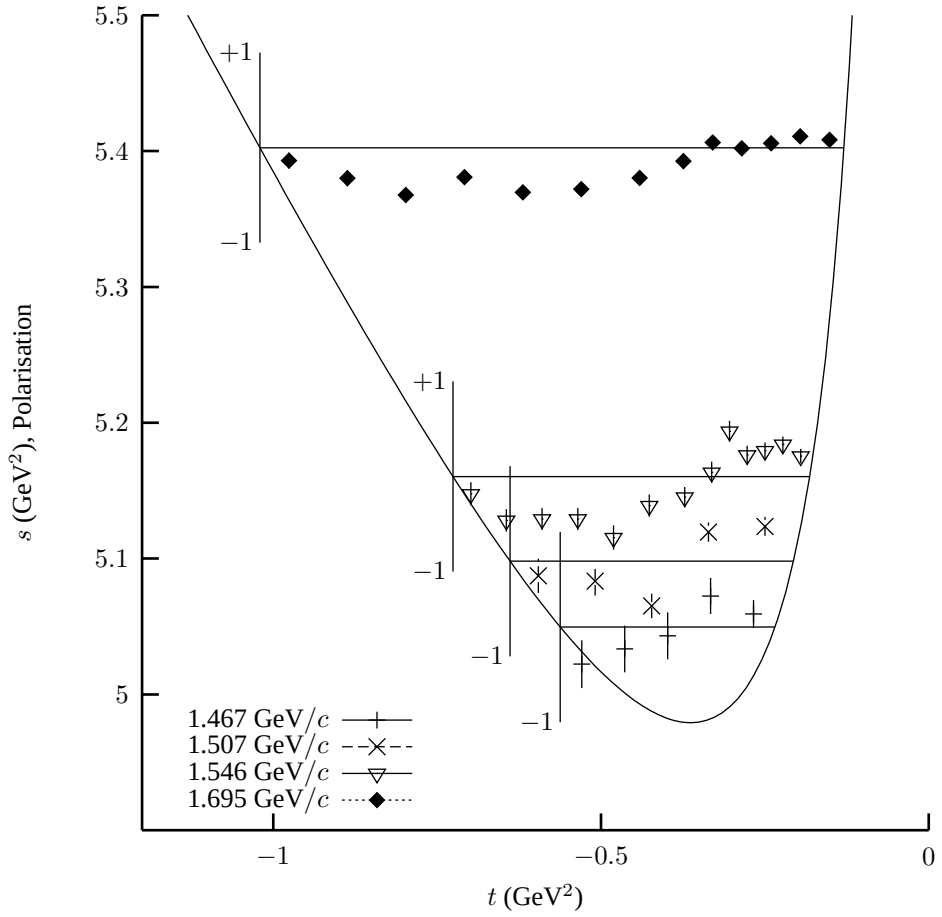

Figure 4.30: Polarisation for $\bar{\rm p}{\rm p} \to \overline{\Lambda}\Lambda$ at various energies.

The polarisation turns from negative to slightly positive values about at the same t -value ($-t \simeq 0.4\ {\rm GeV}^2$) where the forward peak of the differential cross-section starts to rise.

4.8.4 $\overline{\Lambda}\Lambda$ spin correlations

The spin correlation coefficients have been extracted for several values of the momenta. Early data [126] corresponding to $p_{\rm lab} = 1546$ and $1695\,{\rm MeV}/c$ are shown in Fig. 4.31. The measurements done at $p_{\rm lab} = 1.726$ and $1.771\,{\rm GeV}/c$ [127] are displayed in Fig. 4.32. Here F_0 is the spin-singlet fraction, introduced in Sect. 3.2. In principle, $F_0 > 0$, so data showing negative values illustrate how difficult these measurements are. Similarly a value $|C_{ij}| > 1$ is in principle not allowed.

At selected energies and angles, the correlation coefficients are remarkably large, saturating the simple unitarity limits, or even exceeding them, due to experimental uncertainties. As seen in Chapter 3, this implies strong constraints on the amplitudes and restricts drastically the range of variation of the remaining observables.

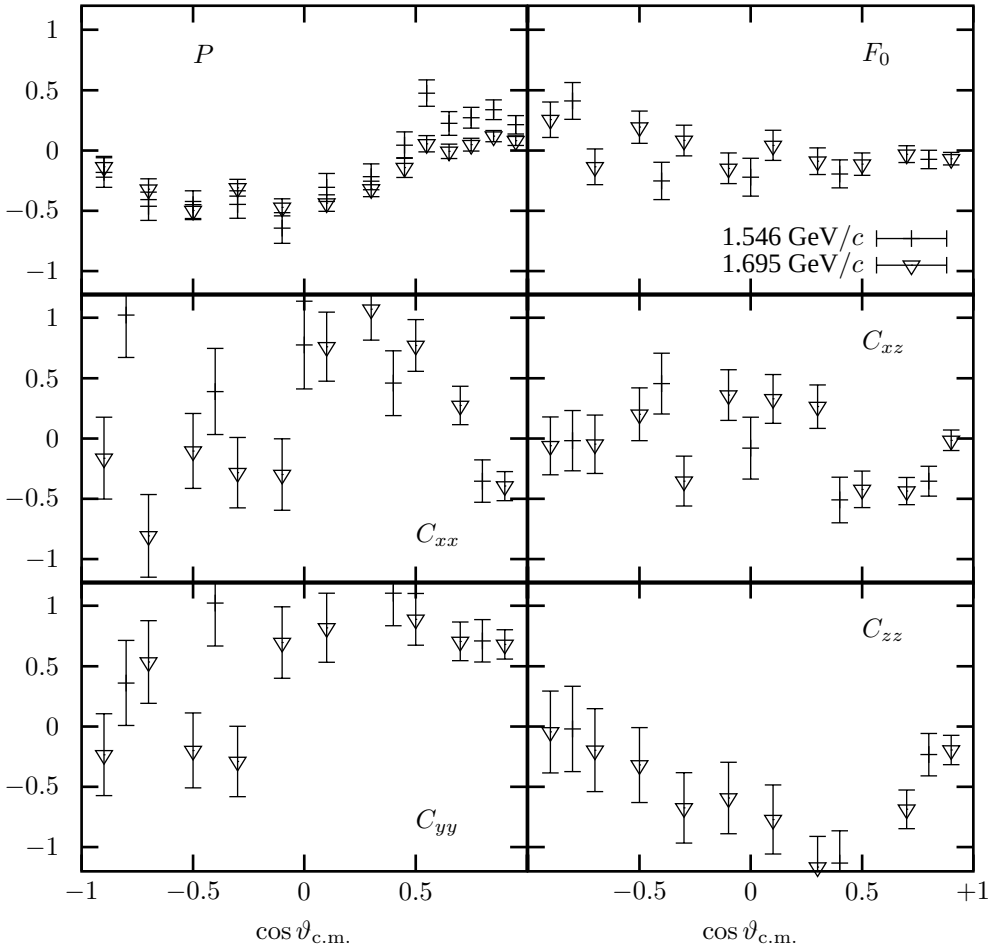

Figure 4.31: Spin observables for $\bar{\mathrm{p}}\mathrm{p} \to \overline{\Lambda}\Lambda$ at 1546 and $1695\,\mathrm{MeV}/c$.

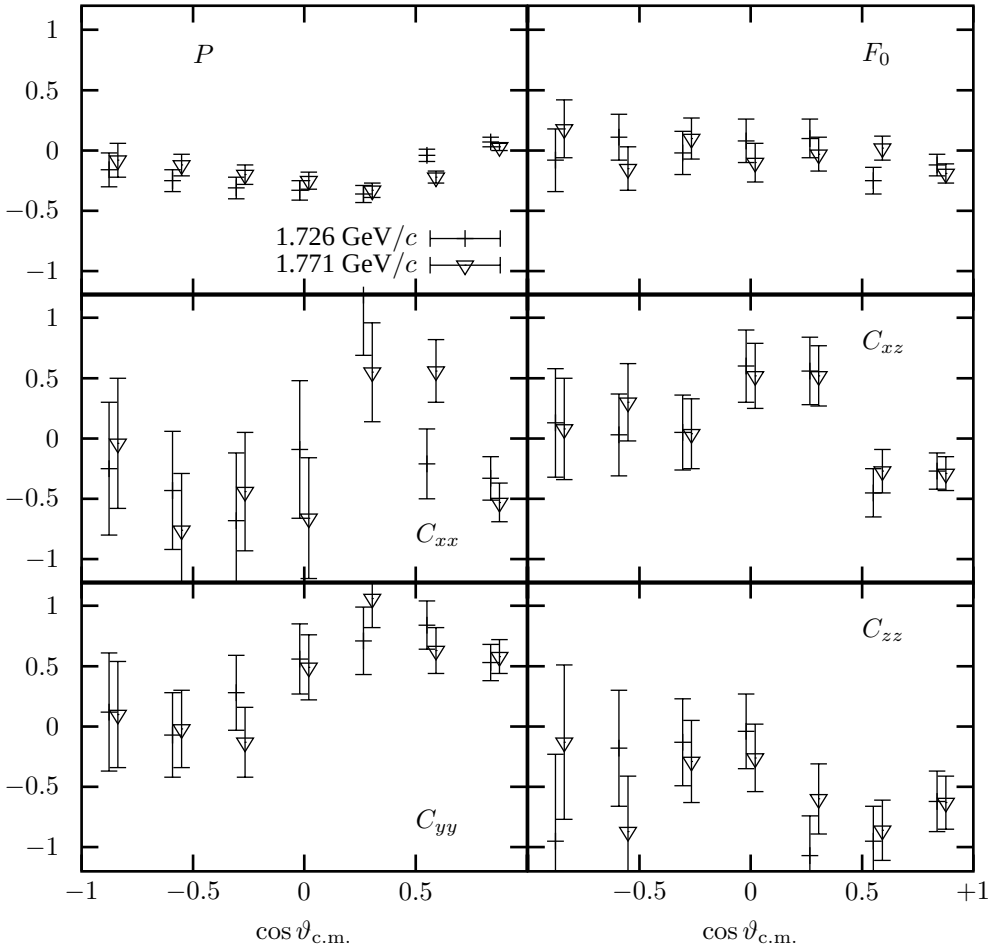

Figure 4.32: Spin observables for $\bar{\mathrm{p}}\mathrm{p} \to \overline{\Lambda}\Lambda$ at 1726 and 1771 MeV/c.

The polarisation and the spin-correlation parameters have also been measured with high statistics at 1.642 and $1.918\,\mathrm{GeV}/c$ [127]. large values of $|C_{yy}|$ or $|C_{zz}|$ are still observed at some angles. At the highest momentum, there are definitively spin-singlet contributions, i.e., $F_0 > 0$.

4.8.5 Further spin observables for $\overline{\Lambda}\Lambda$ production

The last runs of PS185 were devoted to measurements using a polarised hydrogen target, transverse to the beam.

The motivation was inspired by Holinde et al. [341, 342], Ellis et al. [215] and others. Both the K-exchange mechanism of Fig. 3.11 and the s-channel gluon-exchange process of Fig. 3.12 can accommodate the trend of the data taken on a unpolarised target, in particular the small spin-singlet fraction. The correlation between initial-state and final-state spin, as measured by D_{nn} or K_{nn}, could be more selective.

A warning, however, is that existing data on the correlations coefficients C_{ij}, if taken seriously, already restrict the domain of variation of D_{nn} and K_{nn} [183, 343].

Data with a transversally polarised target remain anyhow extremely interesting, as they allow several consistency checks. In principle, without limitation on statistics, this would permit reconstruction of all 6 amplitudes (of course to an overall phase) [2].

The last data of PS185 are currently being analysed.

4.8.6 $\overline{\Lambda}\Sigma_0 + \mathrm{c.c.}$ production

The first measurement of $\overline{\Lambda}\Sigma_0 + \mathrm{c.c.}$ by the PS185 collaboration was performed at $1.695\,\mathrm{GeV}/c$ [125]. The cross section is $7.53 \pm 0.35\,\mu\mathrm{b}$. A Legendre analysis in Ref. [125] shows that the magnitude of the partial waves, as the angular momentum increases, decreases less rapidly than for $\overline{\Lambda}\Lambda$ production. The angular distribution is shown in Fig. 4.33.

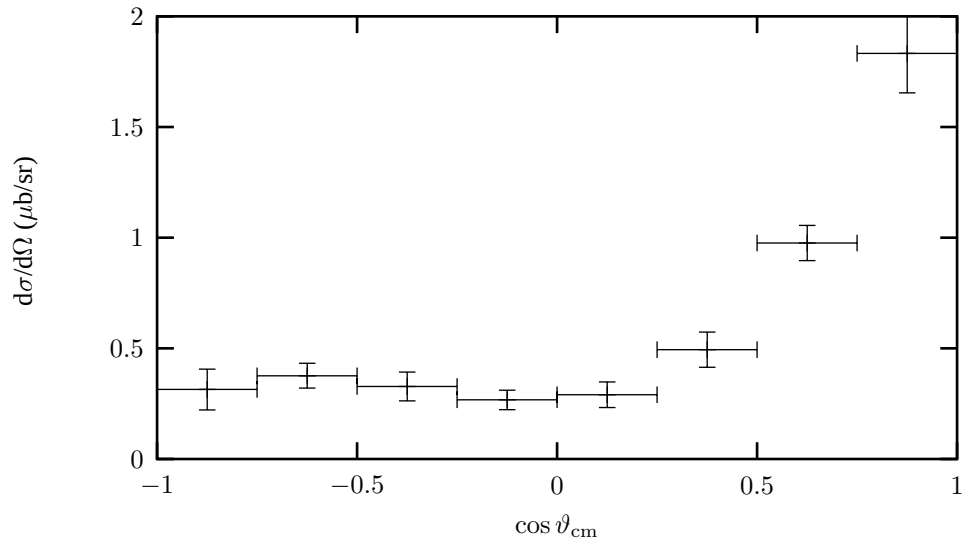

Figure 4.33: Angular distribution for $\overline{\Lambda}\Sigma_0 + \mathrm{c.c.}$ production at $1.695\,\mathrm{GeV}/c$

Other measurements of the $\overline{\Sigma}^0\Lambda$ channel have been done at 1726 and $1771\,\mathrm{MeV}/c$ [128]. The differential cross section is shown in Fig. 4.34. The $\overline{\Sigma}^0\Lambda$ and $\overline{\Lambda}\Lambda$ angular distributions exhibit a

[2] We thank B. Quinn and K. Paschke of the PS185 collaboration for useful correspondence on this subject.

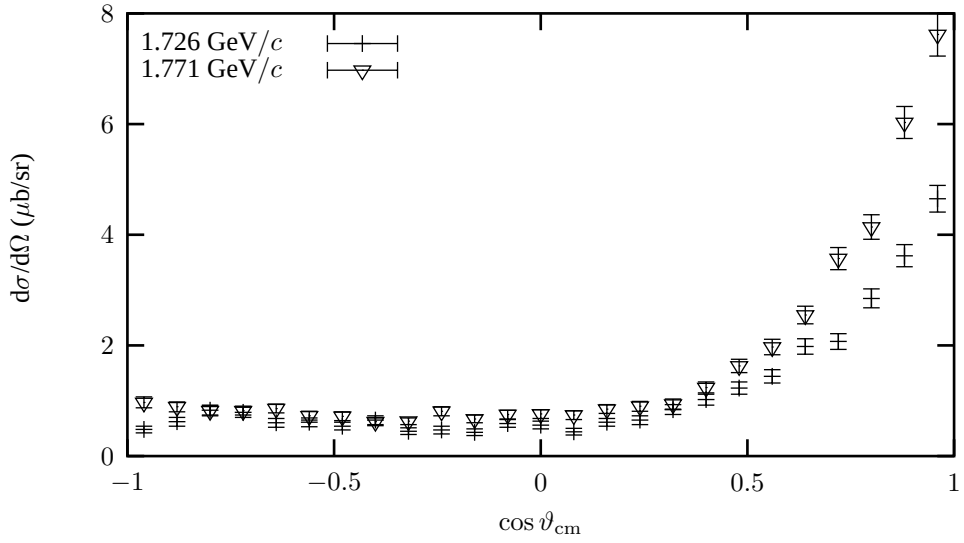

Figure 4.34: Angular distribution for $\overline{\Lambda}\Sigma_0 + \mathrm{c.c.}$ production at 1.726 and $1771\,\mathrm{GeV}/c$.

similar shape at these energies. A more precise comparison of the two reactions at the same excess energy is done in Ref. [128]. The $\overline{\Sigma}^0\Lambda$ differential cross-section, as a function o the invariant transfer t, exhibit a steeper forward peak, with a slope b (defined as $I \propto \exp(-b|t|)$ of about 11 to $14\,\mathrm{GeV}^{-2}$, as compared to $b \sim 8 - 10\,\mathrm{GeV}^{-2}$ for $\overline{\Lambda}\Lambda$.

Some spin parameters have been measured for $\overline{\Sigma}^0\Lambda$ production [128]. However, the Σ^0 polarisation spin correlations in the final state and spin-singlet fraction have error bars of the order of 1 and thus are not very meaningful. At most, one can see that F_0 tends to be larger than in the $\overline{\Lambda}\Lambda$ case, namely $F_0 \sim 0.64 \pm 0.2$ when averaged over energies and angles. This suggests that both spin-triplet and spin-singlet states contribute to the reaction. The Λ polarisation is measured more precisely. The results of [128] are reproduced in Fig. 4.35. As in the $\overline{\Lambda}\Lambda$ case, the magnitude is moderate, ± 0.3 or smaller.

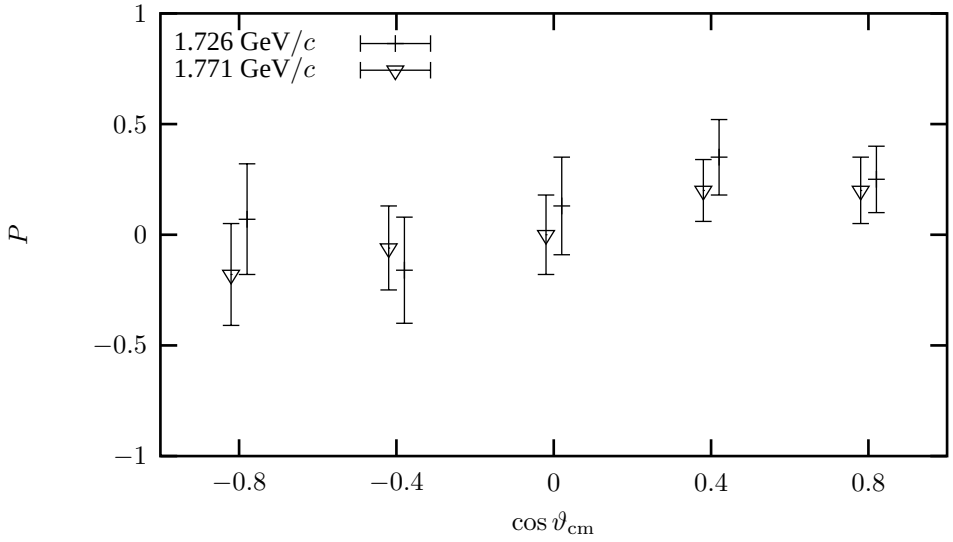

Figure 4.35: Λ polarisation for $\overline{\Lambda}\Sigma_0 + \mathrm{c.c.}$ production at 1.726 and 1771 GeV/c.

The very-low energy behaviour of $\bar{\mathrm{p}}\mathrm{p} \to \overline{\Sigma}^0\Lambda + \mathrm{c.c.}$ is analysed in Ref. [340] and compared to $\bar{\mathrm{p}}\mathrm{p} \to \overline{\Lambda}\Lambda$ at the same excess energy. Figure 3 of this reference is reproduced in our Fig. 4.36. The trend is different, showing a larger P to S ratio in $\bar{\mathrm{p}}\mathrm{p} \to \overline{\Sigma}^0\Lambda + \mathrm{c.c.}$ than in $\bar{\mathrm{p}}\mathrm{p} \to \overline{\Lambda}\Lambda$.

4.8.7 $\overline{\Sigma}\Sigma$ production

A measurement of the $\bar{\mathrm{p}}\mathrm{p} \to \overline{\Sigma}^-\Sigma^+$ cross section has been performed at 1.922 GeV/c and is presented in Ref. [129]. As mentioned by the authors, this corresponds to an excess energy $\epsilon = 23\,\mathrm{MeV}$ close to the $\epsilon = 25\,\mathrm{MeV}$ of the $\overline{\Lambda}\Lambda$ measurement performed at $1.5075\,\mathrm{GeV}/c$, and of the $\overline{\Sigma}^0\Lambda$ data taken at $1.726\,\mathrm{GeV}/c$ and already presented.

The integrated cross-sections is

$$\sigma = 3.68\,^{+0.43+0.34}_{-0.43-0.22}\,\mu\mathrm{b}, \tag{4.8}$$

where the errors are due to statistics and systematics, respectively.

The ratio of cross sections is

$$\sigma(\overline{\Sigma}^-\Sigma^+)/\sigma(\overline{\Lambda}\Lambda) = 0.14 \pm 0.02, \tag{4.9}$$

at $\epsilon(\overline{\Lambda}\Lambda) = 25$ and $\epsilon(\overline{\Sigma}^-\Sigma^+) = 23\,\mathrm{MeV}$, while [128]

$$\sigma(\overline{\Sigma}^0\Lambda)/\sigma(\overline{\Lambda}\Lambda) = 0.29 \pm 0.02, \tag{4.10}$$

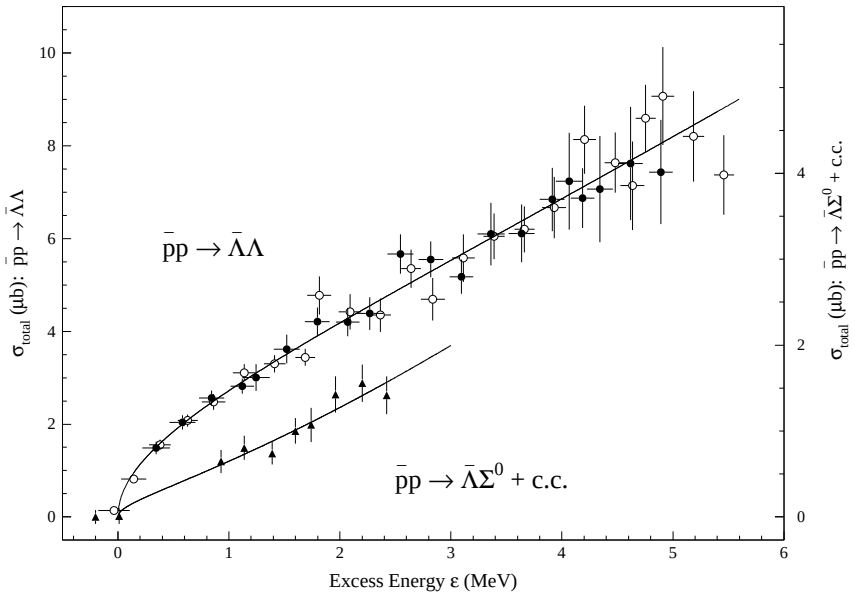

Figure 4.36: Comparison of $\bar{\mathrm{p}}\mathrm{p} \to \overline{\Lambda}\Lambda$ and $\bar{\mathrm{p}}\mathrm{p} \to \overline{\Sigma}^0\Lambda + \mathrm{c.c.}$ cross-sections at very small excess energy above their respective threshold..

at the same $\epsilon = 25\,\mathrm{MeV}$. In a Yukawa picture, this implies a smaller coupling of kaons between a proton and a Σ than between a proton and a Λ. A similar observation is made when studying the parameters required to fit the potential between hyperons and nucleons [344, 345].

The production of $\overline{\Sigma}^-\Sigma^+$ is also compared to that of $\overline{\Sigma}^+\Sigma^-$ at this antiproton momentum $p_{\mathrm{lab}} = 1.992\,\mathrm{GeV}/c$. The ratio

$$\sigma(\overline{\Sigma}^-\Sigma^+)/\sigma(\overline{\Sigma}^+\Sigma^-) = 2.4\,^{+3.0}_{-1.3}\,(90\%\,\mathrm{C.L.}) \tag{4.11}$$

is not very accurately determined and should be considered with care, since the excess energy are $\epsilon = 23$ and $\epsilon = 7\,\mathrm{MeV}$, respectively. It is consistent with measurements done at higher energy (see [129] for references).

The differential cross section for $\overline{\Sigma}^-\Sigma^+$ production at $\epsilon = 23\,\mathrm{MeV}$ excess energy is given in [129]. It is similar to the distribution of $\overline{\Lambda}\Lambda$ and $\overline{\Sigma}^0\Lambda$ at $\epsilon = 25\,\mathrm{MeV}$, but the forward peak is narrower and sharper. This angular distribution is reproduced in Fig. 4.37.

Some details about $\overline{\Sigma}^+\Sigma^-$ production have been given in recent conferences. There is no forward peak. But there seems to be an enhancement in the backward region. The differential cross-section given in Fig. 4.37, whose absolute normalisation is not determined, should be considered as preliminary. The results of the final analysis are expected shortly.

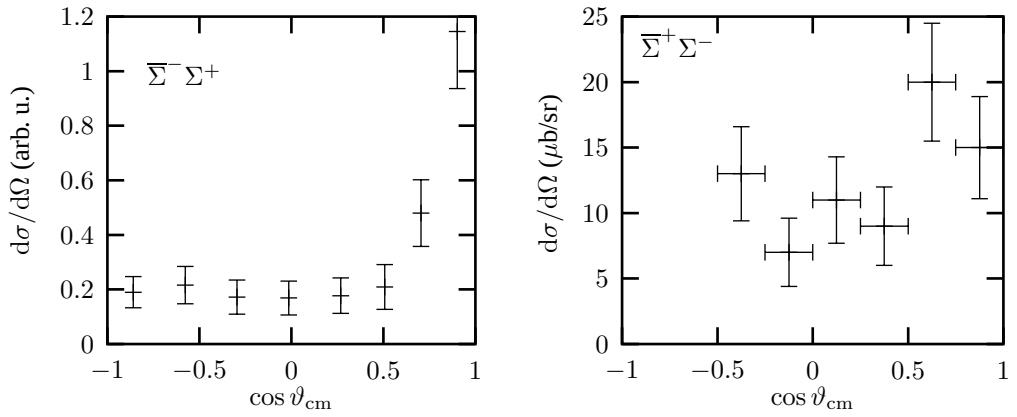

Figure 4.37: Angular distribution for $\overline{\Sigma}^-\Sigma^+$ (left) and $\overline{\Sigma}^+\Sigma^-$ (right) production. In the latter case, the units on the vertical axis are arbitrary.

Chapter 5

Protonium and antiprotonic deuterium

In this Chapter we describe the measurement of X-rays from antiprotonic hydrogen and deuterium atoms and discuss how the strong-interaction parameters are deduced from the data. Many interesting phenomena are associated with this search, a large number having been observed in the Asterix experiment. So, instead of introducing these phenomena as abstract concepts, we discuss them as they show up when presenting results from this experiment.

5.1 PS171: The Asterix experiment

The Asterix experiment was carried out by stopping antiprotons in gaseous H_2 at room temperature and pressure. A short description of the X-ray detector can be found in Sec. 2.4, a report on the performance of the full spectrometer in [150].

5.1.1 X-ray spectra with $\bar{\mathrm{p}}\mathrm{p}$ annihilation into charged particles

Figure 5.1 shows the X-ray spectrum observed in coincidence with two charged particles after stopping $200\,\mathrm{MeV}/c$ antiprotons. A double-peak structure is seen at low energies while the high-energy spectrum contains much fewer entries. The low-energy peak at $1.74\,\mathrm{keV}$ is due to the Balmer-α line, the smaller peak at $3.1\,\mathrm{keV}$ to a convolution of Balmer lines close to the series limit, denoted as L_∞. Part of the $3.1\,\mathrm{keV}$ peak is due to argon fluorescence: charged particles (or high-energy X-rays) kick an electron out of the K shell of an Ar atom. The K shell is then re-populated by emission of a $3\,\mathrm{keV}$ photon. In a segmented detector the photon may escape the local detector segment and convert elsewhere. This contribution can be estimated from the X-ray spectrum observed when there are only neutral particles in the final state (see Fig. 5.3a below) for which the argon fluorescence contribution is much smaller.

The large peak in Fig. 5.1 due to the Balmer-α line is obviously not accompanied by a Lyman-α line of similar strength. The spectrum evidences at the first glance the importance of annihilation from the 2P levels of protonium atoms: $\bar{\mathrm{p}}\mathrm{p}$ atoms in 2P states annihilate instead of radiating Lyman-α X-rays. A fit to the data [152] shows some (weak) evidence for Lyman radiation with a fractional intensity of the K_α line of $(1.0 \pm 0.4) \times 10^{-3}$, compared to a total yield of the Balmer series of (12 ± 2)%. These data are used – together with Eq. (3.73) – to determine an average 2P strong interaction width of (45 ± 18) meV.

The continuous background at higher energies originates from inner bremsstrahlung which is emitted in the spontaneous acceleration of charged particles in the annihilation process. The emission of bremsstrahlung quanta can be calculated in the soft-photon approximation [346]. For a final

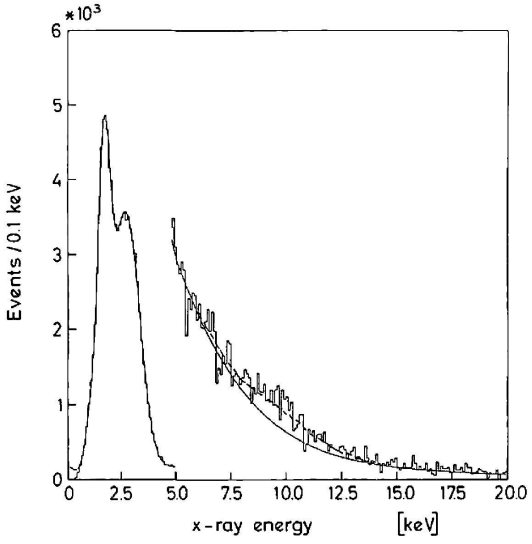

Figure 5.1: Energy spectrum of X-rays emitted by protonium atoms annihilation into final states with two charged particles. The line represents a fit taking into account the Balmer series of $\bar{\mathrm{p}}\mathrm{p}$ atoms, a (small) constant background, inner bremsstrahlung (solid line), and contributions from the Lyman series (dashed curve). The data on the right are multiplied by 20.

state characterized by a partial width $\mathrm{d}\Gamma_0$, the charges Q_i of the outgoing mesons and their four-momenta $\tilde{q}_i$, the differential width for emission of a bremsstrahlung photon (after summation over all polarizations) can be written as

$$\mathrm{d}\Gamma_{\mathrm{B}} = \left(\frac{\alpha}{4\pi^2}\right) \mathrm{d}W_B \omega^{-1} \mathrm{d}\omega \mathrm{d}\Gamma_0, \tag{5.1}$$

with

$$\mathrm{d}W_{\mathrm{B}} = -\sum_i \sum_j Q_i Q_j \frac{\tilde{q}_i . \tilde{q}_j}{(\tilde{q}_i . \tilde{k})(\tilde{q}_j . \tilde{k})} \omega^2 \mathrm{d}\Omega_k, \tag{5.2}$$

where $\tilde{k}$ is the four-momentum vector $(\omega, \vec{k})$ of the photon, and $\mathrm{d}\Omega_k$ the solid angle element into which the photon is emitted. The photon energy distribution (5.1) exhibits the expected ω^{-1} behaviour, and Eq. (5.2) gives the angular correlation between bremsstrahlung and atomic X-rays.

Photons emitted radiatively as part of the atomic cascade lead to a small alignment of the $\bar{\mathrm{p}}\mathrm{p}$ angular momentum states; thus the direction of a primarily produced meson resonance is also correlated with the photon direction [347]. But in the subsequent decay of the resonance, this weak correlation is washed out; angular correlations between, e.g., Balmer X-rays and charged particles can be neglected.

Equations (5.1,5.2) can be evaluated in the rest system of the two charged particles assuming that they are pions; contamination by kaons is known to be small. The measured angular distributions depends on experimental cuts taken into account in the Monte Carlo simulations. In particular, to identify the X-ray, a minimum angular spacing is required between the direction of a X-ray and that of the nearest charged particle.

Figure 5.2 (upper panel) shows the angular distributions for X-rays with energies below $5\,\mathrm{keV}$ (mostly originating from the atomic cascade). The angle θ is defined with respect to the direction of the higher-momentum particle; the angle ϕ is the polar angle, $\phi = \pi$ for X-rays which are found in the direction of the total laboratory momentum of the two charged particles. The solid lines represent an isotropic distribution in the laboratory system. Figure 5.2 (lower panel) shows

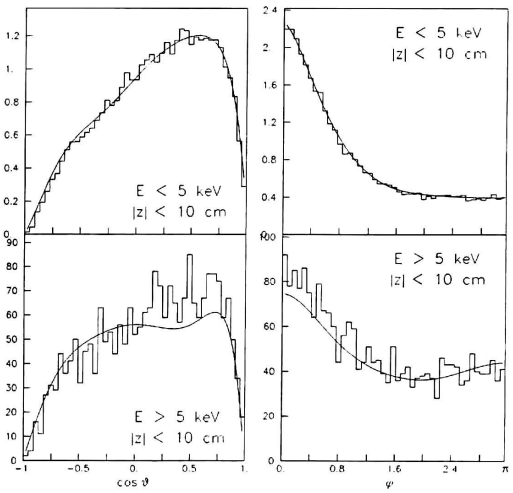

Figure 5.2: Angular distributions of X-rays originating from the atomic cascade of antiprotonic hydrogen atoms ($E < 5\,\mathrm{keV}$) and from inner bremsstrahlung ($E > 5\,\mathrm{keV}$). Histogram: data; solid line: Monte Carlo simulation.

the angular distributions for X-rays above $5\,\mathrm{keV}$ (originating mostly from bremsstrahlung). It was calculated from the measured particle momenta using formula (5.2) to calculate the direction of the photon emission. The differential bremsstrahlung-emission width was calculated for each individual event. After summation over all events, a theoretical bremsstrahlung spectrum is obtained.

The two processes – radiative transitions to lower energy levels with subsequent annihilation and annihilation with emission of inner bremsstrahlung – lead to the same final state, and interference effects may occur. They could be particularly disturbing for the Lyman series since in this case the amplitudes for radiative transitions and for bremsstrahlung are of comparable magnitude. The phase of the amplitude changes by 180° while crossing the resonance position while the phase of the hadronic transition amplitude remains, at least approximately, constant. Wrong results for the line centre and width could be obtained when constructive and destructive interferences on the two sides of the K_α-line are neglected. This effect could be particularly dangerous in low-statistics experiments in which the line shape cannot be unambiguously determined from data. In inclusive protonium experiments, many hadronic final states contribute likely having different, statistically distributed, hadronic phases. Hence there is a good chance that the superposition of all lines should result in an undistorted line shape. Only when exclusive final states are selected, interferences are likely to play a role.

5.1.2 X-ray spectra with $\bar{\mathrm{p}}\mathrm{p}$ annihilation into neutral particles only

The contributions from bremsstrahlung and the residual background can be suppressed quantitatively by two further techniques:

- selecting *all-neutral* events in which the $\bar{\mathrm{p}}\mathrm{p}$ atom annihilates into neutral particles with no associated bremsstrahlung;
- requiring two X-rays in coincidence.

The fraction of $\bar{\mathrm{p}}$ annihilation in liquid H_2 into all-neutral final states is given by the ratio of frequencies f [348]

$$\frac{f(\bar{\mathrm{p}}\mathrm{p} \rightarrow \text{neutral particles})}{f(\text{all annihilations})} = (3.6 \pm 0.4)\% \tag{5.3}$$

In all-neutral final states (defined by the absence of detected charged particles), a small bremsstrahlung contribution survives due to events in which two charged particles were produced but escaped detection. The coincidence requirement (together with an energy cut) displays only those events in which the atomic cascade reached the 2P level. Only the K_α line is observed and thus the interpretation of the resulting X-ray spectrum is facilitated.

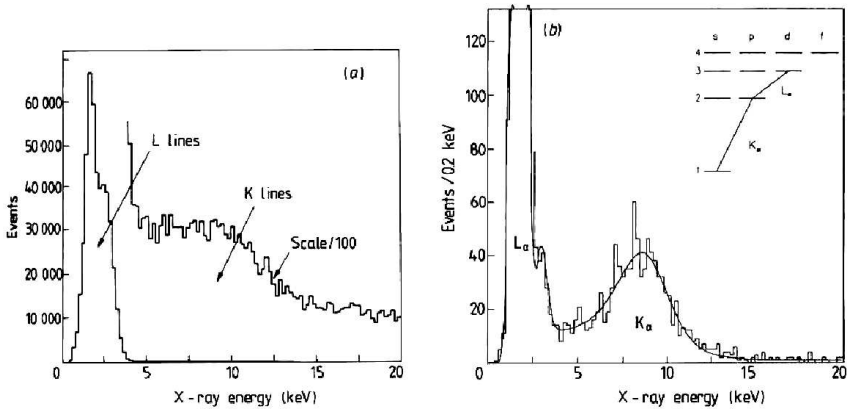

Figure 5.3: X-ray spectrum of protonium for events with neutral particles only in the final state. a) The spectrum shows the Balmer series but the residual background is still too large for an unambiguous identification of the Lyman series. b) X-ray spectrum of protonium for all-neutral events for two coincident X-rays. The energy of the more energetic X-ray is shown. The peak at $8.67\,\mathrm{keV}$ is due to the Lyman-α line. The line shape theory of Ericson and Hambro is used to fit the data.

Results using 300 MeV/c antiprotons were reported in [151]. Figure 5.3a shows the X-ray spectrum obtained by stopping $105\,\mathrm{MeV}/c$ antiprotons and requiring absence of any charged particle in the final state [153]. The spectrum is dominated by the Balmer series and does not yet allow unambiguous conclusions on the presence of the Lyman series. The situation improves when coincidences between two X-rays are required. In Fig. 5.3b only events are considered with two X-rays observed in coincidence; the energy of the more energetic X-ray is plotted. The low-energy peak at $1.74\,\mathrm{keV}$ originates from coincidences of a line belonging to the M series with a L_α line; note the absence of L_∞. The broad peak at about $8\,\mathrm{keV}$ stems from coincidences of an L X-ray with a K_α line. The apparent width of the peak ($\sim 4\,\mathrm{keV}$) is much broader than the experimental resolution of $2.4\,\mathrm{keV}$ indicating a sizable broadening due to strong interactions. When a cut is made to select events with one X-ray in the $(6.9-10.9)\,\mathrm{keV}$ energy interval, the energy distribution of the second X-ray shows contributions from the full Balmer series.

The proper line-shape theory for broad lines (for which $\Gamma \ll \epsilon$ is not satisfied) is by no means trivial. To first order, the K_α line-shape should correspond to a Lorentzian distribution. The detector resolution has to be taken into account. The convolution of a Lorentzian line with a Gaussian resolution function is called Voigt function

$$F(E) = \int_{-\infty}^{+\infty} \frac{A}{(E-E_0)^2 + (\Gamma/2)^2}\, \exp\{-\frac{(E'-E)^2}{2\,\sigma^2}\}\,\mathrm{d}E' \tag{5.4}$$

When the detection efficiency varies across the line, the Voigtian line shape has to be folded with it. The numerator A in (5.4) is constant only when the transition matrix element for the radiative transition does not dependent on energy. This is, however, not the case. Electric dipole transitions prefer more energetic transitions suggesting that A in (5.4) is proportional to E^3. However, this integral would diverge. The situation was analysed by Ericson and Hambro [349] who developed a line-shape theory for broad lines. From the requirement of probability conservation, they deduced

that the term A contains an energy dependence

$$I_{\rm EH}(E) = \frac{(2-\beta)(1+\beta)^2}{\beta^2(2+\beta)^7(4-\beta)^2(3-\beta)^2} \left[{}_2{\rm F}_1\left(5, 1-\beta, 5-\beta; \frac{\beta-2}{\beta+2}\right)\right]^2 , \qquad (5.5)$$

where $\beta = (1/4 + E/12.49)^{-1/2}$ and ${}_2{\rm F}_1$ is the hypergeometric function. In the proximity of the resonance energy E_0, the relation $I_{\rm EH}(E) = E$ holds to a good approximation. A description of results from fitting the data of Fig. 5.3 with different line shape theories can be found in [350]. Eq. (5.5) gives the best description of the data, with a central energy of the line at $E_{\rm 1S} = 8.67 \pm 0.15\,{\rm keV}$. The photon energy is shifted to a lower value than expected from QED ($\epsilon_{\rm 1S}$ is negative), the 1S level is shifted to a higher energy ($\Delta E_{\rm 1S}$ is positive). Thus a final result of

$$\epsilon_{\rm 1S} = -\Delta E_{\rm 1S} = -0.74 \pm 0.15\,{\rm keV}\,, \qquad \Gamma_{\rm 1S} = 1.60 \pm 0.40\,{\rm keV}\,, \qquad (5.6)$$

is obtained.

The yield of Balmer X-rays in all-neutral events is $(13 \pm 2)\%$. This is surprisingly close to the value $(12 \pm 2)\%$ obtained with charged particles in the final state. Annihilation from S-states into all-neutral events proceeds dominantly only via the ${}^1{\rm S}_0$ state (annihilation into any number of π^0 and η requires positive C-conjugation) which has a statistical weight of 1/4. In P-wave, annihilation into all-neutral final states is allowed from spin-triplet states, with a statistical weight of 3/4. In spite of this statistical argument the probability of the protonium atom to annihilate into all-neutral events from P-states is only $(13 \pm 2)/(12 \pm 2)$ times larger from S-states. We deduce

$$\frac{f_{\rm P}(\bar{\rm p}{\rm p} \to \text{neutral particles})}{f_{\rm P}(\text{all annihilations})} = (3.9 \pm 1.0)\%\,. \qquad (5.7)$$

The fraction of all-neutral events in which a K_α X-ray is emitted after a Balmer X-ray is detected is $r_{\rm K} = (0.79 \pm 0.20)\%$. We may now assume that all-neutral events come only from positive-parity states. (This is true for the majority of all-neutral events but not for those which contain strange particles or ω-mesons decaying into $\pi^0\gamma$.) And we assume that the protonium spin is conserved in radiative transitions, that there are no intercombination lines. Then we can deduce the strong interaction width of the $2^1{\rm P}_1$ level.

The total number of L X-ray followed by annihilation into neutral particles is $(13 \pm 2)\% \times (3.9 \pm 1.0)\%$. The number of K_α X-ray followed by all-neutral annihilation is $r_{\rm K}$ times smaller. This gives

$$\Gamma(2^1{\rm P}_1) = 51 \pm 18\,{\rm meV}. \qquad (5.8)$$

5.1.3 The cascade time

The Asterix collaboration determined the cascade time of $\bar{\rm p}{\rm p}$ atoms [154]. For 90 000 events with four tracks coming from a common vertex, the annihilation point was determined (with a resolution of ± 2 mm). The data were split into events with vertices in the entrance counter T2 and in the exit counter T4 and, along the H_2 target, into 12 slices of 5 cm length (see Fig. 2.17). For each of these 14 positions, the mean time of the two inner proportional counters was determined.

Fig. 5.4 shows the mean time spent by antiprotons the scintillation counter at the entrance of the target and their annihilation. The time increases with the distance traveled by antiprotons before capture, but those stopping immediately after the scintillation counter T2 need

$$\tau = (5.1 \pm 0.7)\,{\rm ns} \qquad (5.9)$$

more time than those stopping in T2. The cascade time in solids is some ps only, hence the time difference τ corresponds to the time elapsed between capture in H_2 and annihilation, at normal pressure and temperature,

The solid line in Fig. 5.4 is obtained by numerical integration of the Bethe–Bloch formula. The integration also yields the kinetic energy of antiprotons stopping in front of T4: when they entered the target they had $E_{\rm kin} = 3\,{\rm MeV}$.

The Obelix experiment [351] performed similar measurements using H_2 gas at four different pressures. They determined the time antiprotons need to reach the downstream end of the target. Antiprotons stopping in gas need a long time and produce the Gaussian time distribution in Fig. 5.5. Antiprotons reaching the exit wall may have some residual kinetic energy. These antiprotons traverse the target at a larger speed and the measured time difference is smaller. These antiprotons produce the steep rise at short times in Fig. 5.5. The time of flight of antiprotons stopping on the wall surface is obtained by linear extrapolation to the very latest antiproton annihilation on the wall. The difference between the Gaussian peak and extrapolated value gives the cascade time. A finite time resolution gives entries at late times, neglecting it favors cascade times which are too short. Table 5.1 lists the final results.

In liquid H_2, the cascade time is too short to be measured. However, for the Σ^-p system, the time can be deduced which elapses from the moment where the Σ^- has a residual velocity of 0.004 c (where the sum of the measured decay momenta does not yet vanish) to nuclear absorption [352]. This time is an upper limit for the cascade time and, likely, a good estimate for it. It is included in Table 5.1. For convenience, we summarise the results in Fig. 5.6.

Table 5.1: Cascade time for antiprotons stopping in H_2 as measured in the Asterix and Obelix experiments.

Pressure (mbar)	Atom	Cascade time (ns)	Reference
LH_2	Σ^-p	$\leq 5 \times 10^{-3}$	[352]
STP	$\bar{\rm p}$p	5.1 ± 0.7	[154]
150 ± 1	$\bar{\rm p}$p	6.7 ± 1.1	[351]
9.8 ± 0.05	$\bar{\rm p}$p	34.3 ± 2.4	[351]
5.8 ± 0.05	$\bar{\rm p}$p	59.9 ± 6.0	[351]
3.4 ± 0.05	$\bar{\rm p}$p	84.1 ± 10.3	[351]

5.2 PS174: The cold gas experiment

The cold gas experiment used a variable H_2 gas density over the range from 10 to 1/8 times STP. The first results were obtained using antiprotons with momenta of $300\,{\rm MeV}/c$ and a Si(Li) detector [168]. We discuss here the final results using Si(Li) detectors [169] and two gas-scintillation proportional detectors (GSPD) [167].

Figure 5.7 shows the low-energy part of the X-ray spectrum of antiprotonic hydrogen and deuterium atoms. Contributions from individual lines of the Balmer series are clearly identified. Similar data were obtained for a wide range of H_2 densities; they provide valuable information about the cascade processes which precede the emission of X-ray lines. The intensities are listed in Tables 5.4 and 5.5.

The high-energy part of the X-ray spectrum [169] is shown in Fig. 5.8 for various H_2 densities. There are striking differences between the data sets: at the largest density, only one line is observed which can be identified with the limit of the Lyman series. At moderate densities a further line is seen, the K_α line, which becomes the strongest component at the lowest density. Below atmospheric pressure, background lines from antiprotonic oxygen and carbon show up due to inadequate gas tightness. In comparison to the K_α line, they have narrow widths. The data were fitted

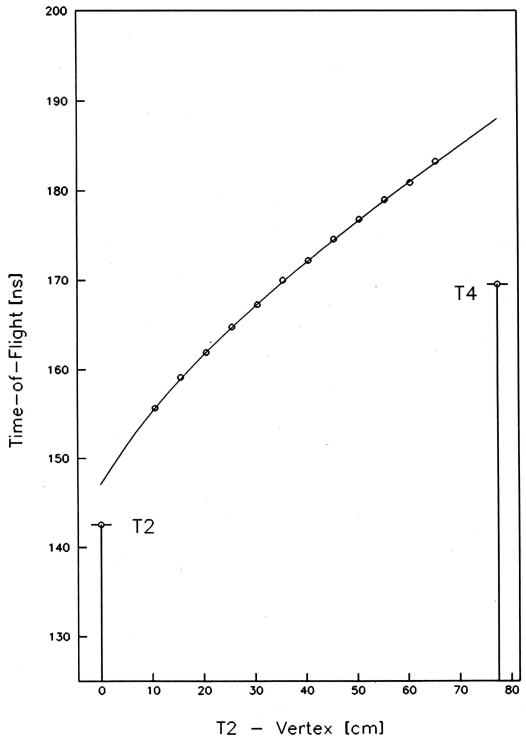

Figure 5.4: The mean time at which annihilation occurs as a function of the annihilation vertex. Annihilation immediately after the entrance window is delayed by 5.1 ns compared to annihilation in the entrance window due to the time which elapsed from capture of an antiproton in gaseous H_2 and annihilation.

Figure 5.5: Annihilation time distribution of events for which the vertex is reconstructed close to the exit wall. In-gas annihilation show a (late) Gaussian distribution. Antiprotons with higher velocities reach the end wall and annihilate early; the latest antiprotons (defined by the linear fit) annihilate on the wall surface.

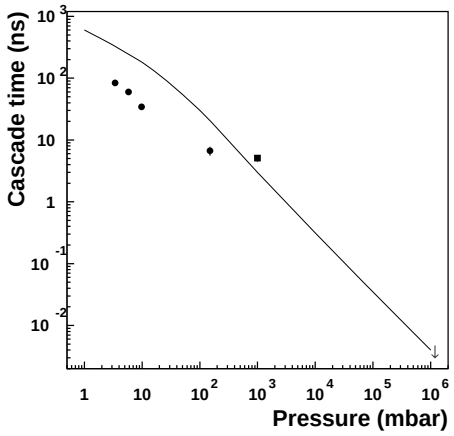

Figure 5.6: Cascade time of antiprotons in H_2. Dots: Obelix; square: Asterix; upper limit (↓): from Σ^- stopping in liquid D_2.

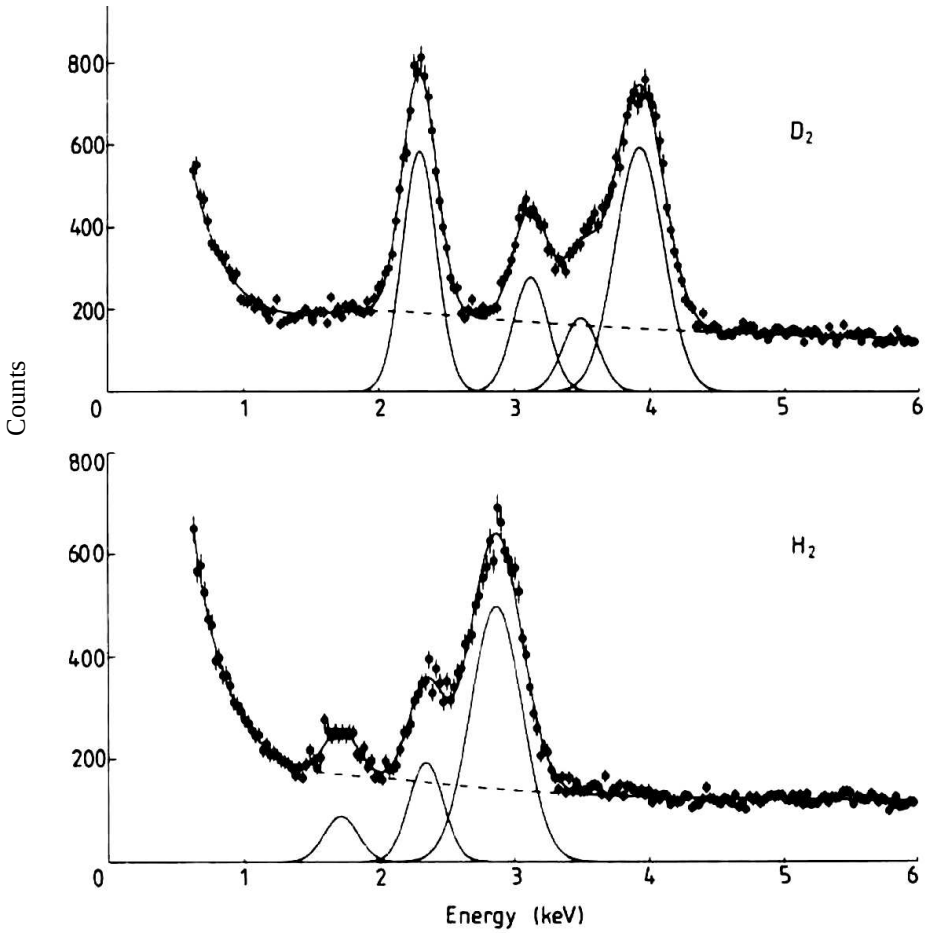

Figure 5.7: X-ray spectrum of protonium and antiprotonic deuterium formed in gas at 0.25 ρ_{STP} as observed in the cold gas experiment by Baker et al. Individual peaks due the the Balmer series are clearly identified. The detection efficiency falls off rapidly at low energies: the L_α line at $1.74\,\mathrm{keV}$ is the strongest line.

with a polynomial background and a complex of eight lines corresponding to K_α, K_β, ..., K_∞ transitions. Their relative strengths were taken from the results of cascade calculations (see Section 5.5). The published strong-interaction parameters were obtained with the Voigt function, the use of the Hambro–Ericson line shape not leading to any significant change [353]. The strong interaction parameters determined from the five data sets are mutually consistent and give average values of

$$\epsilon_{1S} = -0.75 \pm 0.06\,\mathrm{keV}\,, \qquad \Gamma_{1S} = 0.90 \pm 0.18\,\mathrm{keV}\,, \qquad \Gamma_{2P} = 45 \pm 10\,\mathrm{meV}\,. \tag{5.10}$$

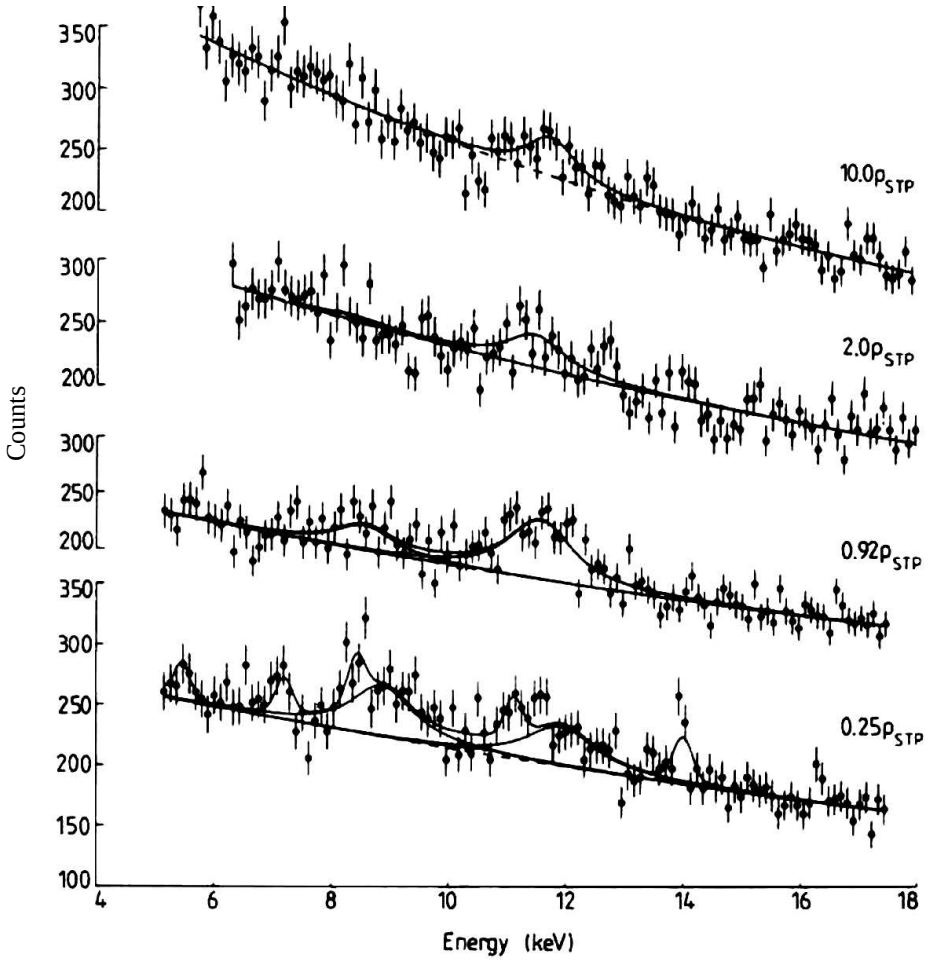

Figure 5.8: X-ray spectrum of protonium atoms for different gas H_2 gas densities. The line at $11.78\,\mathrm{keV}$ is assigned to the Lyman series limit, the line at $8.66\,\mathrm{keV}$ observed at low H_2 densities to the K_α line.

In parallel to the data with the Si(Li) detectors, the GSPD was also used to detect the X-rays.

The fit to the results, shown in Fig. 5.9, gives [170]

$$\epsilon_{1S} = -0.73 \pm 0.05\,\mathrm{keV} \qquad \Gamma_{1S} = 1.13 \pm 0.09\,\mathrm{keV}\,. \tag{5.11}$$

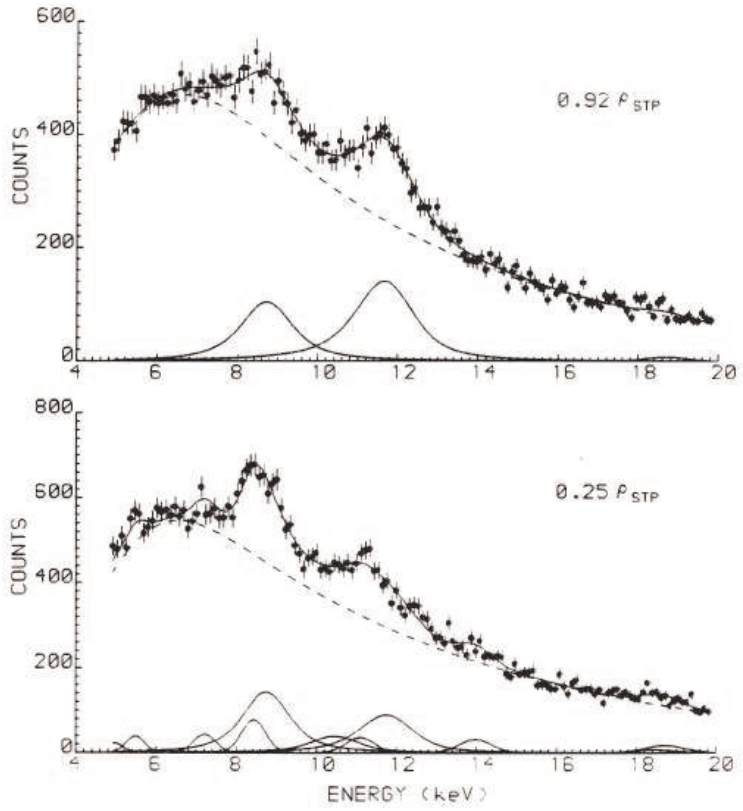

Figure 5.9: X-ray spectrum of protonium atoms. The line at $11.78\,\mathrm{keV}$ is assigned to the Lyman series limit, the line at $8.66\,\mathrm{keV}$ observed at low H_2 densities to the K_α line.

The Balmer series was not observed because of the need of rather thick windows. Thus no value was determined for Γ_{2P}. A search for the Lyman series of $\bar{\mathrm{p}}\mathrm{d}$ atoms was not successful and only upper limits (95% confidence level) for the yield of $K_{\geq\gamma}$ X-rays per stopped antiproton were given: 8×10^{-4} and 5×10^{-4} at 0.25 and 0.92 ρ_{STP}, respectively [170].

5.3 PS175 and PS207: The inverse cyclotron experiment

5.3.1 PS175

The high stopping-power of the inverse cyclotron experiment allowed the use of very thin targets or of very low H_2 gas densities, where Stark mixing plays only a minor role. Early experiments had to use a beam with 300 MeV/c momentum [173]; we show only the final results [174].

Figure 5.10 shows expanded views of a high-statistics run using a target pressure of 30 mbar H_2 (top) and D_2 (bottom). The comparison of the two spectra evidences a peak at above 8 keV, the K_α line and a small contribution from K_∞. No sign is seen from any $\bar{\mathrm{p}}\mathrm{d}$ K-line.

The authors of Ref. [174] tried to extract information on the energy splitting between the $^3S_1$ and $^1S_0$ ground states. The data are compatible with the assumption that the observed energy-distribution (after background subtraction) is composed of two lines, but one line is sufficient to fit the data.

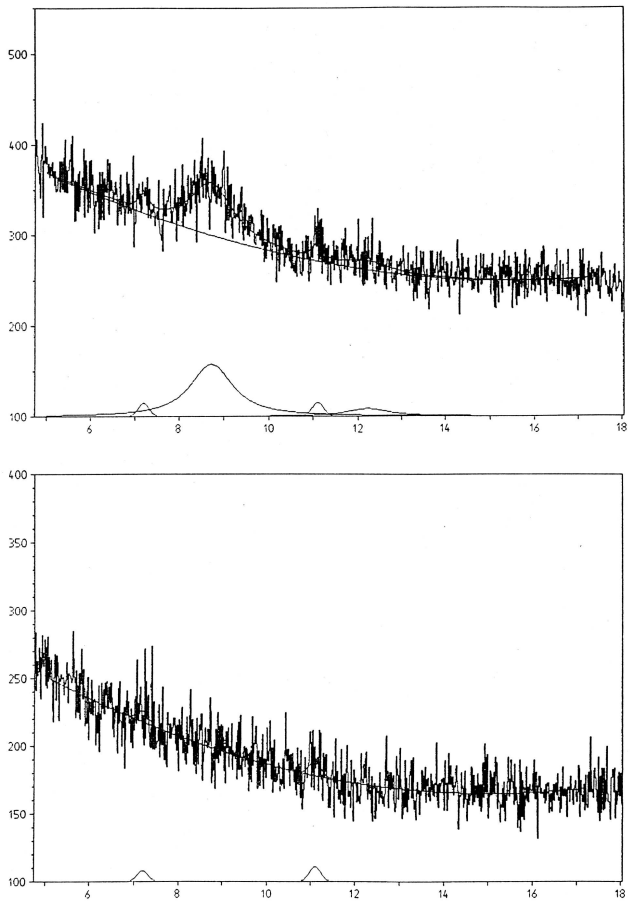

Figure 5.10: X-ray spectrum of protonium (top) and of $\bar{\mathrm{p}}\mathrm{d}$ atoms (bottom). The data are collected using a high-resolution guard-ring protected Si(Li) detector. The low-energy range is shown on the left, the high-energy range on the right.

More data were recorded than shown here. The K-lines were searched for with two Si(Li) detectors and an X-ray drift chamber. The three sets of data were combined into the final results

$$\epsilon_{1S} = -0.727 \pm 0.023\,\mathrm{keV}\ , \qquad \Gamma_{1S} = 1.160 \pm 0.078\,\mathrm{keV}\ . \tag{5.12}$$

Data with lower statistical significance were recorded at pressures from 16 to 120 mbar. The intensities are listed in Tables 5.4 and 5.5.

5.3.2 PS207

In 1990, it was proposed to combine the cyclotron trap with a high-resolution crystal spectrometer to study the line splitting and broadening of the 2P hyperfine levels of $\bar{\mathrm{p}}\mathrm{p}$ and $\bar{\mathrm{p}}\mathrm{d}$ atoms [354]. We first discuss the results obtained using as X-ray detectors three Charged Coupled Devices (CCD's) and not yet the crystal spectrometer. With these detectors, the Balmer series and the Lyman-α line of protonium [175, 176] and of antiprotonic deuterium [177] atoms were studied.

Figure 5.11 shows the energy spectrum observed when antiprotons were stopped in the cyclotron trap operated at 20 mbar of H_2 (a) and D_2 (b) gas. The low-energy range demonstrates remarkable

achievements in technology: individual lines are clearly identified, the L_α being the strongest one. Even the M series limit is observed, in H_2 as a shoulder, in D_2 as a peak.

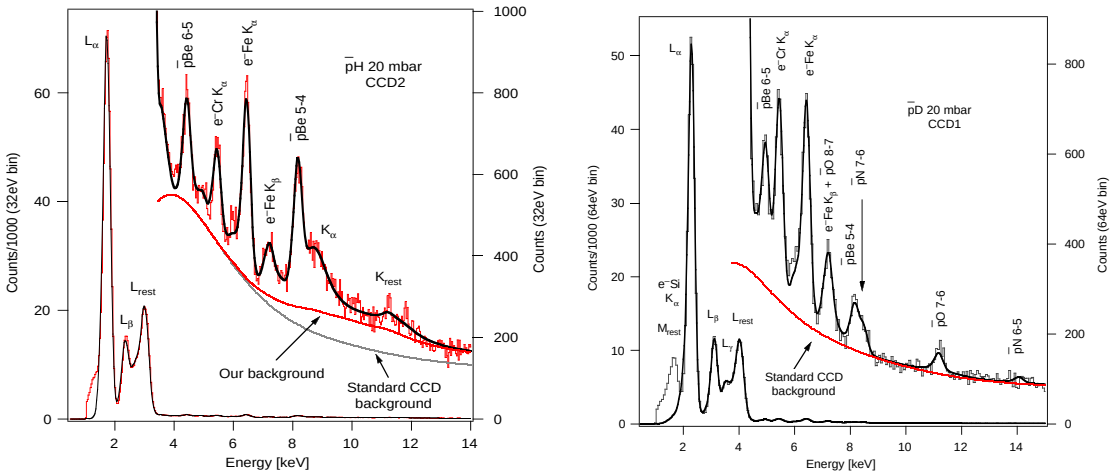

Figure 5.11: X-ray spectrum of protonium (left) and $\bar{p}d$ atoms (right), from experiment PS207.

The high-energy part of the spectrum is contaminated by lines from electronic fluorescence and from heavier antiprotonic atoms. In addition, there are at least two further sources of background. One source is present in $\bar{p}p$ and $\bar{p}d$ data and called 'standard CCD background'. It contains inner bremsstrahlung (as discussed in Section 5.1.1) and contributions from other sources. The 'standard CCD background' was assumed in [176] to be the same for H_2 and D_2. The difference of the spectra for H_2 and D_2 can, however, not be assigned to the Lyman series. There is an additional source of background of unknown origin, present only in the H_2 data. This additional background was assigned to coherent interference between K-lines and bremsstrahlung, and then subtracted incoherently by the requirement that all three CCD's gave compatible results on X-ray energies, widths and yields for the K line series. The correlation of background fit and final result was not taken into account when the final errors were evaluated.

In Fig. 5.12 we present the energy spectra after background subtraction. The observation of K_α lines from $\bar{p}p$ is obvious. The data are fitted with a single Voigtian function. The results from this fit and two analogous fits to data from two further CCD's are displayed in Table 5.2.

Table 5.2: Energy shift and width (in eV) of the 1S width of $\bar{p}p$ and $\bar{p}d$ in the three CCD's and the final result.

	$\epsilon_{\bar{p}p}$	$\Gamma_{\bar{p}p}$	$\epsilon_{\bar{p}d}$	$\Gamma_{\bar{p}d}$
CCD1	$-(642.6 \pm 61.3)$	1109.4 ± 211.0	$-(1077 \pm 380)$	1496 ± 762
CCD2	$-(714.4 \pm 23.8)$	1023.3 ± 74.6	$-(838 \pm 243)$	1130 ± 452
CCD3	$-(751.7 \pm 51.0)$	1182.6 ± 176.0	$-(1358 \pm 98)$	541 ± 205
Final	$-(712.3 \pm 20.3)$	1053.5 ± 65.3	$-(1050 \pm 250)$	1100 ± 750

The authors attempted to split the line into contributions from ortho- and para-protonium even though the data show no visible shoulder. A free fit with two energies, two widths (folded with experimental resolution) and two intensities does, indeed, not converge. Hence the authors decided to guide the fit by subsequentially freezing and releasing parameters. Clearly, the parameter space is

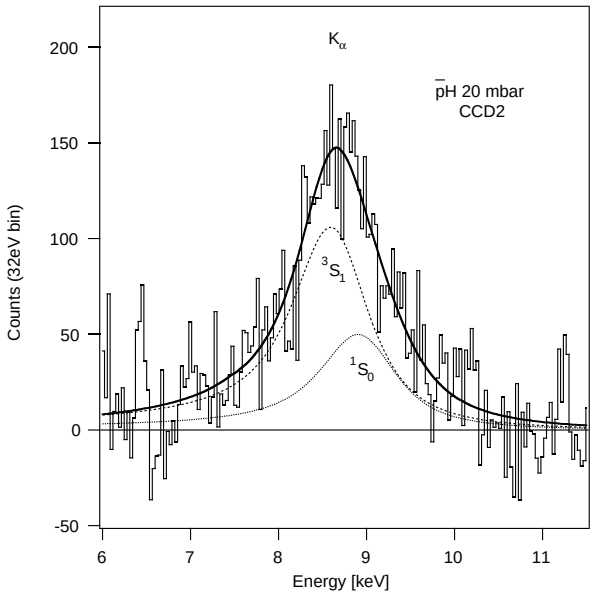

Figure 5.12: X-ray spectrum of protonium atoms after background subtraction and a fit using a Voigtian function. The dashed and dotted lines describe possible contributions from the spin triplet and spin singlet component.

not fully explored. With this warning we quote their result on the hyperfine splitting:

$$^3\mathrm{S}_1: \qquad \epsilon_{1\mathrm{S}} = -0.785 \pm 0.035\,\mathrm{keV}\,, \qquad \Gamma_{1\mathrm{S}} = 0.940 \pm 0.080\,\mathrm{keV}\,. \tag{5.13}$$

$$^1\mathrm{S}_0: \qquad \epsilon_{1\mathrm{S}} = -0.440 \pm 0.075\,\mathrm{keV}\,, \qquad \Gamma_{1\mathrm{S}} = 1.200 \pm 0.250\,\mathrm{keV}\,. \tag{5.14}$$

The intensity ratio of the two hyperfine lines was determined to be

$$Y(\mathrm{2P} \rightarrow {}^3\mathrm{S}_1)/Y(\mathrm{2P} \rightarrow {}^1\mathrm{S}_0) = 2.75 \pm 0.06\,. \tag{5.15}$$

The evidence for K_α lines from $\bar{\mathrm{p}}\mathrm{d}$ atoms is much weaker (Fig. 5.13b). There are several contaminant lines from gas impurities and from the target vessel; in particular the presence of a $\bar{\mathrm{p}}$O(7–6) line at the proposed K_α energy is very unfortunate. Nevertheless it is possible to subtract the background contribution in such a way that an excess of events is seen in the region where the K_α line is expected. The results of fits to the three difference spectra listed in Table 5.2 are not fully compatible. A systematic error is introduced to account for the correlation between the results of the fits and the background subtraction. The final result reads

$$\epsilon_{1\mathrm{S}} = -1.05 \pm 0.25\,\mathrm{keV}\,, \qquad \Gamma_{1\mathrm{S}} = 1.10 \pm 0.75\,\mathrm{keV}\,, \qquad 80 \leq\ \Gamma_{2P} \leq\ 350\,\mathrm{meV}\,. \tag{5.16}$$

We caution the reader that in our view the identification of the observed structure with the K_α line from $\bar{\mathrm{p}}\mathrm{d}$ atoms is not unambiguously established. Also the yield of $(2.3 \pm 1.4) \times 10^{-3}$ at a target pressure of $0.02\rho_{\mathrm{STP}}$ seems rather high. Batty, using cascade calculations, estimates the yield to be lower by one order of magnitude [355].

In parallel to the search for K X-rays, the line profile of the Balmer-α radiation from antiprotonic hydrogen and deuterium atoms was measured with a crystal spectrometer. To combine highest energy resolution with a sufficient count rate, a Bragg spectrometer was set up, in Johann geometry, equipped with spherically bent crystals. Three two-dimensional position-sensitive pixel detectors (CCD's) were used for X-ray recording.

Fig. 5.14 shows the line profile of 3D to 2P transitions for one of the three detectors. The expected splitting of the D levels is negligibly small so that only four lines are expected, corresponding

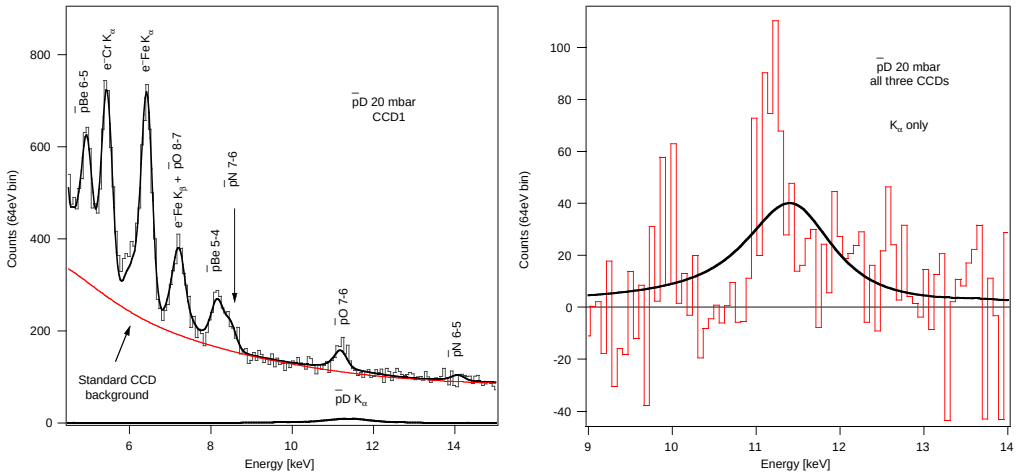

Figure 5.13: X-ray spectrum of $\bar{p}d$ atoms before (left) and after (right) background subtraction. The sum of contamination lines and of a polynomial function is used to subtract the background. right) X-ray spectrum of $\bar{p}d$ atoms after

to transitions to the $2\,^3P_2$, $2\,^3P_1$ $2\,^3P_0$, and $2\,^1P_1$ levels. The data on $\bar{p}p$ exhibit a shoulder at the high energy side. Its relative intensity was determined by a two-component fit to be (9.5 ± 0.9)%, in good agreement with the statistical population of 8.3% for the $2\,^3P_0$ level. This level is expected to have a large strong-interaction shift. Hence, the high-energy tail is likely due to $3\,^3D_1 \rightarrow 2\,^3P_0$ transitions. The main part of the line is attributed to the (unresolved) transitions to the three hyperfine levels, labeled $(2^3P_2, 2^1P_1, 2^3P_1)$.

The mean energy of the D $\rightarrow(2^3P_2, 2^1P_1, 2^3P_1)$ transitions and the energy of the individual D$\rightarrow 2\,^3P_0$ line were determined from a two-component fit to the measured line shape. The energy profile of the group was constructed from the individual contributions with positions and widths calculated from QED (see Tab. 3.3) and from $\overline{N}N$ potential models or using a single (broadened) Gaussian or Voigtian distribution. Both treatments lead to the same results on strong interaction parameters for the $2\,^3P_0$ line. The relative intensities were always fixed to the statistical values. Under these assumptions the authors derived

$$\epsilon(2^3P_2, 2^1P1, 2^3P_1) = +4.0 \pm 5.8\,\mathrm{MeV}\,, \qquad \Gamma(2^3P_2, 2^1P_1, 2^3P_1) = \ 38 \pm \ 9\,\mathrm{MeV}\,, \quad (5.17)$$

$$\epsilon(2^3P_0) = +139 \pm 20\,\mathrm{MeV}\,, \qquad \Gamma(2^3P_0) = 120 \pm 25\,\mathrm{MeV}\,. \quad (5.18)$$

The energy shifts quoted in (5.17,5.18) are of hadronic nature. The determination of the average hadronic width $\Gamma(2^3P_2, 2^1P_1, 2^3P_1)$ relies on the (very reasonable) assumption that the small splittings within the multiplet are known with sufficient precision.

From the intensity ratio $r' = K_\alpha / L_{\mathrm{tot}}$ (see Eq. 3.73) the authors deduce a spin-averaged value

$$\Gamma_{2P} = 44 \ \pm \ 8\,\mathrm{meV} \quad (5.19)$$

The results on r' and on the direct crystal spectrometer measurement were combined assuming that $\Gamma_X \ll \Gamma(2^3P_2) \approx \Gamma(2^1P_1) \approx \Gamma(2^3P_1)$ yielding:

$$\Gamma(2\,^3P_0) \ = \ 120 \ \pm \ 25 \ \mathrm{meV} \quad (5.20)$$

$$\overline{\Gamma}(2^3P_2, 2^1P_1, 2^3P_1) \ = \ 30.5 \ \pm \ 2.0 \ \mathrm{meV} \quad (5.21)$$

$$\overline{\Gamma}_{2P} \ = \ 38.0 \ \pm \ 2.8 \ \mathrm{meV}. \quad (5.22)$$

The last value uses our knowledge on the different fine-structure levels and is thus more reliable than (5.19), and more precise.

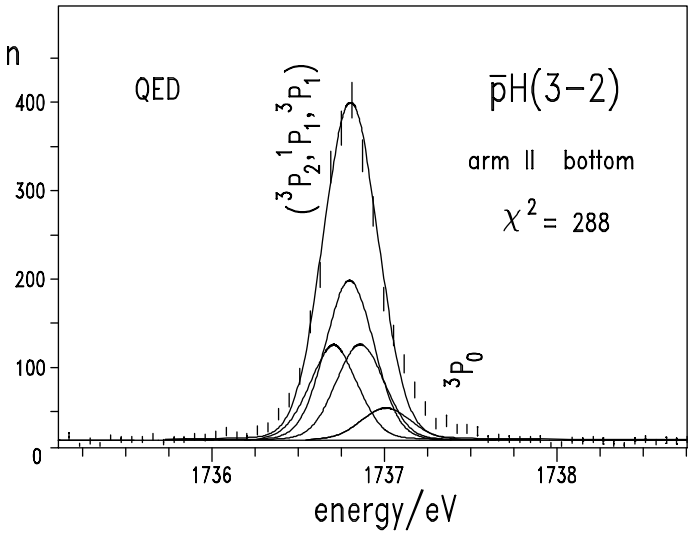

Figure 5.14: Balmer series of protonium atoms. The fine structure components $2\,^3\mathrm{P}_2$, $2\,^1\mathrm{P}_1$ have common strong interaction shifts and widths, the fine structure component $2\,^3\mathrm{P}_0$ can be identified as individual contribution.

Using the same set up, data were taken also with D_2 as target gas. The splittings within the D levels were again neglected; hence a line quintuplet is expected. In a first attempt, QED splittings as given in [259] were used with a common resolution given by the $\bar{\mathrm{p}}^{20}$Ne calibration line. The fit did not reproduce the data. Much better agreement was obtained when the electromagnetic hyperfine splittings from [260] (Table 3.3) were used. These splittings are small enough to treat the whole multiplet as a single line which is fitted with one Voigt profile. Imposing the splittings from [260] and the hadronic shifts as given by [261] did not effect the final result. A common broadening of all substates was a free parameter in the fits. The relative intensities of the hyperfine transitions were frozen to represent a statistical population of the 2P sublevels. The three detectors gave consistent results; we quote the weighted average as final result for the spin-averaged hadronic shift (negative, i.e., repulsive) and broadening of the 2P levels of antiprotonic deuterium:

$$\overline{\epsilon}_{2\mathrm{P}} = -243 \pm 26 \text{ meV}, \tag{5.23}$$

$$\overline{\Gamma}_{2\mathrm{P}} = 489 \pm 30 \text{ meV}. \tag{5.24}$$

5.4 Summary of results on $\bar{\mathrm{p}}$p and $\bar{\mathrm{p}}$d atoms

The results on the strong interaction shift and width given in (5.10,5.11,5.12) and the mean value from from Table 5.2 are fully compatible even though we believe the errors to be sometimes underestimated. We give the linear average of the four measurements with a conservative estimate of the error:

$$\epsilon_{1\mathrm{S}} = -0.730 \pm 0.030\,\mathrm{keV}, \qquad \Gamma_{1\mathrm{S}} = 1.060 \pm 0.080\,\mathrm{keV}. \tag{5.25}$$

Using the Trueman formula (3.90), we can relate these values to the complex S-wave scattering length

$$a_o^{\mathrm{sc}} = (0.88 \pm 0.04) - i(0.64 \pm 0.05)\,\mathrm{fm}. \tag{5.26}$$

Similarly, we obtain the imaginary part of the P-wave scattering volume:

$$\mathcal{I}\mathrm{m}\, a_1^{\mathrm{sc}} = -(0.77 \pm 0.06)\,\mathrm{fm}^3. \tag{5.27}$$

Table 5.3: Strong interaction shifts and widths of antiprotonic hydrogen and deuterium atoms.

Antiprotonic hydrogen atoms					
Energy shift			Energy width		
ϵ_{1S}	=	$-730 \pm 30\,\mathrm{eV}$	Γ_{1S}	=	$1060 \pm 80\,\mathrm{eV}$
$\epsilon(2^3P_2, 2^1P_1, 2^3P_1)$	=	$+4.0 \pm 5.8\,\mathrm{meV}$	$\Gamma(2^3P_2, 2^1P_1, 2^3P_1)$	=	$30.5 \pm 2.0\,\mathrm{meV}$
$\epsilon(2^3P_0)$	=	$+139 \pm 20\,\mathrm{meV}$	$\Gamma_(2^3P_0)$	=	$120 \pm 25\,\mathrm{meV}$
			$\Gamma_(2^1P_1)$	=	$51 \pm 18\,\mathrm{meV}$
Mean 2P level widths					
using (3.72)			using (3.73)		
Γ_{2P}	=	$38.0 \pm 2.8\,\mathrm{meV}$	$\overline{\Gamma}_{2P}$	=	$44 \pm 8\,\mathrm{meV}$
S-wave scattering length			P-wave scattering volume, imag. part		
$a_o^{sc} = (0.88 \pm 0.04) - i(0.64 \pm 0.05)\,\mathrm{fm}$			$\mathcal{I}\mathrm{m}\, a_1^{sc}$ = - $(0.77 \pm 0.06)\mathrm{fm}^3$		
ρ-parameter at threshold					
$\rho(E=0)$	=	-1.38 ± 0.12			
Antiprotonic deuterium atoms					
Energy shift			Energy width		
ϵ_{1S}	=	$-1.05 \pm 0.25\,\mathrm{keV}$	Γ_{1S}	=	1.10 ± 0.75 keV
$\bar{\epsilon}_{2P}$	=	243 ± 26 meV	$\bar{\Gamma}_{2P}$	=	489 ± 30 meV

The ratio of the real to imaginary part of strong-interaction amplitude is read as

$$\rho(E=0) = \frac{2\epsilon_{1S}}{\Gamma_{1S}} = -1.38 \pm 0.12\,. \tag{5.28}$$

In Table 5.3 we summarize the results on strong interaction parameters. They will be compared to theoretical predictions in Chapter 6.

The experiments gave X-ray yields over a wide range of pressures. These are reproduced in Tables 5.4 and 5.5.

Table 5.4: Intensities (in %) of L and K X-rays radiation from $\bar{\mathrm{p}}$p atoms for different target densities.

Density	L x-ray intensity			K x-ray intensity			Ref.
ρ_{STP}	L_α	L_β	L_{tot}	K_α	K_β	K_{tot}	
0.016	51.9 ± 11.0	9.2 ± 2.5	70.6 ± 11.6				[173]
0.016	53.2 ± 9.3	7.7 ± 2.4	71.9 ± 10.0				[174]
0.03	40.7 ± 8.5	3.7 ± 1.3	52.3 ± 8.9	0.62 ± 0.17		0.91 ± 0.19	[173]
0.03	40.2 ± 5.0	6.2 ± 1.3	55.1 ± 5.6	0.81 ± 0.15			[174]
0.06	34.7 ± 7.5	3.5 ± 1.5	47.7 ± 8.0				[173]
0.06	31.9 ± 3.8	4.8 ± 0.9	44.3 ± 4.1				[174]
0.120	26.5 ± 3.3	5.2 ± 1.0	38.9 ± 3.7				[174]
0.125	17.2 ± 6.5	8.4 ± 1.9	35.7 ± 7.0				[170]
0.25	10.3 ± 2.2	5.2 ± 0.6	24.0 ± 2.4	0.28 ± 0.08	$0.03^{+0.05}_{-0.03}$	0.52 ± 0.12	[169]
0.25				0.37 ± 0.05	0.09 ± 0.04	0.78 ± 0.08	[170]
0.30	9.5 ± 2.6	1.6 ± 1.1	17.8 ± 3.6				[173]
0.92	3.4 ± 0.8	2.4 ± 0.3	11.2 ± 1.0	0.10 ± 0.04	$0.01^{+0.04}_{-0.01}$	0.36 ± 0.07	[169]
0.92	3.4 ± 0.8	2.4 ± 0.3	11.2 ± 1.0	0.18 ± 0.04	< 0.02	0.53 ± 0.06	[170]
1.0			13.0 ± 2.0	0.26 ± 0.14		0.65 ± 0.32	[151]
1.0	5.5 ± 1.5		12.0 ± 2.0	0.10 ± 0.05		0.14 ± 0.06	[152]
2.0	3.4 ± 0.9	1.5 ± 0.2	8.1 ± 1.0	$0.04^{+0.09}_{-0.04}$	< 0.07	0.25 ± 0.17	[169]
4.0			6.0 ± 3.0	< 0.6			[134]
10	< 0.4	0.4 ± 0.2	1.6 ± 0.3	< 0.06	< 0.08	0.25 ± 0.17	[169]

Table 5.5: Intensities (in %) of L X-ray radiation from $\bar{\mathrm{p}}$d atoms for different target densities.

Density	L X-ray intensity			Ref.
ρ_{STP}	L_α	L_β	$\mathrm{L}_{\mathrm{tot}}$	
0.016	53.2 ± 9.3	7.7 ± 2.4	71.9 ± 10.0	[174]
0.03	40.2 ± 5.0	6.2 ± 1.3	55.1 ± 5.6	[174]
0.06	31.9 ± 3.8	4.8 ± 0.9	44.3 ± 4.1	[174]
0.12	26.5 ± 3.3	5.2 ± 1.0	38.9 ± 3.7	[174]
0.25	19.0 ± 2.1	2.9 ± 0.2	29.1 ± 2.2	[169]
0.92	7.9 ± 0.9	1.6 ± 0.1	14.1 ± 1.0	[169]
2.0	5.0 ± 0.6	1.1 ± 0.1	9.0 ± 0.7	[169]
4.0			6.0 ± 3.0	[146]
10	1.0 ± 0.2	0.5 ± 0.1	2.4 ± 0.3	[169]

5.5 Cascade processes in $\bar{\mathrm{p}}$p and $\bar{\mathrm{p}}$d atoms

Most experiments on proton–antiproton annihilation at rest into exclusive final states were carried out by stopping antiprotons in a liquid hydrogen target. Annihilation at rest takes place from atomic orbits, when antiprotons with a kinetic energy of a few eV were captured by the Coulomb field of a proton or deuteron. The $\bar{\mathrm{p}}\mathrm{p}$ system annihilates only from a small number of states with given quantum numbers which can be determined or at least restricted by using selection rules or by observing the X-rays emitted in the course of the atomic cascade. The distribution of initial states can be changed by varying the target density. Hence we have a unique situation where annihilation processes can be studied with *ab initio* knowledge of the quantum numbers. In scattering experiments or in annihilation in flight, several partial-wave amplitudes contribute to the observables.

5.5.1 The capture process

Antiprotons stopping in H_2 or D_2 loose energy in collisions. Their energy loss per unit length is given by the Bethe–Bloch formula as long as their velocity is larger than αc, corresponding to $\bar{\mathrm{p}}$ energies of $\sim 25\,\mathrm{keV}$. In H_2 gas at STP, the range of, e.g., 3 MeV antiprotons is about 75cm; the antiprotons need 40 ns before they come to rest. Range and energy loss calculated with the Bethe–Bloch equation are in good agreement with data [154] even though precision experiments reveal a small difference between energy-loss curves of protons and antiprotons [356].

Below $25\,\mathrm{keV}$ the $\bar{\mathrm{p}}$ continues to loose its energy by ionisation until its energy is in the few eV range. Then it is captured by the Coulomb field of a proton by Auger emission of an electron.

$$\bar{\mathrm{p}} + \mathrm{H}_2 \longrightarrow \bar{\mathrm{p}}\mathrm{p}(nl) \; + \mathrm{e}^- + \mathrm{H} \tag{5.29}$$

The capture process can be followed numerically using the Classical Trajectory Monte Carlo (CTMC) method. It describes a three-body problem (antiproton, proton and electron) using a classical Hamiltonian to derive equations of motion, which are solved for a statistical choice of the so-called microcanonical variables. Figure 5.15 shows the simulation of a capture process. The H atom is described by a classical $\mathrm{p} + \mathrm{e}^-$ system with a radius corresponding to the first Bohr orbit. Phases and eccentricity are chosen randomly. After ejection of the electron, antiproton and proton are bound in a flat ellipse, corresponding to a classical radius of 0.5 Å and to a principal quantum number $n \sim 32$.

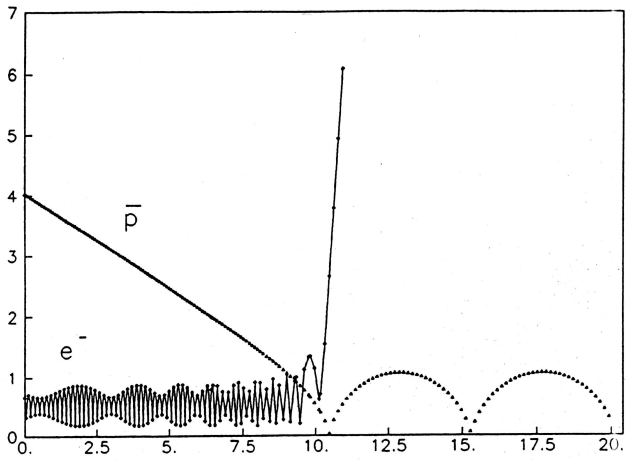

Figure 5.15: Simulation of the capture of a $5eV$ antiproton by a H atom using the Classical Trajectory Monte Carlo method. The plot shows the respective distances between proton and antiproton and electron (from [357]).

The cross section for protonium formation rises steeply for very low energies and is 2-3 Å^2 for $\bar{\mathrm{p}}$ energies below 13.6 eV [358]. Most antiprotons are captured when their energy is below the H ionisation energy; the principal quantum number n is most often between 30 and 50 (sometimes even larger than 100) and the average orbital angular momentum ℓ about 20 [358]. Qualitatively, the preference for protonium capture into high Rydberg states can be understood when the overlap of electronic and antiprotonic wave functions is considered. Capture will occur with high probability, when the classical radius of protonium atoms is matched to the size of ground-state hydrogen atoms. The expectation value of the atomic radius is related to n and ℓ via

$$\langle r_{n,\ell} \rangle = \frac{a_0}{2} \left(3n^2 - \ell(\ell+1) \right) \tag{5.30}$$

The "best" choice of the principal quantum number is then in the range

$$\sqrt{\frac{2m}{m_e}} < n_c < -3/2 + \sqrt{\frac{9}{4} + \frac{3}{2}\frac{2m}{m_e}}\,, \tag{5.31}$$

or $32 < n_c < 36$. For the angular momentum states after capture, a statistical population seems plausible. Calculations show that the preferred distribution in ℓ has its maximum at about $n/2$ [359].

5.5.2 Collisions between protonium atoms and H_2 molecules

Collisions

Once formed, protonium atoms collide with H_2 molecules where they experience large electric fields inducing transitions from initial (n, ℓ) protonium states to other levels via dissociation of neighbouring molecules, Auger effect or Stark mixing. They are schematically represented in Fig. 5.16.

Chemical effects

In very high levels (for $n \geq 20$), $\bar{\mathrm{p}}\mathrm{p}$ atoms de-excite by dissociation of the colliding H_2 molecules:

$$\begin{aligned} &(\bar{\mathrm{p}}\mathrm{p})^{n_i,\ell_i} + \mathrm{H}_2 \longrightarrow (\bar{\mathrm{p}}\mathrm{p})^{n_f,\ell_f} + \mathrm{H} + \mathrm{H}\,, \\ &\Gamma_{\mathrm{chem}} = N\, v\, \pi\, \left(r_{n_i}\right)^2 \qquad \text{for} \qquad \delta E_{n_i \to n_f} \geq \Delta\,, \qquad \ell_i = \ell_f\,. \end{aligned} \tag{5.32}$$

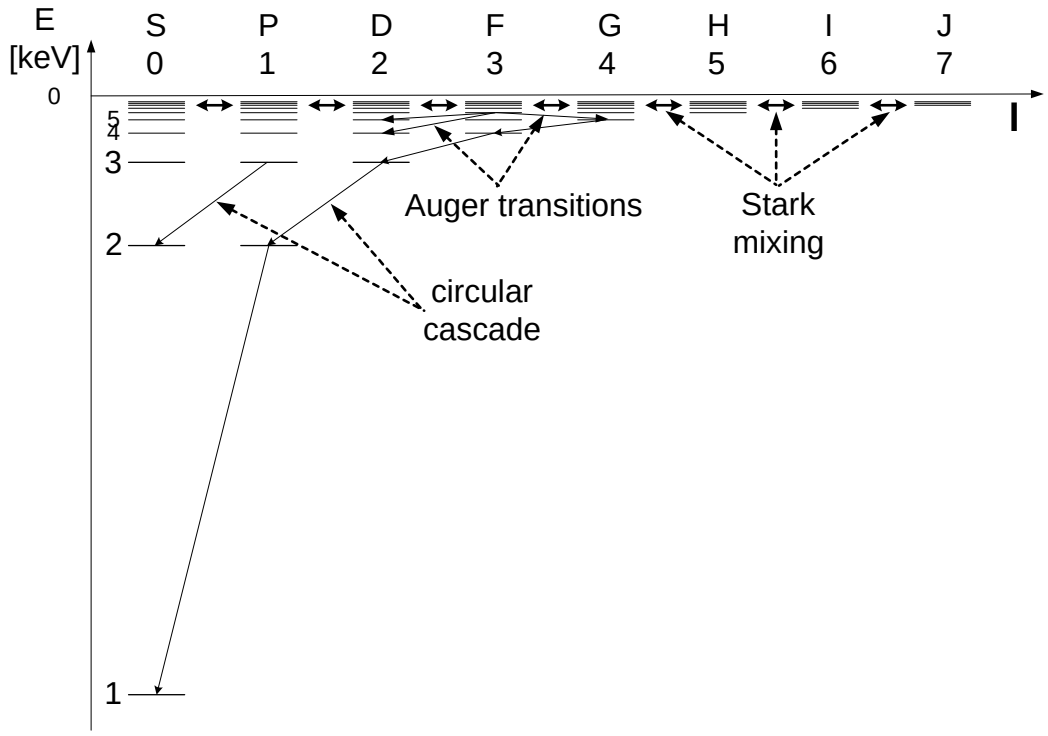

Figure 5.16: Level scheme and atomic cascade of antiprotonic hydrogen.

The rate for this effect is assumed to be given by the classical "size" of the $\bar{\mathrm{p}}\mathrm{p}$ atom and the collision frequency [140]. $\Delta = 4.7$ eV is the dissociation energy of H_2 molecules, N is the density of hydrogen atoms, and v is the protonium velocity.

Auger effect

For $n \sim 20$ the classical radius becomes too small to allow chemical effects to play a significant role. Yet one of the H atoms of a H_2 molecule can be ionized and an Auger process can take place.

$$\begin{aligned} &(\bar{\mathrm{p}}\mathrm{p})^{n_i,\ell_i} + \mathrm{H}_2 \longrightarrow (\bar{\mathrm{p}}\mathrm{p})^{n_f,\ell_f} + \mathrm{H} + \mathrm{p} + \mathrm{e}^- \ , \\ &\Gamma_{\mathrm{Auger}} = \frac{16\pi}{3}\frac{N}{m_{\bar{\mathrm{p}}}^2}\left(R_{n_i}^{n_f}\right)^2 (2\delta E + 1.39)^{-1/2} \qquad \text{for} \qquad \delta E + 1.39 \geq 15.2\,\mathrm{eV} \ . \end{aligned} \tag{5.33}$$

The Auger effect is induced by the electric field seen by the $\bar{\mathrm{p}}\mathrm{p}$ atom in the collision and is governed by the same matrix element $\left(R_{n_i}^{n_f}\right)^2$ as radiative de-excitation. But while radiative transitions prefer large transition energies, Auger transitions occur most frequently with a minimal change in the principal quantum number. The energy gain is then just sufficient to knock out an electron. As in radiative transitions, angular momentum changes according to $l_f = l_i \pm 1$.

In collisions, peak electric field strengths of typically $\sim$V/Å are experienced (for an impact parameter of 1.5 Å) for about 20 fs. The electron density integrated over the collision time is $\sim 0.1\rho_0$ fs where ρ_0 is the electron density of H atoms at $r = 0$. Protonium atoms are neutral; hence they move along straight lines if the is attraction between the two collision partners is neglected. The path can be calculated using, e.g., the CTMC method [360]. For an impact parameter b of 1.5 Å, the minimal distance shrinks with increasing principal quantum number of the protonium atom. For

$n = 20$, the minimal distance is by a factor 2 smaller than the impact parameter, for $n = 5$ this effect is negligible. The straight-line approximation therefore underestimates the effect of the electric field and in particular the Stark mixing probability.

Stark mixing

Stark mixing of states with different angular momenta is extremely important for the cascade of $\bar{\mathrm{p}}\mathrm{p}$ and $\bar{\mathrm{p}}\mathrm{d}$ atoms, as first demonstrated by Day, Snow and Sucher [139]. Many transitions between different nearly mass-degenerate angular momentum states occur in a single collision between a $\bar{\mathrm{p}}\mathrm{p}$ or $\bar{\mathrm{p}}\mathrm{d}$ atom and a H_2 molecule. The electric field induces Stark mixing transitions between different orbital angular momentum states having the same principal quantum number n. Since the direction of the electric field changes during the collision, not only transitions with $\Delta m = 0$ occur but also transitions in which $\Delta m = \pm 1$. In principle, the theory involves n^2 coupled Schrödinger equations with a time-dependent electric field. Leon and Bethe avoided this difficulty and use instead a shuffling model which takes into account the net effect of back and forth transitions between different ℓ. T

$$\Gamma_{n,\ell\to n,\ell+1} = \frac{2\ell+1}{2\ell-1}\,\Gamma_{n,\ell\to n,\ell-1} = \pi N v \rho_0^2 \tag{5.34}$$

In a microscopic model, the n^2 coupled differential equation are integrated numerically and transition rates from any initial state (n,ℓ) to the other states (n,ℓ') are determined.

5.5.3 The cascade

The microscopic cascade model of Reifenröther and Klempt [361] begins with an initial population $p_{n,\ell}$ of the protonium levels. All levels can radiate to lower levels or annihilate at any time. Collisions with different impact parameters may take place with their respective probabilities. Five different impact parameters are chosen in a way that the electric field strength in a collision reaches a maximum value of $10^{-2}, 10^{-1}, .., 10^2 V/\text{Å}$. The impact parameters corresponding to these field values and hence the collision frequencies depend on n. These collisions induce external Auger effect and Stark mixing. For the Figures presented here, the Auger effect was enhanced by a factor 2. This adjustment leads to a better agreement with data.

The cascade model starts at $n = 30$ and assumes an initial distribution in ℓ and calculates the depopulation of these states until the residual population of 0.1% is reached. Each X-ray emission or annihilation from a S or P state is recorded. Thus the X-ray yields, the fraction of S and P state capture and the cascade time are determined. The X-ray intensities listed in Table 5.4 are shown in Fig. 5.17 and 5.18 and compared with the calculation.

The cascade of $\bar{\mathrm{p}}\mathrm{d}$ atoms is very similar to that of protonium. Cascade calculations concentrated on the role of S- wave and P-wave capture [361]. The X-ray yields are reproduced in Fig. 5.19.

5.5.4 S- versus P capture

Cascade models predict the density-dependent probability for a protonium atom to annihilate from an atomic S-state or from a P-state. This is an important issue since the dynamics of the annihilation process depends on the angular momentum state from which annihilation occurs.

The fraction of S- and P-state capture can be determined using selection rules. For instance, annihilation at rest into $\mathrm{K^0_s K^0_l}$ is allowed from the $^3\mathrm{S}_1$ state, into $\mathrm{K^0_s K^0_s}$ from the states $^3\mathrm{P}_0$ and $^3\mathrm{P}_2$. The number of $\mathrm{K^0_s K^0_l}$ and $\mathrm{K^0_s K^0_s}$ events found in bubble chambers at BNL and CERN [348]:

$$\begin{aligned} 787 \text{ events} \qquad \bar{\mathrm{p}}\mathrm{p} &\to \mathrm{K^0_s K^0_l}\,, \\ 4 \text{ events} \qquad \bar{\mathrm{p}}\mathrm{p} &\to \mathrm{K^0_s K^0_s}\,, \end{aligned} \tag{5.35}$$

show a strong preference for the annihilation into $\mathrm{K^0_s K^0_l}$ and evidence the dominance of S-wave capture. It was therefore a great surprise when Devons *et al.* [141] found an unexpectedly large

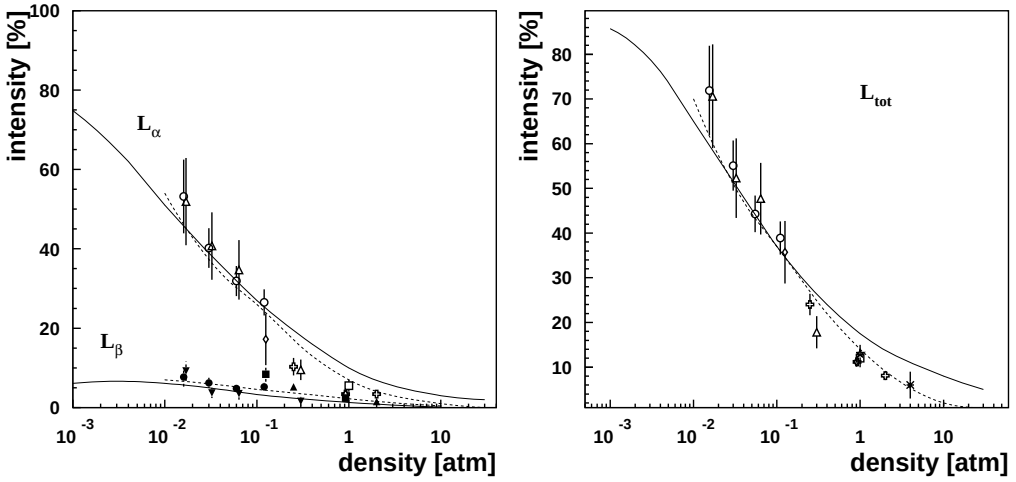

Figure 5.17: L X-ray intensity of $\bar{\mathrm{p}}$p atoms as a function of target density. Left: L_α and L_β intensity; right: sum of intensities of L-line series. The solid line is from the Mainz cascade model, the dotted line from Batty [362].

branching ratio for the reaction $\bar{\mathrm{p}}$p annihilation $\rightarrow \pi^0\pi^0$, forbidden from S-state orbitals. After a long history of conflicting results, the Crystal Barrel Collaboration found a rate for $2\pi^0$ production of $(6.93 \pm 0.43)\,10^{-4}$ [363] for antiprotons stopping in liquid H_2, fully compatible with the old findings of Devons *et al.* [141]. When compared to the $\pi^+\pi^-$ rate, a P-wave fraction of 45% to $\bar{\mathrm{p}}$p annihilation at rest in liquid H_2 can be derived [364].

This large discrepancy is derived from two rare channels, with frequencies of about 0.3% for $\bar{\mathrm{p}}\mathrm{p}\rightarrow\ \pi^+\pi^-$ and about 0.1% for $\bar{\mathrm{p}}\mathrm{p}\rightarrow \mathrm{K}^0_{\mathrm{s}}\mathrm{K}^0_{\mathrm{l}}$. It reflects the a large coupling to $\pi\pi$ and a small coupling to $\mathrm{K\overline{K}}$ from P states. With the measured rates for $\bar{\mathrm{p}}\mathrm{p}\rightarrow\pi\pi$ [156] and to $\mathrm{K\overline{K}}$ [157] from P-states, the P-state contribution reduces to $\sim (30 \pm 15)\%$, and there is no more conflict between the results derived from $\mathrm{K\overline{K}}$ and from $\pi\pi$.

In the derivation of the new P-state fraction, the assumption is made that, at the moment of annihilation, the statistical distribution of the fine-structure levels $^{2s+1}\mathrm{P_J}$-states for large n is the same as for $n = 2$. This assumption is likely not true: in high-n levels, Stark mixing of atomic states is very strong. The $^3\mathrm{P}_0$ level has a strong interaction width four times larger than the mean 2P width (compare (5.20) and (5.21)). High-n $^3\mathrm{P}_0$ levels can be repopulated after annihilation via Stark mixing collisions and the $^3\mathrm{P}_0$ levels have a larger chance to contribute to annihilation. There is practically no Stark mixing for n=2; $\bar{\mathrm{p}}\mathrm{p}$ atoms in the 2 P fine-structure levels annihilate and the $^3\mathrm{P}_0$ level is not refilled after annihilation. When this effect is taken into account, the fraction of P-state capture for antiprotons stopping in liquid hydrogen reduces from $28.8 \pm 3.5\%$ to $12 \pm 2\%$ [362,363]. This is a value compatible with most partial-wave analyses. Figure 5.20 shows the fraction of P-state annihilation as a function of H_2 density.

Batty [362] also determined the fractional contributions of individual hyperfine structure states to annihilation as a function of the hydrogen density. He found that for any selected channel, the contributions of individual hyperfine states change by an enhancement factor B_{HFS}. Figure 5.21 shows these factors as functions of the H_2 density.

We notice a substantial increase of the contribution of the $^3\mathrm{P}_0$ state with increasing density. This increase is responsible for the large $\pi^0\pi^0$ branching ratio. In turn, this large branching ratio is only compatible with other determinations of the P-state capture rate, when we assign the majority of $\bar{\mathrm{p}}\mathrm{p}$ annihilations into $2\pi^0$ to the $^3\mathrm{P}_0$ and not to the $^3\mathrm{P}_2$ initial state.

The fraction of P-state annihilation in $\bar{\mathrm{p}}$n annihilations is even more uncertain. From a com-

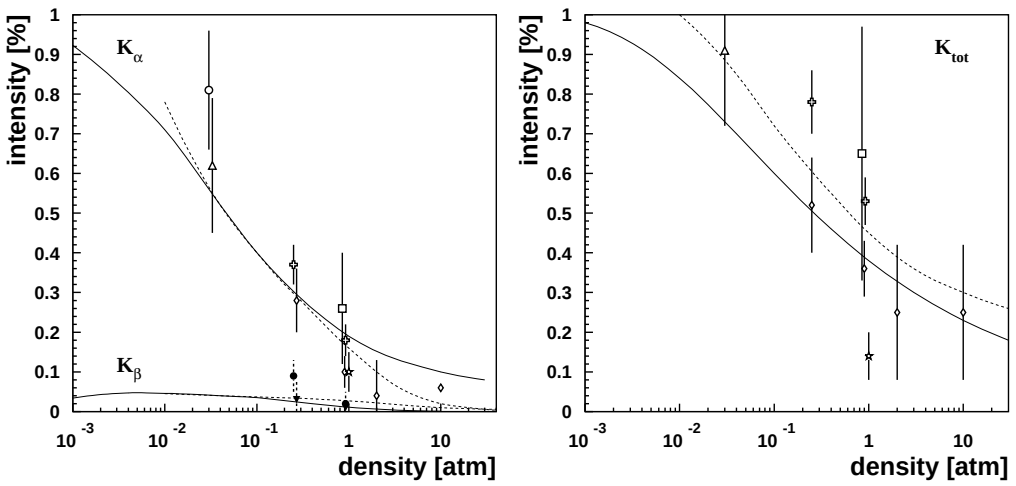

Figure 5.18: K X-ray intensity of $\bar{p}p$ atoms as a function of target density. Left: K_α and K_β intensity; right: sum of intensities of K-line series. The solid line is from the Mainz cascade model, the dotted line from Batty [362].

parison of $\bar{p}p$ annihilation into $\pi^0\pi^0$ in liquid H_2 and D_2, the P-state capture fraction in D_2 was estimated to (22 ± 4)% (after a cut on the proton momentum to ensure annihilation on a quasi-free nucleon) [365]. Batty [355] estimated the P-state annihilation frequency from $\bar{p}d$ annihilations into $\pi\pi$ and into $K\overline{K}$ and derived a fraction (34 ± 4)% P-state capture. From cascade calculations he estimated this fraction to 40%. In summary, a P-state fraction of 30% for antiprotons stopping in liquid H_2 seems realistic.

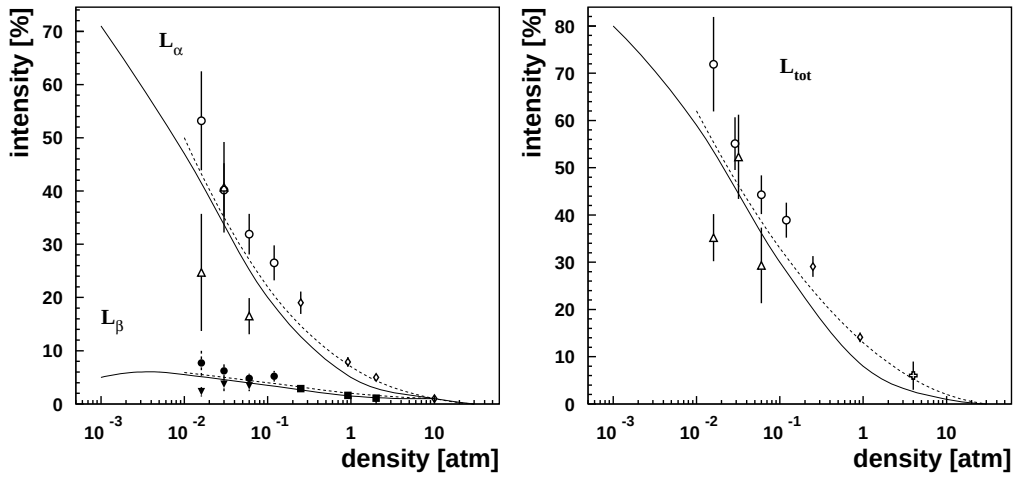

Figure 5.19: L X-ray intensity of $\bar{p}d$ atoms as a function of target density. Left: L_α and L_β intensity; right: sum of intensities of L-line series. The solid line is from the Mainz cascade model, the dotted line from Batty.

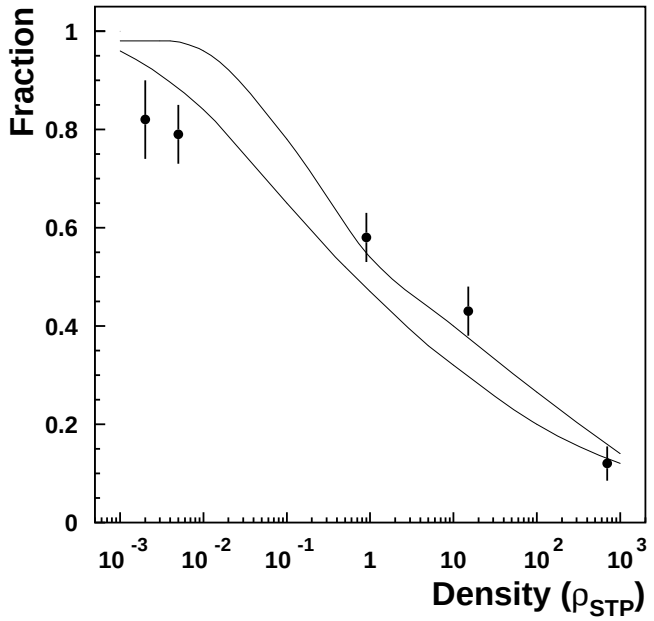

Figure 5.20: Fraction of P-state capture as a function of H_2 density. The lower line reproduces results from the Mainz cascade model; the upper line uses the Borie–Leon model. The "experimental" points are derived in [362].

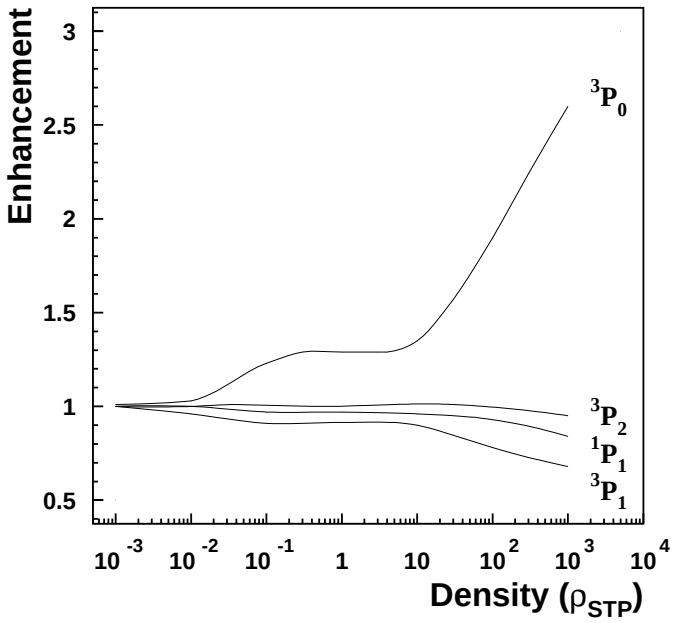

Figure 5.21: Change in the population of protonium levels as functions of H_2 density.

Chapter 6

Phenomenology of the nucleon–antinucleon interaction

In this chapter, we resume the discussion on the theoretical approaches to $\overline{\mathrm{N}}\mathrm{N}$ interaction entering elastic, charge-exchange and strangeness-exchange scattering, and protonium. We focus on the progress on phenomenological analyses made possible by LEAR data.

6.1 Comparison of scattering data with the predictions of the early optical models

The basic features of the data, i.e., the shape of integrated cross-sections and the trend of the elastic and charge-exchange differential distributions, can be reproduced by the simple optical models introduced in Chapter 3, where the meson-exchange part is taken from NN scattering, via G-parity rule, and supplemented by an energy- and state-independent imaginary absorptive potential, to simulate the effect of annihilation.

Some representative data are compared with various model calculations in Fig. 6.1– 6.4.

6.1.1 Integrated cross-sections

The data shown in Fig. 6.1 exhibit a smooth behaviour as a function of the incident momentum. In particular, no narrow resonance emerges! This stems naturally from optical potentials, as illustrated by the Kohno–Weise model [212]. To maintain the proper annihilation-to-elastic ratio and the smallness of the charge-exchange cross-section as energy increases, one needs a wide enough annihilation core. Otherwise, one has to play with the energy-dependence and non-locality parameters, in more sophisticated models.

6.1.2 Differential cross-sections

A representative set of data is displayed in Figs. 6.2, for the elastic and charge-exchange cases.

The main trend of the elastic differential cross section is rather well reproduced. Some adjustments are necessary to match exactly the shape of the charge-exchange differential cross-section. Minor changes in the models change the shoulder shape into a dip-bump structure, or vice-versa. This effect was pointed out in particular by H. Poth (private communication) and F. Myhrer [60, 238, 366]. The changes could consist either in an adjustment of the ρ-meson coupling or an alteration of the shape of the annihilation potential. We also remark from Fig. 4.15 in Chap. 4, that the angular distribution of charge-exchange varies from one energy to another. The charge-exchange angular

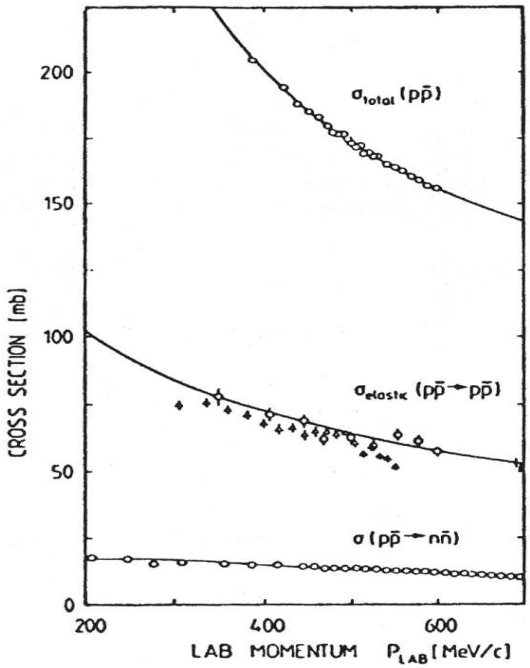

Figure 6.1: Total, annihilation and charge-exchange cross-sections as a function of the $\bar{\mathrm{p}}$ momentum. The curves are the calculations with the Kohno–Weise model [212].

distribution at 287 MeV/c poses a more serious problem: no model can account for the ample decrease of the cross section suggested by the data.

6.1.3 Elastic-scattering analysing power

The $\bar{\mathrm{p}}\mathrm{p} \to \bar{\mathrm{p}}\mathrm{p}$ analysing-power measurements from experiment PS172 are shown in Fig. 6.3. The continuous lines are the predictions of the first version of the Paris model [237], to be discussed in more detail later in this chapter. The dashed line corresponds to the predictions of the Dover–Richard model [211], also based on the G-parity transformed NN Paris potential, but with a simpler treatment of absorption.

Comments are in order. It is impressive how the overall trend of the data is predicted by these models. To obtain a better agreement with the data, it was necessary to tune more extensively the parameters of the potential, including its non-local terms. The early Paris model [237] was adjusted to fit pre-LEAR analysing-power data.

6.1.4 Charge-exchange analysing power

The analysing-power parameter A_n of the charge-exchange reaction was measured for the first time at LEAR by experiment PS199. The data are compared in Fig. 6.4 with the model calculations which were published before the data appeared: the models DR1, DR2 and KW were already introduced in Chap. 3, as well as the boundary-condition model of Myhrer and Dalkarov, referred to as M; the label N corresponds to an early analysis of the Nijmegen group, on which more later. The broad range of predictions comes from this observable being very sensitive to small contributions to the scattering amplitudes, as already stressed in Sec. 4.6 (π-exchange, which is the dominating dynamical mechanism, does not contribute to the analysing power at first order).

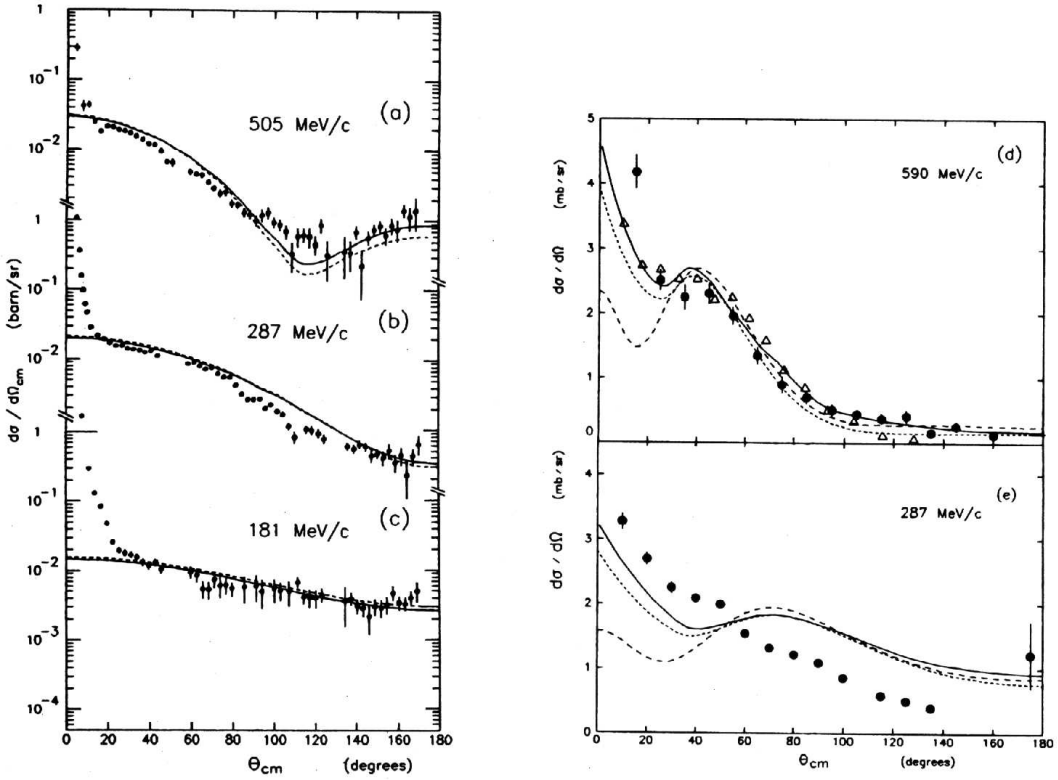

Figure 6.2: Differential cross-section in the elastic (left) and charge-exchange (right) channels. The data are from experiment PS173. The figures are from Ref. [219]: the solid line represents a simple optical model fitted to the data, the dotted line is the earlier Dover–Richard model [211], the dashed one, the Paris model [237].

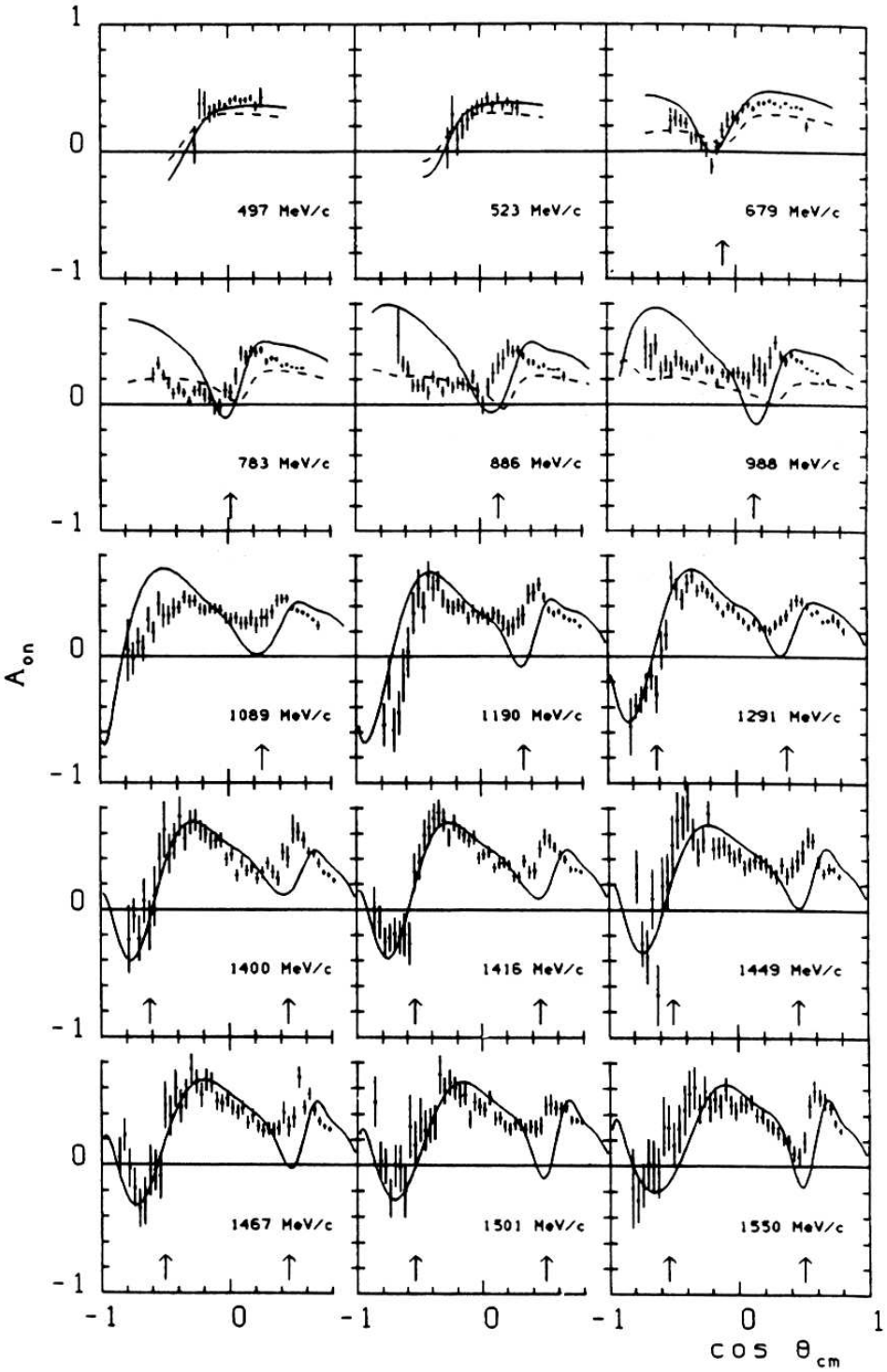

Figure 6.3: The $\bar{p}p \to \bar{p}p$ analysing power as measured by PS172 at15 momenta, compared with the predictions of the Paris (continuous line) and Dover–Richard (dashed line) models.

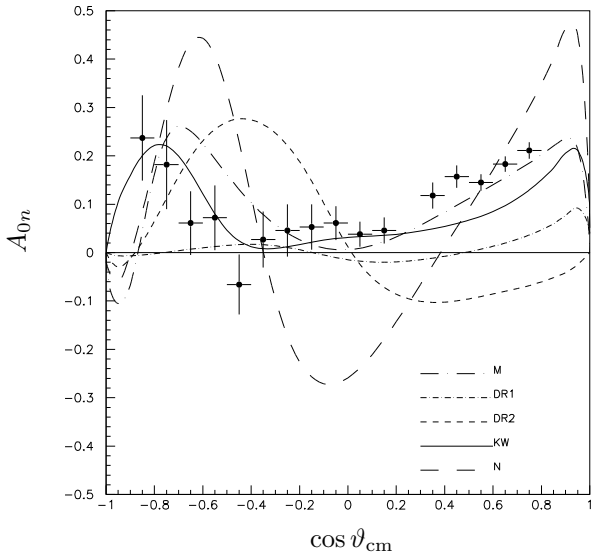

Figure 6.4: Analysing power at 656 MeV/c, compared to early models: Dover–Richard (DR1,DR2), Kohno–Weise (KW), Myhrer–Dalkarov (M), and an early analysis by the Nijmegen group (N).

Agreement with the data could not be obtained by simply tuning the absorptive part of these simple optical models; much more refined models are needed to reproduce the data. Even in the case of the latest Paris potential [367], which describes the short-range potential with thirty parameters (see Sec. 6.3), the agreement with the data is not perfect. Note that the authors of this model insisted on having an annihilation potential looking short ranged; as a consequence, they slightly overestimate the integrated charge-exchange cross-section; so it is not too much a surprise that they also face difficulties for the spin observables of this reaction.

Note that in their latest analysis, the Nijmegen group was able to produce good fits to these data. We will come back to this point later.

In Fig. 6.4, the best agreement between the measured data at 656 MeV/c and the model calculations is observed with the boundary-condition model of Myhrer and Dalkarov [228]. As seen in Fig. 6.5 showing the set of data measured by PS199 below 900 MeV/c, the agreement remains at the lowest energies, but only in the forward hemisphere.

6.2 Comparison with coupled-channel models

6.2.1 The Lebedev school

The Lebedev-Institute group, led by I.S. Shapiro, carried out a pioneering work on the coupled-channel-model (CCM) description of $\overline{\mathrm{N}}\mathrm{N}$ scattering. A rather comprehensive summary has been given in Refs. [240, 242], of which one can highlight the following points.

The motivation for a coupled-channel approach stems from a criticism of optical models. Unitarity is not explicitly fulfilled in optical models (though room is left for the annihilation channels which are integrated out). It is delicate to interpret and handle the non-orthogonal wave functions generated by optical models. It is even argued in [240] that "the optical model potentials take annihilation into account but do not reproduce the effect of the reappearance of the initial particles, so that the baryon–antibaryon wave-functions would usually be underestimated". To our knowl-

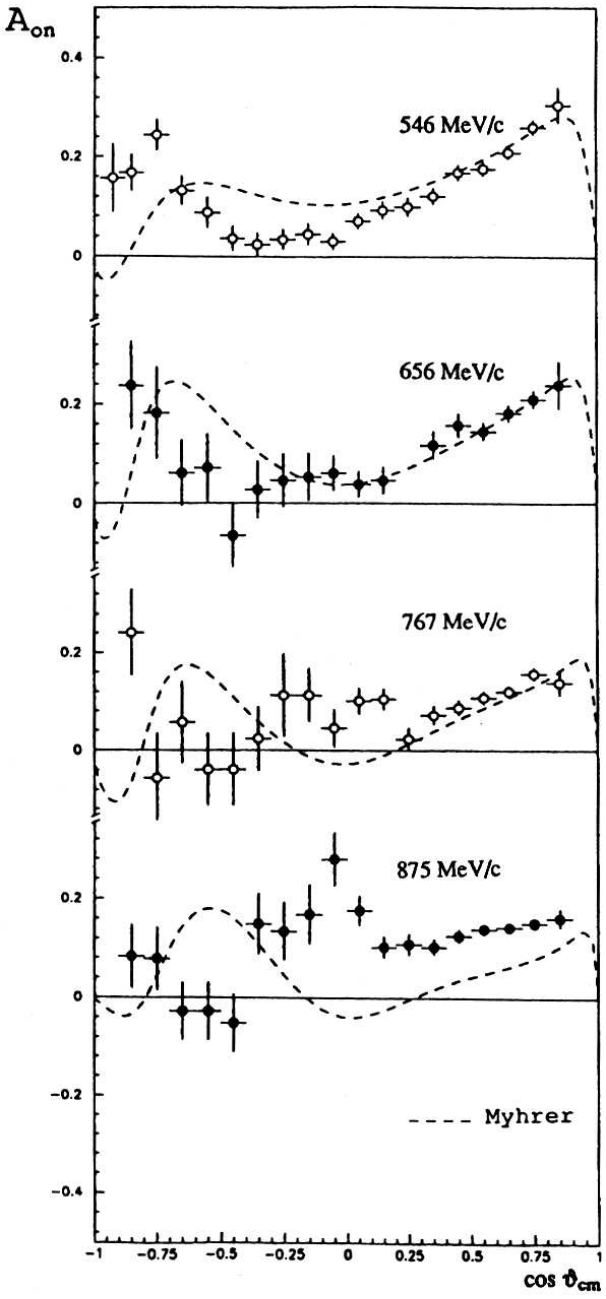

Figure 6.5: Analysing power below 900 MeV/c, compared to the predictions of the Myhrer-Dalkarov model.

edge, there is no such a criticism for the optical model approach to nuclear reactions, as initiated by Feshbach [218]. Anyhow, Shapiro in [240] has underlined that the CCM is more consistent.

In practice, the Lebedev group considered a simple CCM with a minimal number of mesons in the annihilation channels. To have non-relativistic kinematics, it was also assumed that the masses of the two mesons are equal to the ρ mass.

Besides the coupling which are obtained by G-conjugation of the NN OBEP, two sets of parameters must be settled by fitting the data, namely
- the annihilation constant λ_ℓ for each angular momentum $\ell = 0$, 1, or 2.
- the cut-off distances $r_c(\ell)$ for the singular OBEP terms, for the different ℓ, at which the NN potentials were put to 0. Depending on the quantum numbers, the values of r_c varied between 0.50 and 0.72 fm.

The fitting procedure does not give a unique set of values for the annihilation constants λ_ℓ. But if one retains only the parameters corresponding to a potential well that is not too deep, then the solution becomes unique. In the fit, only the annihilation cross-section, and the integrated $\bar{\mathrm{p}}\mathrm{p} \to \bar{\mathrm{p}}\mathrm{p}$ and $\bar{\mathrm{p}}\mathrm{p} \to \bar{\mathrm{n}}\mathrm{n}$ cross-section data were used.

The fit reproduces quite well the angular dependence of the $\bar{\mathrm{p}}\mathrm{p} \to \bar{\mathrm{p}}\mathrm{p}$ differential cross-section at 287 MeV/c, whose strong angular anisotropy results from an interference between the S- and P-waves, and the trend of the ρ parameter as a function of the $\bar{\mathrm{p}}$ momentum.

In Ref. [240], the Lebedev group gave a comparison between their results and the experimental $\bar{\mathrm{p}}\mathrm{p}$ scattering and atomic data. Though the agreement is rather encouraging, we should note that:

1. Only the very-low energy region was investigated.
2. The work was limited by presumably poor computing facilities. In particular, the influence of the mass of effective mesons, of the number of channels which are introduced, etc., was not studied.
3. Also, the influence of the parameters on the angular distributions has not been examined in detail. The spin observables were ignored.

Finally, they calculated the spectrum of the near-threshold $\overline{\mathrm{N}}\mathrm{N}$ quasi-nuclear levels, finding at least five near-threshold P-levels, and confirming the theoretical expectation given in earlier papers by this group.

6.2.2 Liu and Tabakin

Liu and Tabakin have worked out an elaborated coupled-channel description of $\overline{\mathrm{N}}\mathrm{N}$ scattering [229]. They considered explicitly the $\pi^+\pi^-$ and $\mathrm{K}^+\mathrm{K}^-$ channels, calculated the angular distribution and analysing power for these channels, and compared them with the interesting data taken at LEAR [81].

Acceptable fits to the differential cross-section of both $\overline{\mathrm{N}}\mathrm{N}$ scattering and two-meson production data were obtained, as shown in Fig. 6.6, taken from Ref. [229].

The analysing power was estimated for $\bar{\mathrm{p}}\mathrm{p} \to \pi^+\pi^-$ and $\mathrm{K}^+\mathrm{K}^-$, and for the elastic and charge-exchange $\overline{\mathrm{N}}\mathrm{N}$ channels. See Fig. 6.7, again from Ref. [229]. It is a pity that such a promising model has never been applied to calculate more spin observables and compare them with the predictions of optical models.

6.2.3 The Bonn group

The Bonn group (more precisely, the Bonn–Jülich group) has achieved an impressive amount of work on $\overline{\mathrm{N}}\mathrm{N}$ physics, over many years.

Their goal was rather ambitious: develop for the short-range region a coherent model which is consistent with the long-range dynamics. This means describing annihilation in terms of baryon exchange, with the same baryon–meson coupling as in the Yukawa potential. For the sake of comparison, this group also considered some quark-model scenarios.

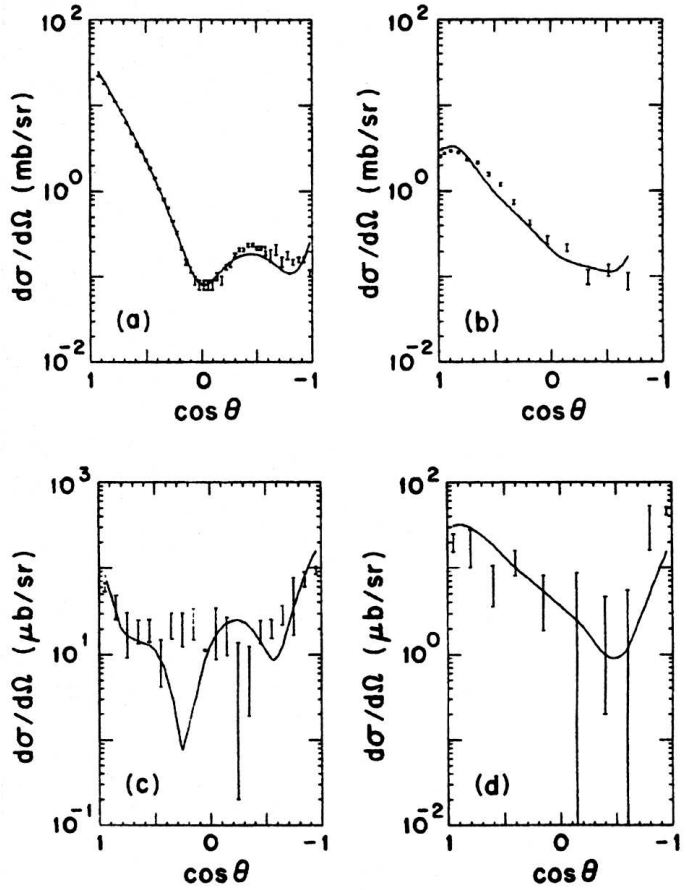

Figure 6.6: Differential $\bar{\mathrm{p}}\mathrm{p}$ cross-sections at 780 MeV/c: (a) elastic, (b) charge-exchange, (c) $\pi^+\pi^-$, (d) $\mathrm{K}^+\mathrm{K}^-$. Solid curves refer to one of the coupled-channel solutions of Ref. [229], where references for the data can also be found.

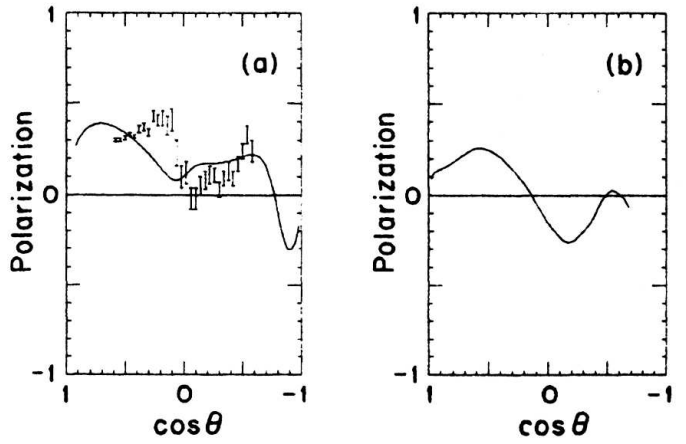

Figure 6.7: Analysing power for $\bar{\mathrm{p}}\mathrm{p} \to \bar{\mathrm{p}}\mathrm{p}$ (a) and $\bar{\mathrm{p}}\mathrm{p} \to \bar{\mathrm{n}}\mathrm{n}$ (b) at 780 MeV/c compared to one of the coupled-channel solutions of Ref. [229].

A pure hadron picture of $\overline{\mathrm{N}}\mathrm{N}$ scattering and annihilation might look at first rather obsolete or nostalgic of the physics of the 50's and 60's. On the other hand, it can be viewed as anticipating "effective theories" designed as an approximation to QCD.

As compared to Liu and Tabakin, the Bonn group has considerably enlarged the set of the two-meson channels explicitly included: besides the pseudoscalar mesons π, η and K, they considered all possible contributions of the lowest-mass mesons with $J^{PC} = 0^{++}$, 1^{--}, 1^{++} and 2^{++} quantum numbers for both isospin $I = 0$ and $I = 1$.

In practice, the Bonn group proceeded by steps, namely [232]:

- model A (BOX) is a mere phenomenological optical model based on the G-parity transformed of the celebrated Bonn NN potential,
- model C contains some explicitly-calculated channels, whose strength is artificially enhanced to account for the missing channels. This leads to a very pronounced spin and isospin dependence.
- model D is presumably more realistic, since it contains contributions of two-meson intermediate states made of π, η, ρ, ω, a_0, f_0, a_1, f_1, a_2, f_2, (via N or Δ exchange) and K, K* (via Λ or Σ, Σ^* exchange), as shown in Fig. 6.8. These two-body (in case of narrow mesons) or quasi-two-body (in case of resonances) channels represent only about 30% of the annihilation which is required to fit the data. The missing part is described by means of a phenomenological, state-independent potential V_{opt}.

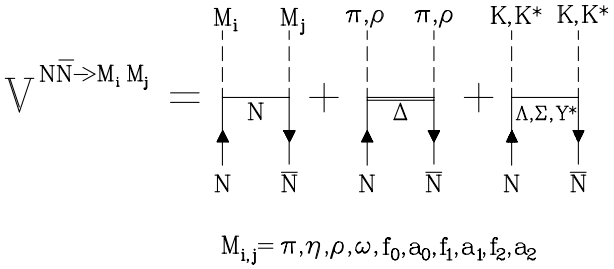

Figure 6.8: Bonn model: transition potentials included explicitly in the microscopic annihilation model.

The formalism developed in Eqs. (3.58–3.60) should thus be slightly extended. The coupled equation for the $\overline{\mathrm{N}}\mathrm{N}$ scattering amplitude $\mathcal{T}^{\overline{\mathrm{N}}\mathrm{N}\to\overline{\mathrm{N}}\mathrm{N}}$ and the transition amplitudes $\mathcal{T}^{\overline{\mathrm{N}}\mathrm{N}\to\mathrm{M}_1\mathrm{M}_2}$ for the annihilation in two mesons, which proceeds via baryon exchange, can be written as

$$\begin{aligned} \mathcal{T}^{\overline{\mathrm{N}}\mathrm{N}\to\overline{\mathrm{N}}\mathrm{N}} &= V^{\overline{\mathrm{N}}\mathrm{N}\to\overline{\mathrm{N}}\mathrm{N}} + V^{\overline{\mathrm{N}}\mathrm{N}\to\overline{\mathrm{N}}\mathrm{N}} G^{\overline{\mathrm{N}}\mathrm{N}\to\overline{\mathrm{N}}\mathrm{N}} \mathcal{T}^{\overline{\mathrm{N}}\mathrm{N}\to\overline{\mathrm{N}}\mathrm{N}} \ , \\ \mathcal{T}^{\overline{\mathrm{N}}\mathrm{N}\to\mathrm{M}_1\mathrm{M}_2} &= V^{\overline{\mathrm{N}}\mathrm{N}\to\mathrm{M}_1\mathrm{M}_2} + V^{\overline{\mathrm{N}}\mathrm{N}\to\mathrm{M}_1\mathrm{M}_2} G^{\overline{\mathrm{N}}\mathrm{N}\to\overline{\mathrm{N}}\mathrm{N}} \mathcal{T}^{\overline{\mathrm{N}}\mathrm{N}\to\overline{\mathrm{N}}\mathrm{N}} \ . \end{aligned} \tag{6.1}$$

The $\overline{\mathrm{N}}\mathrm{N}$ interaction $V^{\overline{\mathrm{N}}\mathrm{N}\to\overline{\mathrm{N}}\mathrm{N}}$ consists of an elastic and an annihilation part, say,

$$V^{\overline{\mathrm{N}}\mathrm{N}\to\overline{\mathrm{N}}\mathrm{N}} = V_{\mathrm{el}} + V_{\mathrm{ann}} \ , \tag{6.2}$$

where V_{el} is the G-parity transformed of the full NN potential, and

$$V_{\mathrm{ann}} = \sum_{ij} V^{\overline{\mathrm{N}}\mathrm{N}\to\mathrm{M}_i\mathrm{M}_j} G^{\mathrm{M}_i\mathrm{M}_j} V^{\overline{\mathrm{N}}\mathrm{N}\to\mathrm{M}_i\mathrm{M}_j} + V_{\mathrm{opt}} \ . \tag{6.3}$$

The diagrams corresponding to the three pieces of the $\overline{\mathrm{N}}\mathrm{N}$ interaction are shown in Fig. 6.9.

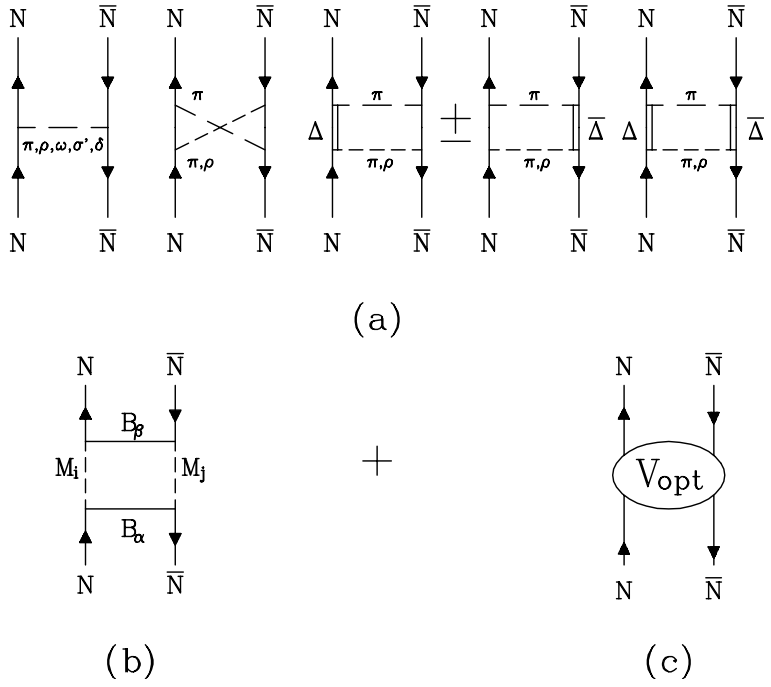

Figure 6.9: Bonn model: elastic (a), microscopic annihilation (b), and phenomenological annihilation (c) part of the $\overline{\mathrm{N}}\mathrm{N}$ interaction model.

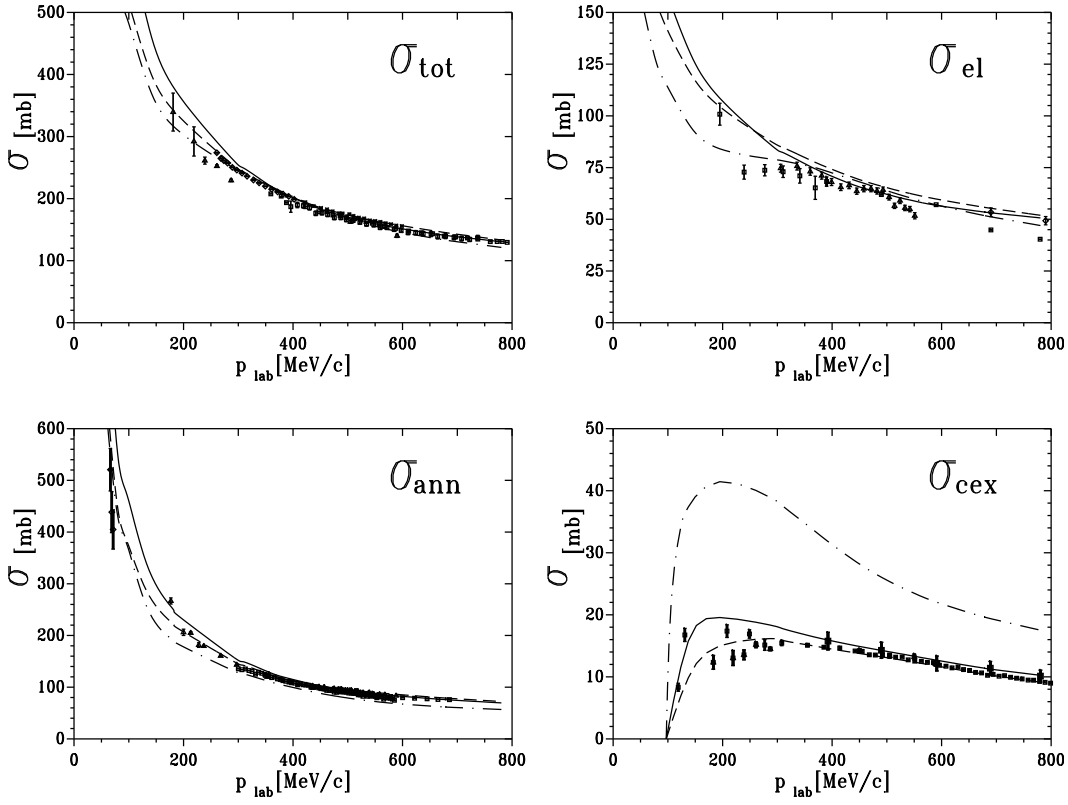

Figure 6.10: Total, elastic, charge-exchange, and annihilation cross-sections for $\bar{\mathrm{p}}\mathrm{p}$ scattering compared with the Bonn models D (solid curve), A (dashed curve), and C (dotted-dashed curve) calculations.

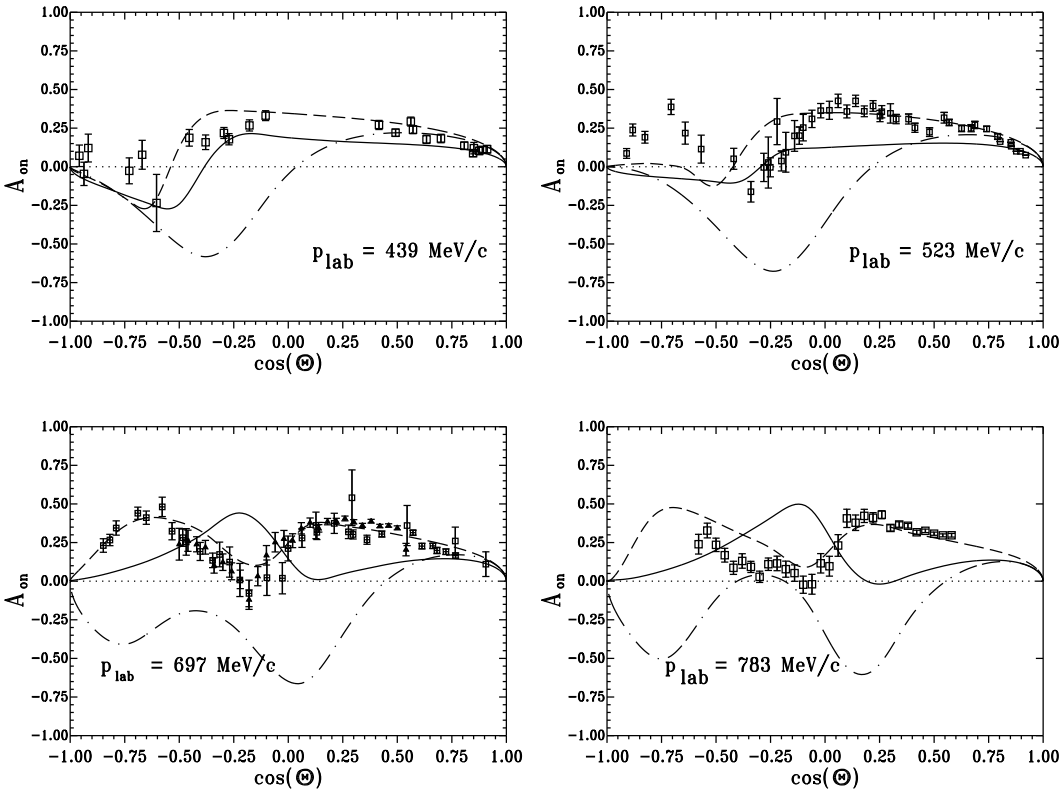

Figure 6.11: Elastic $\bar{p}p$ polarisation data compared with the Bonn models D (solid curve), A (dashed curve), and C (dotted-dashed curve) calculations.

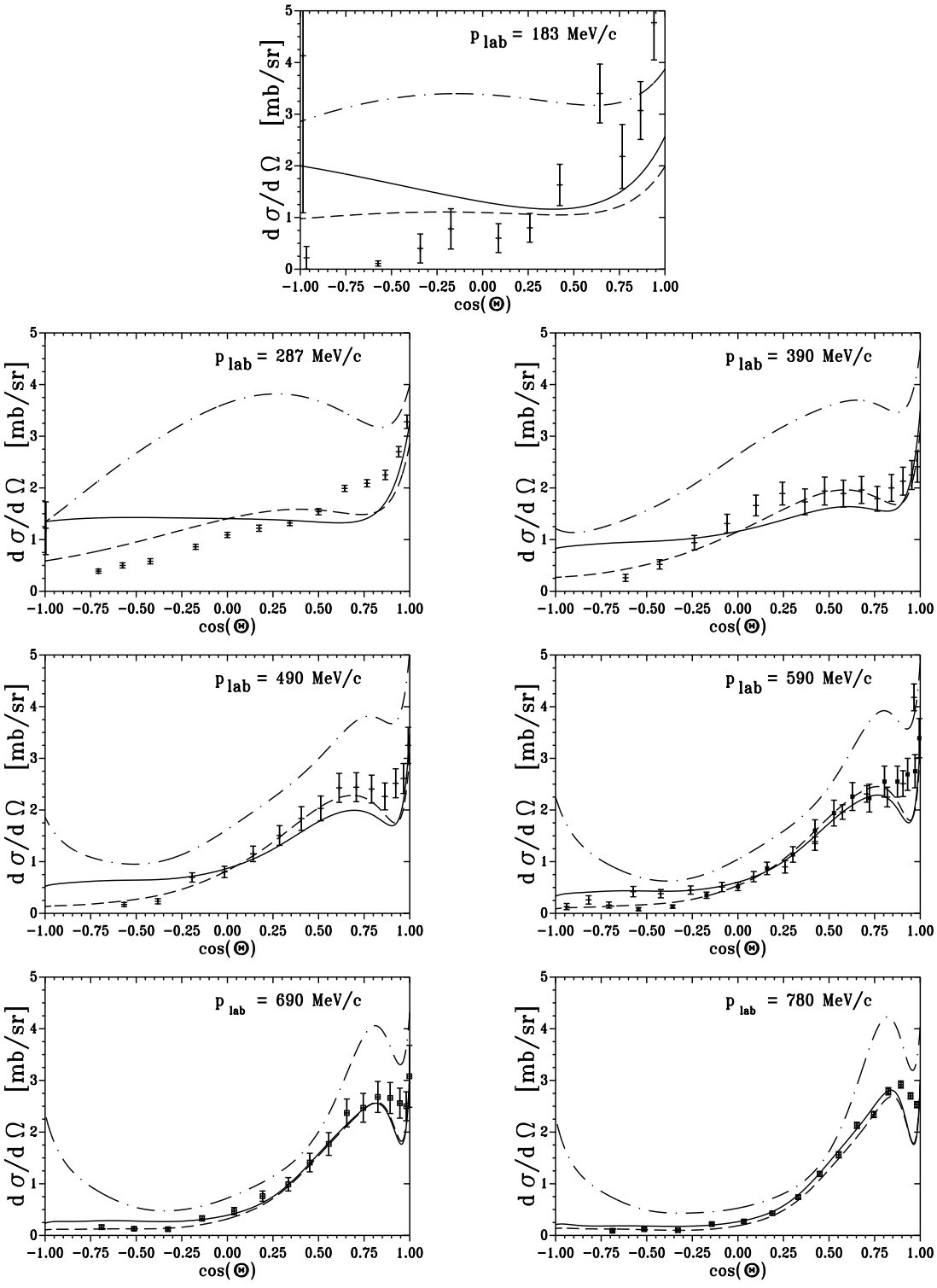

Figure 6.12: Charge exchange $\bar{p}p \rightarrow \bar{n}n$ differential cross-section compared with the Bonn models D (solid curve), A (dashed curve), and C (dotted-dashed curve) calculations.

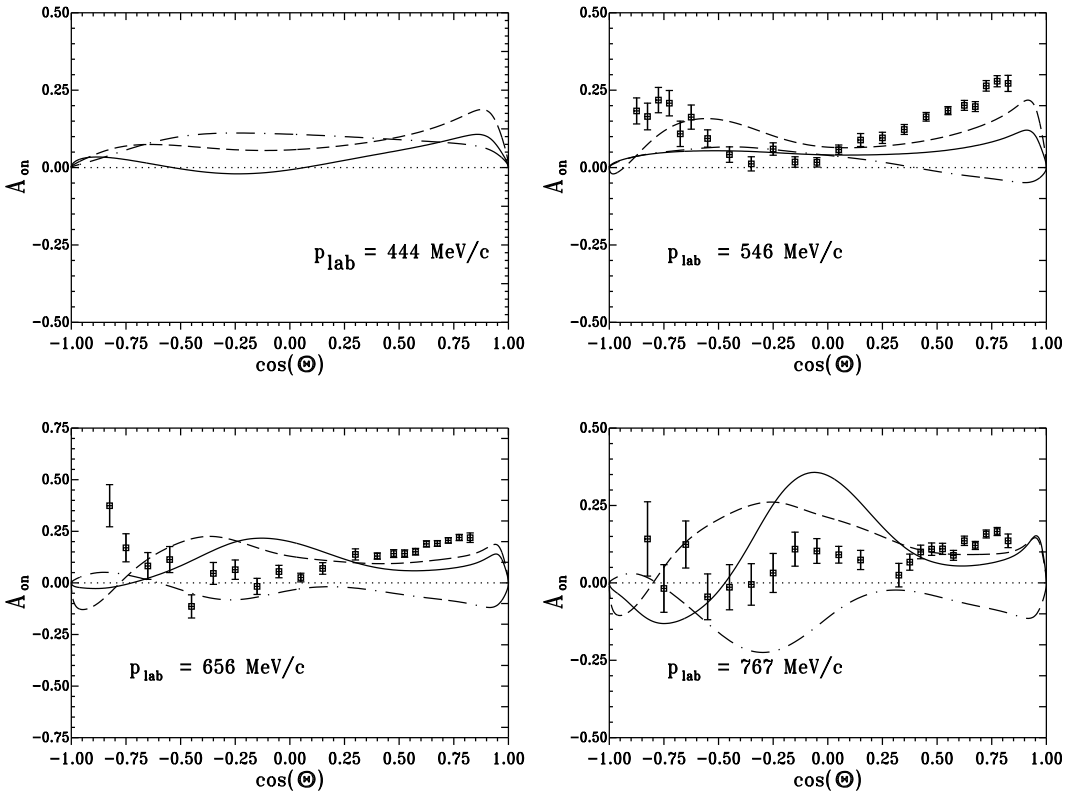

Figure 6.13: Charge exchange $\bar{p}p \rightarrow \bar{n}n$ polarisation compared with the Bonn models D (solid curve), A (dashed curve), and C (dotted-dashed curve) calculations.

Results obtained with the three Bonn models can be seen in Fig. 6.10 to 6.13, for the integrated cross-sections, angular distributions, and analysing power parameters.

Model C fails almost everywhere in reproducing the data. There is not enough absorption in this model. In particular, the integrated charge-exchange cross-section is coarsely overestimated, as apparent in Fig. 6.10. Models A and D reproduce fairly well the differential cross-sections, with the exception of the charge-exchange data below 300 MeV/c (Fig. 6.12). For what concerns analysing power, model A has some success with the elastic channel in the forward hemisphere (Fig, 6.11), while no model reproduces the charge-exchange data (Fig. 6.13).

6.2.4 The Nijmegen Group

In the last decades, the Nijmegen group concentrated a large effort on the study of both the NN and the $\overline{\mathrm{N}}\mathrm{N}$ interaction. They started with the construction of semi-phenomenological potentials, with a meson-exchange tail and an empirical core. Later on, they used their expertise to perform a partial-wave analysis (PWA) of the scattering data, to be discussed below. The results of the PWA's were used to improve the potentials, so that there is an interplay between the two approaches.

In analysing the data, they followed a purely statistical approach: the model parameters are adjusted to the data by comparing the theoretical predictions with the experimental data using a least squared-fitting procedure. In this procedure, the experimental data are scrutinised and filtered: if a contribution to the χ^2 is too large according to rules which can be found, e.g., in Ref. [368], the corresponding data point or set of data is rejected.

They end in 1993 with the "Nijmegen $\overline{\mathrm{N}}\mathrm{N}$ database" [279], which they regard as important as the coupled-channel model or the PWA they produce simultaneously. More comments on the data selection will be given in section 6.4, while presenting the PWA. The so-called CC84 Nijmegen coupled-channels model was constructed in 1984 by P. Timmers et al. [368]. Fitting to the then available pre-LEAR data resulted in a quite satisfactory fit with $\chi^2/N_d = 1.39$. An update of the model CC84 was made in 1991 [369] ("Nijmegen model CC93"). The results were reported at LEAP94 [370].

The $\overline{\mathrm{N}}\mathrm{N}$ coupled channels are not treated in the isospin basis, but in the ($\bar{\mathrm{p}}\mathrm{p}$, $\bar{\mathrm{n}}\mathrm{n}$) basis. This allows to introduce symmetry-breaking effects due to Coulomb interaction in the $\bar{\mathrm{p}}\mathrm{p}$ channel and to the mass difference between the neutron and the proton and between the exchanged π^0 and $\pi^{\pm}$.

The $\overline{\mathrm{N}}\mathrm{N}$ channels are also coupled to annihilation channels. Those are mimicked by the Nijmegen group by two pairs of fictitious mesons with equal masses, one pair with total mass 1700 MeV/c^2, and another one with total mass 700 MeV/c^2, in both isospin $I = 0$ and $I = 1$. See Ref. [371].

In the neutral case, one ends up with six coupled channels. There are also six coupled channels for most initial $\bar{\mathrm{p}}\mathrm{p}$ partial waves, such as ${}^1\mathrm{S}_0$, ${}^1\mathrm{P}_1$, ${}^1\mathrm{D}_2$, ${}^1\mathrm{F}_3$, etc. Due to the tensor force, there are 12 coupled waves for each of the $\bar{\mathrm{p}}\mathrm{p}$ states with natural parity: ${}^3\mathrm{S}_1 + {}^3\mathrm{D}_1$, ${}^3\mathrm{P}_2 + {}^3\mathrm{F}_2$, ${}^3\mathrm{D}_3 + {}^3\mathrm{G}_3$, etc.

The authors use a Schrödinger equation with relativistic kinematics in coordinate space. The interaction is then described by either a 6×6 or a 12×12 potential matrix, schematically

$$V = \begin{pmatrix} V_{\overline{\mathrm{N}}\mathrm{N}} & \tilde{V}_{\mathrm{ann}} \\ V_{\mathrm{ann}} & 0 \end{pmatrix} . \tag{6.4}$$

The 2×2 (or 4×4) sub-matrix $V_{\overline{\mathrm{N}}\mathrm{N}}$ can be written as

$$V_{\overline{\mathrm{N}}\mathrm{N}} = V_{\mathrm{c}} + V_{\mathrm{MM}} + V_{\mathrm{OBE}} , \tag{6.5}$$

where for V_{c} denotes the Coulomb potential with relativistic corrections, V_{MM} the magnetic moment interaction, and V_{OBE} the charge-conjugated Nijmegen NNpotential Nijm78 [372]. The diagonal interaction in the annihilation channels is neglected. The annihilation potential V_{ann} connects the

$\overline{\mathrm{N}}\mathrm{N}$ channels to the two-meson annihilation channels. It is either a 2×4 matrix or a 4×8 matrix. This potential is decomposed as

$$V_{\mathrm{ann}}(r) = \left(V_C + V_{SS}\, \vec{\sigma}_1.\vec{\sigma}_2 + V_T S_{12} m_a r + V_{SO}\, \vec{L}.\vec{S} \frac{1}{m_a^2 r} \frac{\mathrm{d}}{\mathrm{d}r} \right) \frac{1}{1+\exp(m_a r)} \tag{6.6}$$

The factor $m_a r$ is introduced in the tensor component to force its vanishing at the origin. The cut-off mass m_a is taken to be the mass of the meson in the channel, either 850 MeV/c^2 or 350 MeV/c^2. This annihilation potential depends on the spin structure of the initial state.

For each isospin and for each meson channel five parameters are introduced: V_c , V_{SS}, V_T , V_{SO}, and m_a. This gives a model with altogether $4 \times 5 = 20$ parameters, which can be adjusted to fit the $\overline{\mathrm{N}}\mathrm{N}$ data. The best agreement is found with $\chi^2/N_d = 3.5$. The conclusion of the authors was that "although the old Nijmegen soft-core potential Nijm78 is a pretty good NN potential, it is definitely not the ultimate potential."

Extra parameters were thus introduced: the coupling constants of the ρ, ω, $\epsilon(760)$, and $\mathrm{a}_0(980)$ mesons, as well as that of the Pomeron. Varying these parameters within a reasonable range resulted in an appreciable improvement of the fit. The results shown at the LEAP94 conference at Bled [21] indicated, indeed, a dramatically lower $\chi^2/N_d = 1.58$, on the 1993 data set) [370]. In Fig. 6.14, the results of this coupled channel model are compared to the PS199 data on charge-exchange differential cross-section at 693 MeV/c and the analysing power at 656 MeV/c. The agreement with the data is very good.

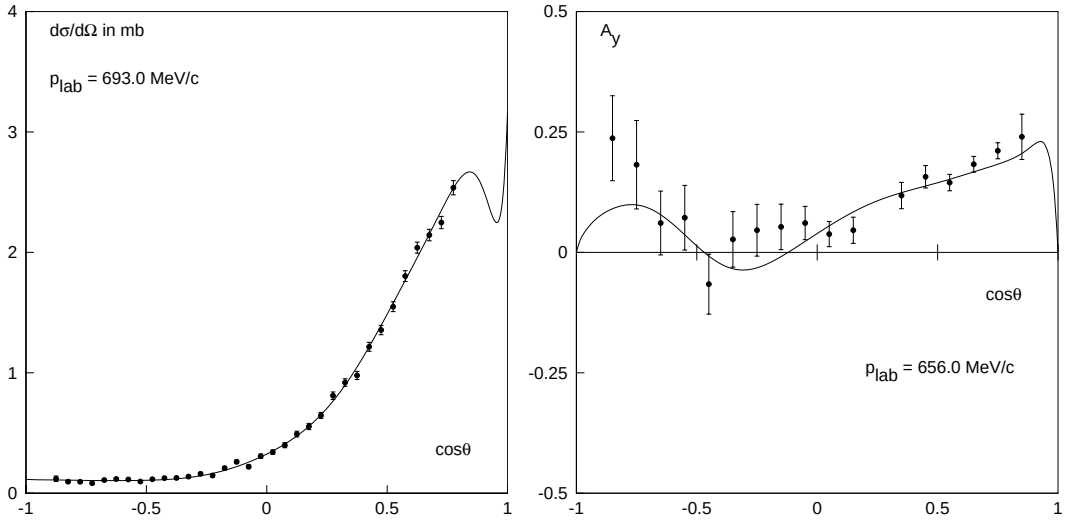

Figure 6.14: Charge-exchange differential cross section and analysing power at 693 and 656 MeV/c. The data are from PS199; the curves are from the Nijmegen Coupled-channel model [370].

6.3 Refined optical model: Paris potential

Early fits to $\overline{\mathrm{N}}\mathrm{N}$ data, such as these by Bryan and Philipps [210], Dover and Richard [214], or Kohno and Weise [212] were done by using a short-range potential which is spin and isospin independent, for simplicity. The spin-isospin dependence of the meson-exchange tail was, however, taken into account (except sometimes an unjustified neglect of the orbital-mixing component $\ell = J - 1 \;\leftrightarrow\; \ell = J + 1$ of the tensor force).

It was then natural to improve the phenomenological studies by introducing some channel dependence in the annihilation potential. We already mentioned in Chap. 3 the work of Bydzovsky et al. [222], where the absorptive potential is allowed to be isospin dependent. A step forward was made by the Paris group in Refs. [237, 277, 367, 373]: in this series of fits, besides some energy dependence, a complete spin dependence (central, spin-spin, spin-orbit and tensor terms) is introduced in the short-range potential for each isospin state. In particular, the imaginary potential is written in each isospin state as

$$\mathcal{I}\mathrm{m}\, V = \left[g_{\mathrm{C}}(1 + f_{\mathrm{c}} T_{\mathrm{L}}) + g_{\mathrm{SS}}(1 + f_{\mathrm{SS}} T_L)\vec{\sigma}_1.\vec{\sigma}_2 + g_{\mathrm{T}} S_{12} + \frac{g_{\mathrm{LS}}}{2m^2}\vec{L}.\vec{S}\,\frac{1}{r}\frac{\mathrm{d}}{\mathrm{d}r} \right] \frac{K_0(2mr)}{r} \,, \quad (6.7)$$

where T_{L} is the kinetic energy of the antiproton in the target frame, and K_0 the modified Bessel function, whose occurence is inspired by considerations on the box diagram 3.8 of Chap. 3.

The meson-exchange potential is kept for distances larger than $r_c = 0.84$ fm. For smaller distances, it is replaced by a polynomial which matches continuously the external potential at r_c, and whose values at $r_2 = 0.6$ fm is a free parameter in the fit.

The authors display their best fit in each paper. The parameters of the successive versions of this Paris potential are compared in Tables 6.1 and 6.2[1]. Our reading of Tables 6.1 and 6.2 is that

Table 6.1: Parameters of the imaginary part in the successive versions of the Paris potential [237, 277, 367, 373]. These are the dimensionless strength factors g_i^I or the slope f_i^I (in MeV^{-1}) of the energy dependence, for isospin I.

Parameter	1982	1991	1994	1999
g^0_{C}	850.	1109.	180.	125.
g^0_{SS}	–570.	–774.	30.	–4.
g^0_{LS}	74.	55	8.	35.
g^0_{T}	53.	99.	–6.	2.
f^0_{C}	0.019	0.011	0.022	0.020
f^0_{SS}	0.015	0.003	0.005	–0.037
g^1_{C}	660.	548	64.	78.
g^1_{SS}	–474.	–299.	11.	20.
g^1_{LS}	74.	7.	7.	12.
g^1_{T}	23.	126.	9.	5.
f^1_{C}	0.019	0.033	0.050	0.033
f^1_{SS}	0.026	0.060	0.058	0.041

several solutions lead to comparable low χ^2, and that new data tend to promote a solution that was only ranked second or third on the basis of the previous data set.

In other words, the fit, however precise and interesting, is far from being unique. This is not too much a surprise. One needs several spin observables, involving complicated polarisation devices and final-spin measurements, to determine the full S-matrix of spin 1/2–spin 1/2 scattering. In the $\overline{\mathrm{N}}\mathrm{N}$ case, we are unfortunately restricted to polarisation (or analysing power) measurements and to a meager set of depolarisation data. In short, fitting the data does not determine the detailed spin and isospin dependence of the core uniquely.

It remains that the very good quality of the fit demonstrates that the LEAR data are compatible with the long- and medium-range interaction of the Paris model, i.e., with the current understanding

[1] We are indebted to B. Loiseau for his help in collecting these values

Table 6.2: Values of the real potential ${}^{I}V_{\alpha}$ at $r_2 = 0.6\,\mathrm{fm}$, for each isospin I, in the successive versions of the Paris potential. Those values were free parameters adjusted to fit the data. The central and spin–spin components are recombined here into a singlet $V_0 = V_{\mathrm{C}} - 3V_{\mathrm{SS}}$ and triplet $V_1 = V_{\mathrm{C}} + V_{\mathrm{SS}}$ components, both with a static and an energy-dependent parts, $V_s = V_s^a + T_{\mathrm{L}} V_s^b$. Units are MeV, except V^b, dimensionless.

Potentials	1982	1991	1994	1999
${}^0V_0^a(r_2)$	–550.	–677.	–1287.	–1014.
${}^0V_0^b(r_2)$	1.23	0.84	0.10	0.15
${}^0V_1^a(r_2)$	–753.	–796.	–1936.	–1613.
${}^0V_1^b(r_2)$	–1.66	–1.92	0.47	–0.23
${}^0V_{\mathrm{LS}}(r_2)$	749.	701.	328.	151.
${}^0V_{\mathrm{T}}(r_2)$	377.	231.	353.	195.
${}^1V_0^a(r_2)$	–1670.	–1037.	–2972.	358.
${}^1V_0^b(r_2)$	–0.15	0.075	–0.44	0.07
${}^1V_1^a(r_2)$	–1107.	–1238.	–658.	–291.
${}^1V_1^b(r_2)$	–1.80	–2.42	–0.44	–0.27
${}^1V_{\mathrm{LS}}(r_2)$	–391.	–108.	–341.	–178.
${}^1V_{\mathrm{T}}(r_2)$	104.	183.	–357.	–221.

of the meson-exchange dynamics. For illustration, we reproduce below some figures (Figs. 6.15–6.20) of the latest paper by the Paris group [367].

The agreement is extremely precise. Even the sharp structure in the elastic differential distribution is well reproduced. In the charge-exchange case, the shape of the angular distribution can evolve from a shoulder to a more pronounced dip-bump structure by tuning the parameters, as already stressed. The rise of the analysing power near 150°, at 546 MeV/c, raises some difficulties, as in other models. Figure 6.18, for instance, illustrates how an earlier version of the Paris potential failed in predicting the forward $\bar{\mathrm{p}}\mathrm{p} \to \bar{\mathrm{n}}\mathrm{n}$ angular distribution. On the other hand, this early Paris potential was rather successful in predicting D_{0n0n}, as illustrated in Fig. 6.20.

6.4 Partial wave analysis

6.4.1 Method

The Nijmegen group is the only one to have performed a partial-wave analysis (PWA) of $\overline{\mathrm{N}}\mathrm{N}$ scattering including the LEAR data. An earlier attempt was done by Laloum [374], in a restricted energy range.

For almost 15 years, the Nijmegen group has worked on partial-wave analyses of NN data, developing rather sophisticated and accurate methods [375–377]. In the early 90's, they applied their techniques to $\bar{\mathrm{p}}\mathrm{p}$ in exactly the same way as to their NN PWA. An account was presented at the NAN93 Conference [371]). The final result is published in Ref. [279].

The paper [279] is entitled "phase-shift analysis", but it is close in spirit to potential models. The authors, indeed, use a Schrödinger equation with relativistic kinematics, with a tail potential including a refined Coulomb interaction and meson exchanges, and a combination of boundary condition and optical model to account for annihilation.

The boundary radius is fixed rather precisely at $R = 1.3$ fm from the width of the diffraction

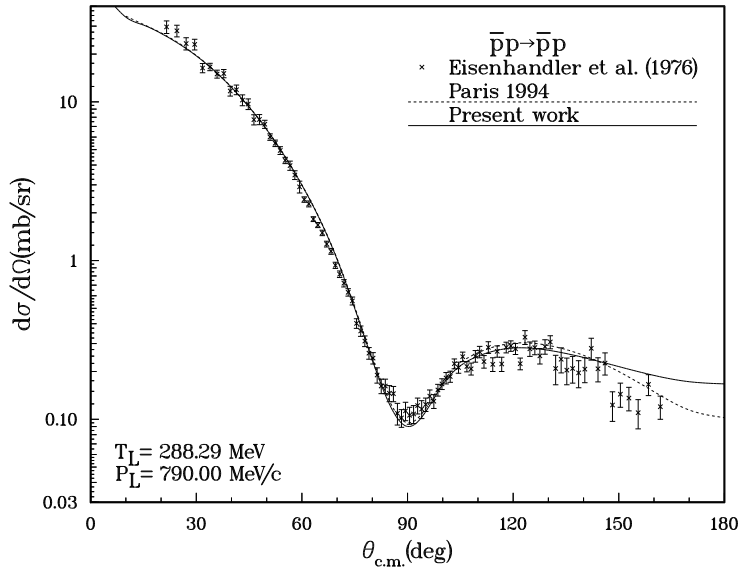

Figure 6.15: $\bar{p}p \rightarrow \bar{p}p$ differential cross-section. The curves are from Ref. [367].

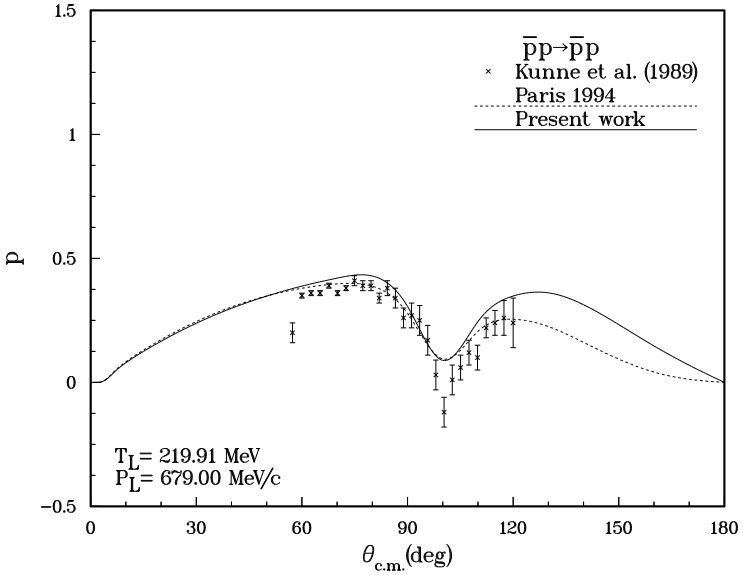

Figure 6.16: $\bar{p}p \rightarrow \bar{p}p$ analysing power. The curves are from Ref. [367].

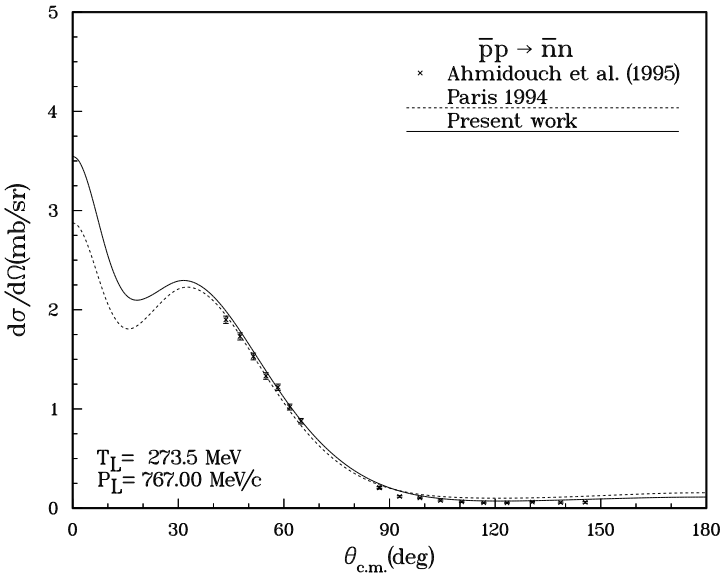

Figure 6.17: $\bar{p}p \to \bar{n}n$ differential cross-section. The data are from PS199, the curves are from Ref. [367].

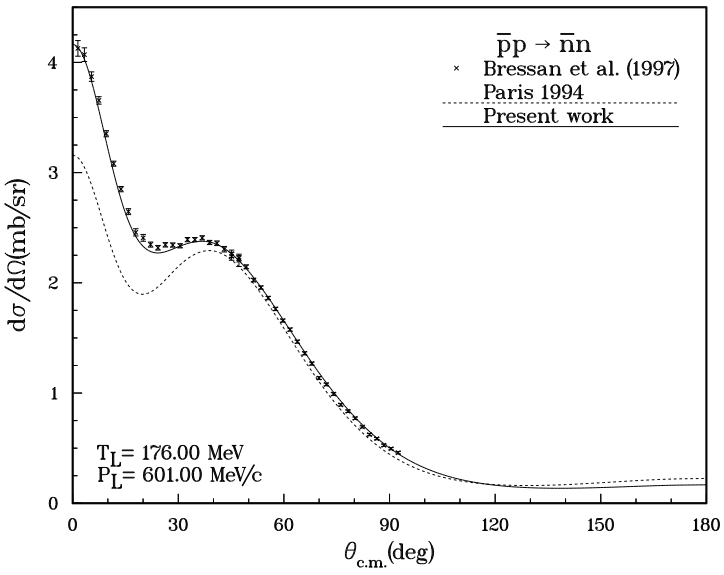

Figure 6.18: $\bar{p}p \to \bar{n}n$ differential cross-section. The data are from PS206, the curves are from Ref. [367].

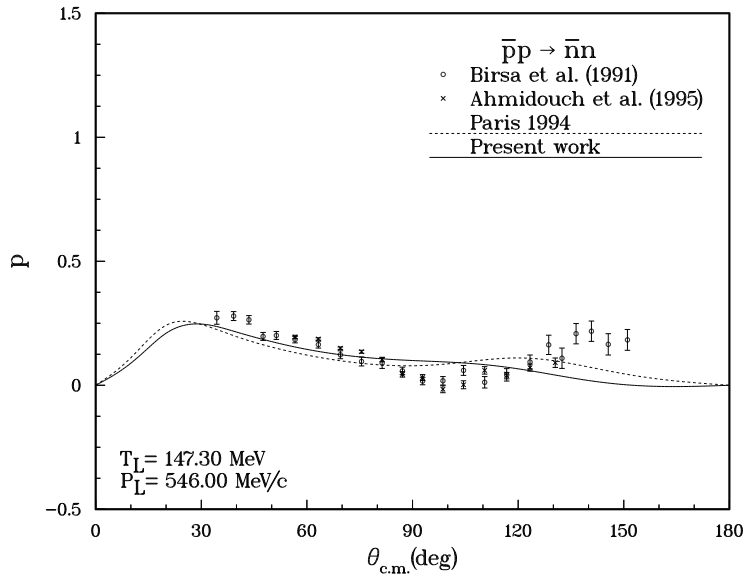

Figure 6.19: $\bar{\mathrm{p}}\mathrm{p} \to \bar{\mathrm{n}}\mathrm{n}$ analysing power. The data are from PS199, the curves are from Ref. [367].

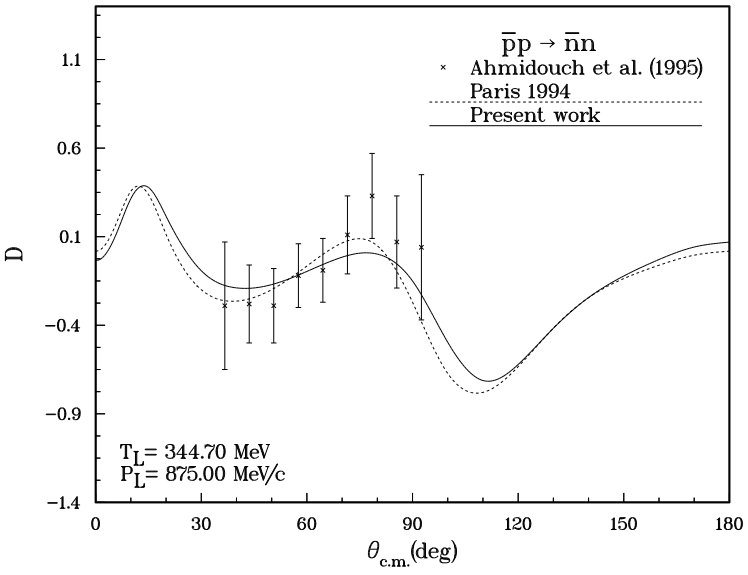

Figure 6.20: D_{0n0n} data from PS199. The curves are from Ref. [367].

peak. In each partial wave L, the long-range potential V_L for $r > R$ is

$$V_L = V_{\overline{\mathrm{N}}\mathrm{N}} + V_{\mathrm{c}} + V_{\mathrm{MM}} \ , \tag{6.8}$$

where the electromagnetic terms V_{c} and V_{MM} are defined in Sec. 6.2.4, and $V_{\overline{\mathrm{N}}\mathrm{N}}$ is the charge-conjugated Nijmegen NN potential, Nijm78 [372].

The boundary condition at $r = R$ may be energy dependent. For the uncoupled waves (like $^1\mathrm{S}_0$, $^1\mathrm{P}_1, \ldots$, and $^3\mathrm{P}_0$, $^3\mathrm{P}_1$, $^3\mathrm{D}_2, \ldots$), an optical-potential picture is adopted, with a square-well optical potential for $r \leq R$, the short-range potential V_S being written

$$V_S = U_S - iW_S \ . \tag{6.9}$$

A slightly more complicated procedure is adopted for the natural-parity partial waves, which are coupled by tensor forces.

A thorough minimisation, by tuning the parameters in the partial waves, led to a remarkably good fit to the subset of data which has been selected. As the phase-shifts are unavoidably computed on the way from the potential to the observables, the authors chose to present their work as a phase-shift analysis.

6.4.2 Data selection

The Nijmegen group had to face several problems in fitting the data. A large amount of work was devoted by the authors to collect the existing data, check their internal consistency and select a subset of data which in their opinion is suitable for the a refined analysis. The Nijmegen group also used normalisation errors sometimes larger than those given by the experiments. The same has been done by the Paris group, in their last fits.

A most delicate issue was the construction of the Nijmegen $\overline{\mathrm{N}}\mathrm{N}$ data set, in which some measurements were not included. In the $\overline{\mathrm{p}}\mathrm{p}$ case, the Nijmegen rejected 744 data points, corresponding to 17% of their final dataset. The detailed description of the criteria applied for data selection can be found in Ref. [279]. They essentially say that the rejected data are not necessarily "bad" data, but had to be rejected to allow them to apply statistical methods satisfactorily. The authors applied a similar practice for analysing proton–proton scattering.

A striking feature of the Nijmegen analysis is that of the final data set only 22% of the data points comes from LEAR . The Nijmegen group has, however, acknowledged the important contribution of LEAR for charge-exchange and polarisation. Still, it is a little disappointing, given the unique potential of LEAR, and the claim that this new facility would have provided much better data than the previous ones. In particular, no experiment dedicated to precision measurements of the $\overline{\mathrm{p}}\mathrm{p} \to \overline{\mathrm{p}}\mathrm{p}$ differential cross section (these data constitute a large fraction of the $\overline{\mathrm{N}}\mathrm{N}$ data bases) was performed at LEAR. The reasons are diverse. The beam allocation to scattering experiments was certainly not sufficient. Other measurements were given more priority. The decision of CERN to give low priority to reaction-dynamics studies at LEAR, taken at Cogne at the beginning of the ACOL era [70], undoubtely discouraged the experimental groups to propose scattering measurements.

6.4.3 Results of the PWA

The results of the Nijmegen PWA on the "accepted" data are really very good. They reached $\chi^2/N_{df} = 1.085$ for 3646 data points, corresponding to $N_{df} = 3503$. The free parameters include the model parameters (30) and normalisation parameters (113) introduced for the different measurements.

The experimental data are compared with the PWA results in Figs. 6.21–6.26 reproduced from Ref. [279].

Integrated cross sections

In Fig. 6.21 the total cross sections from PS172 and the annihilation cross sections from PS173 (see Chap. 4 for references) are compared to the cross-sections calculated with the PWA.

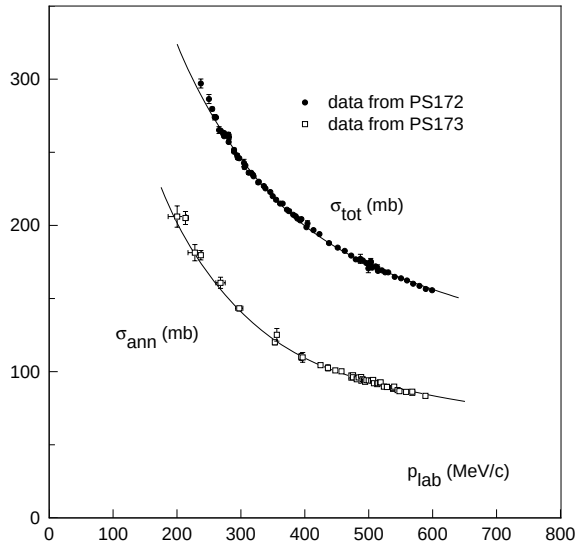

Figure 6.21: Total and annihilation cross-section as a function of the incoming $\bar{\mathrm{p}}$ momentum. The curves are the result of the Nijmegen PWA, the data are from PS172 and PS173.

$\bar{\mathrm{p}}\mathrm{p}$ angular distribution

An example of fits to the $\bar{\mathrm{p}}\mathrm{p}$ differential cross-section can be seen in Fig. 6.22, where the elastic differential cross section data at $p_L = 790\ \mathrm{MeV}/c$ as measured by Eisenhandler et al. are plotted. The fit is excellent and reproduces the smooth trend of the data in the full angular range. As already pointed out in Chapter 4, and underlined also by the Paris group, there are several $\bar{\mathrm{p}}\mathrm{p}$ differential cross-section measurements which are incompatible. Moreover, the quoted errors are often so small that any smooth fit to the entire dataset unavoidably ends up with a very large χ^2. The authors studied the different sets of data coming to the conclusion that the pre-LEAR data by Eisenhandler et al. are incompatible with the LEAR and KEK experiments; also, they could obtain reasonable fits to the LEAR data only at the expense of rejecting the data of Eisenhandler et al. and those of Sakamoto et al. The PS173 data could be reasonably fitted only by rejecting the very forward points, adding point-to-point systematic errors, and assuming a 5% normalisation error not quoted in the publications. Also for the PS198 data they had to add point-to-point errors. At the end, they used the Eisenhandler et al. data, even if with a word of caution. We can only agree with their conclusion that new dedicated experiments (which were essentially not performed at LEAR) "might shed some light on this issue".

$\bar{\mathrm{p}}\mathrm{p} \rightarrow \bar{\mathrm{n}}\mathrm{n}$ angular distribution

The $\bar{\mathrm{p}}\mathrm{p} \rightarrow \bar{\mathrm{n}}\mathrm{n}$ differential cross-section data at 693 MeV/c from PS199 is compared with the PWA fit in Fig. 6.23. These experiments are considered by the authors as "one of the most constraining experiments in the database". To fit these data, they had to take into account orbital momenta up to $\ell = 10$. When this PAW analysis was performed, the PS206 experiment was just approved, and no good quality data in the dip-bump region were available. Before the PS206 data were published, the

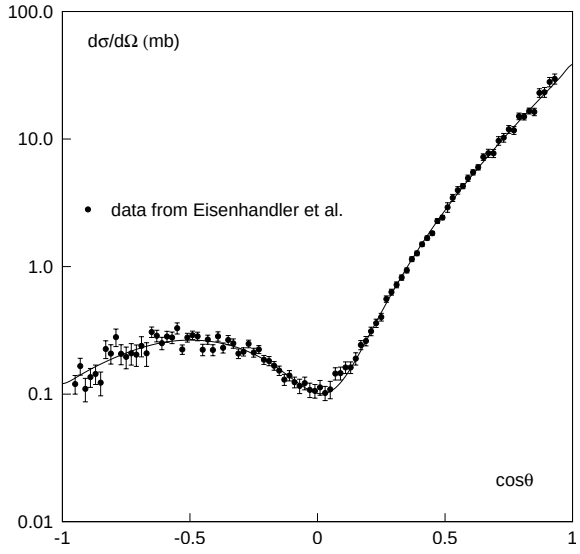

Figure 6.22: Differential cross section for elastic scattering at 790 MeV/c. The data are from Eisenhandler et al. The curve from the PWA.

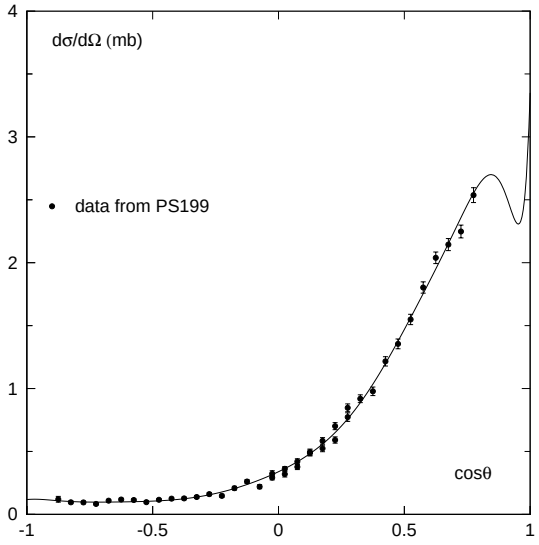

Figure 6.23: Differential cross section for charge-exchange scattering at 693 MeV/c. The data are from PS199. The curve from the PWA.

prediction at 601 MeV was asked[2], and the comparison can be seen in Fig. 6.24. The shape is almost perfect, and the difference in the absolute normalisation between the Nijmegen prediction and the PS206 final result is within the quoted errors.

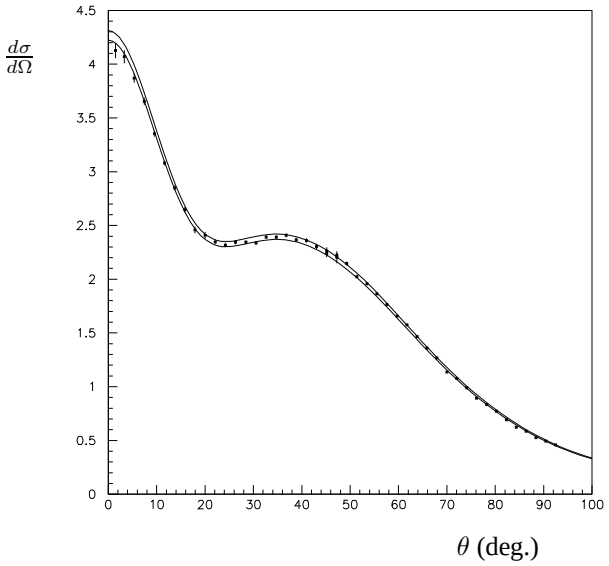

Figure 6.24: Nijmegen private communication: predictions for the $\bar{\mathrm{p}}\mathrm{p} \rightarrow \bar{\mathrm{n}}\mathrm{n}$ differential cross-section, multiplied by 0.955 and 0.975; the data are from PS206.

It was already widely acknowledged (see, for instance, Sec. 6.1.2 and the discussion at the Archamps workshop [378]), that the charge-exchange differential cross sections measurements at very low energy poses a challenge for every model. The Nijmegen group confirms this conclusion, though it is phrased differently: they basically wish to reject the PS173 data, which contribute too much to their χ^2. They are, however, refrained from doing so completely, because there is no alternative data available below 300 MeV/c, and they adopt the philosophy that "imperfect data are perhaps better than no data at all. "

Analysing power

The Nijmegen PWA could fit very well also the $\bar{\mathrm{p}}\mathrm{p} \rightarrow \bar{\mathrm{p}}\mathrm{p}$ and $\bar{\mathrm{p}}\mathrm{p} \rightarrow \bar{\mathrm{n}}\mathrm{n}$ analysing power data, as can be seen in Fig. 6.25 and 6.26.

π coupling

As the PWA includes explicitly the possibility of exchanging a light particle, the analysis confirms the one-pion-exchange contribution, with a mass compatible with the measured mass for $\pi^{\pm}$. The coupling is also an output of the fit. Charge-exchange is particularly sensitive to the pion coupling.

From their analysis of $\overline{\mathrm{N}}\mathrm{N}$ data, the Nijmegen group published results for the $\pi\mathrm{NN}$ coupling constant. In 1991, a PWA on the charge-exchange data alone(which included the first PS199 results of Ref. [111]) lead to a coupling constant $f_c^2 = 0.0751 \pm 11$ [322]. After the publication of all the PS199 analysing-power data in 1994, and using the full PWA93 $\overline{\mathrm{N}}\mathrm{N}$ data set, they found $f_c^2 = 0.0732 \pm 11$.

This result is considered by the authors as evidence for one-pion exchange in the $\overline{\mathrm{N}}\mathrm{N}$ interaction, and evidence for the G-parity rule.

[2] R.G.E. Timmermans, private communication

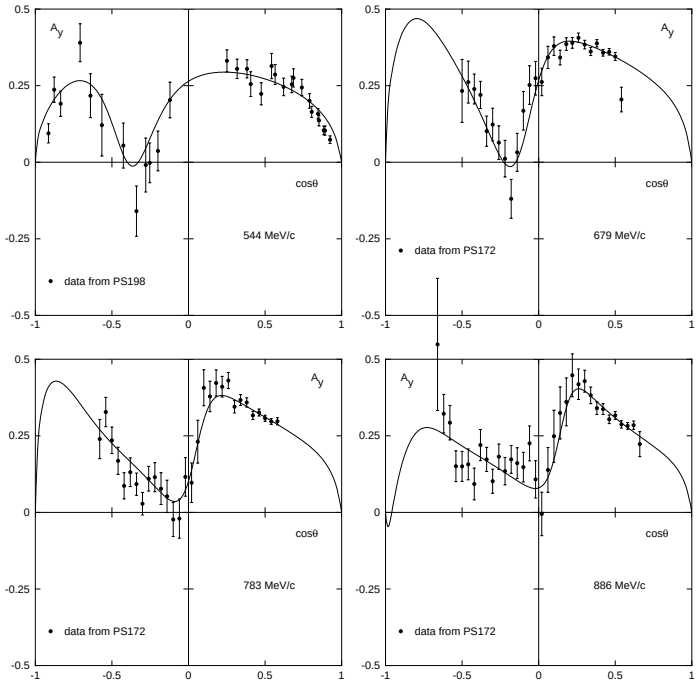

Figure 6.25: Analysing power in elastic scattering at 544, 679, 783, and 886 MeV/c. The data from the LEAR experiments PS172 and PS198 are compared with the PAW fits.

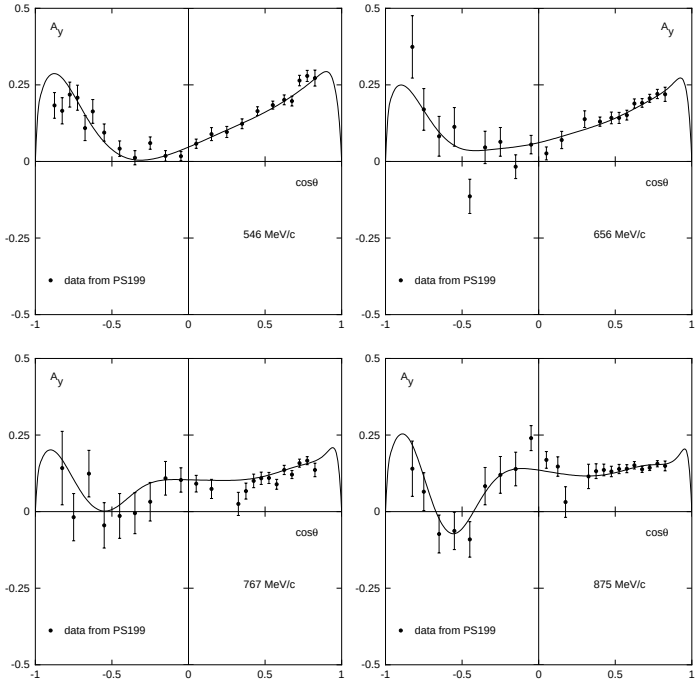

Figure 6.26: Analysing power in charge-exchange scattering at 546, 656, 767, and 875 MeV/c. The data are from the LEAR experiment PS199. The curves are the PWA fits.

6.4.4 Uniqueness of the solution of the PWA

As stressed in Chap. 3, one needs several spin measurements to determine completely a spin 1/2–spin 1/2 reaction. The Nijmegen PWA was based essentially on angular-distribution and analysing-power data. The depolarisation data for $\bar{\mathrm{p}}\mathrm{p}$ have enormous error bars. No accurate spin-transfer or spin-correlation is available.

As for the fits by the Paris group, one may address the question of the uniqueness of the solution, due to the lack of data. This is debated in Refs. [379, 380]. Of course, the uniqueness is even less established for the earlier phase-shift analysis [374], done at a time when available data were even more scarce. The authors of the Nijmegen PWA have given a detailed answer. Let us quote them [370]: "A valid question is therefore: Can one do a PWA of the $\bar{\mathrm{p}}\mathrm{p}$ data, when there are essentially no "spin data"? The answer is yes! The proof that it can be done lies in the fact that we actually produced a $\bar{\mathrm{p}}\mathrm{p}$ PWA with a very good χ^2/N_d. We have also checked this at length in our pp PWA's. We convinced ourselves that a pp PWA using only differential cross-section and analysing power data gives a pretty good solution. Of course, adding spin-transfer and spin-correlation data was helpful and tightened the error bands. However, most spin-transfer and spin-correlation data in the pp dataset actually did not give any additional information. "

Other invocated reasons were the knowledge of the long-range potential with π, ρ, ω, ϵ exchange, and the easy access to powerful computers.

In our opinion, the situation of PWA is comparable to that of optical potentials with detailed spin and isospin dependence. In this latter case, it was clearly shown (see Tables 6.1, 6.2) that drastically different parameters lead to comparable fits.

6.5 Strangeness-exchange reactions

The results of the various runs of the PS185 experiment has motivated many phenomenological studies. We shall give below a brief account of some of the contributions. Clearly, some studies done independently and simultaneously are a little redundant, but equally valuable. So it is a little arbitrary to present in more detail one rather that another.

6.5.1 Main features

The most intriguing aspects of the PS185 measurements of the $\bar{\mathrm{p}}\mathrm{p} \to \overline{\Lambda}\Lambda$ reactions are

1. the energy dependence of the cross-section immediately after the threshold. It cannot be accommodated by a dominant S-wave. This is an indication for P-waves and even higher ℓ contributing very early. This is confirmed by the shape of the angular distribution and the content of their Legendre analysis. It was even speculated (on the basis of early results which were not confirmed) that narrow resonances are responsible for this behaviour. Even if the resonance interpretation is questionable, it remains that there is a specific dynamical mechanism to be identified, giving rise to the early onset of high partial waves, in spite of the centrifugal barrier. This mechanism was searched for either in K, K^* exchange process or in a specific topology of quark diagrams. Is is difficult to distinguish between the two approaches, as pointed out, e.g., in Ref. [381], where the low-energy behaviour is examined.
2. the $\overline{\Lambda}\Lambda$ production occurs practically always in a triplet state, the singlet contribution being almost completely suppressed. This property was noticed in earlier experiments [382, 383]. The debate on how to reproduce the observed spin correlations focused again on the issue of kaon-exchange vs. quark dynamics.

It was hoped that measurement of spin transfer from the proton target will be more decisive to discriminate among the models. The preliminary results are somewhat disappointing, with values in between the predictions of simple quark models and those of simple kaon-exchange models. The final analysis of the last runs of PS185 are, however, not yet published.

6.5.2 Kaon-exchange models

This is the nuclear-physics type of approach to $\bar{\rm p}{\rm p} \to \overline{\Lambda}\Lambda$. As the exchange of charged mesons such as π^+ or ρ^+ mediates the charge-exchange process $\bar{\rm p}{\rm p} \to \bar{\rm n}{\rm n}$, exchanging a strange meson induces a transition from $\overline{\rm N}{\rm N}$ to $\overline{\rm Y}{\rm Y}$, where Y denotes a hyperon. Several groups have studied this mechanism, sometimes in parallel with quark-model pictures, to be discussed later.

Lebedev Institute study of $\bar{\rm p}{\rm p} \to \overline{\Lambda}\Lambda$

In the reviews summarising the work of the Lebedev group on $\overline{\rm N}{\rm N}$ dynamics with the coupled-channel model (CCM) [240, 242], the last part is dedicated to the modifications done to describe the reaction $\bar{\rm p}{\rm p} \to \overline{\Lambda}\Lambda$ near threshold with this CCM: $\overline{\Lambda}\Lambda$ is introduced as a new channel, with an explicit diagonal interaction, and a transition potential from $\overline{\rm N}{\rm N}$ to $\overline{\Lambda}\Lambda$.

For instance, Carbonell, Protasov and Dalkarov [384] have analysed the very-low energy data on the $\bar{\rm p}{\rm p} \to \overline{\Lambda}\Lambda$ cross-section, at the time where a near-threshold resonance was suggested by the data. Their results are reproduced in Fig. 6.27. A resonance is produced with $J^{PC} = 1^{--}$ in the

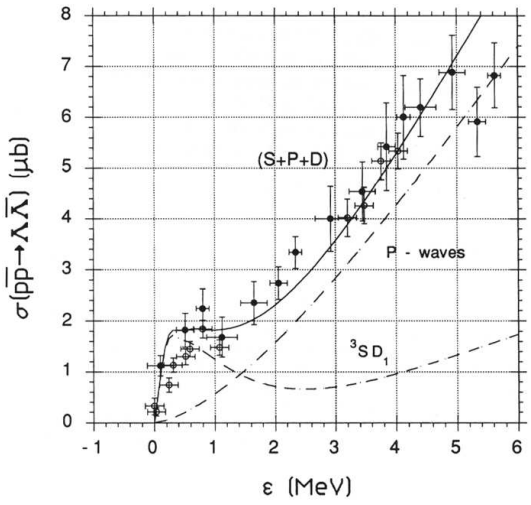

Figure 6.27: Cross-section for $\bar{\rm p}{\rm p} \to \overline{\Lambda}\Lambda$ as measured in early PS185 runs, and analysed by Carbonell et al. within the Lebedev model.

$^3{\rm SD}_1$ coupled waves. It is remarkable that D-wave contributions are necessary to understand the data at such low energy above the threshold. This is confirmed in the model-independent analysis of Ref. [381].

$\bar{\rm p}{\rm p} \to \overline{\Lambda}\Lambda$ analysis by Tabakin et al.

Tabakin and Eisenstein were among the first to develop a formalism to analyse the $\bar{\rm p}{\rm p} \to \overline{\Lambda}\Lambda$ reaction. Their paper [385] contains a comprehensive formalism that was used by other authors.

They studied in some detail the meson-exchange mechanism, including K, $\rm K^*$ and $\rm K^{**}$. They found that the two latter are particularly important, in contrast to the conclusions by Kohno and Weise [386], or by LaFrance et al. [387].

They produce predictions for several spin observables, not yet measured at the time of the paper. Their polarisation is obviously too small. However, the large and positive values of C_{nn} are remarkably anticipated.

In a second paper [388], Tabakin et al. concentrated on the region very near threshold. Assuming only S and P wave (plus $^3{\rm D}_1$ which is coupled to $^3{\rm S}_1$), they were able to determine the contribution

of these complex amplitudes (up to an overall phase). They found large S-D mixing, and large differences between the different P-waves, confirming what was implicitly found by other authors.

$\bar{\mathrm{p}}\mathrm{p} \to \overline{\Lambda}\Lambda$ analysis by the Helsinki group

The Helsinki group has made extensive studies of $\overline{\mathrm{N}}\mathrm{N}$ dynamics, in particular of annihilation mechanisms. In Ref. [389], Niskanen fitted the data with a CCM, using a variant of the Dover–Richard model for $\overline{\mathrm{N}}\mathrm{N}$ and K and K^* exchange for the transition. See also the review articles by Green and Niskanen [390].

Note that $\Delta - \overline{\Delta}$ and $\Sigma - \overline{\Sigma}$ channels are introduced explicitly. The cross-sections are fitted, and then predictions are produced for the spin observables. In particular, this model easily accommodates a very small spin-singlet fraction. Also the large and positive values of the spin-correlation coefficient C_{nn} were predicted. For the other spin observables, the predictions were not confirmed by the data.

$\bar{\mathrm{p}}\mathrm{p} \to \overline{\Lambda}\Lambda$ analysis by LaFrance et al.

In a first paper [391], LaFrance et al. sketched a meson-exchange picture of the $\bar{\mathrm{p}}\mathrm{p} \to \overline{\Lambda}\Lambda$ reaction, and underlined the role of initial- and final-state interaction. In Ref. [387], LaFrance and Loiseau proposed a more detailed study: they use the G-parity transformed Paris potential in the entrance channel, and a similar meson-exchange potential for $\overline{\Lambda}\Lambda$. The transition is mainly due to K exchange, as for Kohno and Weise. The K^* contribution becomes appreciable only when energy increases.

An interesting result is displayed in Table 1 of this paper: they give predictions for $\overline{\Lambda}\Lambda \to \overline{\Lambda}\Lambda$ cross-section, which is heavily dominated by its inelastic part.

$\bar{\mathrm{p}}\mathrm{p} \to \overline{\Lambda}\Lambda$ analysis by the Regensburg group

The Regensburg group has studied several aspects of $\overline{\mathrm{N}}\mathrm{N}$ physics. We mentioned several times the Kohno–Weise optical model of $\overline{\mathrm{N}}\mathrm{N}$, with applications to $\overline{\mathrm{N}}\mathrm{N}$ scattering and specific two-meson annihilation channels. Concerning $\bar{\mathrm{p}}\mathrm{p} \to \overline{\Lambda}\Lambda$, Ref. [386] stressed the importance of initial and final state distortion for obtaining realistic transition rates. In Ref. [392], Kohno and Weise found a good agreement with the data using K-exchange only, without need for K^* or higher resonances. Again, it seems difficult to distinguish K-exchange from simple quark dynamics on the basis of $\bar{\mathrm{p}}\mathrm{p} \to \overline{\Lambda}\Lambda$ only. It is argued, however, that a systematic measurement of strangeness-exchange reactions should allow one to make a choice. See also, Ref. [393].

$\bar{\mathrm{p}}\mathrm{p} \to \overline{\Lambda}\Lambda$ analysis by the Bonn group

The Bonn group has published several interesting papers on strangeness-exchange reactions.

In Ref. [394], Haidenbauer et al. developed a meson-exchange model, a natural extension of their work for $\overline{\mathrm{N}}\mathrm{N}$. They stressed the role of the coherent superposition of K and K^* exchanges, building a strong tensor forces, that naturally leads to a dominance of triplet states. Their conclusion is thus somewhat intermediate between Kohno et al., LaFrance et al., who are satisfied with K exchange, and Tabakin et al, who call for even higher kaon resonances (K^{**}) in the t-channel.

The articles [341,342] were rather influential for the last measurements at LEAR. It is pointed out that the depolarisation parameter D_{nn} is predicted to be positive in simple quark model and negative in their meson-exchange picture, so that its measurement, made possible by scattering antiprotons off a polarised target, could distinguish between the two mechanisms. Their figure is reproduced below, in Fig. 6.28. More details are provided in Ref. [342], where all measured or measurable spin observables are considered at several energies.

In Ref. [395, 396], the study is extended to other hyperon–antihyperon channels. The data on $\bar{\mathrm{p}}\mathrm{p} \to \overline{\Sigma}^0\Lambda + \mathrm{c.c.}$ are rather well reproduced, as illustrated in Fig. 6.29.

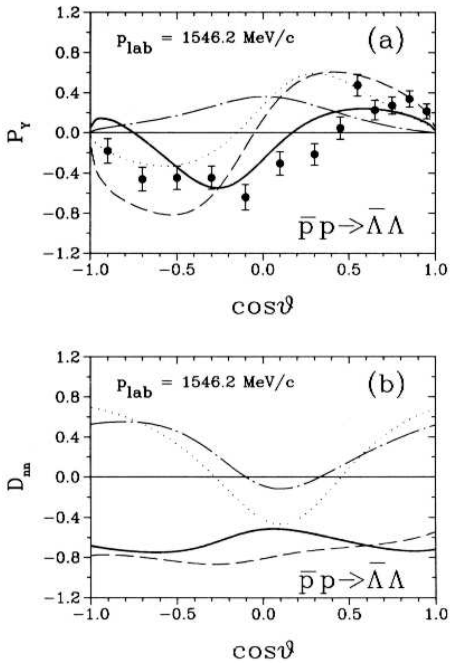

Figure 6.28: Polarisation and depolarisation parameter for $\bar{\mathrm{p}}\mathrm{p} \rightarrow \overline{\Lambda}\Lambda$ as predicted by the Bonn group [341]. The solid curve corresponds to a meson-exchange picture (the dashed one to a variant), while the dashed-dotted and dotted curves are obtained from simple quark-gluon models.

An interesting result is that the $\bar{\mathrm{p}}\mathrm{p} \rightarrow \overline{\Sigma}^{+}\Sigma^{-}$ reaction, which requires exotic states in its t-channel, is not very much suppressed as compared to $\bar{\mathrm{p}}\mathrm{p} \rightarrow \overline{\Sigma}^{-}\Sigma^{+}$ which can proceed via a single kaon exchange. But this later mechanism is not too much effective in their model, because the $\mathrm{pK}\Sigma$ coupling is small. Then both $\bar{\mathrm{p}}\mathrm{p} \rightarrow \overline{\Sigma}^{+}\Sigma^{-}$ and $\bar{\mathrm{p}}\mathrm{p} \rightarrow \overline{\Sigma}^{-}\Sigma^{+}$ get dominant contributions from $\overline{\Lambda}\Lambda$ intermediate states, and thus tend to be of the same order of magnitude.

A further extension to $\bar{\mathrm{p}}\mathrm{p} \rightarrow \overline{\Xi}\Xi$ is proposed in Ref. [397]. This, of course, would require energies which were not accessible at LEAR.

$\bar{\mathrm{p}}\mathrm{p} \rightarrow \overline{\Lambda}\Lambda$ analysis by the Nijmegen group

The Nijmegen group has extended its study of $\overline{\mathrm{N}}\mathrm{N}$ to strangeness-exchange, again insisting on the low value of their χ^2, which reflects, indeed, a good agreement with the data [398–400].

The transition is described in terms of kaon exchange. It is found that the data allow one to recover the mass of the kaon, $m(\mathrm{K}) = 480 \pm 60\ \mathrm{MeV}/c^2$, to be compared to the experimental value 493.7. The $\Lambda\mathrm{NK}$ coupling constant at the pole is found $f^2_{\Lambda\mathrm{NK}} = 0.071 \pm 0.007$. This value is in agreement with the value $f^2_{\Lambda\mathrm{NK}} = 0.0734$ used in the recent soft-core Nijmegen hyperon-nucleon potential [344]. Note, however, that these hyperon–nucleon potentials are regularly updated; see, for instance, Ref. [345].

When presenting their $\bar{\mathrm{p}}\mathrm{p} \rightarrow \overline{\Lambda}\Lambda$ results at a Conference [400], the Nijmegen group provided a number of comments:

- It is underlined that accurate data for the reactions $\bar{\mathrm{p}}\mathrm{p} \rightarrow \overline{\Sigma}^{0}\Lambda + \mathrm{c.c.}$ could give access to the $\Sigma\mathrm{NK}$ coupling constant, and thus to the SU(3) ratio $\alpha = F/(F+D)$.

- They obviously favour meson-exchange, with a well-defined formalism and well-determined coupling, as compared to quark models, whose low-energy limit is not very much under control.

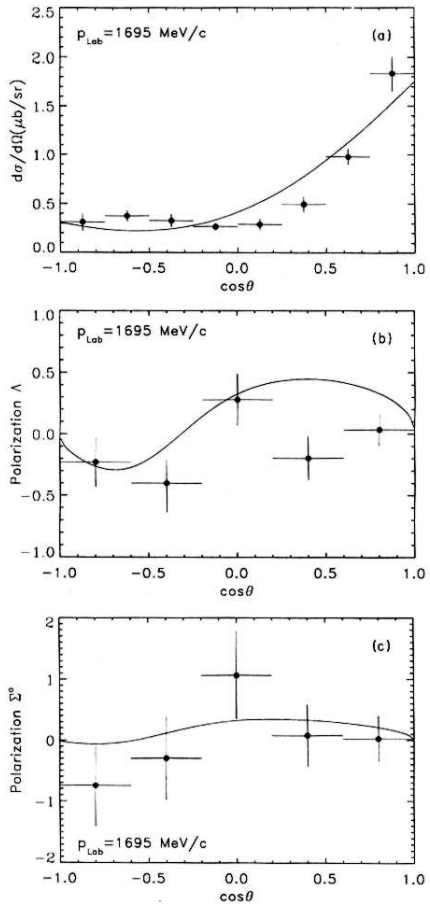

Figure 6.29: Some observables for the $\bar{\mathrm{p}}\mathrm{p} \rightarrow \overline{\Sigma}^0\Lambda + \mathrm{c.c.}$ reaction at $p_{\mathrm{lab}} = 1695\ \mathrm{MeV}/c$, as calculated by the Bonn group [395].

.

- They again overestimate the power of their fitting technology, and do not encourage performing further experiments. To quote Ref. [400]: "It is absolutely not necessary to measure the spin transfer to distinguish between the K(494)- and K^*(892)-exchange picture and a simple quark-gluon-exchange picture. This distinction has already been made using our PWA as a tool and using just the differential cross sections and polarisations."

We do not share this opinion: two observables are not sufficient to fix six complex amplitudes.

- The dominance of triplet states is explained by the crucial role of tensor forces, which act in triplet and vanish for singlet states.

6.5.3 Quark models for $\bar{\mathrm{p}}\mathrm{p} \to \overline{\mathrm{Y}}\mathrm{Y}$

In simple constituent models, the ud pair in a Λ hyperon has spin 0 and isospin 0, and the quantum numbers of the Λ are carried by the strange quark s. Thus measuring how a $\overline{\Lambda}\Lambda$ pair is produced indicates in which state an $\mathrm{s}\bar{\mathrm{s}}$ pair of quark is created out of the available energy. The $^3\mathrm{P}_0$ model has been developed to describe the strong decay of meson and baryon resonances. In this model, which is reviewed in [401], a $\mathrm{q}\bar{\mathrm{q}}$ pair is created with vacuum quantum numbers. On the other hand, a $^3\mathrm{S}_1$ configuration would correspond to the quantum numbers of the gluon. The question of the quantum numbers of the $\mathrm{q}\bar{\mathrm{q}}$ pair also arises in baryon and meson decay, multiparticle production, hadronisation, etc.

This is perhaps too naive a point of view to believe that $\mathrm{q}\bar{\mathrm{q}}$-creation contributes in a single partial wave. However, given the intricate and non-perturbative nature of QCD, one should look at opportunities to extract some simple signals from the background [402].

Rubinstein and Snellman

This paper [402] contains considerations on the relative rates for the various proton–antiproton to baryon–antibaryon reactions, as a function of the assumed $^{2s+1}\ell_J$ partial wave for the annihilating $\mathrm{q}\bar{\mathrm{q}}$ pair and the created $\mathrm{s}\bar{\mathrm{s}}$ pair.

Kroll and Schweiger

In Ref. [403], the $\bar{\mathrm{p}}\mathrm{p} \to \overline{\mathrm{Y}}\mathrm{Y}$ reactions are analysed in a diquark model already used by the authors, or others, in different contexts. A diquark–antidiquark mechanism supplements the quark–antiquark annihilation of Fig. 3.12 of Chap. 3. This provides in particular transitions from $\bar{\mathrm{p}}\mathrm{p}$ to $\overline{\Sigma}^+\Sigma^-$ and to $\overline{\Xi}\Xi$. High-energy data are well reproduced in this model. To our knowledge, it has not been adapted to the PS185 energy-range.

$\bar{\mathrm{p}}\mathrm{p} \to \overline{\Lambda}\Lambda$ analysis by the Genz and Tatur

In Refs. [404, 405], Genz and collaborators analysed various reactions where $\bar{\mathrm{p}}\mathrm{p}$ is transformed into an antibaryon–baryon pair. Reduced cross-sections (with phase-space factors removed) can be compared with various assumptions for the quantum numbers of the $\mathrm{q}\bar{\mathrm{q}} \to \mathrm{s}\bar{\mathrm{s}}$ transition. Assuming gluon quantum numbers ($^3\mathrm{S}_1$) leads to a good agreement with most data.

$\bar{\mathrm{p}}\mathrm{p} \to \overline{\Lambda}\Lambda$ analysis by the CERN–Seattle group

Mary Alberg, with varying but always eminent collaborators, showed a persistent interest in these strangeness-exchange reactions. She also gave several enlightening talks at Conferences, in particular at LEAP98 [47] and LEAP2000 [48].

In Ref. [406], in collaboration with W. Weise, the problem of the spin-singlet fraction is addressed. A rather natural cancellation of pseudo-scalar intermediate states (η, η', ..) is found in a generalisation of the Nambu–Jona-Lassinio model. It remains to extend this idea to spin-singlet states with higher L ($^1\mathrm{P}_1$, etc.).

In an interesting note [338], Alberg at al. discuss the respective merits of the $^3\mathrm{P}_0$ and $^3\mathrm{S}_1$ models of quark-pair creation or annihilation, following a debate initiated by Burkardt and Dillig [337]. They underline the role of initial and final state interaction, and suggest a superposition of both mechanisms to fit the data.

In an often-cited paper [215], Alberg et al. suggested an alternative to kaon exchange or $\mathrm{s\bar{s}}$ creation following $\mathrm{q\bar{q}}$ annihilation: strangeness exchange is achieved by "extracting" an $\mathrm{s\bar{s}}$ pair out of the sea of the proton (or antiproton). See Figs. 3.12 and 3.13 in Chap. 3. As this sea is likely to be polarised, from the analysis of the proton structure functions, very specific effects on the spin-transfer observables are predicted, in particular on D_{nn}.

This investigatory paper did not account for the corrections due to initial or final state interaction, and also ignored that the allowed range for D_{nn} is already bound from the existing data on the correlations coefficients [183, 343]. It had, however, the great merit to trigger the interest on this development of the PS185 experiment.

Their model predicted $D_{nn} < 0$, while conventional quark models tend to predict $D_{nn} > 0$. Meson-exchange models predict also $D_{nn} < 0$. Preliminary experimental results, displayed in Fig. 6.32 below, give $D_{nn} \simeq 0$. Remember that $-1 \leq D_{nn} \leq 1$, and that $D_{nn} = 1$ in absence of any spin-dependent force.

$\bar{\mathrm{p}}\mathrm{p} \to \overline{\Lambda}\Lambda$ analysis by the Tübingen group

In Ref. [407], Furui and Faessler also considered $^3\mathrm{P}_0$ vs. $^3\mathrm{S}_1$ model for creating or annihilating a quark–antiquark pair. They pointed out that the former can digest a change of angular momentum when going from $\overline{\mathrm{N}}\mathrm{N}$ to $\overline{\Lambda}\Lambda$, mimicking a kind of tensor force. They concluded that $^3\mathrm{P}_0$ is favoured.

The paper considered an alternative mechanism with K, K^*, $\mathrm{K}^{**}(J^P = 2^+)$ exchange. They found that the quark model with $^3\mathrm{P}_0$ differs very little from a Yukawa model with K and K^*.

The authors made an interesting comparison between $\mathrm{K}^+\mathrm{K}^-$ vs. $\pi^+\pi^-$ final states, or $\overline{\Sigma}^-\Sigma^+$ vs. $\overline{\Delta}^{--}\Delta^{++}$ final states, concluding – within the assumed mechanism – that $\mathrm{s\bar{s}}$ creation is significantly suppressed. This is a hot subject, as we shall see when reviewing annihilation. For instance, when one starts from a perfectly unbiased initial state and with enough phase-space, one observes almost perfect SU(3) symmetry, as seen from the decay of J/Ψ into various baryon–antibaryon pairs.

Note that the authors predict (in their Fig. 7) the values of the spin-correlation coefficient in their favourite model. We reproduce their curves below, in Fig. 6.30.

s-channel picture of $\bar{\mathrm{p}}\mathrm{p} \to \overline{\Lambda}\Lambda$

An improved quark model approach was proposed by Roberts [227]. Instead of naive diagrams with $\mathrm{q\bar{q}}$ annihilated and $\mathrm{s\bar{s}}$ created, he introduced fully-interacting four-quark states as intermediate states. Tuning the parameters gives a very good agreement with the data, as seen in Fig. 6.31 below. This approach can easily be extended to other hyperon–antihyperon channels.

6.5.4 Impact of further observables

At the Venice Conference [48], the PS185 collaboration presented some preliminary results [408] on the spin tranfer observables D_{nn} and K_{nn}, and even some rank-3 observables. The analysing power A_n (left-right production asymmetry) is shown to differ somehow from the final-state polarisation P_n. Correlations have been measured, and found consistent with previous data.

An updated version of the plot of K_{nn} and D_{nn} shown at Venice [408] is given in Fig. 6.32 below. The data are just in between the quark-model and the kaon-exchange predictions, leading the author to a somewhat pessimistic conclusion: "This demonstrates that the dynamics of strangeness production are not well understood".

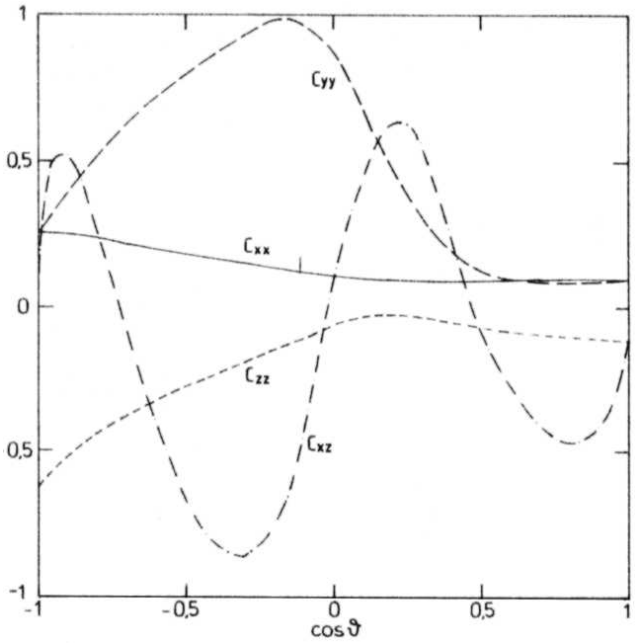

Figure 6.30: Spin correlations coefficients for $\bar{\mathrm{p}}\mathrm{p} \to \overline{\Lambda}\Lambda$ at 1.5 GeV/c, as predicted by Furui and Faessler in Ref. [407].

6.6 Protonium and low energy $\bar{\mathrm{p}}$N scatering

6.6.1 ρ parameter

There have been several discussions about the ρ-parameter, the real-to-imaginary ratio of the forward scattering amplitude. If one takes seriously the nominal value published by different experimental groups, and the point at zero-energy deduced from protonium measurement, one observes a puzzling structure. See Fig. 4.12.

The authors of the Nijmegen PWA insisted on the difficulty in extracting this ρ-parameter from the raw data, and the underestimation of systematic errors. A comparison of the LEAR data with the values of ρ calculated with their PWA is given in Fig. 6.33, taken from Ref. [279].

6.6.2 $\bar{\mathrm{p}}\mathrm{p}$ annihilation at low energy

Cross sections at very low energies are used to extract scattering lengths. The annihilation cross section has been measured down to 44 MeV/c [96, 97, 409]. At these low momenta interference with the Coulomb forces become important [410], and the cross section does no longer scale with the relative velocity but rather with the squared velocity [411].

A first fit to low-energy scattering data using (3.96) was performed in Ref. [295]. Later, more experimental points were added, leading to the fit of Ref. [412] which is presented in Fig. 6.34. The fit returned the $\bar{\mathrm{p}}\mathrm{p}$ S-wave scattering length as

$$\mathcal{I}\mathrm{m}\, a_0^{\mathrm{sc}} = -[0.69 \pm 0.01(\mathrm{stat}) \pm 0.03(\mathrm{sys})]\ \mathrm{fm}\ , \tag{6.10}$$

in excellent agreement with the protonium result given in (5.26). The fit also yielded the P-wave scattering volume

$$\mathcal{I}\mathrm{m}\, a_1^{\mathrm{sc}} = -[0.75 \pm 0.05(\mathrm{stat}) \pm 0.04(\mathrm{sys})]\ \mathrm{fm}^3\ , \tag{6.11}$$

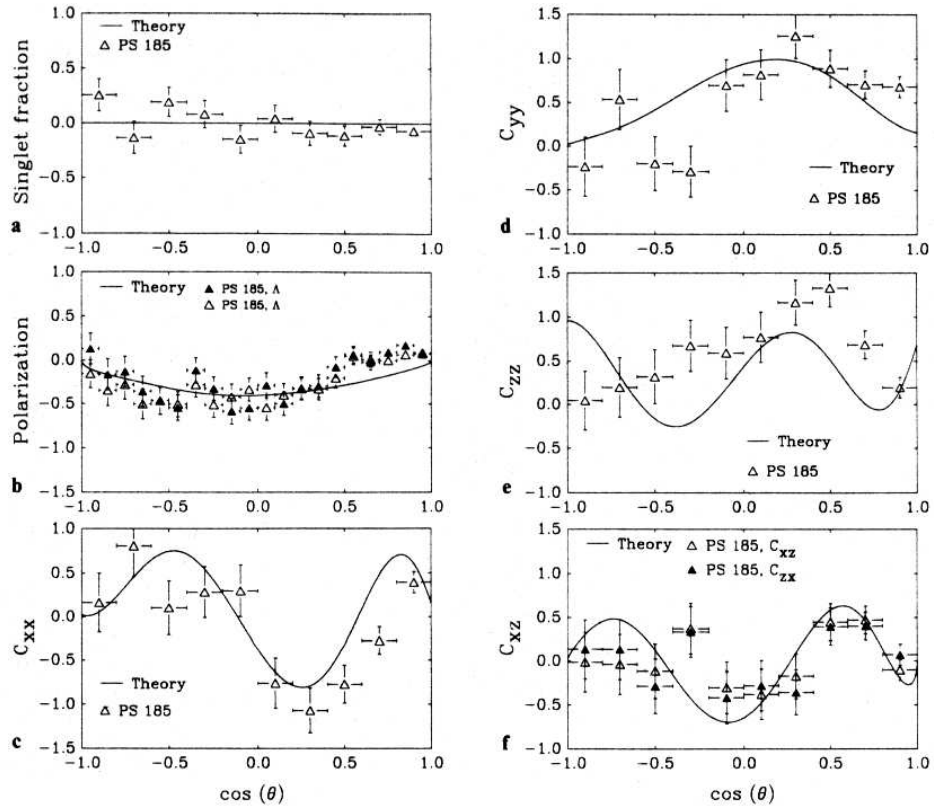

Figure 6.31: Spin parameters for $\bar{\mathrm{p}}\mathrm{p} \to \overline{\Lambda}\Lambda$, as predicted by Roberts in Ref. [227].

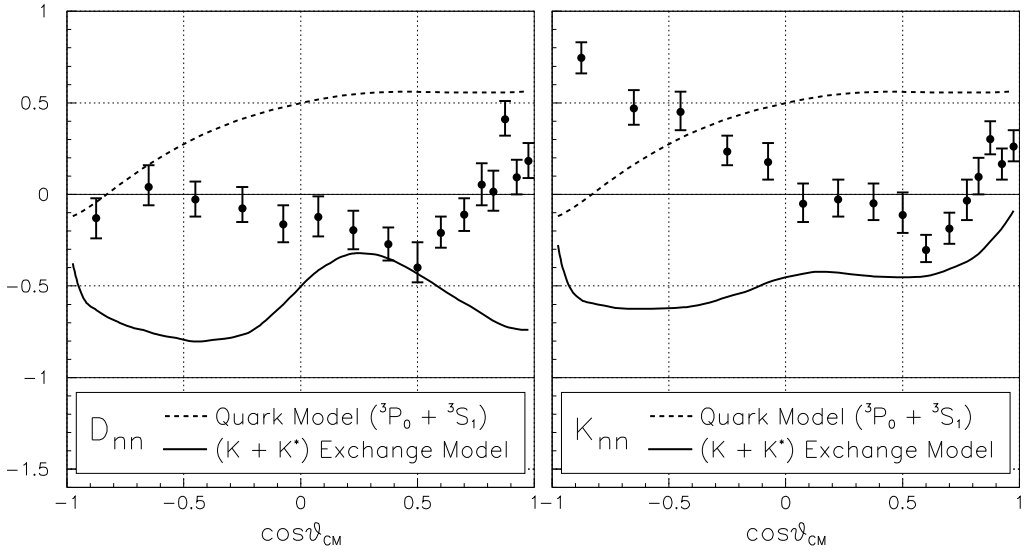

Figure 6.32: Depolarisation and spin transfer parameters for $\bar{\mathrm{p}}\mathrm{p} \to \overline{\Lambda}\Lambda$ at 1.637 GeV/c, as measured at LEAR, compared to a kaon-exchange and a quark-model prediction [342].

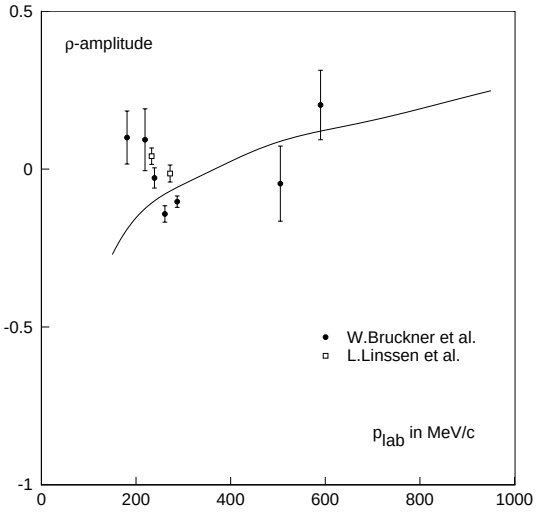

Figure 6.33: Comparison between the ρ parameter data from PS172 and PS173 and the predictions from the Nijmegen PWA.

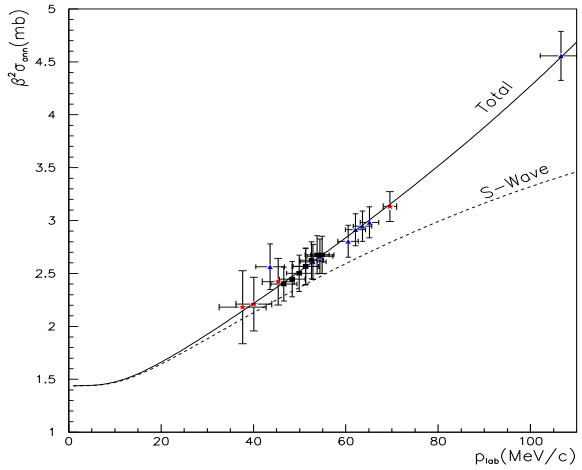

Figure 6.34: The total $\bar{p}p$ annihilation cross section multiplied by the square of the incoming beam velocity. Data are from [96] (▲), [409] (■), and [97] ($\star$). The error bars represent the sum of the statistical and systematic errors. Not included is an overall normalization error (3.4% for [96, 409] and 2.5% for [97]). The theoretical curves are the result of a fit. The full line is the total annihilation cross section, the dashed line represents the S-wave contribution.

which is also in very good agreement with the results from the protonium atom (5.27). The systematic errors in (6.10) or (6.11) come from normalisation uncertainties.

The results obtained from the annihilation cross section at low momenta obviously extrapolate very well to the strong interaction widths of protonium levels. This beautiful agreement gives credit to both types of measurement and to the theoretical frame within which the data were analysed.

6.6.3 $\bar{\mathrm{p}}\mathrm{d}$ annihilation at low energy

The strong interaction shift and width of the 1S level of the $\bar{\mathrm{p}}\mathrm{d}$ atom [177] are of the same order of magnitude as those of the $\bar{\mathrm{p}}\mathrm{p}$ atom. The errors in the scattering lengths one can deduce from these numbers are rather large and a comparison with data on the low-energy $\bar{\mathrm{p}}\mathrm{d}$ annihilation cross section is not very enlightening.

The authors of Ref. [412] adopted a different strategy. They fixed the real part of the S-wave scattering ampltude (to which the annihilation cross section is not sensitive) to the 1S level shift and the P-wave parameters to the average 2P level width (which are fairly precise). Then they performed a fit to the annihilation cross section data with the imaginary part of the S-wave scattering length as only parameter. Their fit and the corresponding scattering data are shown in Fig. 6.35. The fit

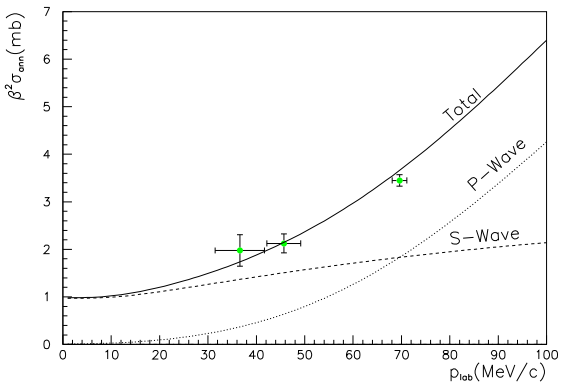

Figure 6.35: The total $\bar{\mathrm{p}}\mathrm{d}$ annihilation cross section multiplied by the square of the incoming beam velocity. Data are from [274]. The theoretical curves are the result of a fit. The full line is the total annihilation cross section, the dashed line represents the S-wave contribution, the dotted one, the P-wave contribution.

provided the imaginary part of the scattering length:

$$\mathcal{I}\mathrm{m}\, a_0^{\mathrm{sc}}(\bar{\mathrm{p}}\mathrm{d}) = -[0.62 \pm 0.02(\mathrm{stat}) \pm 0.05(\mathrm{sys})]\mathrm{fm}\ . \tag{6.12}$$

The imaginary part of the $\bar{\mathrm{n}}\mathrm{p}$ (or equivalently $\bar{\mathrm{p}}\mathrm{n}$) scattering length was determined from $\bar{\mathrm{n}}\mathrm{p}$ annihilation data [274]. The authors quote

$$\mathcal{I}\mathrm{m}\, a_0^{\mathrm{sc}}(\bar{\mathrm{n}}\mathrm{p}) = -[0.83 \pm 0.07(\mathrm{stat})]\mathrm{fm}\ . \tag{6.13}$$

Within a naive geometrical approach to annihilation, one could expect the imaginary part of the $\bar{\mathrm{p}}\mathrm{d}$ scattering length (6.12) to be approximately equal to the sum of the $\bar{\mathrm{p}}\mathrm{n}$ (6.13) and $\bar{\mathrm{p}}\mathrm{p}$ (6.10) contributions:

$$\mathcal{I}\mathrm{m}\, a_0^{\mathrm{sc}}(\bar{\mathrm{p}}\mathrm{d}) \approx \mathcal{I}\mathrm{m}\, a_0^{\mathrm{sc}}(\bar{\mathrm{p}}\mathrm{n}) + \mathcal{I}\mathrm{m}\, a_0^{\mathrm{sc}}(\bar{\mathrm{p}}\mathrm{p})\ . \tag{6.14}$$

The results show that this view is too naive: the three-body problem has to be faced properly. As we shall see, the Faddeev approach resolves this apparent discrepancy.

6.7 Strong interaction effects in protonium

The effects of strong interactions on the energy levels of protonium atoms were predicted long before protonium spectroscopy was accessible to measurement. A detailed comparison of potential-

model calculations with experimental results will be made shortly. We first discuss qualitatively the physical significance of the LEAR data using very simple models.

6.7.1 The 1S upwards shift

The 1S ground-state level is shifted upwards by about 0.73 keV, i.e., experiences a repulsive energy-shift due to strong interacions. This is surprising: the nuclear forces between proton and antiproton are attractive and one may expect additional binding. There are two simple explanations of this phenomenon:

1. We have seen in Chap. 3 that with a superposition of a Coulomb and short-range potential, when the latter supports a bound state, the atomic "1S" state, in the keV range, is in fact a radial excitation of the nuclear bound state. The node generates extra kinetic energy, and thus the energy is shifted upwards with respect to a pure Coulomb state. In other words, the observation of a positive value of $\Delta E_{1\mathrm{S}}$ may be the consequence of the strong binding force of nuclear interactions leading to nuclear bound states with zero orbital angular momentum with $^1\mathrm{S}_0$ and $^3\mathrm{S}_1$ quantum numbers !

2. A more conservative interpretation focusses on the annihilation part of the interaction. Annihilation is very strong at short distances, and the protonium wave function vanishes or is very small for radii of less than a fm. The Coulomb interaction thus looses a highly attractive part and, again, the 1S levels are pushed upwards. We may use our simple model to examen this possibility. For large positive values of λ, the wave function vanishes in the central part, and indeed the energy shift adopts negative values. $\Delta E = 0.7\,\mathrm{keV}$ is reached for a nuclear range of $a = 1.8\,\mathrm{fm}$, see Fig. 3.23. This is not unreasonable as an estimate for the range of nuclear interactions, but this is obviously too large a value for the annihilation range.

The sign and strength of the 1S-level strong interaction shift results in fact from a combination effect of long-range and short-range mechanisms, and is well reproduced in realstic potential models.

6.7.2 2P levels

We can also understand intuitively the large strong interaction widths of the 2P levels [147]. For $\ell = 1$ between proton and antiproton, the potential at large distances comprises the Coulomb part ($\propto -1/r$) and the centrifugal part ($\propto r^{-2}$). The sum forms a Colomb well which is schematically depicted in Fig. 3.26. Without strong interaction, the centrifugal barrier diverges for $r \to 0$. Strong interaction forces are, however, attractive. The centrifugal barrier and the strong interaction potential form a barrier through which tunneling is possible. As soon as a protonium atom tunnels through this barrier, it is sucked into the annihilation region from which there is no return: the atom annihilates. The annihilation probability is obviously dominated by the well-known long-range interaction between proton and antiproton. Details of short-range interaction are not relevant.

6.7.3 Strong interaction effects: predictions versus experiment

We compare in Table 6.3 the experimental results with the corresponding calculated quantities. The latter values are weighted means assuming a statistical population of the fine-structure levels. The comparison is rather good, in particular for the KW model. Only the experimental shift of the $^3\mathrm{P}_0$ level is not correctly predicted. This quantity is only measured in one experiment; and a confirmation would of course be desirable . If the present data are taken seriously, the attraction in the $^3\mathrm{P}_0$ channel is even stronger than in current potentials. May be, in the these models, the coherent tensor force due to pseudoscalar and vector exchanges is too much regularised at short distances.

The 1S results are also summarised in Fig. 6.36.

Table 6.3: Energy shifts and widths of low-lying levels of protonium; comparison of models with experimental results. The largest contribution to χ^2 comes from the width of the $^3\mathrm{P}_0$ state. Excluding this entry from the χ^2 evaluation, there is good agreement between data and predictions, in particular for the Kohno-Weise model. For DR1, DR2, and KW models, the protonium calculations are from Ref. [265]. For the Paris potential, P1 refers to Schweiger et al. [230], who use a separable approximation to the Paris potential, while P2 corresponds to a direct calculation by Moussalam [413].

	P1	P2	DR1	DR2	KW	Exp.	
$\Delta E_{1\mathrm{S}}$	0.84	0.75	0.71	0.76	0.71	0.73 ± 0.03	keV
$\Gamma_{1\mathrm{S}}$	1.01	1.02	0.93	0.95	1.05	1.06 ± 0.08	keV
$\Delta E(^3\mathrm{P}_0)$	–84	–72	–74	–62	–69	-139 ± 20	meV
$\Gamma(^3\mathrm{P}_0)$	130	111	114	80	96	120 ± 25	meV
$\Delta E(^3\mathrm{P}_2, ^3\mathrm{P}_1, ^1\mathrm{P}_1)$	1.9	–0.8	0.5	0.6	–3.9	$+4 \pm 5.8$	meV
$\Gamma(^3\mathrm{P}_2, ^3\mathrm{P}_1, ^1\mathrm{P}_1)$	28	26	26	27	29.5	30.5 ± 2.0	meV
$\Gamma(^1\mathrm{P}_1)$	26	28	26	28	26	51 ± 18	meV
χ^2	25.2	19.4	21.0	25.3	17.7	all data	
χ^2/N_F	2.9	1.4	1.7	1.7	0.9	without $\Delta E(^3\mathrm{P}_0)$	

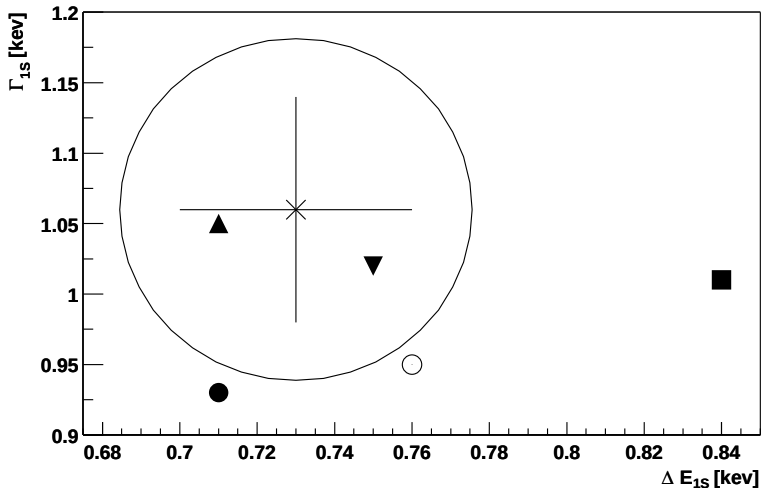

Figure 6.36: . Average experimental result for the 1S energy shift and width, compared to the predictions of the potential models P1 (■); P2 (▼); DR1 (●); DR2 (○); KW (▲), and the 70% C.L. contour plot.

6.7.4 Isospin mixing

We do not need the full machinery of coupled radial equations (3.101) to compute the energy shifts and widths safely. The main advantage of equations (3.101) is to provide the full wave function in addition to energy shifts and widths. In particular, one can estimate the role of $\bar{\mathrm{p}}\mathrm{p} \to \bar{\mathrm{n}}\mathrm{n}$ transitions in protonium.

The results reveal some suprises. The overall amount of the $\bar{\mathrm{n}}\mathrm{n}$ wave function $w(r)$ since the

Table 6.4: Ratio of isovector to isoscalar fraction of the protonium wave function for various initial states $^{2s+1}\mathrm{L}_J$. The three theoretical values correspond to different $\overline{\mathrm{N}}\mathrm{N}$ potentials, as compiled in Ref. [265].

Initial	Potentials			Data analysis	
state	KW	DR1	DR2	Ref. [414]	Ref. [365]
$^1\mathrm{S}_0$	0.68	0.68	0.8	$0.72^{+0.24}_{-0.18}$	$0.50^{+0.48}_{-0.29}$
$^3\mathrm{S}_1$	1.22	0.95	1.26	$1.17^{+0.39}_{-0.28}$	$1.17^{+0.30}_{-0.23}$
$^3\mathrm{P}_0$	0.03	0.03	0.05	1.16 ± 0.34	$0.41^{+0.11}_{-0.09}$
$^3\mathrm{P}_1$	9.4	9.7	6.5	9 ± 5	
$^1\mathrm{P}_1$	0.96	0.82	0.61	0.81 ± 0.51	

exponential damping at large distances $w(r) \sim \exp[-(4m_{\mathrm{r}}\delta m)^{1/2}r]$, for the $\bar{\mathrm{n}}\mathrm{n}$ component is much more effective than the damping $u(r) \sim \exp(-kr)$, with $k = [-2m_{\mathrm{r}}\mathcal{R}\mathrm{e}(E)]^{1/2}$, for the main $\bar{\mathrm{p}}\mathrm{p}$ component. The $\bar{\mathrm{n}}\mathrm{n}$ contribution to the normalisation is of the order of 10^{-6} or 10^{-7} for 1S, and 10^{-9} or smaller for 2P. Also, the change of the energy shift $\Delta\, E$ due to the charge-exchange potential is generally very small, except perhaps for $^3\mathrm{P}_0$.

However, the amount of $\bar{\mathrm{n}}\mathrm{n}$ is predicted to be considerable at short distances. In fact, for $r \lesssim 1\,\mathrm{fm}$, the $\bar{\mathrm{p}}\mathrm{p}$ and $\bar{\mathrm{n}}\mathrm{n}$ wave functions are of comparable magnitude, and when one reconstructs the isospin eigenstates, as per Eq. (3.103), one is very far from the situation with 50% $I = 0$ and 50% $I = 1$. This is seen in Table 3.5. Here the hadronic width is split via Eq. (3.105) into $I = 0$ and $I = 1$ components. Even with an isospin-independent annihilation potential, as in the simple models used in Table 3.5, the ratio Γ_1/Γ_0 of $I = 1$ width to $I = 0$ width is far from the value that it would assume with a pure $\bar{\mathrm{p}}\mathrm{p}$ state. This effect, which was often underlined, could play an important role in the dynamics of annihilation. Isospin mixing is dramatic for two of the P states: the $^3\mathrm{P}_0$ state is predicted to be a pure isoscalar state, the $^3\mathrm{P}_1$ a nearly pure isovector state.

It is interesting to examine to which extent the isospin distortion is seen in annihilation data. Though this is the subject of the forthcoming review article [64], we give below a skeletal summary of the state of the art.

The first attempt to deduce the isospin ratios from experiment was made in [414]. The model assumed that the transition matrix element for annihilation into two mesons is entirely determined by the isospins involved. There are transitions from the $I = 0$ initial state to two isoscalars and to two isovectors, and from the $I = 1$ initial state to one isoscalar and an isovector. The transition matrix elements are then supposed to be independent of the quantum numbers of the initial state, apart from a normalisation which could be different for different initial states. The results are certainly model-dependent, and the errors are large. The isospin-mixing coefficients are found compatible with the predictions of potential models, but, due to the large errors, also with the absence of mixing effects. In annihilation from S-states, the effect of isospin mixing is not very large; in annihilation from P states, the accuracy was rather limited. The subject was further discussed by Dover et al. [270] and more recently by the Crystal Barrel collaboration [365].

The best possibility to test the prediction of isospin mixing is the use of the $^3\mathrm{P}_0$ initial state which is predicted to have only a very small isovector component. We now show that the isovector component of the $^3\mathrm{P}_0$ is not small, using the following series of arguments:

1. The annihilation process $\bar{\mathrm{p}}\mathrm{p}\to\pi^0\pi^0$ is found to proceed via the $^3\mathrm{P}_0$ state and not via the $^3\mathrm{P}_2$ state.

2. The annihilation process $\bar{\mathrm{p}}\mathrm{p}\to\pi^0\eta$ is found to proceed via the same initial state as $\bar{\mathrm{p}}\mathrm{p}\to\pi^0\pi^0$.

Table 6.5: Branching ratios for $\bar{\mathrm{p}}\mathrm{p}$ annihilation at rest in liquid H_2

Annihilation	from $I=0$	Ref.	Annihilation	from $I=1$	Ref.
BR($\bar{\mathrm{p}}\mathrm{p}\to\pi^0\pi^0$)	$(6.93\pm0.43)\cdot10^{-4}$	[364]	BR($\bar{\mathrm{p}}\mathrm{p}\to\pi^0\eta$)	$(2.12\pm0.12)\cdot10^{-4}$	[364]
BR($\bar{\mathrm{p}}\mathrm{p}\to\pi^0\pi^0$)	$(6.14\pm0.40)\cdot10^{-4}$	[415]	BR($\bar{\mathrm{p}}\mathrm{p}\to\pi^0\eta$)	$(2.50\pm0.30)\cdot10^{-4}$	[415]
BR($\bar{\mathrm{p}}\mathrm{d}\to\pi^0\eta$n)	$(1.64\pm0.10)\cdot10^{-4}$	[364]	BR($\bar{\mathrm{p}}\mathrm{d}\to\pi^-\eta$p)	$(4.06\pm1.00)\cdot10^{-4}$	[365]
BR($\bar{\mathrm{p}}\mathrm{p}\to\pi^0\eta'$)	$(2.16\pm0.25)\cdot10^{-4}$	[364]	BR($\bar{\mathrm{p}}\mathrm{p}\to\pi^0\eta'$)	$(1.23\pm0.13)\cdot10^{-4}$	[364]

3. The size of the branching ratio for this reaction is not due to an extremely large coupling to $\pi^0\eta$ from a small isovector $^3\mathrm{P}_0$ component.

4. The conclusion is confirmed looking at a further channel.

First we recall that the $2\pi^0$ final state is produced from the $^3\mathrm{P}_0$ initial state (see section 5.5.4). Otherwise, we should observe 30% P-state annihilation in most channels while partial-wave analyses give about 10%.

The $\pi^0\pi^0$ over $\pi^0\eta$ ratio does not change when going from liquid H_2 to H_2 gas at NTP; the ratios are

$$\mathrm{LH}_2: \quad \frac{\mathrm{BR}(\bar{\mathrm{p}}\mathrm{p}\to\pi^0\eta)}{\mathrm{BR}(\bar{\mathrm{p}}\mathrm{p}\to\pi^0\pi^0)} 0.303\pm0.010 \ \text{[364]}\,, \qquad 0.407\pm0.056 \ \text{[415]}\,, \tag{6.15}$$

$$\mathrm{GH}_2: \quad \frac{\mathrm{BR}(\bar{\mathrm{p}}\mathrm{p}\to\pi^0\eta)}{\mathrm{BR}(\bar{\mathrm{p}}\mathrm{p}\to\pi^0\pi^0)} = 0.366\pm0.035 \ \text{[415]}\,. \tag{6.16}$$

Since the fractional contribution of the $^3\mathrm{P}_0$ state to annihilation increases dramatically with increasing pressure while the $^3\mathrm{P}_2$ contribution remains constant, as seen in Fig. 5.21, the two reactions $\bar{\mathrm{p}}\mathrm{p}\to\pi^0\pi^0$ and $\bar{\mathrm{p}}\mathrm{p}\to\pi^0\eta$ need to proceed via the same initial state. The cascade arguments at the end of section 6.7 require this to be the $^3\mathrm{P}_0$ state. Of course, the reaction $\bar{\mathrm{p}}\mathrm{p}\to\pi^0\eta$ goes via the isovector part of the $\bar{\mathrm{p}}\mathrm{p}$ wave function.

We now compare (Table 6.5) the branching ratios for BR($\bar{\mathrm{p}}\mathrm{d}\to\pi^0\eta$n) and BR($\bar{\mathrm{p}}\mathrm{d}\to\pi^-\eta$p): the former ratio should be reduced compared to the latter one by the fraction of the isovector component in the $\bar{\mathrm{p}}\mathrm{p}$ subsystem (the $\bar{\mathrm{p}}\mathrm{n}$ subsystem is pure $I=1$). According to this argument, the isovector component in the $\bar{\mathrm{p}}\mathrm{p}$ wave function annihilation to $\pi\eta$ is 0.40 ± 0.10.

Finally, the same arguments can be made, with reduced accuracy, using annihilation into $\pi\eta'$. The isovector component is also needed at a smaller momentum (which may correspond to a larger annihilation range) .

In seeking a possible explanation for the apparent failure of the potential models we notice that, possibly, the prediction of potential models for the ratio of $I=1$ to $I=0$ decay widths only applies to the total hadronic width, with an average of five pions in the final state. The decay into two light mesons involves the short range part of the wave function. Perhaps some balance between the $I=0$ and $I=1$ components is restored there, as mentioned in Sec. 4.1, since both isospin components experience an overall suppression due to the strong absorption. Of course, optical models where annihilation is treated globally, reach their limits there. It would be interesting to repeat protonium calculations with coupled-channel models and examine whether the $I=1$ to $I=0$ ratio depends on the mass of the mesons which are introduced in the various channels.

To conclude, isospin mixing in protonium remains rather enigmatic. It is rather firmly predicted in potential models, independent of the particular optical model which is chosen, since mainly driven by pion exchange, which is well established. The effect has been confirmed by different groups. Other predictions of potential models have been verified to a good precision, see Table 6.3, in particular concerning the large width and shift of the $^3\mathrm{P}_0$ as compared to the other states. On the other

hand, the isospin mixing is not seen in current analyses of annihilation data. We are aware that these analyses are partly based on a long chain of arguments which include our present understanding of cascade effects.

6.7.5 Antiprotonic deuterium

There are many common features between protonium and antiprotonic deuterium. However, the microscopic calculation within a potential model is somewhat more complicated in the latter case. If one looks only at the complex energy shifts, then one can use simple approximations for the (n, p, $\bar{\mathrm{p}}$) 3-body problem. This is discussed for instance in [416], with references to earlier works. We are aware of two calculations of the complex energy shift of $\bar{\mathrm{p}}$d atoms. Weighted with the hyperfine structure multiplicities, shift and width were calculated to $\Delta E_{1\mathrm{S}} = 2.17\,\mathrm{keV}, \Gamma_{1\mathrm{S}} = 1.24\,\mathrm{keV}$ [261] and $\Delta E_{1\mathrm{S}} = 1.64\,\mathrm{keV}, \Gamma_{1\mathrm{S}} = 0.78\,\mathrm{keV}$ [417], respectively. The latter calculation uses Fadeev equations and the 3-body problem seems to be treated in a more adequate manner. It is not inconsistent with the experimental values $\Delta E_{1\mathrm{S}} = 1.05 \pm 0.25$ keV and $\Gamma_{1\mathrm{S}} = 1.10 \pm 0.75$ keV which were quoted in (5.16).

Chapter 7

Conclusions

In this review article we have presented the results obtained at LEAR on $\overline{\mathrm{N}}\mathrm{N}$ elastic scattering, charge-exchange and strangeness-exchange, and also on protonium and antiprotonic deuterium. Emphasis was on the ideas which drove the experiments, their realisation, the results, and the impact of the data on the theoretical description of $\overline{\mathrm{N}}\mathrm{N}$ interaction.

The lowest momenta in $\overline{\mathrm{N}}\mathrm{N}$ scattering were accessed by studying strong interaction shifts and widths in protonium atoms. These agree very well with the predictions of models based on meson-exchange potentials. From the strong interaction shifts and widths one can deduce S-wave scattering length and P-wave scattering volume. Cross-section measurements at very low energies allow extrapolation and independent determination of scattering lengths. Both methods give results in good agreement.

In the region of $100\,\mathrm{MeV}/c$ a cross-over from $1/v^2$ to $1/v$ scaling of the cross section is observed. This transition region is required to exist because of the interplay between Coulomb and strong forces.

The momentum range from $150\,\mathrm{MeV}/c$ to $2000\,\mathrm{MeV}/c$ was explored by many experiments: total and differential cross sections as well as analysing power and a few two-spin observables were measured for elastic scattering, charge-exchange, and strangeness-exchange.

The early onset of higher partial waves was a lively-debated subject in $\overline{\mathrm{N}}\mathrm{N}$ physics. P-wave contributions play a prominent role in $\overline{\mathrm{N}}\mathrm{N}$ scattering at momenta where NN scattering is still dominated by S-wave amplitudes. The large P-wave contribution even at lowest momenta was qualitatively assigned to a particular P-wave enhancement of the $\overline{\mathrm{N}}\mathrm{N}$ forces, with the predicted consequence of $\overline{\mathrm{N}}\mathrm{N}$ bound states close to the $\overline{\mathrm{N}}\mathrm{N}$ threshold, but also to the suppression of the S-wave due to the strong annihilation in this partial wave. Now the phenomenon is understood as combined effect of the long-range forces attracting the $\overline{\mathrm{N}}\mathrm{N}$ system into a region where annihilation is strong. The beautiful agreement between the P-wave scattering volume derived from the protonium atoms and the prediction of the one-pion exchange model demonstrates that the large P-wave contribution to annihilation is a genuine effect of G-parity-transformed nuclear forces, and that no special mechanism is needed to explain this effect.

The charge-exchange reaction has allowed for an important contribution of antiproton physics: the $g^2_{\pi\mathrm{NN}}$ coupling constant could be determined at LEAR, and turned out to be smaller than thought before. It would be important to improve on the precision of the $g^2_{\pi\mathrm{NN}}$ value extracted from $\overline{\mathrm{N}}\mathrm{N}$ data and assess its equality with the value extracted from NN and $\pi\mathrm{N}$ data, an interesting test of C invariance of the strong interactions. The charge exchange reaction also identifies the contribution of 2π exchange, likely dominated by the ρ meson.

It was not possible at LEAR to determine a sufficient number of variables which would have allowed a full partial wave analysis. So our knowledge of $\overline{\mathrm{N}}\mathrm{N}$ interactions is not as complete as in the nucleon–nucleon case. Still, a first partial wave analysis of $\overline{\mathrm{N}}\mathrm{N}$ scattering data was performed imposing meson-exchange and Coulomb interaction at large distances.

Meson-exchange models make a few rather general predictions for $\overline{\mathrm{N}}\mathrm{N}$: the $\overline{\mathrm{N}}\mathrm{N}$ interactions should be strongly attractive, tensor forces should be very strong in some partial waves; a strong isospin dependence is expected. These features are well reproduced by the data. On the other hand, meson-exchange contributions, when expressed in the form of a real potential, predict quasinuclear states above and below the $\overline{\mathrm{N}}\mathrm{N}$ threshold. Some of them are deeply bound isoscalar states, several are expected close to the $\overline{\mathrm{N}}\mathrm{N}$ threshold and a large number of $\overline{\mathrm{N}}\mathrm{N}$ resonances was predicted. The search for these states was certainly one of the main motivations to build LEAR, but the premises turned out to be incorrect. In the high-mass range, a series of resonances is observed; none of them has a particularly large coupling to $\overline{\mathrm{N}}\mathrm{N}$. The non-observation of baryonium states underlines the importance of annihilation: even a small overlap of the $\overline{\mathrm{N}}\mathrm{N}$ wave function seems to lead to its collapse.

Strangeness exchange is a short-range phenomenon which was extensively studied at LEAR in the hope that the process could reveal the dynamics of constituent quarks. Due to the self-analysing power of the hyperons, many different polarisation observables are accessible experimentally, and several were measured at LEAR. In spite of this effort, it was not possible to identify the relevant degrees of freedom: there is neither a convincing case that hadronic physics alone is responsible for the observed phenomena, nor have quark models demonstrated superiority in explaining the data. Strong interaction physics, in this energy regime, remains puzzling and resists simple explanations.

The largest uncertainty in the predictions of the potential models stems from annihilation and the contribution of annihilation to the real part of potential. To reproduce the main features of the cross-sections, global isospin independent Wood–Saxon potentials can be assumed, and the annihilation potential is 'black' carrying no characteristic features. The success of black-sphere models, where the incoming wave vanishes at a boundary, underlines both the importance of annihilation and our ignorance about the short-range part of $\overline{\mathrm{N}}\mathrm{N}$ interactions. Still, the use of these simple models allowed to extract important physical information from the data, like the interaction ranges: charge exchange takes place preferentially at 2.5 fm, the mean radius for strong interaction is 1.5 fm, and 1 fm for annihilation.

When the full variety of the existing data set (which includes accurate differential cross-sections and analysing power at many energies) is considered, much more sophisticated models are needed, with typically thirty or more free parameters. In these models the annihilation is no longer black, a spin, isospin, and energy dependence develops, and precise agreement with the data can be obtained only at the expense of simplicity. Understanding the annihilation process therefore is the key for a deeper insight into this realm of physics. In $\overline{\mathrm{N}}\mathrm{N}$ scattering and protonium only the global properties of annihilation could be determined, in the language of potential models. In the annihilation process three quarks and three anti-quarks may annihilate on each other, rearrange and may be recreated to form outgoing $\mathrm{q}\bar{\mathrm{q}}$ mesons. This process must be understood at the quark level; it is hard to imagine that a baryon exchange picture can be applied in a region in which quark wave functions overlap and direct colour-colour interactions must come into the play. A takeover of quark physics, of the colour degrees of freedom, may be the reason why quasinuclear bound states were not found, in spite of considerable experimental efforts.

A prerequisite to further progress in this field is new data. The advent of LEAR has stimulated the work we have summarised in this report. New antiproton facilities are needed to stimulate experimental and theoretical work and try to find the answers to the many questions still left open. In particular more experiments should be done to extend the set of observables and the energy range covered by LEAR. As underlined several times in this review, one needs further tests of our current ideas on the $\overline{\mathrm{N}}\mathrm{N}$ interaction. In particular, spin transfer and spin correlation measurements are necessary; for this purpose, an important goal is to produce polarised antiproton and antineutron beams. Already now, accurate measurements of $\overline{\mathrm{N}}\mathrm{N}$ scattering at very low energy could be done at the CERN AD. Super-LEAR type facilities, with low and medium-energy antiprotons are presently being proposed in Japan (JHF) and in Europe (GSI project), and on a longer time scale could allow to resume the study of this fascinating chapter of hadronic physics.

List of Figures

List of Tables

Bibliography

[1] A. Pais, *Inward Bound of Matter and Forces in the Physical World* (Clarendon Press, Oxford, 1986).

[2] E. Segrè, *From X-rays to Quarks: Modern Physicists and their Discoveries* (Freeman, San Francisco, 1980).

[3] R.N. Cahn and G. Goldhaber, *The Experimental Fundations of Particle Physics* (Cambridge University Press, Cambridge, 1989).

[4] L.M. Lederman and D. Teresi, *The God Particle: if the Universe is the Answer, what is the Question ?* (Houghton Mifflin, Boston, 1993).

[5] C.D. Anderson, "The positive electron," Phys. Rev. **43** (1933) 491.

[6] O. Chamberlain, E. Segrè, C. Wiegand and T. Ypsilantis, "Observation of antiprotons," Phys. Rev. **100** (1955) 947.

[7] O. Chamberlain et al., "Example of an antiproton-nucleon annihilation," Phys. Rev. **102** (1956) 921.

[8] M.D. Kaplan, "Perspects for low-energy antiproton physics at Fermilab", in [48].

[9] G.P. Jackson, "Accelerator possibilities for low energy antiprotons at the Fermi National Laboratory", in *Workshop On Low-Energy Pbar Storage Ring (Pbar2000)*, Chicago, USA, 3-5 August 2000. D.M. Kaplan and H.A. Rubin (eds.); Illinois Institute of Technology, Chicago, IL60616.

[10] *International Workshop on JHF Science (JHF 98)*, Tsukuba, Japan, 4-7 Mar. 1998. J. Chiba, M. Furusaka, H. Miyatake, S. Sawada (eds.); KEK, Tsukuba, Japan (1998).

[11] Y. Mori, C. Ohmori et al., "50-GeV proton synchrotron for JAERI/KEK joint project," in [48].

[12] V. Metag, "Hadron physics with anti-protons: The HESR-project at GSI," in [48].

[13] C. Baglin et al., "Search for the P-wave singlet charmonium state in $\bar{\mathrm{p}}\mathrm{p}$ annihilations at the CERN Intersecting Storage Ring," Phys. Lett. B **171** (1986) 135.

[14] C. Baglin et al., "Formation of the χ_1 and χ_2 charmonium resonances in antiproton-proton annhilation and measurements of their masses and total widths," Phys. Lett. B **172** (1986) 455.

[15] T.A. Armstrong et al., "Observation of the P-wave singlet state of charmonium," Phys. Rev. Lett. **69** (1992) 2337.

[16] *International Conference on Antinucleon- and Nucleon-Nucleus Interactions*, Telluride, Colorado, 18-21 Mar. 1985 G.E. Walker, Ch.D. Goodman, and Ch. Olmer (eds.); New York Plenum (1985).

[17] *International Symposium on Medium-Energy Nucleon and Antinucleon Scattering . Medium energy nucleon and antinucleon scattering*, Bad Honnef, Fed. Rep. Germany, 18-21 June 1985. H.V. von Geramb (ed.); Berlin Springer (1985) 576 p.

[18] J. Cugnon et al., "Geometrical effects in anti-proton annihilation on nuclei", Phys. Rev. C63 (2001) 027301.

[19] T.A. Armstrong et al., "Fission of heavy hypernuclei formed in antiproton annihilation," Phys. Rev. C **47** (1993) 1957.

[20] J.-M. Richard, "Some aspects of antiproton–nucleus physics," in [21].

[21] *3^{rd} Biennial Conference on Low-Energy Antiproton Physics: LEAP '94*, Bled, Slovenia, 12-17 Sep. 1994. G. Kernel, P. Krizan, and M. Mikuz (eds.); Singapore World Scientific (1995).

[22] R.S. Hayano et al., "Laser spectroscopy of antiprotonic helium and stringent constraint on the antiproton charge and mass," Nucl. Phys. A **663** (2000) 955.

[23] See, e.g., A. Apostolakis et al., "A detailed description of the analysis of the decay of neutral kaons to $\pi^+\pi^-$ in the CPLEAR experiment," Eur. Phys. J. C **18** (2000) 41, and references therein.

[24] S. Maury, "AA/AC/AD and Future Antiproton Complex at KEK," in [10].

[25] F. Balestra et al., "Antiproton - Helium annihilation around 44 MeV/c", Phys. Lett. B **230** (1989) 36.

[26] A.G. Cohen, A. De Rujula and S.L. Glashow, "A matter–antimatter universe?," Astrophys. J. **495** (1998) 539.

[27] S. Orito et al., "Precision measurement of cosmic-ray antiproton spectrum," Phys. Rev. Lett. **84** (2000) 1078.

[28] T. Saeki et al., "A new limit on the flux of cosmic antihelium," Phys. Lett. B **422** (1998) 319.

[29] I.S. Shapiro, "The physics of nucleon-antinucleon systems," Phys. Rept. **35** (1978) 129.

[30] W.W. Buck, C.B. Dover and J.-M. Richard, "The interaction of nucleons with antinucleons. 1. General features of the $\mathrm{N\overline{N}}$ spectrum in potential models," Annals Phys. **121** (1979) 47.

[31] *Symposium on Nucleon-Antinucleon Annihilations*, Chexbres, Switzerland, 27-29 Mar. 1972. L. Montanet (ed.); CERN "Yellow" report CERN 72-10.

[32] *Symposium on Nucleon-Antinucleon Interactions*, Liblice-Prague, Czech Republic, 25-28 June, 1974. L. Montanet (ed.); CERN "Yellow" report CERN-74-018.

[33] *European Symposium on Antinucleon-Nucleon Interactions*, Stockholm, 9-13 July, 1976. G. Ekspong and S. Nilsson (eds.); Oxford Pergamon (1977).

[34] *European Antiproton Symposium*, Barr (Strasbourg), France, 25-30 June 1978. A. Fridman (ed.) ; CNRS, Paris (1979).

[35] *European Symposium on Nucleon-Antinucleon Interactions*, Bressanone, Italy, 23-28 June 1980. Istituto Nazionale di Fisica Nucleare, Padova; Padova CLEUP (1980), Ed. M. .cresti.

[36] *European Symposium on Nucleon - Antinucleon and Quark - Antiquark Interactions*, Santiago de Compostela, Spain, 30 Aug. - 3 Sep. 1982. An. Fis. A 79 (1983) v1, Ed. J. Campos.

[37] *7^{th} European Symposium on Antiproton Interactions: from LEAR to the Collider and beyond - Antiproton '84*, Durham, UK, 9-13 July 1984. M.R. Pennington (ed.); Bristol Hilger (1985).

[38] *European Symposium on Nucleon - Antinucleon Interactions: Antiproton '86*, Thessaloniki, Greece, 1-5 Sep. 1986. S. Charalambous, C. Papastefanou, and P. Pavlopoulos (eds.); Singapore World Scientific (1987).

[39] *9^{th} European Symposium on Proton - Antiproton Interactions and Fundamental Symmetries*, Mainz, Fed. Rep. Germany, 5-10 Sep. 1988. K. Kleinknecht and E. Klempt (eds.); Nucl. Phys. B (Proc. Suppl.) 8 (1989).

[40] *Workshop on Physics with Cooled Low-Energetic Antiprotons.* CERN-KfK workshop, Karlsruhe, 19-21 Mar. 1979. H. Poth (ed.); KFK report 2836.

[41] *Workshop on Physics at LEAR with Low-energy Cooled Antiprotons*, Erice, Italy, 9-16 May 1982. U. Gastaldi and R. Klapisch (eds.); New York Plenum (1984).

[42] *3^{rd} LEAR Workshop: Physics in the ACOL Era with Low-Energy Cooled Antiprotons*, Tignes, France, 19 - 26 Jan 1985. U. Gastaldi et al. (eds.); Ed. Frontières, Gif-sur-Yvette (1985).

[43] *4^{th} LEAR Workshop: Physics at LEAR with Low-Energy Antiprotons*, Villars-sur-Ollon, Switzerland, 6 - 13 Sep 1987. C. Amsler et al. (eds.); Harwood, Chur. Nucl. Sci. Res. Conf. Ser. 14 (1988).

[44] *1^{st} Biennial Conference on Low-energy Antiproton Physics*, Stockholm, Sweden, 2-6 July 1990. P. Carlson, A. Kerek, and S. Szilagyi (eds.); Singapore World Scientific (1991).

[45] *2^{nd} Biennial Conference on Low-Energy Antiproton Physics: LEAP '92*, Courmayeur, Italy, 14 - 19 Sep 1992. C. Guaraldo, F. Iazzi and A. Zenoni (eds.); Nucl. Phys. A 558 (1993).

[46] *4^{th} Biennial Conference on Low-energy Antiproton Physics: LEAP '96*, Dinkelsbühl, Fed. Rep. Germany, 27 - 31 Aug. 1996. H. Koch, M. Kunze, and K. Peters (eds.); Nucl. Phys. A (Proc. Suppl.) 56 (1997).

[47] *5^{th} Biennial Conference on Low Energy Antiproton Physics: LEAP '98*, Villasimius, Italy, 7 - 12 Sep. 1998. C. Cicalò, A. De Falco, G. Puddu et al. (eds.); Nucl. Phys. A (Proc. Suppl.) 655 (1999).

[48] *6^{th} Biennial Conference on Low Energy Antiproton Physics: LEAP 2000,* Venice, Italy, 20 - 25 Aug. 2000. W. Dünnweber, M. Faessler et al.(eds.) Nucl. Phys. A **692** (2001).

[49] *Workshop On Nucleon-AntiNucleon Interactions*, Moscow, USSR, 27-31 May 1991. Yu.S. Kalashnikova, L.A. Kondratyuk and N.Ya. Smorodinskaya (eds.); Sov. J. Nucl. Phys. 55 (1992).

[50] *2^{nd} Biennial Workshop On Nucleon-AntiNucleon Interactions*, Moscow, USSR, 13-18 Sep. 1993. Yu. Kalashnikova and L. Kondratyuk (eds.); Phys. Atom. Nucl. 57 (1994).

[51] *3^{rd} International Conference On Nucleon - Antinucleon Physics*, Moscow, Russia, 11-16 Sep. 1995. Yu. Kalashnikova, L. Kondratyuk, A. Kudryavtsev and N. Smorodinskaya (eds.); Phys. Atom. Nucl. 59 (1996).

[52] *International School of Physics with Low-Energy Antiprotons: Fundamental Symmetries*, Erice, Italy, 26 Sep.-3 Oct. 1986. Ph. Bloch, P. Pavlopoulos, and R. Klapisch (eds.); New York Plenum (1987).

[53] *International School of Physics with Low-Energy Antiprotons: Spectroscopy of Light and Heavy Quarks*, Erice, Italy, 23 - 31 May 1987. U. Gastaldi, R. Klapisch and F.E. Close (eds.); New York Plenum (1989).

[54] *International School of Physics with Low-Energy Antiprotons. Antiproton-Nucleon and Antiproton-Nucleus Interactions*, Erice, Italy, 10-18 June 1988. F. Bradamante, J.-M. Richard, an R. Klapisch (eds.); New York Plenum (1990).

[55] *International School of Physics with Low-Energy Antiprotons, Medium-Energy Antiprotons and the Quark-Gluon Structure of Hadrons*, Erice, Italy, 25-31 Jan. 1990. R. Landua, J.-M. Richard, and R. Klapisch (eds.); New York Plenum (1991).

[56] *Workshop on the Elementary Structure of Matter*, Les Houches, France, 24 Mar.- 2 Apr. 1987. J.-M. Richard, E. Aslanides, and N. Boccara (eds.); Berlin Springer (1988).

[57] *Physics at SuperLEAR*, Zurich, Switzerland, 9-12 Oct. 1991. C. Amsler and D. Urner (eds.); Institute of Physics, Bristol IOP (1992).

[58] *Workshop on Intense Hadron Facilities and Antiproton Physics*, Turin, 23-25 Oct. 1989. T. Bressani, F. Iazzi, and G. Pauli (eds.); Bologna Italian Physical Society (1990).

[59] T. Walcher, "Experiments at the low-energy antiproton ring (LEAR)", Ann. Rev. Nucl. Part. Sci. 38 (1988) 67.

[60] C. Amsler and F. Myhrer, "Low-energy antiproton physics," Ann. Rev. Nucl. Part. Sci. **41** (1991) 219.

[61] C.B. Dover, T. Gutsche, M. Maruyama and A. Faessler, "The physics of nucleon-antinucleon annihilation," Prog. Part. Nucl. Phys. **29** (1992) 87.

[62] C. Amsler, "Proton antiproton annihilation and meson spectroscopy with the Crystal Barrel," Rev. Mod. Phys. **70** (1998) 1293.

[63] J. Eades and F.J. Hartmann, "Forty years of antiprotons," Rev. Mod. Phys. **71** (1999) 373.

[64] E. Klempt et al., "Nucleon–antinucleon interaction at low energy: annihilation dynamics", in preparation.

[65] A. Skrinsky et al., "Electron cooling and new possibilities in elementary particle physics", in *18^{th} International Conference on High-Energy Physics*, Tbilisi, USSR, 15-21 July 1976. N.N. Bogolyubov et al.(eds.); Dubna, Joint Institute for Nuclear Research (1977).

[66] G.I. Budker and A.N. Skrinsky, "The Electron Cooling And New Possibilities In Elementary Particle Physics," Usp. Fiz. Nauk **124** (1978) 561.

[67] R. Cappi, R. Giannini and W. Hardt, "Ultraslow extraction (status report)", in [41].

[68] L. Montanet, G.C. Rossi and G. Veneziano, "Baryonium physics", Phys. Rept. **63** (1980) 149.

[69] R.D. Tripp, "Review of $\bar{\mathrm{p}}\mathrm{p}$ formation experiments", in [35].

[70] Closed PSCC meeting, Cogne, 12-15 September 1990.

[71] W. Haeberli, "Progress toward an antiproton spin filter for LEAR", in [43].

[72] A. Penzo et al., "Perspectives for polarized antiproton at LEAR: the spin splitter", in [43].

[73] Y. Onel, A. Penzo and R. Rossmanith, "Polarised antiprotons in LEAR", CERN-PSCC-86-22, PSCC/M258; CERN (Geneva), 1986.

[74] N. Akchurin et al., "The spin splitter : study of a method for polarizing antiprotons at LEAR", CERN-PSCC-89-23, PSCC-S-120; CERN (Geneva), 1989.

[75] R. Birsa et al., "Polarization at small angles in elastic $\bar{\mathrm{p}}\mathrm{p}$ and $\bar{\mathrm{p}}\mathrm{C}$ scattering at 550 MeV/c ", Phys. Lett. **B155** (1985) 437.

[76] A. Martin et al., "Polarization at small angles in antiproton - Carbon elastic scattering at LEAR energies", Nucl. Phys. **A487** (1988) 563.

[77] A.S. Clough et al., "Evidence against the S meson", Phys. Lett. **B146** (1984) 299.

[78] D.V. Bugg et al., "$\bar{\mathrm{p}}\mathrm{p}$ total cross-sections below 420 MeV/c ", Phys. Lett. **B194** (1987) 563.

[79] L. Linssen et al., "Measurement of antiproton-proton small angle elastic scattering at low momentum", Nucl. Phys. **A469** (1987) 726.

[80] P. Schiavon et al., "Real to imaginary ratio of the $\bar{\mathrm{p}}\mathrm{p}$ forward elastic scattering amplitude at 550 MeV/c, 757 MeV/c and 1077 MeV/c ", Nucl. Phys. **A505** (1989) 595.

[81] A. Hasan et al., "Differential cross-sections and analyzing powers for $\bar{\mathrm{p}}\mathrm{p}\rightarrow\pi^-\pi^+$ and $\mathrm{K}^-\mathrm{K}^+$ from 360 MeV/c to 1550 MeV/c ", Nucl. Phys. **B378** (1992) 3.

[82] G. Bathas and W.M. Kloet, "Left-right asymmetry in $\bar{\mathrm{p}}\mathrm{p}\rightarrow\pi^-\pi^+$", Phys. Rev. C **47** (1993) 2207.

[83] M. Elchikh and J.-M. Richard, "Meson exchange and nonlocality effects in proton antiproton annihilation into two pseudoscalar mesons", Phys. Rev. **C48** (1993) 17.

[84] S. Takeuchi, F. Myhrer and K. Kubodera, "Maximum asymmetry phenomena in $\bar{\mathrm{p}}\mathrm{p}\rightarrow\pi^-\pi^+$ and $\bar{\mathrm{p}}\mathrm{p}\rightarrow\mathrm{K}^-\mathrm{K}^+$ reactions", Nucl. Phys. **A556** (1993) 601.

[85] R.A. Kunne et al., "Asymmetry in $\bar{\mathrm{p}}\mathrm{p}$ elastic scattering", Phys. Lett. **B206** (1988) 557.

[86] R.A. Kunne et al., "Measurement of $\mathrm{d}\sigma/\mathrm{d}\Omega$ and A_{0n} in $\bar{\mathrm{p}}\mathrm{p}$ elastic scattering between 497 MeV/c and 1550 MeV/c ", Nucl. Phys. **B323** (1989) 1.

[87] R.A. Kunne et al., "First measurement of D_{0n0n} in $\bar{\mathrm{p}}\mathrm{p}$ elastic scattering", Phys. Lett. **B261** (1991) 191.

[88] W. Brückner et al., "An apparatus for the measurement of antiproton-proton cross-sections at low momenta", Nucl. Instrum. Meth. **A269** (1988) 527.

[89] W. Brückner et al., "Search for a narrow resonance in antiproton-proton annihilation cross-sections in the beam momentum range between 400 MeV/c and 600 MeV/c ", Phys. Lett. **197B** (1987) 463.

[90] W. Brückner et al., "Measurements of the antiproton-proton annihilation cross-section in the beam momentum range between 180 MeV/c and 600 MeV/c ", Z. Phys. **A335** (1990) 217.

[91] W. Brückner et al., "Antiproton-proton elastic cross-sections in the momentum range between 180 MeV/c and 600 MeV/c ", Phys. Lett. **B166** (1986) 113.

[92] W. Brückner et al., "Measurements of the antiproton-proton elastic cross-section in the beam momentum range between 180 MeV/c and 600 MeV/c ", Z. Phys. **A339** (1991) 367.

[93] W. Brückner et al., "Real-to-imaginary ratio of the $\bar{\mathrm{p}}\mathrm{p}$ forward elastic scattering amplitude in the momentum range between 180 MeV/c and 590 MeV/c ", Phys. Lett. **B158** (1985) 180.

[94] W. Brückner et al., "Measurement of the $\bar{\mathrm{p}}\mathrm{p} \to \bar{\mathrm{n}}\mathrm{n}$ cross-section at low $\bar{\mathrm{p}}$ momenta", Phys. Lett. **B169** (1986) 302.

[95] A. Adamo et al., "First physics results from OBELIX", in [49].

[96] A. Bertin et al., "$\bar{\mathrm{p}}\mathrm{p}$ annihilation cross-section at very low-energy", Phys. Lett. **B369** (1996) 77.

[97] A. Zenoni et al., "New measurements of $\bar{\mathrm{p}}\mathrm{p}$ annihilation cross section at very low energy", Phys. Lett. **B461** (1999) 405.

[98] M. Agnello et al., "The antineutron beam at OBELIX", Nucl. Instrum. Meth. **A399** (1997) 11.

[99] S. Marcello, "Five years of antineutron physics at LEAR", in [47].

[100] F. Iazzi et al., "Antineutron proton total cross section from 50 MeV/c to 400 MeV/c", Phys. Lett. **B475** (2000) 378.

[101] T. Armstrong et al., "Measurement of antineutron proton total and annihilation cross-sections from 100 MeV/c to 500 MeV/c", Phys. Rev. **D36** (1987) 659.

[102] L. Cugusi et al., "A low-momentum tagged antineutron beam", Nucl. Instrum. Meth. **A270** (1988) 354.

[103] S. Tessaro, "Interazione antineutrone-protone: misura della sezione d'utro di annichilazione e totale tra 60 e 400 MeV/c", PhD Thesis, VI Ciclo, Trieste University.

[104] A. Bertin et al., "$\bar{\mathrm{n}}\mathrm{p}$ annihilation in flight in two mesons in the momentum range between 50 and 400 MeV/c with OBELIX", in [46].

[105] A. Feliciello, "Total and annihilation $\bar{\mathrm{n}}\mathrm{p}$ cross section from 50 to 400 MeV/c", in [47].

[106] R. Bertini et al., "Full angular distribution of the analyzing power in $\bar{\mathrm{p}}\mathrm{p}$ elastic scattering at 697 MeV/c", Phys. Lett. **B228** (1989) 531.

[107] F. Perrot-Kunne et al., "Measurement of the analyzing power in $\bar{\mathrm{p}}\mathrm{p}$ elastic scattering at 439 MeV/c and 544 MeV/c", Phys. Lett. **B261** (1991) 188.

[108] H. Catz, thesis, Note CEA-N 2251 (1981).

[109] A. Ahmidouch et al., "Plastic detectors for medium energy neutrons", Nucl. Instrum. Meth. **A326** (1993) 538.

[110] R. Birsa et al., "The limited streamer tubes for experiment PS199 at LEAR", Nucl. Instrum. Meth. **A300** (1991) 43.

[111] R. Birsa et al., "Measurement of the analyzing power and the differential cross-section of the $\bar{\mathrm{p}}\mathrm{p}$ charge exchange reaction at LEAR", Phys. Lett. **B246** (1990) 267.

[112] R. Birsa et al., "Measurement of the analyzing power of the charge exchange $\bar{\mathrm{p}}\mathrm{p} \to \bar{\mathrm{n}}\mathrm{n}$ reaction in the momentum range 546 MeV/c - 875 MeV/c at LEAR", Phys. Lett. **B273** (1991) 533.

[113] R. Birsa et al., "Measurement of the analyzing power of the charge exchange $\bar{\mathrm{p}}\mathrm{p} \to \bar{\mathrm{n}}\mathrm{n}$ reaction in the momentum range 546 MeV/c - 1287 MeV/c at LEAR", Nucl. Phys. **B403** (1993) 25.

[114] M. Lamanna et al., "A high statistics measurement of the $\bar{\mathrm{p}}\mathrm{p} \to \bar{\mathrm{n}}\mathrm{n}$ charge exchange reaction at 875 MeV/c ", Nucl. Phys. **B434** (1995) 479.

[115] A. Ahmidouch et al., "Charge exchange $\bar{\mathrm{p}}\mathrm{p} \to \bar{\mathrm{n}}\mathrm{n}$ differential cross-sections between 546 MeV/c and 1287 MeV/c ", Phys. Lett. **B364** (1995) 116.

[116] A. Martin et al., "An antineutron detectors calibration method for $\bar{\mathrm{p}}\mathrm{p} \to \bar{\mathrm{n}}\mathrm{n}$ charge exchange differential cross-section measurement", Nucl. Instrum. Meth. **A346** (1994) 237.

[117] R. Birsa et al., "First measurement of the depolarization parameter D_{0n0n} of the $\bar{\mathrm{p}}\mathrm{p} \to \bar{\mathrm{n}}\mathrm{n}$ charge exchange reaction", Phys. Lett. **B302** (1993) 517.

[118] A. Ahmidouch et al., "First measurement of the $\bar{\mathrm{p}}\mathrm{p} \to \bar{\mathrm{n}}\mathrm{n}$ depolarization parameter D_{0n0n} at 546 MeV/c and 875 MeV/c ", Nucl. Phys. **B444** (1995) 27.

[119] A. Ahmidouch et al., "First measurement of the spin transfer parameter K_{n00n} in the $\bar{\mathrm{p}}\mathrm{p} \to \bar{\mathrm{n}}\mathrm{n}$ reaction at 875 MeV/c ", Phys. Lett. **B380** (1996) 235.

[120] R. Birsa et al., "High precision measurement of the $\bar{\mathrm{p}}\mathrm{p} \to \bar{\mathrm{n}}\mathrm{n}$ charge exchange differential cross-section", Phys. Lett. **B339** (1994) 325, Phys. Lett. **B405** (1997) 389 (erratum).

[121] A. Bressan et al., "A new measurement of the $\bar{\mathrm{p}}\mathrm{p} \to \bar{\mathrm{n}}\mathrm{n}$ charge-exchange differential cross-section at LEAR", Nucl. Phys. **A625** (1997) 10.

[122] B. Bassalleck et al., "A measurement of depolarization and spin transfer in $\bar{\mathrm{p}}\mathrm{p} \to \overline{\Lambda}\Lambda$," proposal CERN/SPSLC 95-13 (1995).

[123] P.D. Barnes et al., "Study of the reaction $\bar{\mathrm{p}}\mathrm{p} \to \overline{\Lambda}\Lambda$ near threshold," Phys. Lett. B **189** (1987) 249.

[124] P.D. Barnes et al., "Threshold measurement of the reaction $\bar{\mathrm{p}}\mathrm{p} \to \overline{\Lambda}\Lambda$ at LEAR," Phys. Lett. B **229** (1989) 432.

[125] P.D. Barnes et al., "'Measurement of the reaction $\bar{\mathrm{p}}\mathrm{p} \to \overline{\Sigma}^0\Lambda + \mathrm{c.c.}$ at 1.695-GeV$/c$," Phys. Lett. B **246** (1990) 273.

[126] P.D. Barnes et al., "Study of the reaction $\bar{\mathrm{p}}\mathrm{p} \to \overline{\Lambda}\Lambda$ at 1.546 GeV$/c$ and 1.695 GeV$/c$," Nucl. Phys. A **526** (1991) 575.

[127] P.D. Barnes et al., "Observables in high-statistics measurements of the reaction $\bar{\mathrm{p}}\mathrm{p} \to \overline{\Lambda}\Lambda$," Phys. Rev. C **54** (1996) 1877.

[128] P.D. Barnes et al., "Measurement of $\bar{\mathrm{p}}\mathrm{p} \to \overline{\Lambda}\Lambda$ and $\bar{\mathrm{p}}\mathrm{p} \to \overline{\Sigma}^0\Lambda + \mathrm{c.c.}$ reactions at 1.726 GeV$/c$ and 1.771 GeV$/c$," Phys. Rev. C **54** (1996) 2831.

[129] P.D. Barnes et al., "Measurement of the reactions $\bar{\mathrm{p}}\mathrm{p} \to \overline{\Sigma}^-\Sigma^+$ and $\bar{\mathrm{p}}\mathrm{p} \to \overline{\Sigma}^+\Sigma^-$ close to threshold," Phys. Lett. B **402** (1997) 227.

[130] P.D. Barnes et al., "CP Invariance in the Reaction $\bar{\mathrm{p}}\mathrm{p} \to \overline{\Lambda}\Lambda \to \bar{\mathrm{p}}\pi^+\mathrm{p}\pi^-$ at 1.546 GeV$/c$," Phys. Lett. B **199** (1987) 147.

[131] B. Quinn et al., "Status of PS185 search for $\xi(2230)$," in [43].

[132] T.A. Armstrong et al., "Precision measurements of antiproton proton forward elastic scattering parameters in the 3.7 GeV/c to 6.2 GeV/c region", Phys. Lett. **B385** (1996) 479.

[133] S. Trokenheim, M. Sarmiento, K.K. Seth and L. Bartoszek, "A $\mathrm{p}\bar{\mathrm{p}}$ luminosity monitor for Fermilab experiment E760," Nucl. Instrum. Meth. **A355** (1995) 308.

[134] E.G. Auld et al., "First observation of X-rays from antiprotonic hydrogen," Phys. Lett. **77B** (1978) 454.

[135] M. Izycki et al., "Results on the measurement of K-series X-rays from antiprotonic hydrogen atoms," Z. Phys. A297 (1980) 1.

[136] J.R. Lindenmuth et al., "Antiprotonic atoms in gaseous H_2 and He and in liquid H_2," Phys. Rev. **C30** (1984) 1740.

[137] A. Bamberger et al., "First observation of antiprotonic atoms," Phys. Lett. **C33** (1970) 233.

[138] R. Armenteros and B. French, "$\overline{\mathrm{N}}\mathrm{N}$ interactions," in *High Energy Physics*. E.H.S. Burhop (ed.); Academic Press Inc., New York, Vol. **4** (1969) 383.

[139] T.B. Day, G.A. Snow and J. Sucher, "High-orbital S-state capture of π^- mesons by protons," Phys. Rev. **118** (1960) 864.

[140] M. Leon and H.A. Bethe, "Negative meson absorption in liquid hydrogen," Phys. Rev. **127** (1962) 636.

[141] S. Devons et al., "Observation of $\bar{\mathrm{p}}\mathrm{p} \to 2\pi^0$ at rest: evidence concerning S-state annihilation," Phys. Rev. Lett. **27** (1971) 1614.

[142] C.R. Sun, S. Dhar, M. Dickinson and B. Krinsky, "Study of $\bar{\mathrm{p}}\mathrm{D} \to \pi^+\pi^-$(n) with stopped antiprotons," Phys. Rev. **D14** (1976) 1188.

[143] G. Carboni et al., "Measurement of the $2S_{1/2}$ - $2P_{3/2}$ level splitting in muonic helium: a test of quantum electrodynamics predictions on electronic vacuum polarization," Nuovo Cim. **34A** (1976) 493.

[144] B. Budick, J.R. Toraskav and I. Yaghoobia, "Study of $\bar{\mathrm{p}}\mathrm{D} \to \pi^+\pi^-$(n) with stopped antiprotons," Phys. Lett. **B34** (1971) 539.

[145] J.M. Bailey et al."Muonic X-rays from liquid hydrogen," Phys. Lett. **B33** (1970) 369.

[146] E.G. Auld et al., "$\bar{\mathrm{p}}\mathrm{p}$ and $\bar{\mathrm{p}}\mathrm{D}$ interactions at threshold in gaseous H_2 and D_2 targets," in [36].

[147] W.B. Kaufmann and H. Pilkuhn, "Black sphere model for the line widths of P state protonium," Phys. Rev. **C17** (1978) 215.

[148] W. Dahme et al., "$(q\bar{q})$ spectroscopy and search for glueballs, baryonia and other boson resonances in $\bar{\mathrm{p}}\mathrm{p}$ annihilations at rest with the Asterix experiment at Lear," in [41].

[149] U. Gastaldi et al., "Protonium spectroscopy and identification of P wave and S wave initial states of P $\bar{\mathrm{p}}\mathrm{p}$ annihilations at rest with the Asterix experiment at Lear," in [41].

[150] S. Ahmad et al., "The Asterix Spectrometer at LEAR," Nucl. Instrum. Meth. **A286** (1990) 76.

[151] S. Ahmad et al., "First observation of K X-rays from $\bar{\mathrm{p}}\mathrm{p}$ atoms," Phys. Lett. **B157** (1985) 333.

[152] U. Schäfer et al., "X-rays from $\bar{\mathrm{p}}\mathrm{p}$ annihilation into charged final states," Nucl. Phys. **A495** (1989) 451.

[153] M. Ziegler et al., "Measurement of the strong interaction shift and broadening of the ground state of the $\bar{\mathrm{p}}\mathrm{p}$ atom," Phys. Lett. **206B** (1988) 151.

[154] G. Reifenröther et al., "Cascade time of antiprotons in gaseous hydrogen," Phys. Lett. **B214** (1988) 325.

[155] S. Ahmad et al., "Search for monochromatic pion emission in $\bar{\mathrm{p}}\mathrm{p}$ annihilation from atomic P states," Phys. Lett. **B152** (1985) 135.

[156] M. Doser et al., "Antiproton-proton annihilation into $\pi^+\pi^-$ and $\mathrm{K}^+\mathrm{K}^-$ from atomic P states," Nucl. Phys. **A486** (1988) 493.

[157] M. Doser et al., "Antiproton-proton annihilation into $\mathrm{K}_0\ \bar{\mathrm{K}}_0$ in hydrogen gas," Phys. Lett. **B215** (1988) 792.

[158] B. May et al., "Observation of an isoscalar meson AX(1565) in annihilation of the $\bar{\mathrm{p}}\mathrm{p}$ atom from P states," Phys. Lett. **B225** (1989) 450.

[159] J. Riedlberger et al., "Antiproton annihilation at rest in Nitrogen and Deuterium gas," Phys. Rev. **C 40** (1989) 2717.

[160] K.D. Duch et al., "Observation and analysis of E mesons in $\bar{\mathrm{p}}\mathrm{p}$ annihilation at rest in H_2 gas," Z. Phys. **C45** (1989) 223.

[161] E. Klempt et al., "Evidence for a multi-quark state in $\bar{\mathrm{p}}\mathrm{p}$ annihilation at rest," Nucl. Phys. **A508** (1990) 317.

[162] B. May et al., "Antiproton-proton annihilation at rest in H_2 gas into $\pi^+\pi^-\pi^0$. 1: Annihilation from S states," Z. Phys. **C46** (1990) 191.

[163] B. May et al., "Antiproton-proton annihilation at rest in H_2 gas into $\pi^+\pi^-\pi^0$. 2: Annihilation from P states," Z. Phys. **C46** (1990) 203.

[164] P. Weidenauer et al., "Antiproton-proton annihilation at rest into $\pi^+\pi^-\eta'$ and $\pi^+\pi^-\eta$ from atomic S and P states," Z. Phys. **C47** (1990) 353.

[165] J. Reifenroether et al., "Φ production in $\bar{\mathrm{p}}\mathrm{p}$ annihilation at rest," Phys. Lett. **B267** (1991) 299.

[166] P. Weidenauer et al., "$\overline{\mathrm{N}}\mathrm{N}$ annihilation at rest into five pions," Z. Phys. **C59** (1993) 387.

[167] W.J. Okx, C.W. Van Eijk, R.W. Hollander and A. Zoutendijk, "A gas scintillation proportional detector for exotic atom x-rays with charged particle rejection," Nucl. Instrum. Meth. **A273** (1988) 544.

[168] T.P. Gorringe et al., "X-rays from antiprotonic hydrogen and deuterium," Phys. Lett. **162B** (1985) 71.

[169] C.A. Baker et al., "Measurement of X-rays from antiprotonic hydrogen and deuterium," Nucl. Phys. **A483** (1988) 631.

[170] C.W. Van Eijk et al., "K series X-rays from antiprotonic hydrogen and deuterium," Nucl. Phys. **A486** (1988) 604.

[171] P. Hauser et al., "New developments in crystal spectroscopy at PSI," PiN Newslett. (1997) NO.13201.

[172] S. Lenz et al., "A new determination of the mass of the charged pion," Phys. Lett. **416B** (1998) 50.

[173] R. Bacher et al., "Measurement of Balmer and Lyman X-rays in antiprotonic hydrogen isotopes at pressures below 300-hpa," Z. Phys. **A334** (1989) 93.

[174] K. Heitlinger et al., "Precision measurement of antiprotonic hydrogen and deuterium X-rays," Z. Phys. **A342** (1992) 359.

[175] D. F. Anagnostopoulos et al., "New results on strong-interaction effects in antiprotonic hydrogen, Nucl. Phys. **A655** (1999) 305.

[176] M. Augsburger et al., "Measurement of the strong interaction parameters in antiprotonic hydrogen and probable evidence for an interference with inner bremsstrahlung," Nucl. Phys. **A658** (1999) 149.

[177] M. Augsburger et al., "Measurement of the strong interaction parameters in antiprotonic deuterium," Phys. Lett. **B461** (1999) 417.

[178] D. Gotta et al., "Balmer alpha transitions in antiprotonic hydrogen and deuterium," Nucl. Phys. **A660** (1999) 283.

[179] D.E. Groom et al.[Particle Data Group Collaboration], "Review of particle physics," Eur. Phys. J. C **15** (2000) 1.

[180] A.D. Martin and T. Spearman, *Elementary particle theory* (North-Holland, Amsterdam, 1970).

[181] J. Bystricky, F. Lehar and P. Winternitz, "Formalism of nucleon-nucleon elastic scattering experiments," Journal de Physique **39** (1978) 1.

[182] P. LaFrance, F. Lehar, B. Loiseau and P. Winternitz, "Antinucleon - nucleon scattering formalism and possible tests of CPT invariance," Helv. Phys. Acta **65** (1992) 611.

[183] M. Elchikh and J.-M. Richard, "Constraints on spin observables in $\bar{\mathrm{p}}\mathrm{p} \to \overline{\Lambda}\Lambda$," Phys. Rev. C **61** (2000) 035205.

[184] K. Paschke and B. Quinn, "Spin observables in $\bar{\mathrm{p}}\mathrm{p} \to \overline{\Lambda}\Lambda$ with a transverse initial state polarization," Phys. Lett. B **495** (2000) 49.

[185] P. LaFrance and P. Winternitz, "Scattering formalism for non-identical spinor particles", J. Phys. (France) **41** (1980) 1391.

[186] W.M. Kloet and F. Tabakin, "Constraints on vector meson photoproduction spin observables," Phys. Rev. C **61** (2000) 015501.

[187] R.G. Newton, *Scattering Theory of Waves and Particles* (New York, USA, Springer, 1982).

[188] J. Ball et al., "Direct reconstruction of isosinglet amplitudes for nucleon nucleon elastic scattering," Eur. Phys. J. C **5** (1998) 57.

[189] G. Ihle, H.J. Pirner and J.-M. Richard, "S-wave nucleon-antinucleon interaction in the constituent quark model," Nucl. Phys. A **485** (1988) 481.

[190] G.E. Brown and A.D. Jackson, *The Nucleon–Nucleon Interaction* (North-Holland, Amsterdam, 1976).

[191] R. Vinh-Mau, in *Mesons in Nuclei*. M. Rho and D.H. Wilkinson (eds.); North-Holland, Amsterdam (1979).

[192] R. Machleidt, K. Holinde and C. Elster, "The Bonn meson exchange model for the nucleon-nucleon interaction," Phys. Rept. **149** (1987) 1.

[193] R. Wilson, *The Nucleon–Nucleon Interaction, Experimental and Phenomenological Aspects* (Interscience Publishers, N.Y., 1963).

[194] D. Amati, E. Leader and B. Vitale, "Theory of Low-Energy Nucleon–Nucleon Scattering", Nuovo Cimento **17** (1960) 68; **18** (1960) 409; **18** (1960) 458; Phys. Rev. **130** (1960) 750.

[195] S. Furuichi, "Dispersion theoretical treatment fon nucleon-nucleon scattering at large impact parameter", *Prog. Theo. Phys. (Kyoto)* **27** (1962) 51.

[196] R. Machleidt, "The high-precision, charge-dependent Bonn nucleon-nucleon potential (CD-Bonn)," Phys. Rev. C **63** (2001) 024001.

[197] F. Myhrer and J. Wroldsen, "The nucleon-nucleon force and the quark degrees of freedom," Rev. Mod. Phys. **60** (1988) 629.

[198] M. Oka, K. Shimizu and K. Yazaki, "Quark cluster model of baryon baryon interaction," Prog. Theor. Phys. Suppl. **137** (2000) 1.

[199] S. Weinberg, "Effective chiral Lagrangians for nucleon-pion interactions and nuclear forces," Nucl. Phys. B **363** (1991) 3.

[200] C. Ordonez and U. van Kolck, "Chiral Lagrangians and nuclear forces," Phys. Lett. B **291** (1992) 459.

[201] C. Ordonez, L. Ray and U. van Kolck, "Nucleon-nucleon potential from an effective chiral Lagrangian," Phys. Rev. Lett. **72** (1994) 1982.

[202] M. Walzl, U.G. Meissner and E. Epelbaum, "Charge-dependent nucleon nucleon potential from chiral effective field theory", Nucl. Phys. A693 (2001) 663.

[203] K.A. Scaldeferri, D.R. Phillips, C.W. Kao and T.D. Cohen, "Short-range interactions in an effective field theory approach for nucleon nucleon scattering," Phys. Rev. C **56** (1997) 679.

[204] T.D. Cohen, "Regularization, renormalization, and range: The nucleon nucleon interaction from effective field theory," Phys. Rev. C **55** (1997) 67.

[205] U. van Kolck, "Chiral Lagrangians and few-nucleon forces," in *14^{th} International IUPAP Conference On Few Body Problems In Physics*, Williamsburg, Virginia, 26-31 May 1994. F. Gross (ed.); Amer. Inst. Phys., N.Y. (1995).

[206] W. Pauli and F. Villars, "On the invariant regularization in relativistic quantum theory," Rev. Mod. Phys. **21** (1949) 434.

[207] E. Fermi and C.N. Yang, "Are mesons elementary particles?," Phys. Rev. **76** (1949) 1739.

[208] J. Ball and G. Chew, "$\overline{\mathrm{N}}\mathrm{N}$ interaction at interediate energies", Phys. Rev. **109** (1958) 1385.

[209] M. Gourdin, B. Jancovici and L. Verlet, "On the nucleon-antinucleon interactions", Nuovo Cim. **8** (1958) 485.

[210] R.A. Bryan and R.J. Phillips, "Nucleon-antinucleon potential from single meson exchanges," Nucl. Phys. B **5** (1968) 201; Nucl. Phys. B **7** (1968) 481 (erratum).

[211] C.B. Dover and J.-M. Richard, "Elastic, charge exchange, and inelastic $\bar{\mathrm{p}}\mathrm{p}$ cross-sections in the optical model," Phys. Rev. C **21** (1980) 1466.

[212] M. Kohno and W. Weise, "Proton-antiproton scattering and annihilation into two mesons," Nucl. Phys. A **454** (1986) 429.

[213] C.B. Dover and J.-M. Richard, "Strong tensor forces and the possibility of high-spin states in the nucleon-antinucleon system," Phys. Rev. D **17** (1978) 1770.

[214] C.B. Dover and J.-M. Richard, "Spin observables in low-energy nucleon-antinucleon scattering," Phys. Rev. C **25** (1982) 1952.

[215] M. Alberg, J. Ellis and D. Kharzeev, "The proton spin puzzle and depolarization in $\bar{\mathrm{p}}\mathrm{p} \to \overline{\Lambda}\Lambda$," Phys. Lett. B **356** (1995) 113.

[216] H.J. Lipkin, "The Alexander ... Zweig rules and what is wrong with pseudoscalar mesons", in *Deeper pathways in high-energy physics*, Orbis Scientiae, Coral Gables, Fla., Jan. 17-21, 1977. B. Kursunoglo, A. Perlmutter and L.F. Scott (eds.); New York Plenum (1977).

[217] A. Martin, "Range of the Nucleon-Antinucleon Potential", Phys. Rev. **124** (1961) 614.

[218] H. Feshbach, "A unified theory of nuclear reactions. II," Annals Phys. **19** (1962) 287.

[219] T.A. Shibata, "Antiproton-proton potential from cross-section data at small momenta," Phys. Lett. B **189** (1987) 232.

[220] J.-M. Richard and M.E. Sainio, "Nuclear effects in protonium," Phys. Lett. B **110** (1982) 349.

[221] M. Maruyama and T. Ueda, "$\overline{\mathrm{N}}\mathrm{N}$ bound- and scattering-states due to the quark rearrangement, annihilation and the one-boson exchange," Prog. Theor. Phys. **74** (1985) 526.

[222] P. Bydzovsky, R. Mach and F. Nichitiu, "Isospin effects in antinucleon-nucleon scattering and annihilation," Phys. Rev. C **43** (1991) 1610.

[223] H. Feshbach and E. Lomon, "The boundary condition model of strong interactions", *Ann. Phys. (N.Y.)* **29** (1964) 19.

[224] R.L. Jaffe and F.E. Low, "The connection between quark model eigenstates and low-energy scattering," Phys. Rev. D **19** (1979) 2105.

[225] A.E. Dorokhov, N.I. Kochelev and Y.A. Zubov, "Four quark states and nucleon-antinucleon annihilation within the quark model with QCD-vacuum induced interaction," Z. Phys. C **65** (1995) 667.

[226] W. Roberts, B. Silvestre-Brac and C. Gignoux, "Can four-quark states be easily detected in baryon antibaryon scattering?," Phys. Rev. D **41** (1990) 2258.

[227] W. Roberts, "Four-quark states in hyperon pair production," Z. Phys. C **49** (1991) 633.

[228] O.D. Dalkarov and F. Myhrer, "A simple model for proton-antiproton scattering at low energies," Nuovo Cim. A **40** (1977) 152.

[229] G.Q. Liu and F. Tabakin, "Coupled-channel study of antiproton-proton reactions," Phys. Rev. C **41** (1990) 665.

[230] W. Schweiger, J. Haidenbauer and W. Plessas, "Separable model for the antinucleon-nucleon elastic and annihilation interaction," Phys. Rev. C **32** (1985) 1261.

[231] W. Schweiger, W. Plessas and J. Haidenbauer, "Antinucleon-nucleon interaction in a coupled channel approach with separable potentials," in *Internationale Universitatswochen fur Kernphysik: nucleon-nucleon and nucleon-antinucleon interactions from low to high energies*, Schladming, Austria, 20 Feb.- 1 Mar. 1985. H. Mitter and W. Plessas (eds.); Acta Phys. Austr. (Suppl.) 27 (1985).

[232] V. Mull and K. Holinde, "Combined description of $\overline{\mathrm{N}}\mathrm{N}$ scattering and annihilation with a hadronic model," Phys. Rev. C **51** (1995) 2360.

[233] A.M. Green, J.A. Niskanen and J.M. Richard, "$\overline{\mathrm{N}}\mathrm{N}$ scattering in the rearrangement model", Phys. Lett. B121 (1983) 101.

[234] A.M. Green, J.A. Niskanen, "From phenomenological to microscopic descriptions of $\overline{\mathrm{N}}\mathrm{N}$ annihilation," Inter. Rev. Nucl. Phys., **Vol.2** . T.T.S Kuo (ed.); World Scientific Co., Singapore (1984).

[235] J. Haidenbauer, T. Hippchen and R. Tegen, "The Bonn nucleon-nucleon meson exchange model with a relativistic quark-gluon annihilation potential," Phys. Rev. C **44** (1991) 1812.

[236] T. Hippchen, J. Haidenbauer, K. Holinde and V. Mull, "Meson-baryon dynamics in the nucleon-anti-nucleon system. 1. The nucleon-antinucleon interaction," Phys. Rev. C **44** (1991) 1323.

[237] J. Cote, M. Lacombe, B. Loiseau, B. Moussallam and R. Vinh Mau, "On The nucleon-antinucleon optical potential," Phys. Rev. Lett. **48** (1982) 1319.

[238] V. Mull et al., "The $\overline{\mathrm{N}}\mathrm{N}$ scattering data and the nature of the n n repulsion", Phys. Lett. B288 (1992) 239.

[239] J.-M. Richard, "Low-energy nucleon-antinucleon interaction", in [39].

[240] I.S. Shapiro, "Baryon-antibaryon nuclear interactions", in [54].

[241] S.J. Brodsky, "Anti-proton annihilation in quantum chromodynamics", in [54].I.

[242] I.S. Shapiro, "Baryon-antibaryon interactions in potential approach," in [39].

[243] C. Evangelista et al., "Study of the reaction $\bar{\mathrm{p}}\mathrm{p} \to \phi\phi$ from 1.1 GeV/c to 2.0 GeV/c,", Phys. Rev. D57 (1998) 5370.

[244] S.J. Brodsky, "Testing quantum chromodynamics in antiproton reactions", in [43].

[245] M. Jacob and G.F. Chew, *Strong Interaction Physics* (Benjamin, N.Y., 1964);
G.F. Chew, *The Analytic S–Matrix: a Basis for Nuclear Democracy* (Benjamin, N.Y., 1966).

[246] J.S. Ball, A. Scotti and D.Y. Wong, "One-boson-exchange model of NN and $\overline{\mathrm{N}}\mathrm{N}$ interaction," Phys. Rev. **142** (1966) 1000.

[247] C.B. Dover and J.-M. Richard, "The interaction of nucleons with antinucleons. 2. Narrow mesons near threshold: experiment and theory," Annals Phys. **121** (1979) 70.

[248] C.B. Dover, T. Gutsche and A. Faessler, "The case for quasinuclear $\overline{\mathrm{N}}\mathrm{N}$ bound states," Phys. Rev. C **43** (1991) 379.

[249] F. Myhrer and A.W. Thomas, "The influence of absorption on possible nucleon-antinucleon resonances and bound states," Phys. Lett. B **64** (1976) 59.

[250] A.M. Green, M.E. Sainio and J.-M. Richard, "Antinucleon-nucleon pionic capture," J. Phys. G**G6** (1980) 437.

[251] A.M. Green, M.E. Sainio and S. Wycech, "The imaginary part of the $\overline{\mathrm{N}}\mathrm{N}$ potential," J. Phys. G**G6** (1980) L17.

[252] M. Lacombe, B. Loiseau, B. Moussallam and R. Vinh Mau, "Nucleon antinucleon resonance spectrum in a potential model," Phys. Rev. C **29** (1984) 1800.

[253] R.L. Jaffe, "Multiquark hadrons. 1. The phenomenology of $\mathrm{q}^2\bar{\mathrm{q}}^2$ mesons," Phys. Rev. **D15** (1977) 267.

[254] R.L. Jaffe, "$\mathrm{q}^2\bar{\mathrm{q}}^2$ resonances in the baryon–antibaryon system," Phys. Rev. **D17** (1978) 1444.

[255] H.M. Chan and H. Høgaasen, "A Model for Baryonium," Nucl. Phys. **B136** (1978) 401.

[256] H.M. Chan, "Baryonium spectroscopy as a test for color dynamics," in [34].

[257] A. Martin, "Regge trajectories in the quark model," Z. Phys. **C32** (1986) 359.

[258] D. Gromes, "Sextet string tension, mock baryonia and the u (3.1) resonance", Z. Phys. C41 (1988) 427.

[259] S. Barmo, H. Pilkuhn, and H.G. Schlaile, "Energy levels of light antiprotonic atoms with l¿0," Z. Phys. **A301** (1981) 283.

[260] S. Boucard and P. Indelicato, private communication, quoted in [178].

[261] S. Wycech, A.M. Green and J.A. Niskanen, "On the energy levels in antiprotonic deuterium," Phys. Lett. **B152** (1985) 308.

[262] C. Quigg and J. L. Rosner, "Quantum Mechanics With Applications To Quarkonium," Phys. Rept. **56** (1979) 167.

[263] T.L. Trueman, "Energy level shifts in atomic states of strongly interacting particles," *Nucl. Phys.* **26** (1961) 57.

[264] V. Mandelzweig, "Radius perturbation theory and its application to pionic atoms," *Nucl. Phys.* **A292** (1977) 333.

[265] J. Carbonell, J.-M. Richard and S. Wycech, "On the relation between protonium level shifts and nucleon-antinucleon scattering amplitudes," Z. Physik A **343** (1992) 325.

[266] *Handbook of Mathematical Functions with Formulas, Graphs and Mathematical Tables*. M. Abramovitz and I.A. Stegun (eds.); Dover, N.Y. (1964).

[267] C.J. Batty, E. Friedman and A. Gal, "Unified optical-model approach to low-energy antiproton annihilation on nuclei and to antiprotonic atoms", Nucl. Phys. A689 (2001) 721, nucl-th/0010006.

[268] J. Carbonell and K.V. Protasov, "Annihilation of slow anti-protons in flight and in traps," Z. Phys. A **355** (1996) 87.

[269] Ya.B. Zel'dovich, "Energy levels in a distorted Coulomb field", Sov. J. Solid State, **1** (1960) 1497.

[270] C.B. Dover, J.-M. Richard and J. Carbonell, "Isospin mixing in protonium and annihilation dynamics," Phys. Rev. C **44** (1991) 1281.

[271] A. Gal, E. Friedman and C.J. Batty, "On the interplay between coulomb and nuclear states in exotic atoms", Nucl. Phys. A606 (1996) 283.

[272] Askok Raina and Jean-Marc Richard, work in preparation.

[273] H.J. Pirner, B. Kerbikov and J. Mahalanabis, "Updating the effective range expansion of low-energy $\overline{\mathrm{N}}\mathrm{N}$ scattering," Z. Phys. **A338** (1991) 111.

[274] G.S. Mutchler et al., "Measurement of the imaginary part of the I = 1 $\overline{\mathrm{N}}\mathrm{N}$ S-wave scattering length," Phys. Rev. **D38** (1988) 742.

[275] J. Mahalanabis, H.J. Pirner and T.A. Shibata, "Coupled channel effective range expansion of low-energy $\overline{\mathrm{N}}\mathrm{N}$ scattering," Nucl. Phys. **A485** (1988) 546.

[276] I.L. Grach and B.O. Kerbikov, "S-wave nucleon-antinucleon interaction in a model with confined channel," Sov. J. Nucl. Phys. **52** (1990) 523.

[277] M. Pignone, M. Lacombe, B. Loiseau and R. Vinh Mau, "Paris $\overline{\mathrm{N}}\mathrm{N}$ potential and recent proton antiproton low-energy data," Phys. Rev. **C50** (1994) 2710.

[278] T. Gutsche, R. Vinh Mau, M. Strohmeier-Presicek and A. Faessler, "Radiative proton antiproton annihilation and isospin mixing in protonium," Phys. Rev. C **59** (1999) 630.

[279] R. Timmermans, T.A. Rijken and J.J. de Swart, "Antiproton - proton partial-wave analysis below 925 MeV/c ", Phys. Rev. **C50** (1994) 48.

[280] V. Flaminio et al.(High-Energy Reactions Analysis Group), *Compilation of cross-sections. III. Proton and antiproton induced reactions*, CERN-HERA 84-01, CERN, Geneva (1984).

[281] R.P. Hamilton, T.P. Pun, R.D. Tripp, D.M. Lazarus and H. Nicholson, "Search for the S meson", Phys. Rev. Lett. **44** (1980) 1182.

[282] S.N. Ganguli et al., "Properties of the $\bar{\mathrm{p}}\mathrm{p}$ annihilations into strange particles at 702 MeV/c and 757 MeV/c ", Nucl. Phys. **B183** (1981) 295.

[283] K. Nakamura et al., "Search for narrow structures in $\bar{\mathrm{p}}\mathrm{p}$ total cross-section from 395 MeV/c to 740 MeV/c ", Phys. Rev. **D29** (1984) 349.

[284] V. Chaloupka et al., "Measurement of the total and partial $\bar{\mathrm{p}}\mathrm{p}$ cross-section between 1901 MeV and 1950 MeV", Phys. Lett. **B61** (1976) 487.

[285] R. Bizzarri et al., "Antiproton - deuteron low-energy cross-section", Nuovo Cim. **A22** (1974) 225.

[286] M. Coupland et al., "Antiproton - proton total elastic cross-sections in the T and U regions (0.69 GeV/c to 2.43 GeV/c)", Phys. Lett. **B71** (1977) 460.

[287] M. Alston-Garnjost et al., "Measurement of the $\bar{\mathrm{p}}\mathrm{p}$ charge exchange cross-section below 1 GeV/c ", Phys. Rev. Lett. **35** (1975) 1685.

[288] T. Kalogeropoulos and G.S. Tzanakos, "Total and partial $\bar{\mathrm{p}}\mathrm{d}$ cross-section from 0.26 to 0.47 GeV/c ", Phys. Rev. **D22** (1980) 2585.

[289] T. Brando et al., "Search for narrow structure in proton antiproton annihilation cross-sections from 1900 MeV to 1960 MeV", Phys. Lett. **B158** (1985) 505.

[290] E. Eisenhandler et al., "Differential cross-sections for antiproton - proton elastic scattering between 0.69 GeV/c and 2.43 GeV/c ", Nucl. Phys. **B113** (1976) 1.

[291] R.P. Hamilton et al., "Measurement of the $\bar{\mathrm{p}}\mathrm{p}$ charge exchange cross-section from 0.119 GeV/c to 1.046 GeV/c ", Phys. Rev. Lett. **44** (1980) 1179.

[292] D. Cutts et al., "Antiproton - proton charge-exchange between 1 GeV/c and 3 GeV/c", Phys. Rev. **D17** (1978) 16.

[293] C. Amsler, "$\bar{\mathrm{p}}\mathrm{p}$ interaction and the quest for baryonium", Adv. Nucl. Phys. **18**(1987) 183.

[294] E.P. Wigner, "On the behaviour of cross sections near thresholds", Phys. Rev. **73** (1948) 1002.

[295] J. Carbonell, K.V. Protasov and A. Zenoni, "$\bar{\mathrm{p}}\mathrm{p}$ low energy parameters from annihilation cross section data", Phys. Lett. **B397** (1997) 345.

[296] T. Bressani et al., "Measurement of antiproton proton elastic and annihilation cross section below 100 MeV/c ", CERN-SPSC-2000-022-REV.

[297] G. Bendiscioli et al., "Isospin effects in $\bar{\mathrm{p}}\ ^3$He annihilation at rest", in [39].

[298] F. Balestra et al., "Evidence of isospin effects in antiproton - nucleus annihilation", Nucl. Phys. **A491** (1989) 572.

[299] C.J. Batty et al., "Measurement of the differential cross-section in proton - proton scattering at 49.41 MeV", Nucl. Phys. **A98** (1967) 489.

[300] S. Sakamoto, T. Hashimoto, F. Sai and S.S. Yamamoto, "Study of $\bar{\mathrm{p}}\mathrm{p}$ elastic scattering in the momentum range 374 MeV/c to 680 MeV/c ", Nucl. Phys. **B195** (1982) 1.

[301] T.A. Shibata et al., "Antiproton - proton cross-section at small momenta", in [54].

[302] J. Carbonell, O.D. Dalkarov, K.V. Protasov and I.S. Shapiro, "The origin of P wave enhancement in the optical model for low-energy proton - antiproton scattering", Nucl. Phys. **A535** (1991) 651.

[303] P. Jenni et al., "Measurement of the real part of the forward amplitude in $\bar{\mathrm{p}}\mathrm{p}$ elastic scattering", Nucl. Phys. **B94** (1975) 1.

[304] M. Cresti, L. Peruzzo and G. Sartori, "A measurement of the $\bar{\mathrm{p}}\mathrm{p}$ differential elastic cross-section and of the Coulomb - nuclear interference between 353 MeV/c and 578 MeV/c ", Phys. Lett. **B132** (1983) 209.

[305] V. Ashford et al., "Measurement of the real to imaginary ratio of the $\bar{\mathrm{p}}\mathrm{p}$ forward scattering amplitudes", Phys. Rev. Lett. **54** (1985) 518.

[306] M. Lacombe, B. Loiseau, B. Moussallam and R. Vinh Mau, "Spin effects in low-energy proton-antiproton forward elastic scattering", Phys. Lett. **B124** (1983) 443.

[307] H. Iwasaki et al., "Measurement of the real-to-imaginary ratio of the $\bar{\mathrm{p}}\mathrm{p}$ forward amplitude at beam momenta between 400 and 730 MeV/c ", Phys. Lett. **B103** (1981) 247.

[308] O.D. Dalkarov and K.V. Protasov, "Ratio of the real and imaginary parts of $\bar{\mathrm{p}}\mathrm{p}$ scattering amplitude near the $\overline{\mathrm{N}}\mathrm{N}$ threshold", JETP Lett. **44** (1986) 638.

[309] J.A. Niskanen, "A study of the forward amplitude real-to-imaginary ratio in low energy $\bar{\mathrm{p}}\mathrm{p}$ scattering", in [43].

[310] P. Kroll and W. Schweiger, "The ρ-parameter in low energy $\bar{\mathrm{p}}\mathrm{p}$ forward scattering", in [43].

[311] J.-M. Richard, "Spin dependence in $\overline{\mathrm{N}}\mathrm{N}$ at low-energy", in [41].

[312] J.-M. Richard, "Spin dependence in $\overline{\mathrm{N}}\mathrm{N}$ scattering at low-energy", CERN-TH-2978, Oct 1980, in *International Symposium on High Energy Physics with Polarized Beams and Polarized Targets*, Lausanne, Switzerland, Sep 25 - Oct 1, 1980. C. Joseph and J. Soffer (eds.); Birkhauser, Experientia Supplementum, v. 38 (1981).

[313] HEPDATA: REACTION DATA Database (Durham-UK), BRUCKNER 85 - Experiment CERN-PS-173 (RED 2050) (2001), http://durpdg.dur.ac.uk/HEPDATA/REAC.

[314] K. Nakamura et al., "Measurement of the $\bar{\mathrm{p}}\mathrm{p} \to \bar{\mathrm{n}}\mathrm{n}$ differential cross-sections at low momenta and confirmation of the forward dip", Phys. Rev. Lett. **53** (1984) 885.

[315] H. Kohno et al., "$\bar{\mathrm{p}}\mathrm{p}$ elastic and charge exchange scattering at 230 MeV", Nucl. Phys. **B41**(1972) 485.

[316] A. Colebourne et al., "The total and differential cross-section for the reaction $\bar{\mathrm{p}}\mathrm{p} \rightarrow \bar{\mathrm{n}}\mathrm{n}$ at 1.13 GeV/c ", Nucl. Phys. **B70**(1974) 205.

[317] S. Banerjee et al., "Studies of $\bar{\mathrm{p}}\mathrm{p} \rightarrow \bar{\mathrm{n}}\mathrm{n}$ and $\bar{\mathrm{n}}\mathrm{p}$ annihilation at incident momenta of 700 MeV/c and 760 MeV/c ", Z. Phys. **C28** (1985) 163.

[318] M. Bogdanski et al., "Observation of a dip-bump structure in differential cross-section for $\bar{\mathrm{p}}\mathrm{p} \rightarrow \bar{\mathrm{n}}\mathrm{n}$ in the 700 MeV/c to 760 MeV/c momentum range", Phys. Lett. **B62** (1976) 117.

[319] J.J. de Swart, M.C. Rentmeester and R.G. Timmermans, "The status of the pion nucleon coupling constant," in *7^{th} International Symposium on Meson - Nucleon Physics and the Structure of the Nucleon*, Vancouver, Canada, 28 July - 1 August 1997. H.-M. Staudemaier (ed.); PiN Newslett. **13** (1997).

[320] T.E. Ericson, "The πNN coupling constant," in *13^{th} International Conference on Few Body Problems in Physics*, Adelaide, Australia, 5-11 January 1992. I.R. Arnan and R.T. Cahill (eds.); Nucl. Phys. A **543** (1992).

[321] R.J.N. Phillips, "Antinuclear forces", Rev. Mod. Phys. **39**(1967) 681.

[322] R.G. Timmermans, T.A. Rijken and J.J. de Swart, "Determination of the charged pion coupling constant from data on the charge exchange reaction $\bar{\mathrm{p}}\mathrm{p} \rightarrow \bar{\mathrm{n}}\mathrm{n}$", Phys. Rev. Lett. **67** (1991) 1074.

[323] F. Bradamante and A. Martin, "Manifestation of the pion pole in $\bar{\mathrm{p}}\mathrm{p} \rightarrow \bar{\mathrm{n}}\mathrm{n}$ charge exchange scattering", Phys. Lett. **B343** (1995) 427.

[324] F. Bradamante, A. Bressan, M. Lamanna and A. Martin, "Determination of the charged pion-nucleon coupling constant from $\bar{\mathrm{p}}\mathrm{p} \rightarrow \bar{\mathrm{n}}\mathrm{n}$ differential cross-section", Phys. Lett. **B343** (1995) 431.

[325] T.E.O. Ericson and B. Loiseau, "Systematic corrections in the extraction of the πNN coupling from $\bar{\mathrm{p}}\mathrm{p} \rightarrow \bar{\mathrm{n}}\mathrm{n}$ differential cross sections", in [46].

[326] A. Martin, "Results on $\overline{\mathrm{N}}\mathrm{N}$ scattering", in [46].

[327] F. Bradamante, "Critical review of $\overline{\mathrm{N}}\mathrm{N}$ scattering", in [47].

[328] W. Brückner et al., "Ranges of interaction in $\bar{\mathrm{p}}\mathrm{p}$ scattering at low-energies", Z. Phys. **A339** (1991) 379.

[329] L.I. Schiff, *Quantum Mechanics*, McGraw-Hill, New York, 3^{rd} edition (1968).

[330] J. Haidenbauer, T. Hippchen, K. Holinde and J. Speth, "On the range of the nucleon anti-nucleon interaction", Z. Phys. **A334** (1989) 467.

[331] J. Haidenbauer, T. Hippchen and K. Holinde, "The Bonn $\overline{\mathrm{N}}\mathrm{N}$ potential and the range of $\overline{\mathrm{N}}\mathrm{N}$ annihilation", Nucl. Phys. **A508** (1990) 329C.

[332] M.G. Albrow et al., "Polarization in elastic antiproton-proton scattering between 0.9 and 2.5 GeV/c ", Nucl. Phys. **B37** (1972) 349.

[333] W.H. Frahn and R.H. Venter, "Strong absorption model for elastic nuclear scattering and polarization of spin-$\frac{1}{2}$ particles", Annals of Physics **27**(1964) 135, 385.

[334] M.P. Macciotta et al., "Extension od Experiment PS199: further study of the spin structure of $\bar{\mathrm{p}}\mathrm{N}$ scattering at LEAR", CERN-PSCC-90-12, PSCC-P93 Add. 2; CERN (Geneva), 1990.

[335] M.P. Macciotta et al., "Extension od Experiment PS199: measurement of the analysing power in $\bar{\mathrm{p}}\mathrm{n}$ elastic scattering", CERN-PSCC-90-38, PSCC-P93 Add. 3; CERN (Geneva), 1990.

[336] P.D. Barnes et al., "Status and future of experiment PS-185 ($\bar{\mathrm{p}}\mathrm{p} \to \overline{\Lambda}\Lambda$) at Cern," in [42].

[337] M. Burkardt and M. Dillig, "The $\bar{\mathrm{p}}\mathrm{p} \to \overline{\Lambda}\Lambda$ reaction in the one-gluon exchange and the $^3\mathrm{P}_0$ models," Phys. Rev. C **37** (1988) 1362.

[338] M.A. Alberg, E.M. Henley and L. Wilets, "Comment on 'The $\bar{\mathrm{p}}\mathrm{p} \to \overline{\Lambda}\Lambda$ reaction in the one-gluon exchange and the triplet P-wave models'," Phys. Rev. C **38** (1988) 1506.

[339] P.D. Barnes et al., "Results from PS185," in [47].

[340] P.D. Barnes et al., "High-statistics measurements of the $\bar{\mathrm{p}}\mathrm{p} \to \overline{\Lambda}\Lambda$ and $\bar{\mathrm{p}}\mathrm{p} \to \overline{\Sigma}^0\Lambda + \mathrm{c.c.}$ + c.c. reactions at threshold", Phys. Rev. C62 (2000) 055203.

[341] J. Haidenbauer, K. Holinde, V. Mull and J. Speth, "Can one discriminate between meson-exchange and quark-gluon transition mechanisms in the $\bar{\mathrm{p}}\mathrm{p} \to \overline{\Lambda}\Lambda$ process?" Phys. Lett. B **291** (1992) 223.

[342] J. Haidenbauer, K. Holinde, V. Mull and J. Speth, "Meson-exchange and quark-gluon transitions in the $\bar{\mathrm{p}}\mathrm{p} \to \overline{\Lambda}\Lambda$ process," Phys. Rev. C **46** (1992) 2158.

[343] J.-M. Richard, "Remarks about spin measurements in $\bar{\mathrm{p}}\mathrm{p} \to \overline{\Lambda}\Lambda$," Phys. Lett. B **369** (1996) 358.

[344] P.M. Maessen, T.A. Rijken and J.J. de Swart, "Soft-core baryon-baryon one-boson-exchange models. 2. Hyperon-nucleon potential," Phys. Rev. C **40** (1989) 2226.

[345] D. Halderson, "Nijmegen soft core Y N potential with bound state restrictions," Phys. Rev. C **60** (1999) 064001.

[346] R. Rückl and C. Zupancic, "Inner bremsstrahlung in low-energy antiproton-proton annihilation," Phys. Lett. **B150** (1985) 225.

[347] F. Kayser and E. Klempt, "Angular correlations between X-raysof $\bar{\mathrm{p}}\mathrm{p}$ atoms and annihilation products," in [42].

[348] R. Armenteros et al., "A study of $\bar{\mathrm{p}}\mathrm{p}$ interactions at rest in a H_2 gas target at LEAR," Proposal P28 to the PSCC, CERN/PSCC/80-101, (1980).

[349] T.E. Ericson and L. Hambro, "The absorptive line shape of hadronic atoms," Annals Phys. **107** (1977) 44.

[350] E. Klempt et al., "X-ray transitions in antiprotonic hydrogen atoms and their line shape," in [43].

[351] A. Bianconi et al., "Measurements of cascade times of antiprotons in molecular hydrogen and helium," Phys. Lett. **B487** (2000) 224.

[352] R.A. Burnstein, G.A. Snow, and H. Whiteside, "Absorption of negative Σ hyperons in liquid hydrogen," Phys. Rev. Lett. **15** (1965) 639.

[353] C.J. Batty, "Antiprotonic hydrogen atoms," Rept. Prog. Phys. **52** (1989) 1165.

[354] D. Anagnostopoulos et al., "Precision measurement of the energies and line shapes of antiprotonic Lyman and Balmer transitions from hydrogen and helium isotopes," Proposal To The Pscc, CERN-PSCC-90-9.

[355] C.J. Batty, "S- versus P-state annihilation in $\bar{\mathrm{p}}\mathrm{d}$ interactions at rest," Nucl. Phys. A **703** (2002) 17.

[356] A. Adamo et al., "Antiproton stopping power in hydrogen below 120-keV and the Barkas effect," Phys. Rev. A **47** (1993) 4517.

[357] G. Reifenröther, "Leichte antiprotonische Atome von der Bildung bis zur Vernichtung," Dissertation, Mainz 1989 (unpublished).

[358] J.S. Cohen and N.T. Padial, "Initial distributions, cascade, and annihilation of $\bar{\mathrm{p}}\mathrm{p}$ atoms formed in $\bar{\mathrm{p}}$ + H and $\bar{\mathrm{p}}$ + H^- collisions in near-vacuum," Phys. Rev. **A41** (1990) 3460.

[359] G.A. Baker, "Stopping of π^- and K^- mesons on hydrogen in nuclear emulsion," Phys. Rev. 117 (1960) 1130.

[360] J.S. Cohen, "Comment on the classical-trajectory Monte Carlo method for ion-atom collisions," Phys. Rev. A26 (1982) 3008.

[361] G. Reifenroether and E. Klempt, "Annihilation of antiprotons at rest in H_2 and D_2: S versus P state capture," Phys. Lett. B **245** (1990) 129.

[362] C.J. Batty, "S- and P-state annihilation in $\bar{\mathrm{p}}\mathrm{p}$ interactions at rest," Nucl. Phys. **A601** (1996) 425.

[363] C. Amsler et al., "P wave versus S wave $\bar{\mathrm{p}}\mathrm{p}$ annihilation at rest in LH_2," Phys. Lett. **B297** (1992) 214.

[364] C. Amsler et al., "Antiproton-proton annihilation at rest into two body final states," Z. Phys. **C58** (1993) 175.

[365] A. Abele et al., "Test of $\overline{\mathrm{N}}\mathrm{N}$ potential models: Isospin relations in $\bar{\mathrm{p}}\mathrm{d}$ annihilations at rest and the search for quasinuclear bound states," Eur. Phys. J. **C17** (2000) 583.

[366] F. Myhrer, "Antinucleon-nucleon scattering", AIP Conf. Proc. 243 (1992) 325, in *4^{th} Conference On The Intersections Between Particle And Nuclear Physics*, Tucson, Arizona, 24-29 May 1991.

[367] B. El-Bennich, M. Lacombe, B. Loiseau and R. Vinh Mau, "Refining the inner core of the Paris $\overline{\mathrm{N}}\mathrm{N}$ potential," Phys. Rev. C **59** (1999) 2313.

[368] P.H. Timmers, W.A. van der Sanden and J.J. de Swart, "An antinucleon-nucleon potential", Phys. Rev. D29 (1984) 1928.

[369] R. Timmermans, Ph.D. thesis, University of Nijmegen, The Netherlands (1991).

[370] J.J. de Swart and R. Timmermans, "The antibaryon-baryon interactions", in [21].

[371] J.J. de Swart, T.A. Rijken and R. Timmermans, "$\bar{\mathrm{p}}\mathrm{p}$ partial wave analysis and $\overline{\mathrm{N}}\mathrm{N}$ potentials", in [50].

[372] M.M. Nagels, T.A. Rijken and J.J. de Swart, "A low-energy nucleon-nucleon potential from regge pole theory", Phys. Rev. D17 (1978) 768.

[373] M. Pignone, M. Lacombe, B. Loiseau and R. Vinh Mau, "Recent proton-antiproton low-energy data and the Paris $\overline{\mathrm{N}}\mathrm{N}$ potential," Phys. Rev. Lett. **67** (1991) 2423.

[374] M. Laloum, "$\bar{\mathrm{p}}\mathrm{p}$ partial-wave analysis at 400MeV/c and 500 Mev/c," Phys. Lett. **58B** (1975) 491.

[375] J.R. Bergervoet et al., "Optimal polynomial theory applied to 0 MeV - 350 MeV scattering", Phys. Rev. C38 (1988) 770.

[376] J.R. Bergervoet et al., "Phase-shift analysis of all proton-proton scattering data below T(lab) = 350 MeV", Phys. Rev. C41 (1990) 1435.

[377] V.G.J. Stoks et al., "Partial wave analysis of all nucleon-nucleon scattering data below 350 MeV", Phys. Rev. C48 (1993) 792.

[378] F. Bradamante, R. Hess and J.M. Richard, "Antinucleon-nucleon scattering and potential models", Few Body Syst. 14 (1993) 37, (Summary of a Workshop held at Archamps).

[379] J.-M. Richard, "Comment on 'Antiproton-proton partial wave analysis below 925 MeV/c'," Phys. Rev. C **52** (1995) 1143.

[380] R. Timmermans, T.A. Rijken and J.J. de Swart, "Reply to: Comment on 'Antiproton-proton partial wave analysis below 925 MeV/c'," Phys. Rev. C **52** (1995) 1145.

[381] A.G. Schneider-Neureither, H.J. Pirner, B. Kerbikov and J. Mahalabanis, "Scattering length expansion of the coupled channels $\bar{\mathrm{p}}\mathrm{p} \to \overline{\Lambda}\Lambda$ and $\overline{\Lambda}\Lambda \to \overline{\Lambda}\Lambda$ near the Λ production threshold," Z. Phys. A **344** (1993) 317.

[382] J. Badier et al., "Reactions $\bar{\mathrm{p}}\mathrm{p} \to \overline{\Lambda}\Lambda$ at 2.5 GeV/c," Phys. Lett. **25B** (1967) 152.

[383] N. Kwak et al., "Spin correlations in $\bar{\mathrm{p}}\mathrm{p} \to \overline{\Lambda}\Lambda$ at 2.19 GeV/c", Phys. Rev. 186 (1969) 1392.

[384] J. Carbonell, K.V. Protasov and O.D. Dalkarov, "On a possible near threshold $\overline{\Lambda}\Lambda$ state," Phys. Lett. B **306** (1993) 407.

[385] F. Tabakin and R.A. Eisenstein, "Meson exchange calculation of the $\bar{\mathrm{p}}\mathrm{p} \to \overline{\Lambda}\Lambda$ reaction," Phys. Rev. C 31 (1985) 1857.

[386] M. Kohno and W. Weise, "Role of Kaon-exchange in the $\bar{\mathrm{p}}\mathrm{p} \to \overline{\Lambda}\Lambda$ reaction," Phys. Lett. B 179 (1986).

[387] P. LaFrance and B. Loiseau, "Study from threshold to high momenta of the $\bar{\mathrm{p}}\mathrm{p} \to \overline{\Lambda}\Lambda$ reaction," Nucl. Phys. A **528** (1991) 557.

[388] F. Tabakin, R.A. Eisenstein and Y. Lu, "Spin observables at threshold for the reaction $\bar{\mathrm{p}}\mathrm{p} \to \overline{\Lambda}\Lambda$," Phys. Rev. C **44** (1991) 1749.

[389] J.A. Niskanen, preprint HU-TFT-85-28.

[390] A. Green and J. Niskanen, "Low-energy antiproton physics in the early LEAR era", Prog. Part. Nucl. Phys. 18 (1987) 93.

[391] P. LaFrance, B. Loiseau, and R. Vinh Mau, "Effects of initial and final state interactions in the $\bar{\mathrm{p}}\mathrm{p} \to \overline{\Lambda}\Lambda$ reaction," Phys. Lett. B 214 (1988) 317 .

[392] M. Kohno and W. Weise, "The $\bar{\mathrm{p}}\mathrm{p} \to \overline{\Lambda}\Lambda$ reaction close to threshold," Phys. Lett. B 206 (1988) 584.

[393] M. Kohno and W. Weise, "Anti-Hyperon - Hyperon production in low-energy anti-proton - proton reactions," in *International Symposium On Strangeness In Hadronic Matter*, Bad Honnef, Germany, 1-5 June 1987, Nucl. Phys. A479 (1988) 433c.

[394] J. Haidenbauer et al., "The reaction $\bar{\mathrm{p}}\mathrm{p} \to \overline{\Lambda}\Lambda$ in the meson exchange picture," Phys. Rev. C **45** (1992) 931.

[395] J. Haidenbauer, K. Holinde, and J. Speth, "Antihyperon-hyperon production in the meson-exchange framework," Phys. Rev. C **46** (1992) 2516.

[396] J. Haidenbauer, K. Holinde, and J. Speth, "A meson-exchange model for the antihyperon-hyperon production," Nucl. Phys. A **562** (1993) 317.

[397] J. Haidenbauer, K. Holinde, and J. Speth, "$\bar{\mathrm{p}}\mathrm{p} \rightarrow \bar{\Xi}\Xi$ reaction in the meson-exchange picture," Phys. Rev. C **47** (1993) 2982.

[398] R.G.E. Timmermans, T.A. Rijken and J.J. de Swart, "Determination of the ΛpK coupling constant from LEAR data on $\bar{\mathrm{p}}\mathrm{p} \rightarrow \overline{\Lambda}\Lambda$", Phys. Lett. **B257** (1991) 227.

[399] R.G.E. Timmermans, T.A. Rijken and J.J. de Swart, "Strangeness exchange in anti-proton proton scattering", Phys. Rev. D45 (1992) 2288.

[400] R.G.E. Timmermans, T.A. Rijken and J.J. de Swart, "Strangeness exchange in proton anti-proton reactions", Nucl. Phys. A479 (1988) 383c, in *International Symposium On Strangeness In Hadronic Matter*, Bad Honnef, Germany, 1-5 June 1987.

[401] A. Le Yaouanc et al., "Hadron transitions in the quark model", Gordon and Breach, N.Y., USA (1988).

[402] H. Rubinstein and H. Snellman, "Dynamics of QCD in the nonperturbative low-energy region," Phys. Lett. 165B (1985) 187.

[403] P. Kroll and W. Schweiger, "A diquark model for $\bar{\mathrm{p}}\mathrm{p}$ annihilation into hyperon - anti-hyperon," Nucl. Phys. A474 (1987) 608.

[404] "Internal fusion diagrams for $\bar{\mathrm{p}}\mathrm{p}$ annihilation," H. Genz and S. Tatur, Phys. Rev. D **30** (1984) 63.

[405] G. Brix, H. Genz and S. Tatur, 'Internal meson dominance for $\bar{\mathrm{p}}\mathrm{p}$ annihilation," Phys. Rev. D **39** (1989) 2054.

[406] M.A. Alberg, E.M. Henley, W. Weise, "Singlet fraction in $\bar{\mathrm{p}}\mathrm{p} \rightarrow \overline{\Lambda}\Lambda$," Phys. Lett. B **255** (1991) 498.

[407] S. Furui and A. Faessler, "Antiproton-proton to hyperon-antihyperon transition potential in the quark model," Nucl. Phys. A **468** (1987) 669.

[408] K. Paschke et al., "Measurement of spin observables in exclusive $\bar{\mathrm{p}}\mathrm{p} \rightarrow \overline{\Lambda}\Lambda$ production", in [48].

[409] A. Benedettini et al., "$\bar{\mathrm{p}}\mathrm{p}$ partial cross-sections at low energy," in [46].

[410] A. Bianconi et al., "Coulomb corrections to low energy antiproton annihilation cross-sections on protons and nuclei," Phys. Rev. **C 62** (2000) 14611.

[411] E.P. Wigner, "On the behaviour of cross sections near thresholds," Phys. Rev. **73** (1948) 1002.

[412] K.V. Protasov, G. Bonomi, E. Lodi Rizzini and A. Zenoni, "Antiproton annihilation on light nuclei at very low energies," Eur. Phys. J. **A7** (2000) 429.

[413] B. Moussallam, "$\bar{\mathrm{p}}\mathrm{p}$ interactions very close to the threshold," Z. Physik A **325** (1986) 1.

[414] E. Klempt, "Antiprotonic hydrogen: initial state interactions," Phys. Lett. **B244** (1990) 122.

[415] A. Abele et al., "Branching ratios for $\bar{\mathrm{p}}\mathrm{p}$ annihilation at rest into two body final states", Nucl. Phys. A679 (2001) 563.

[416] G.Q. Liu, J.-M. Richard and S. Wycech, "Simple approaches to anti-protonic deuterium," Phys. Lett. **B260** (1991) 15.

[417] G. P. Latta and P.C. Tandy, "Annihilation shifts and widths of the $\bar{p}d$ atomic levels," Phys. Rev. C **42** (1990) 1207.